DISCLAIMER
The publication of papers in International Journal of Engineering does not imply that the editorial board, reviewers or publisher accept, approve or endorse the data and conclusions of authors.

CONTENTS

Transactions C: Aspects

International Journal of Engineering

Journal Homepage: www.ije.ir

Design and Analysis of Hetero Dielectric Dual Material Gate Underlap Spacer Tunnel Field Effect Transistor

S. Howldar, B. Balaji*, K. Srinivasa Rao

Department of Electronics and Communication Engineering, Koneru Lakshmaiah Education Foundation, Green Fields, Vaddeswaram, Andhra, India

A B S T R A C T

This paper presents a design and analysis of a Hetero Dielectric Dual Material Gate Underlap Spacer Tunnel Field Effect Transistor, aiming to enhance device performance and overcome inherent limitations. The proposed design incorporates a hetero dielectric gate stack, which consists of two distinct dielectric materials such as high-k-dielectric material as hafnium oxide (HfO_2) and low-k dielectric material as silicon dioxide (SiO_2). With different permittivity values. By selecting these materials, the gate stack can effectively modulate the electric field distribution within the device, improving electrostatic control and reducing ambipolar conduction. Furthermore, an underlap spacer is introduced in the presented structure to create a physical separation between the source and the channel regions. This spacer helps in reducing the direct source-to-drain tunneling current, enhancing the Ion/Ioff current ratio and reducing the subthreshold swing. Additionally, the underlap spacer enables improved gate control over the tunneling process. The proposed Tunnel Field Effect Transistor design is thoroughly analyzed using numerical simulations based on the technology computer-aided design (TCAD) simulator. Performance metrics as the on-state current (Ion), the off-state current (Ioff), ION/IOFF ratio, drain conductance (Gd) and transconductance (Gm) to assess the device's performance. Therefore, these improvements contribute to lower power consumption and improved circuit performance, making it a promising device for low-power applications.

doi: 10.5829/ije.2023.36.12c.01

NOMENCLATURE

HfO_2	Hafnium oxide	Si	Silicon
SiO_2	Silicon dioxide	Ion	On state current
Ioff	Off state current	G_d	Drain conductance
Gm	Transconductance	I_d	Drain Current
Vgs	Gate to source voltage	V_{ds}	Drain to source voltage

1. INTRODUCTION

In recent years, the constant demand for faster and more energy-efficient electronic devices has led to the exploration of novel transistor designs. Traditional metal-oxide-semiconductor field-effect transistors (MOSFETs) have been the cornerstone of the semiconductor industry for several decades. The MOSFET is a fundamental electronic device that forms the building block of modern integrated circuits (ICs) [1]. It is a type of field-effect transistor that relies on the

modulation of an electric field to control the flow of current. MOSFETs are widely used in various electronic devices Such as computers smartphones, power amplifiers and memory chips. However, their performance improvements have encountered significant challenges in recent years, primarily due to limitations related to power consumption and leakage current [2].

TFET is an emerging transistor technology that aims to overcome certain limitations of MOSFETs, particularly in terms of power consumption and subthreshold leakage [3, 4]. TFETs operate based on the

*Corresponding Author Email: vahividi@gmail.com (B. Balaji)

principle of quantum tunneling, where charge carriers (typically electrons) can pass through a thin barrier without requiring high energy. In TFETs, the conducting channel is replaced by a thin insulating barrier (tunneling junction) between the source and drain terminals. By applying a voltage to the gate terminal, a strong electric field is created across the barrier, facilitating quantum tunneling of carriers from the source to the drain. This tunneling mechanism enables TFETs to achieve lower threshold voltages and potentially reduce power consumption compared to MOSFETs [5].

TFET hold promise for low power applications and are actively researched to improve their performance and overcome challenges related to switching speed, on/off current ratio, and manufacturing scalability. However, TFET technology is still in the early stages of development, and practical implementation and widespread adoption are yet to be realized [6].

Dual material Gate TFET is a variation of TFET design that incorporates two different materials in the gate structure such as high-k dielectric material as hafnium oxide (HfO_2) and low-k dielectric material as silicon dioxide (SiO_2) instead of using a single material [7]. The use of distinct materials in the gate region allows for enhanced control over the transistor's behavior and provides unique performance benefits. Dual Material Gate TFETs have gained attention as a potential solution for achieving improved performance and energy efficiency [8].

The operation of dual material TFET is based on the principle of quantum band to band tunneling (BTBT), where charge carriers pass through a thin barrier to control the flow of current. By utilizing two different materials in the gate structure, the transistor's characteristics can be tailored to achieve desired performance metrics [9].

In this paper, we have designed a advanced Hetero Dielectric Dual Material Gate Underlap Spacer TFET, to overcome the limitations of conventional TFET designs and further to improve device performance parameters in submicron technology. The key components of this design include a hetero dielectric gate stack and an underlap spacer [10, 11]. The hetero dielectric gate stack involves the use of two different dielectric materials such as high-k dielectric material as hafnium oxide (HfO_2) and low-k dielectric material as silicon dioxide (SiO_2) [12]. By selecting these dielectric materials in the proposed structure the electric field distribution leading to enhanced electrostatic control. This improved control helps to reduce ambipolar conduction, a significant challenge in TFETs, and allows for efficient modulation of the device's on/off characteristics [13].

In addition to the hetero dielectric gate stack, we have incorporated an underlap spacer in the TFET structure. The underlap spacer creates a physical separation between the source and the channel regions. This separation plays a vital role in reducing the direct source-to-drain tunneling current, which is a major contributor to off-state leakage in TFETs [14]. By minimizing this leakage current, the underlap spacer improves the on/off current ratio and enhances the overall performance of the device.The combination of the hetero dielectric gate stack and the underlap spacer offers significant advantages for TFET performance. However, it requires a comprehensive analysis to understand the impact of these design modifications on various device metrics. Therefore, in this work, we used technology computer-aided design (TCAD) framework to evaluate the performance of the proposed device [15].

The advantages of this model have the significantly reduce leakage current, leading to improved energy efficiency, making them valuable for low power and provide better performance leading to high performance integrated circuits. It could align with the trend of increasing transistor density, which is crucial for advanced semiconductor technology.

The disadvantages of this Design increase the complexity of the fabrication process, higher production costs under various operating conditions and manufacturing variations is essential for real-world applications. Developing comprehensive testing methods for the new design to verify its performance, reliability, and compatibility can be a complex and time-consuming task.

In this paper the proposed device and utilized parameters are presented in second section. The result and discussions are presented in third section. The final section presented with conclusion.

2. STRUCTURE OF PROPOSED DEVICE

The proposed TFET device made of high-k and low-k dielectric materials and is responsible for the tunneling of charge carriers. The gate stack of the TFET incorporates a hetero dielectric material composition. It consists of two distinct dielectric materials such as high-k dielectric material as hafnium oxide (HfO_2) and low-k dielectric material as silicon dioxide (SiO_2). The choice of these materials is critical as it influences the electric field distribution and the tunneling behavior within the device. To enhance the device's performance, an underlap spacer is introduced between the source and channel regions. This spacer physically separates the two regions, reducing direct source-to-drain tunneling current [16].

In the proposed structure different work functions are used to optimize the tunneling characteristics of the HD-DMG-US TFET. By carefully selecting the materials for the source, channel, and drain regions, the bandgap can be tailored to facilitate efficient tunneling. The band gap engineering ensures a favorable alignment of the band edges between the source and channel regions. This alignment promotes efficient carrier tunneling through the tunneling barrier while minimizing leakage current

when the device is in the off-state [17]. Figure 1 shows the conventional TFET utilized high-k dielectric material being hafnium oxide (HfO_2) and low-k dielectric material as silicon dioxide (SiO_2) and silicon(Si).The HD-DMG-US TFET device dimensions of 60 nm, channel length of 5nm, source length of 27.5 nm, drain length of 27.5 nm.A gate is connected to the Silicon Dioxide (SiO_2) material at top and second gate connected to Silicon Dioxide (SiO_2) at the bottom [18]. Figure 2 shows the structure of Dual Material Gate TFETs where the, materials such as high-k and low-k dielectrics and Silicon (Si) are utilized for implementation [19].

Figure 3 shows the HfO_2 Spacer Tunnel FETs .The material utilised for the spacer in the device is HfO_2, and the same high-k dielectric material employed in four spots. Figure 4 shows the Hetero – Dielectirc Dual Material Gate Tunnel FET(HD-DMG-TFET) consists of two dielectric materials at the top and bottom under the gate such as high-k dielectric material as hafnium oxide (HfO_2) and low-k dielectric material as silicon dioxide (SiO_2),where SiO_2 acts as an interfacial layer between HfO_2 and the silicon channel region [20, 21]. This interface layer improves contact between the semiconductor and the HfO_2 and lowers the risk of defect development at the contact. The proposed Underlap Spacer Dielectric Tunnel FET(USD-TFET) as shown in Figure 5 can increase the channel resistance and induce ON-state current degradation [22].

The potential improvement of proposed structur could lead to more energy-efficient and have high-performance metrics such as on-state current, subthreshold slope (SS), and transconductance (gm).
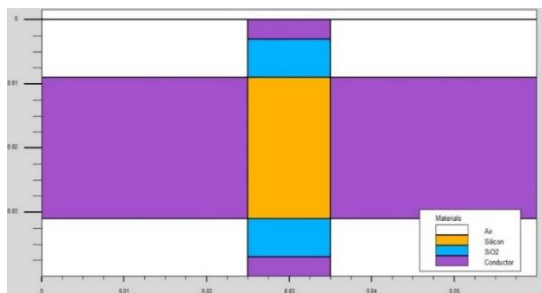
Figure 1. Two Dimensional View of Coventional TFET
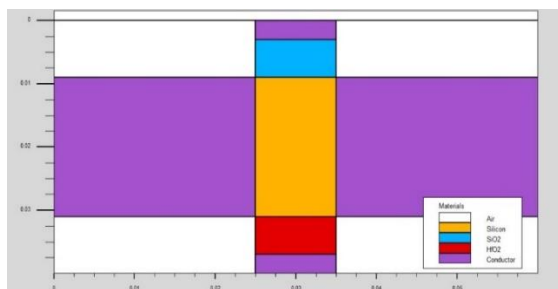
Figure 2. Two Dimensional View of Dual Material Gate TFET
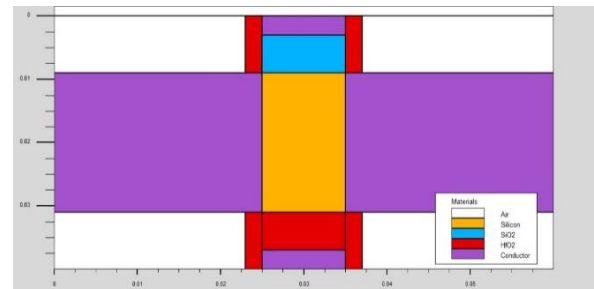
Figure 3. Two Dimensional View of HfO2 Spacer Tunnel TFET
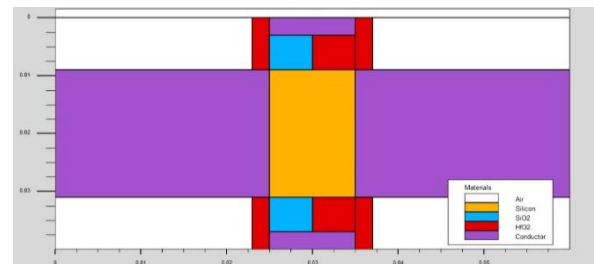
Figure 4. Two Dimensional View of Hetero Dielectric – Dual Material Gate Tunnel FET
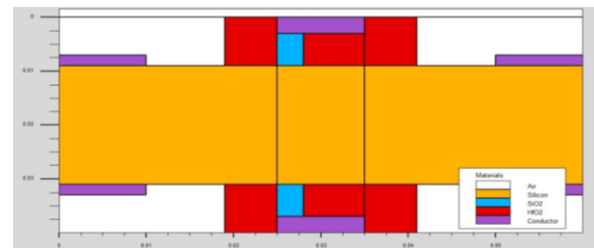
Figure 5. Proposed HD-DMG-US Tunnel FET

Innovative gate engineering techniques and materials are used to achieve lower subthreshold swing and reduced leakage current and performance calulated in nanotechnology. The Hetero Dielectric-DM-US TFET may be adaptable to advanced semiconductor fabrication processes and could be scaled down for future technology nodes, aligning with trends in nanoelectronics.

The HD-DMG-US TFET device utilized the different parameters for simulation as shown in Tables 1, 2 and 3. Table 4 shows the values of Ion and Ioff current, for different structures and different spacer length.

3. THE NOVALITY OF THE PROPOSED MODEL

3. 1. Hetero Dielectric Gate   The hetero dielectric refers to the use of different materials for the gate insulator in different regions of the transistor. This allows for more precise control of the electric field, which can impact the transistor's performance characteristics, such as the subthreshold swing and on-state curren.

TABLE 1. Parameter used for the proposed TFET

Parameter	HD-DMG-US TFET
Device Length (W_L)	60 nm
Gate Length (L_G)	5 nm
Source Length (L_S)	27.5nm
Drain Length (L_D)	27.5nm
Channel Length (L_C)	5nm
Doping of Source (D_S)	1×10^{17} cm^{-3}
Doping of Drain (D_D)	1×10^{18} cm^{-3}
Doping of Channel (D_C)	1×10^{20} cm^{-3}
Metal Gate Work Function (W_F)	4.8eV
Thickness of SiO$_2$	2nm
Thickness of HfO$_2$	3nm

TABLE 2. On-state and Off state currents for various TFET

TFET Architecture	IOFF	ION	ION
C-TFET	1.33E-10	4.01E-05	2.82E+05
DMG-TFET	2.10E-11	3.50E-05	3.13E+05
S-TFET	2.30E-11	3.48E-05	1.46E+06
HD-DMG-TFET	3.30E-11	3.21E-05	4.32E+07
Proposed Device	5.20E-11	2.05E-05	6.33E+07

TABLE 3. On-state and Off-state currents for different spacer length

Gate Length (nm)	I_{OFF}	I_{ON}	I_{ON}/I_{OFF}
5nm	5.10E-12	4.13E-05	5.50E+07
10nm	3.12E-11	4.70E-05	3.20E+06
15nm	2.12E-11	5.20E-05	2.50E+06

TABLE 4. On-state and Off-state currents for doping concentrations

HD-DMG-TFET	I_{OFF}	I_{ON}	I_{ON}/I_{OFF}
1×10^{17} cm^{-3} - Source	1.20E-11	3.35E-05	2.50E+06
1×10^{18} cm^{-3} - Drain	2.10E-11	3.25E-05	3.02E+06
1×10^{20} cm^{-3} -Channel	4.15E-11	3.15E-05	4.50E+07

3. 2. Dual Material Gate   The dual material gate indicates that the gate electrode, which controls the flow of current in the transistor, is composed of two distinct materials with different properties. This design can help optimize the transistor's electrostatics and enhance its switching performance.

3. 3. Underlap Spacer   The underlap spacer material placed between the source and drain regions.

This spacer serves multiple purposes, including reducing the direct source-to-drain tunneling current and improving the overall transistor performance.

4. RESULTS AND DISCUSSIONS

4. 1. Drain Current Characteristics   The Id Vs Vgs characteristics represent the drain current (Id) as a function of the gate-to-source voltage (Vgs). These characteristics provide insights into the transistor's behavior and its operating region. Figure 6 shows the characteristics of designed HD-DMG US TFET results are compared with C-TFET,DMG-TFET,S-TFET and HD-DMG-TFET. It can be seen that HD-DMG-US TFET exhibits much improved ON current compared to other devices. This is possible by the hetero dielectric materials such as high-k dielectric material as hafnium oxide (HfO$_2$) and low-k dielectric material as silicon dioxide (SiO$_2$).Due to heterojunction and dielectric materials lead to increase in the tunneling volume and due to the barrier width reduction [23]. The proposed device is much better than other devices because it uses materials with a lower energy threshold, has a special junction (heterojunction), and includes Hafnium Oxide (HfO$_2$) near where the electrical current flows (source-channel interface). These factors together allow more electrons to move through the device, and they also prevent a certain type of switching (ambipolar switching) at another interface (drain interface). This is achieved by applying a specific type of doping called Gaussian doping, which expands the depleted region where the current flows (drain-channel interface.

The I_d Vs V_{ds} characteristics of USD-TFET with different types of materials such as Hafnium Oxide (HfO$_2$), Silicon(Si), and Silicon Dioxide (SiO$_2$) [24], are found in this construction. The drain current of USD-TFET increased when compared to the other devices as shown in Figure 7.

The diagram illustrates the design of the proposed device, featuring two gates with distinct workfunctions ($\varphi 1$ and $\varphi 2$) for the tunnel gate, control gate, and auxiliary gates. By keeping the workfunctions of the tunnel gate and auxiliary gate constant ($\varphi 1$ and $\varphi 3$) and adjusting the workfunction of the control gate ($\varphi 2$), we can achieve the most efficient switching currents for the specific hetero combination [25].

We compared the DC performance of the HD-DMG-US TFET with a conventional device using dielectric materials. The influence of the source dielectric on the drain current with gate-source voltage (VGS) is depicted. We noticed a higher on-current (Ion) in the HD-DMG-US TFET, primarily attributed to reduced tunneling barriers at the junction, improved subthreshold slope, and a higher Ion/Ioff ratio. These characteristics make the HD-DMG-US TFET structure well-suited for low-power applications [26].
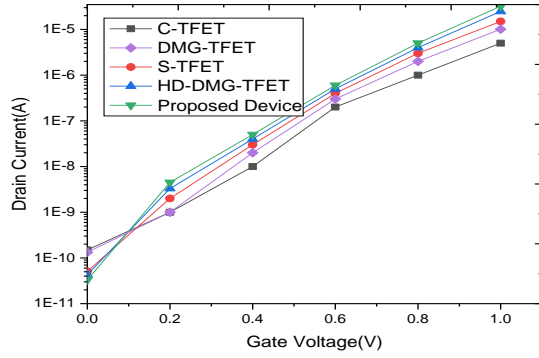
Figure 6. Comparision of Id vs Vgs Characteristics HD-DMG-US TFET with other devices

Figure 7. Comparision of Id vs Vds Characteristics HD-DMG-US TFET with other devices
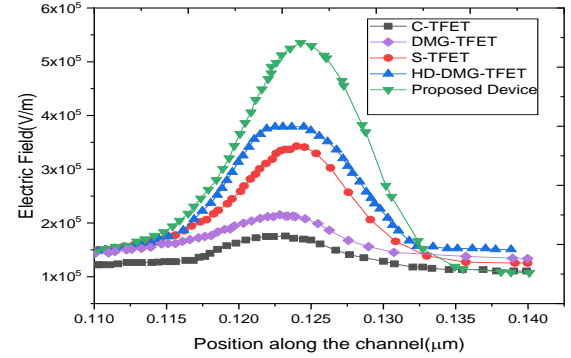
Figure 8. Electric field Comparision of HD-DMG- US TFET with other devices
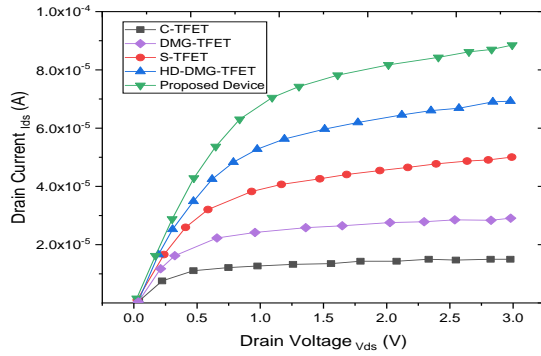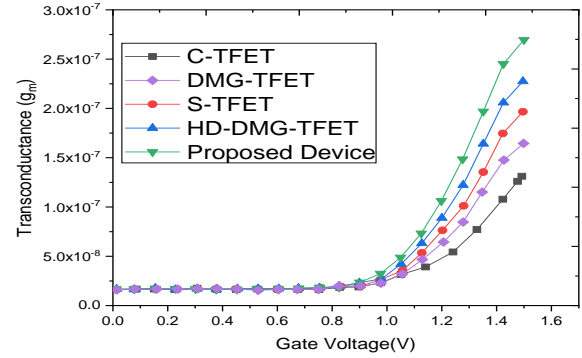
Figure 9. Transconductance Comparision of HD-DMG- US TFET with other devices

Cavity formation expands as the barrier width between the valence and conduction bands increases, indicating reduced electron tunneling. Consequently, the current conduction is diminished. Furthermore, when varying the cavity length, it was observed that the drain current (Id) at Vds = 1.0 V is significantly lower compared to Vds = 0.5 V. Hence, it becomes apparent that the HD-DMG-US-TFET with the gate underlap technique demonstrates the principle of tunneling.

Figure 8 shows the electric field distribution of proposed devices such as Underlap Spacer Dielectric Tunnel FET(USD-TFET), HD-DMG-TFET, Conventional-Tunnel FET, Dual Material Gate-Tunnel FET(DMG-TFET) and HfO₂ Spacer Tunnel FET(S-TFET) Devices.

4. 2. Analog Characteristics   Figure 9 shows transconductance(gm/Ids) of HD-DMG-US TFET comparision with Conventional-Tunnel FET, Dual Material Gate-Tunnel FET(DMG-US TFET) and HfO2 Spacer Tunnel FET(S-TFET) [27, 28]. The devices that turn on at higher voltages (threshold voltages) have low gm/Ids values. Higher gm/Ids values are obtained when the devices are OFF (Vth). Electrically doped devices

turn on at a lower voltage than conventionally doped devices, resulting in high gm/Ids for HD-DMG US TFET [29].

Figure 10 shows drain conductance of proposed device as a function of drain voltage for different structures.The drain ON (ION) and OFF (IOFF) currents as a function of device temperature [30, 31]. These findings revealed that the ON drain current increases linearly as temperature rises, whereas the drain OFF current rises exponentially as temperature rises. The primary electrical factors that govern the transistor's properties in analogue or digital circuits, such as ION /IOFF ratio, drain induced barrier lowering (DIBL), and VT, are all affected by the transistor's working temperature dependent characteristics as shown in Figure 11 [32].

The evaluation of proposed design performs at smaller feature sizes, considering quantum mechanical effects and the potential for use in advanced technology nodes.Analyze the potential for improved energy efficiency in low-power applications, especially in scenarios where the TFET's unique tunneling mechanism provides advantages over traditional MOSFETs. Consider the device's reliability under
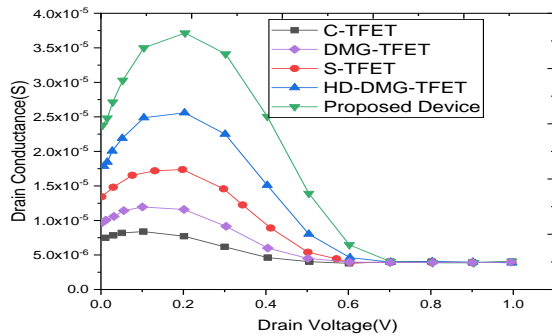
Figure 10. Drainconductance Comparision of HD-DMG-US TFET with other devices
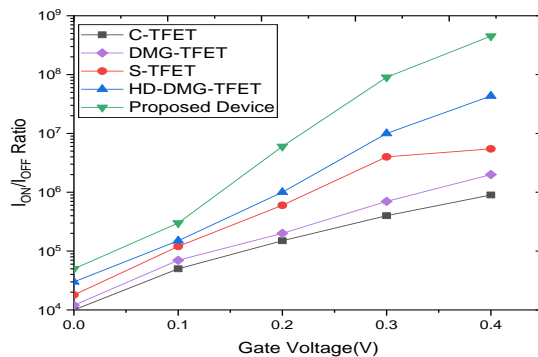
Figure 11. Ion/Ioff ratio Comparision of HD-DMG- US TFET with other devices

different operating conditions, stress, temperature, and process variability, and compare it to existing technologies [33].

5.CONCLUSION

The design and analysis of the Hetero Dielectric Dual Material Gate Underlap Spacer TFET offer significant advancements in the field of transistor technology and made of high-k dielectric material being hafnium oxide (HfO_2) and low-k dielectric material as silicon dioxide (SiO_2). The proposed device incorporates a hetero dielectric gate stack and an underlap spacer. It exhibited an improved on/off current ratio, reduced sub threshold swing, and enhanced gate control over the tunneling process. These improvements contribute to lower power consumption, increased switching efficiency, and better overall device performance. The underlap spacer played a crucial role in reducing off-state leakage current by physically separating the source and channel regions, while the hetero dielectric gate stack improved electrostatic control and minimized am bipolar conduction. The findings from this work highlight the

potential of the Hetero Dielectric Dual Material Gate Underlap Spacer TFET for future low-power electronic applications. Further research can focus on exploring additional combinations of dielectric materials for the gate stack, optimizing band gap engineering, and investigating the device's behavior under different operating conditions. Continued advancements in TFET technology will contribute to meeting the growing demands of the semiconductor industry for energy-efficient electronic devices.

6. REFERENCES

1.   Radhamma, E., Vemana Chary, D., Krishnamurthy, A., Venkatarami Reddy, D., Sreenivasa Rao, D., Gowthami, Y. and Balaji, B., "Performance analysis of high-k dielectric heterojunction high electron mobility transistor for rf applications", *International Journal of Engineering, Transactions C: Aspects*, Vol. 36, No. 9, (2023), 1652-1658. doi: 10.5829/ije.2023.36.09c.09.

2.   Gowthami, Y., Balaji, B. and Srinivasa Rao, K., "Performance analysis and optimization of asymmetric front and back pi gates with dual material in gallium nitride high electron mobility transistor for nano electronics application", *International Journal of Engineering, Transactions A: Basics* Vol. 36, No. 7, (2023), 1269-1277. doi: 10.5829/ije.2023.36.07a.08.

3.   Narang, R., Saxena, M. and Gupta, M., "Modeling and simulation investigation of sensitivity of symmetric split gate junctionless fet for biosensing application", *IEEE Sensors Journal*, Vol. 17, No. 15, (2017), 4853-4861. https://doi.org/10.1109/JSEN.2017.2716102

4.   Wangkheirakpam, V.D., Bhowmick, B. and Pukhrambam, P.D., "Investigation of a dual moscap tfet with improved vertical tunneling and its near-infrared sensing application", *Semiconductor Science and Technology*, Vol. 35, No. 6, (2020), 065013. https://doi.org/10.1088/1361-6641/ab8172

5.   Gowthami, Y., Balaji, B. and Rao, K.S., "Design and performance evaluation of 6nm hemt with silicon sapphire substrate", *Silicon*, Vol. 14, No. 17, (2022), 11797-11804. https://doi.org/10.1007/s12633-022-01900-7

6.   Kumar, P.K., Balaji, B. and Rao, K.S., "Performance analysis of sub 10 nm regime source halo symmetric and asymmetric nanowire mosfet with underlap engineering", *Silicon*, Vol. 14, No. 16, (2022), 10423-10436. doi. https://doi.org/10.1007/s12633-022-01747-y

7.   Howldar, S., Balaji, B. and Srinivasa Rao, K., "Design and qualitative analysis of hetero dielectric tunnel field effect transistor device", *International Journal of Engineering, Transactions C: Aspects* Vol. 36, No. 6, (2023), 1129-1135. doi: 10.5829/ije.2023.36.06c.11.

8.   Karimi, G. and Shirazi, S., "Ballistic (n, 0) carbon nanotube field effect transistors\'iv characteristics: A comparison of n= 3a+ 1 and n= 3a+ 2", *International Journal of Engineering, Transactions A: Basics*, Vol. 30, No. 4, (2017), 516-522. doi: 10.5829/idosi.ije.2017.30.04a.09.

9.   Dixit, A. and Gupta, N., "A compact model of gate capacitance in ballistic gate-all-around carbon nanotube field effect transistors", *International Journal of Engineering, Transactions A: Basics*, Vol. 34, No. 7, (2021), 1718-1724. doi: 10.5829/IJE.2021.34.07A.16.

10. Kim, J.H., Kim, S. and Park, B.-G., "Double-gate tfet with vertical channel sandwiched by lightly doped si", *IEEE*

Transactions on Electron Devices, Vol. 66, No. 4, (2019), 1656-1661. https://doi.org/10.1109/TED.2019

11. Chakrabarty, R., Roy, S., Pathak, T. and Kumar Mandal, N., "Design of area efficient single bit comparator circuit using quantum dot cellular automata and its digital logic gates realization", *International Journal of Engineering, Transactions C: Aspects,*, Vol. 34, No. 12, (2021), 2672-2678. doi: 10.5829/ije.2021.34.12c.13.

12. Goswami, R., Bhowmick, B. and Baishya, S., "Electrical noise in circular gate tunnel fet in presence of interface traps", *Superlattices and Microstructures*, Vol. 86, (2015), 342-354. https://doi.org/10.1016/j.spmi.2015.07.064

13. Roy, A., Mitra, R. and Kundu, A., "Influence of channel thickness on analog and rf performance enhancement of an underlap dg algan/gan based mos-hemt device", in 2019 Devices for Integrated Circuit (DevIC), IEEE. (2019), 186-190.

14. Nishitani, T., Yamaguchi, R., Asubar, J., Tokuda, H. and Kuzuhara, M., "Improved on-state breakdown characteristics in algan/gan mos-hemts with a gate field plate", in 2019 Compound Semiconductor Week (CSW), IEEE. (2019), 1-2.

15. Mehrabani, A.H., Fattah, A. and Rahimi, E., "Design and simulation of a novel hetero-junction bipolar transistor with gate-controlled current gain", *International Journal of Engineering, Transactions C: Aspects*, Vol. 36, No. 03, (2023), 433. doi: 10.5829/ije.2023.36.03c.01.

16. Rafiee, A., Nickabadi, S., Nobarian, M., Tagimalek, H. and Khatami, H., "Experimental investigation joining al 5083 and high-density polyethylen by protrusion friction stir spot welding containing nanoparticles using taguchi method", *International Journal of Engineering, Transactions C: Aspects*, Vol. 35, No. 6, (2022), 1144-1153. doi: 10.5829/ije.2022.35.06c.06.

17. Smith, J.A., Takeuchi, H., Stephenson, R., Chen, Y., Hytha, M., Mears, R.J. and Datta, S., "Experimental investigation of n-channel oxygen-inserted (oi) silicon channel mosfets with high-k/metal gate stack", in 2018 76th Device Research Conference (DRC), IEEE. (2018), 1-2.

18. Kumar, S. and Sahoo, G., "A random forest classifier based on genetic algorithm for cardiovascular diseases diagnosis (research note)", *International Journal of Engineering, Transactions B: Applications*, Vol. 30, No. 11, (2017), 1723-1729. doi: 10.5829/ije.2017.30.11b.13.

19. Balaji, B., Srinivasa Rao, K., Girija Sravani, K., Bindu Madhav, N., Chandrahas, K. and Jaswanth, B., "Improved drain current characteristics of HFO_2/SiO_2 dual material dual gate extension on drain side-tfet", *Silicon*, Vol. 14, No. 18, (2022), 12567-12572. https://doi.org/10.1007/s12633-022-01955-6

20. Kumar, P.K., Balaji, B. and Rao, K.S., "Halo-doped hetero dielectric nanowire mosfet scaled to the sub-10 nm node", *Transactions on Electrical and Electronic Materials*, Vol., No., (2023), 1-11. https://doi.org/10.1007/s42341-023-00448-6

21. Emami, N. and Kuchaki Rafsanjani, M., "Extreme learning machine based pattern classifiers for symbolic interval data", *International Journal of Engineering, Transactions B: Applications,*, Vol. 34, No. 11, (2021), 2545-2556. doi: 10.5829/IJE.2021.34.11B.17

22. Ehteshamuddin, M., Loan, S.A., Alharbi, A.G., Alamoud, A.M. and Rafat, M., "Investigating a dual moscap variant of line-tfet with improved vertical tunneling incorporating fiqc effect", *IEEE Transactions on Electron Devices*, Vol. 66, No. 11, (2019), 4638-4645. https://doi.org/10.1109/TED.2019.2942423

23. Mizutani, T., Ohno, Y., Akita, M., Kishimoto, S. and Maezawa, K., "A study on current collapse in algan/gan hemts induced by bias stress", *IEEE Transactions on Electron Devices*, Vol. 50, No. 10, (2003), 2015-2020. https://doi.org/10.1109/TED.2003.816549

24. Ehteshamuddin, M., Loan, S.A. and Rafat, M., "A vertical-gaussian doped soi-tfet with enhanced dc and analog/rf performance", *Semiconductor Science and Technology*, Vol. 33, No. 7, (2018), 075016. https://doi.org/10.1088/1361-6641/aac97d

25. Musalgaonkar, G., Sahay, S., Saxena, R.S. and Kumar, M.J., "A line tunneling field-effect transistor based on misaligned core–shell gate architecture in emerging nanotube fets", *IEEE Transactions on Electron Devices*, Vol. 66, No. 6, (2019), 2809-2816. https://doi.org/10.1088/1361-6641/aac97d

26. Tallapaneni, N.S. and Megala, V., "Qualitative analysis of dual material gate ($SiO2/HFO_2$) underlapped on drain side tfet (dmgud-tfet) using work function engineering", *Silicon*, Vol. 14, No. 17, (2022), 11667-11673. https://doi.org/10.1007/s12633-022-01890-6

27. Priyadarshani, K.N., Singh, S. and Naugarhiya, A., "Dual metal double gate ge-pocket tfet (dmg-dg-ge-pocket tfet) with hetero dielectric: Dc & analog performance projections", *Silicon*, (2021), 1-12. https://doi.org/10.1007/s12633-021-00955-2

28. Rani, C.S.H., Roach, R.S., Samuel, T.A. and Lawrence, S.E., "Performance analysis of heterojunction and hetero dielectric triple material double gate tfet", *Silicon*, (2021), 1-8. https://doi.org/10.1007/s12633-021-01355-2

29. Bitra, J. and Komanapalli, G., "A comprehensive performance investigation on junction-less tfet (jl-tfet) based biosensor: Device structure and sensitivity", *Transactions on Electrical and Electronic Materials*, (2023), 1-8. https://doi.org/10.1007/s42341-023-00465-5

30. Nigam, K., Kumar, S. and Dharmender, "Temperature sensitivity analysis of dual material stack gate oxide source dielectric pocket tfet", *Journal of Computational Electronics*, Vol. 21, No. 4, (2022), 802-813. https://doi.org/10.1007/s10825-022-01902-z

31. Verma, P., Nigam, K. and Kumar, S., "Impact of gate overlap and underlap on analog/rf and linearity performance of dual-material gate-oxide-stack double-gate tfet", *Applied Physics A*, Vol. 128, No. 11, (2022), 955. https://doi.org/10.1007/s00339-022-06083-x

32. Fouladinia, F. and Gholami, M., "Decimal to excess-3 and excess-3 to decimal code converters in qca nanotechnology", *International Journal of Engineering, Transactions C: Aspects*, Vol. 36, No. 9, (2023), 1618-1625. doi: 10.5829/ije.2023.36.09c.05.

33. Jain, G., Sawhney, R.S., Kumar, R. and Saini, A., "Design and comparative analysis of heterogeneous gate dielectric nanosheet tfet with temperature variance", *Silicon*, Vol. 15, No. 1, (2023), 187-196. https://doi.org/10.1007/s12633-022-02013-x

---

Persian Abstract

چکیده

این مقاله طراحی و تجزیه و تحلیل یک ترانزیستور اثر میدانی تونل دوگانه گیت دو الکتریک هترو دی الکتریک زیرلپ تونل را با هدف افزایش عملکرد دستگاه و غلبه بر محدودیت‌های ذاتی ارائه می‌کند. طرح پیشنهادی ترانزیستور اثر میدانی تونل شامل یک پشته دروازه دی الکتریک هترو است که از دو ماده دی الکتریک متمایز مانند مواد دی الکتریک بالا به عنوان اکسید هافنیوم (HfO2) و مواد دی الکتریک کم k به عنوان دی اکسید سیلیکون (SiO2) تشکیل شده است. با مقادیر گذردهی مختلف با انتخاب این مواد، پشته دروازه می تواند به طور موثر توزیع میدان الکتریکی را در دستگاه تعدیل کند، کنترل الکترواستاتیکی را بهبود بخشد و رسانش دوقطبی را کاهش دهد. علاوه بر این، یک فاصله دهنده زیرپوش در ساختار ترانزیستور اثر میدان تونل برای ایجاد یک جدایی فیزیکی بین منبع و مناطق کانال معرفی شده است. این اسپیسر به کاهش جریان مستقیم تونل منبع به تخلیه، افزایش نسبت جریان یون/آیوف و کاهش نوسان زیرآستانه کمک می کند. علاوه بر این، فاصله‌دهنده زیرپوش، کنترل دروازه‌ای را بر فرآیند تونل‌زنی بهبود می‌بخشد. طرح پیشنهادی ترانزیستور اثر میدانی تونل به طور کامل با استفاده از شبیه‌سازی‌های عددی مبتنی بر شبیه‌ساز طراحی به کمک رایانه (TCAD) تجزیه و تحلیل می‌شود. معیارهای عملکرد به عنوان جریان روشن (Ion)، جریان خارج از حالت (Ioff)، نسبت ION/IOFF، رسانایی تخلیه (Gd) و رسانایی ترانس (Gm) برای ارزیابی عملکرد دستگاه بررسی می‌گردد. بنابراین، این پیشرفت‌ها به مصرف انرژی کمتر و بهبود عملکرد مدار کمک می‌کند و آن را به دستگاهی امیدوارکننده برای کاربردهای کم مصرف تبدیل می‌کند.

International Journal of Engineering

A new Online Hall Effect Sensor Fault Detection and Location in Brushless DC Motor Based on Normalized Phases Currents Analysis

M. Arehpanahi*, M. Zare Ravandy

Department of Electrical Engineering, Tafresh University, Tafresh, Iran

P A P E R   I N F O

A B S T R A C T

In this paper, a new online technique for Hall Effect sensor fault diagnosis in brushless DC (BLDC) motor is proposed. The proposed technique is based on phase current waveform analysis and does not need any Hall sensor information. The normalized phases current values are analyzed per and post-sensor fault in every cycle. Using a definition of suitable conditions and threshold values for normalized currents values, all sensor fault types (i.e. set to 0 and 1) could be detected and located online effectively. The main contribution of this paper is introducing an online BLDC sensor fault detection and location technique under low-speed operation and transient conditions. Simulation results show the effectiveness of the proposed technique in all of the sensor faults types diagnosis without any sensor output value information. Two different types of BLDC motors are considered for fault diagnosis using the proposed technique. Simulation results during starting and low-speed operations of BLDC motor are well confirmed by the experimental results.

NOMENCLATURE		T	Period (s)
V_{dc}	DC link voltage (V)	n	Normalized value
Rs	Stator resistance (Ohm)	$S_{1,2,3,4,5,6}$	Power Switches
L_l	Stator leakage inductance (H)	$I_{A,B,C}$	Phases current

1. INTRODUCTION

High efficiency, high torque density, low-level noise, and wide speed control range are the main benefits of BLDC motors related to the induction motors. Therefore, BLDC motors can be one of the best options for many applications, such as robots, electric bicycles, and computer equipment [1-3]. But torque ripple [3, 4] and dependency on the rotor position are the main drawbacks of the BLDC motors. The switching pattern of a BLDC motor driver for speed control is highly dependent on the position sensors output values. The most common BLDC motor position sensors are Hall Effect sensors. These sensors may be damaged during operation of BLDC motors which can cause serious damage to the motor. Therefore, using an online sensor fault and driver faults

diagnosis technique is very important for the safe operation of the BLDC motor. There are many diagnosis techniques for detection of the sensor faults in BLDC motors. The sensor fault is detected based on the sum of the instantaneous of Hall output signal values with an investigated diagnosis table reported in literatu [5]. Cheshta et al. [5] focussed on the analysis of the output values of hall sensors for detection of faulty sensor. A new technique based on a binary combination of Hall signals values and commutation times between power switches of the BLDC driver is presented by Qian, and Ming [6]. A direct redundancy- based method by utilizing redundant Hall-effect sensors for Fault Tolerant Control (FTC) of a BLDC motor is presented by Aqil and Hur [7]. The online sensor fault diagnosis of BLDC motor are carried out by wavelet package [8], Goertzel

*Corresponding author email: arehpanahi@tafreshu.ac.ir (M. Arehpanahi)

Algorithm [9] and improved ZOA (Zeroth Order Algorithm) technique [10]. The DC-link current second harmonic component monitoring is employed for sensor fault diagnosis [11]. Mehta et al. [12] used analysis of the output sensor signals values sequences as binary numbers, the sensor faults can be detected. In healthy conditions, the sequence of three Hall-Effect sensors values (0 for OFF state and 1 for ON state) is expressed as one of the six binary numbers (from 001 to 110). Therefore, any sequences outside this range will be detected as a fault [13, 14]. No-detection at low-speed operation, is the main drawback of the mentioned techniques. Tashakori and Ektesab [13] analyzed the output sensor waveform based on reference frame theory and Vector-Tracking Observer (VTO) is employed for detection of faults especially at low-speed operation. But complex calculation process and requiring a rotating harmonic vectors models, are the main disadvantages of work reported in literature [15]. A new technique based on line-voltage monitoring using FFT analysis was proposed by Donato et al. [16]. Detection process complexity and no- detection during start-up are the main disadvantages of it. An improved FTC scheme based on FDP (Fault Detection Probability) and VTO for sensor fault diagnosis was proposed by Donato et al. [17]. No-fault detection during start-up is the main drawback of the reported data [15]. Diagnosis of Hall-Effect sensors faults based on output sensors signals values combined with the measured line voltages using Discrete Fourier Transform (DFT) was reported by Mousmi et al. [18]. Analysis of the stator phase currents using Stockwell Transform (S-Transform) for hall sensors faults diagnosis was defined by Gowtham et al. [19]. In general, no-fault detection at low-speed operation or false diagnosis in transient conditions is two challenges of the mentioned techniques. The inability to separate between starting and fault conditions is a main drawback of the most online sensor fault diagnosis techniques. If any sensors fail, they will affect on the stator current waveform directly. The stator current monitoring is a usual and accessible technique for analysis of the motor behavior. Therefore, in this paper, a new online technique based on phase current waveform analysis is proposed. In the proposed technique, using all phases' current waveforms analysis, the sensor fault can be detected and located effectively. The main contribution of the proposed technique is definition of some conditions for normalized three phase currents values with a simple calculation process. The proposed technique, can able to separate transient conditions from fault conditions. This paper is divided into four sections: section 1 proposed method, section 2 simulation results and discussion, section 3 experimental results and section 4 conclusion.

2. PROPOSED METHOD

Usually, during sensor failure time, the output value of the sensor is unchanged (0 or 1). Therefore, in this paper, a constant value of the sensor output is considered as a fault. Figure 1 shows a block diagram of the BLDC motor driver which is used in this paper. Table 1 shows the switching pattern of the BLDC motor driver under sensor A fault (set to 0). If a sensor output value is to be constant, the status of some switches will be always ON or OFF. Then, in half of the period (positive or negative) the corresponding phase current is close to zero. According to Table 1, in a period, it is clear that I_A has positive and negative signs but I_B has negative sign and I_C has positive sign. Therefore, I_C and I_B have a DC component. If this DC component pre and post-fault is well analyzed, the sensor fault could be well detected. DC component of phase currents affects on the average and RMS value of the phase current.

Therefore, in the proposed technique, the average value of the phase current divided by the RMS value of that which is called normalized phase current, is introduced as a fault indicator. The normalized phase current value is expressed in Equation (1):

$$I_{xn} = \frac{1}{T\, I_{Nrms}} \int_t^{t+T} I_x dt \quad x = A,B,C \tag{1}$$

where T, I_{Nrms} n are a period, nominal RMS value of phase current and the normalized value, respectively. In healthy conditions, the average value of all phase

TABLE 1. Switching pattern of BLDC motor driver under sensor A fault (logic 0)

State	Hall Effect sensor status			Active switches	Phase currents sign		
	A	B	C		A	B	C
1	0	0	1	S1,6	positive	negative	none
2	0	0	1	S1,6	positive	negative	none
3	0	0	0	none	none	none	none
4	0	1	0	S5,4	negative	none	positive
5	0	1	0	S5,4	negative	none	positive
6	0	1	1	S5,6	none	negative	positive
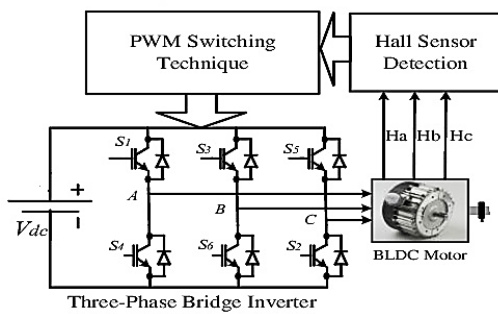
Figure 1. Three- phase BLDC motor driver

currents is close to zero. If one of the hall sensors fails (set to 0 or 1), the average value of all phase current will not be zero anymore. In this condition, according to Table 1, the positive or negative half period of phase current (depended on the sensor number failure) is close to zero approximately. Therefore, the absolute value of the corresponding phase current average will be about 50% of phase current RMS value. Therefore, according to Equation (1), the absolute normalized value of corresponding phases is close to 0.5. then using comparison of the mentioned normalized value with threshold value (i.e. 0.5), the sensor fault can be detected. However, the main problem in fault detection process, is normalized current variation during transient conditions (for example: starting time). To solve this problem, several simulations of different three-phase BLDC motors types (different output powers) during starting time are done. By analysing their results (variation of the all phase normalized currents values), it was found that the absolute normalized phase currents values are no higher than 0.4. Therefore, it can be defined suitable conditions for the normalized phase currents with an appropriate threshold value i.e. 0.4 (which is independent of BLDC motor specification) for fault indicator. The proposed technique, for detection and location of Hall-Effect sensors failure is expressed as six conditions in Tables 2 and 3(for two faults type). The subscript "n" denotes the normalized value.

For example, when three phase normalized currents satisfy in $I_{An} < 0, I_{Bn} < -0.4, I_{Cn} > 0.4$, based on Table 2, the sensor A has failed and set to 0. In diagnosis process, some problems may negatively impact on the fault detection such as rotation direction change, transient

TABLE 2. sensor fault diagnosis (logic 0)

Defective Sensor	Normalized phase current states
A	$I_{An} < 0, I_{Bn} < -0.4, I_{Cn} > 0.4$
B	$I_{An} > 0.4, I_{Bn} < 0, I_{Cn} < -0.4$
C	$I_{An} < -0.4, I_{Bn} > 0.4, I_{Cn} < 0$

TABLE 3. sensor fault diagnosis (logic 1)

Defective Sensor	Phase currents
A	$I_{An} > 0,\ I_{Bn} > 0.4,\ I_{Cn} < -0.4$
B	$I_{An} < -0.4,\ I_{Bn} > 0, I_{Cn} > 0.4$
C	$I_{An} > 0.4, I_{Bn} < -0.4, I_{Cn} > 0$

conditions and low-speed operation. The impacts of these problems on the proposed technique are discussed in this paper. The rotation direction of three-phase BLDC motor is reversed by a shifting any two phases from three phases of the terminal voltages. Therefore, by exchanging only two rows in Table 2 or Table 3, it can be used these tables for reverse rotation direction. Consequently, any change in rotation direction does not effect on the proposed technique results at all. The second problem is transient conditions such as starting. In the proposed technique, this problem has been fixed by selecting 0.4 as a threshold value for the fault indicators. The normalized phase currents values in transient condition do not satisfy in conditions that are expressed in Table 2 or Table 3 with this threshold value.

3. SIMULATION RESULTS AND DISCUSSION

In order to performance analysis of the proposed technique, two BLDC motors types (motors 1 and 2) with different specifications are considered. The specifications of both motors are listed in Tables 4 and 5.

Both motors (motors 1 and 2) have been started under different load conditions (no-load and full-load). Then sensor faults (logic 0 and logic 1) have been applied to all sensors individually when motors reach steady-state conditions. All simulation results have been done in MATLAB/Simulink software. For example, in motor 1, the fault (logic 0) is applied to the sensor A under full

TABLE 4. BLDC motor1 specification

Parameter	Value	Parameter	Value
V_{dc}	48 V	Poles	4
R_s	0.28Ω	Rated power	200 W
L_l	0.45mH	Rated Speed	4000 rpm

TABLE 5. BLDC motor2 specifications

Parameter	Value	Parameter	Value
V_{dc}	48 V	Poles	4
R_s	0.069Ω	Rated power	1500 W
L_l	0.2mH	Rated Speed	5000 rpm

load conditions at time t=0.255 s (Figures 2 and 3). For motor 2, another sensor fault type (logic 1) is applied to sensor B, under no load conditions at time t=0.25 s (Figures 4 and 5). The phase current waveforms and their normalized values waveforms for motor 1 under full load pre and post-fault are illustrated in Figures 2 and 3. According to Figure 3 ($I_{An} < 0, I_{Bn} < -0.4, I_{Cn} > 0.4$) and based on row 1 from Table 2 it is clear that the sensor A has failed (logic 0). The phase currents waveforms for motor 2, under no load pre and post- fault are shown in Figures 4 and 5. According to Figure 5 ($I_{An} < -0.4, I_{Bn} > 0, I_{Cn} > 0.4$) and based on row 2 from Table 3, sensor B has failed (logic 1). Therefore, the proposed technique could detect and locate sensor fault.

The normalized phase currents values of motor1 under no-load, during starting time is illustrated in Figure 6. During starting time 0.015s<t<0.018s based on Figure
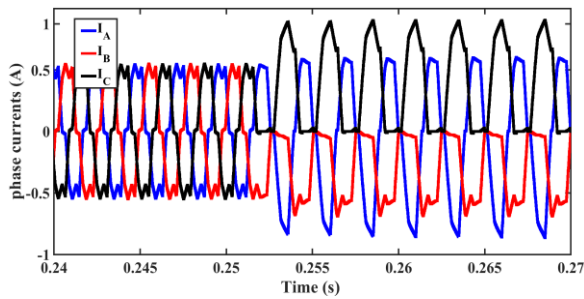
Figure 2. Phase currents of motor1 under full load and sensor A fault (logic 0)
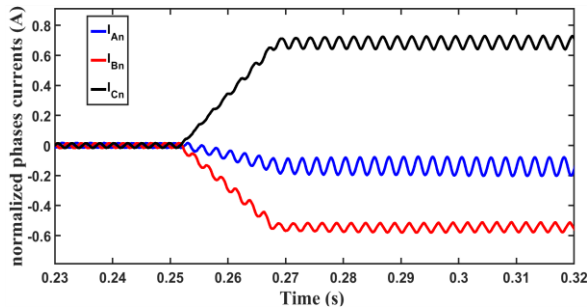
Figure 3. Normalized phase currents of motor1 under full load and sensor A fault (logic 0)
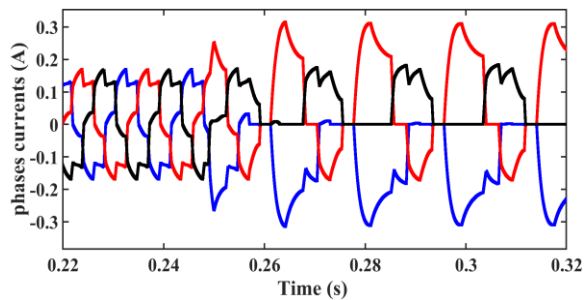
Figure 4. Phase currents of moto 2 under no-load and sensor B fault (logic 1)
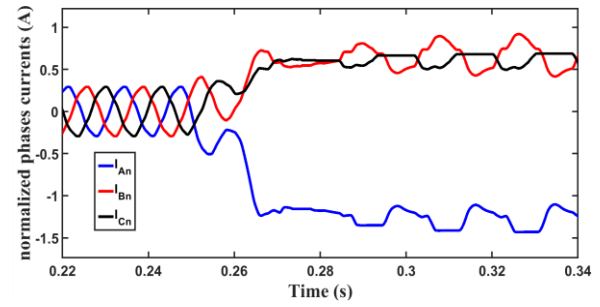
Figure 5. Normalized phase currents of moto 2 under no-load and sensor B fault (logic 1)
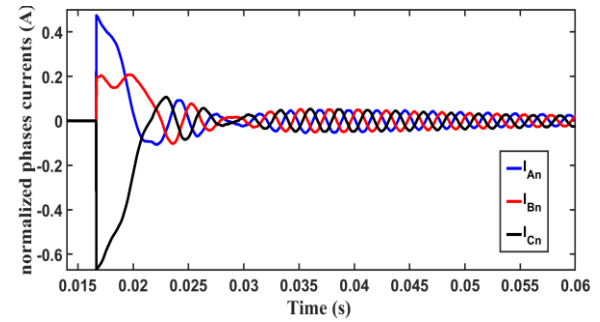
Figure 6. Normalized phase currents of motor 1 (starting)

6, the normalized phase currents values satisfy in $I_{An} > 0.4, I_{Bn} > 0, I_{Cn} < -0.4$.

As a result, motor 1 normalized current values during start-up do not satisfy in Tables 2 and 3 conditions. Consequently, the proposed technique is robust against transient conditions, especially during start-up. At low-speed operation, the phase current waveforms are changed related to the normal speed and contain low order harmonics. These waveforms are similar to the faulty cases. The sensor fault (sensor C, logic 1) is applied to motor 1 at 300 rpm (7.5% of rated speed). The sensor fault (sensor B, logic 1) is applied to motor 2 at 250 rpm (5% of rated speed). The phase current waveforms and their normalized values of motor 1 pre and post-fault are shown in Figures 7 and 8. The phase current waveforms and their normalized values of motor 2 pre and post-fault are shown in Figures 9 and 10.
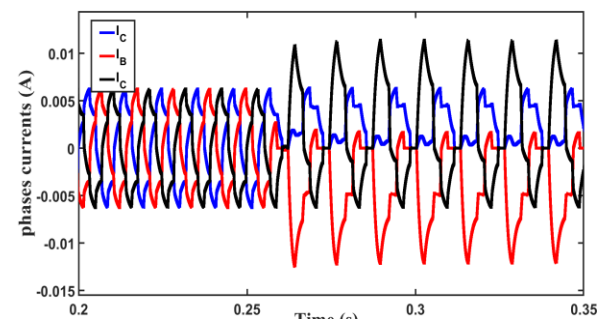
Figure 7. Phase currents (motor 1) at low speed (300 rpm)
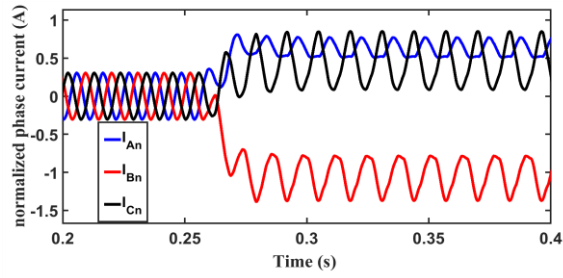
Figure 8. Normalized phase currents (motor 1) at low speed (300 rpm)
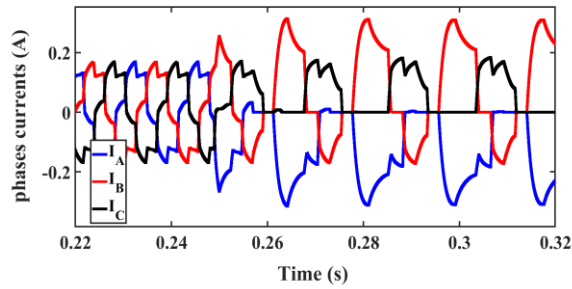
Figure 9. Phase currents (motor 2) at low speed (250 rpm)
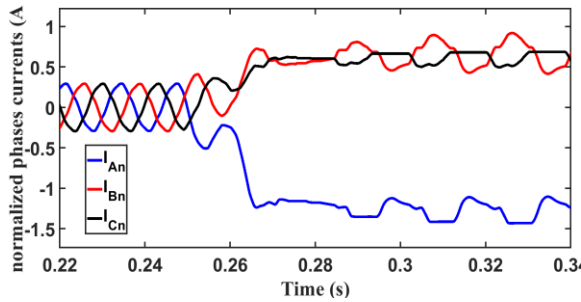
Figure 10. Normalized phase currents (motor 2) at low speed (250 rpm)

According to Figure 8, it is clear that the normalized phase current values of motor 1 in post- fault time are $I_{An} > 0.4, I_{Bn} < -0.4, I_{Cn} > 0$ which satisfies in row 3 in Table 3. Therefore, sensor C has failed (logic 1). Also, the normalized phase currents values of motor2 (Figure 10) in post-fault time are $I_{An} < -0.4, I_{Bn} > 0, I_{Cn} < 0.4$ which satisfies in row 2 in Table 3. Consequently, sensor B has failed (logic 1). Therefore, the proposed technique could online detect and locate all of the Hall-Effect sensor faults types in transient conditions, no- load, full-load and low-speed operation effectively.

4. EXPERIMENTAL RESULTS

In order to experimentally verify the proposed technique, a prototype BLDC motor is considered (Figure 11). The

prototype BLDC motor is designed for analysis of the motor under sensor fault conditions. In other words, the motor driver software is designed to be able to apply sensor faults. Specification of the prototype BLDC motor is listed in Table 6. The BLDC motor starts under no-load conditions. In steady-state conditions, sensor A is disconnected from the driver at t=0.4s (logic 0). Three-phase currents pre and post fault is illustrated in Figures 12, 13 and 14.

According to the phase currents waveforms and the normalized phase currents which are shown in Figures 15, 16 and 17, the normalized phases currents satisfy in

TABLE 6. BLDC motor specification for testing

Parameter	Value	Parameter	Value
V_{dc}	24 V	Nominal current	2.32 A
R_s	0.5 Ω	Rated torque	83 mNm
L_l	0.55mH	Rated Speed	5250 rpm

Figure 11. Set-up of the prototype BLDC motor
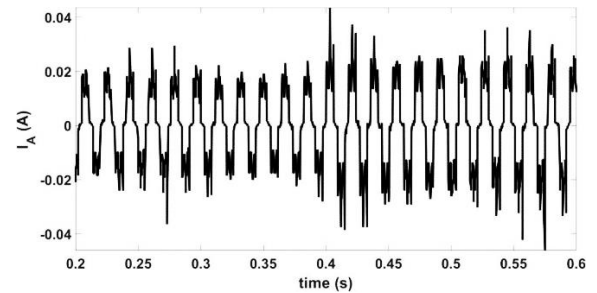
Figure 12. Phase A current waveform pre and post fault
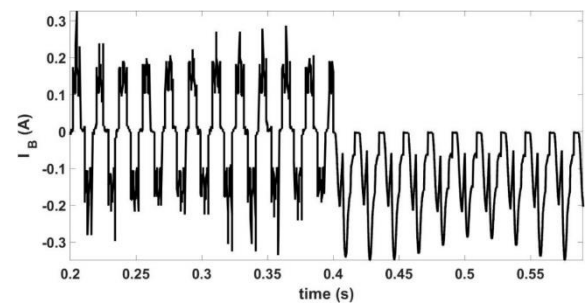
Figure 13. Phase B current waveform pre and post fault
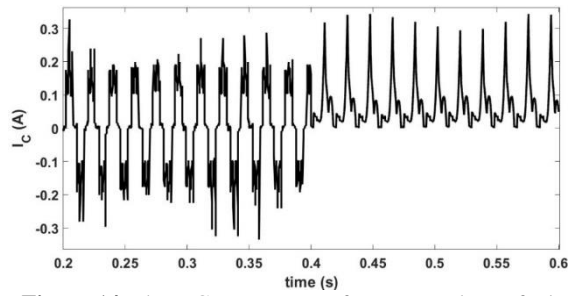
Figure 14. Phase C current waveform pre and post fault
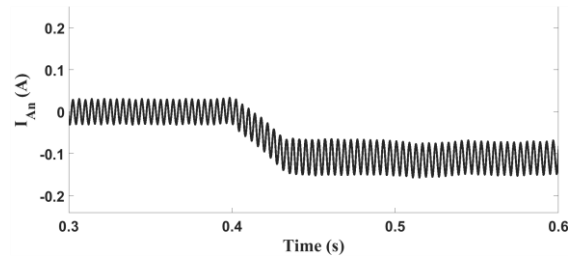
Figure 15. Normalized of I_A waveform pre and post fault
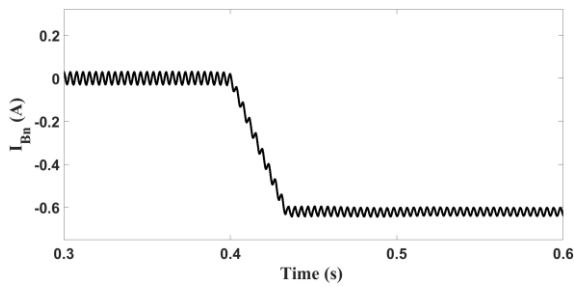
Figure 16. Normalized of I_B waveform pre and post fault
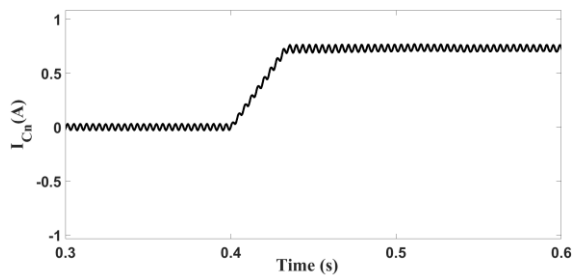
Figure 17. Normalized of I_C waveform pre and post fault

Figure 18. I_A waveform pre and post fault (250 rpm)
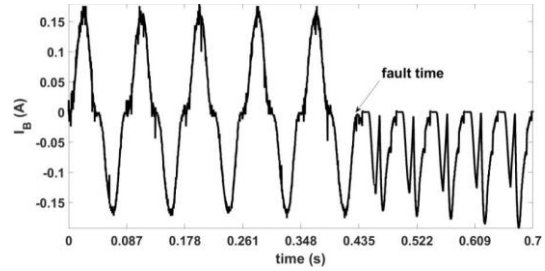
Figure 19. I_B waveform pre and post fault (250 rpm)
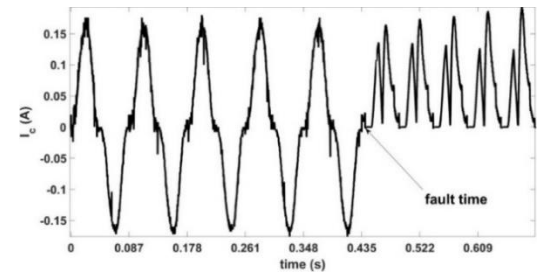
Figure 20. I_C waveform pre and post fault (250 rpm)
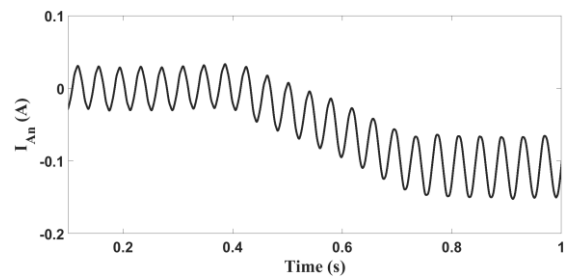
Figure 21. Normalized I_A waveform pre and post fault (250 rpm)
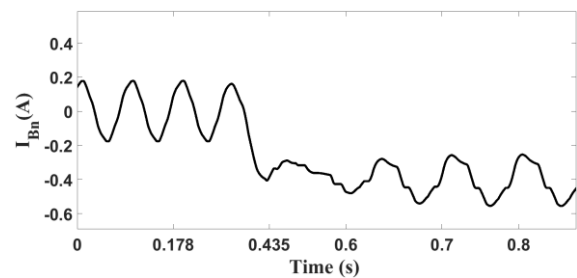
Figure 22. Normalized I_B waveform pre and post fault (250 rpm)

$I_{An} < 0, I_{Bn} < -0.4, I_{Cn} > 0.4$. Therefore, based on row 1 in Table 2, sensor A is failed (logic 0).

To analysis of the proposed technique under low-speed operations, the prototype BLDC motor operates at low- speed i.e. 250 rpm. The sensor fault is applied to the sensor A (logic 0) at t=0.43s. The three phase currents of the BLDC motor are illustrated in Figures 18, 19 and 20. The normalized value of three phase currents are illustrated in Figures 21, 22 and 23. According to these figures, the normalized phase currents satisfy in $I_{An} <$

Figure 23. Normalized I_C waveform pre and post fault (250 rpm)

$0, I_{Bn} < -0.4, I_{Cn} > 0.4$. As a result, based on row 1 in Table 2, the sensor A is failed (logic 0). Consequently, the proposed technique could detect and locate online all of the sensor faults types at different operation conditions.

5. CONCLUSION

This paper presents a new online detection technique for Hall-Effect sensor faults in brushless DC motors. In the proposed technique, the sensor fault is detected and located online by the normalized phase currents analysis. The proposed technique is also able to detect sensor faults at low speeds. Using a comparison of all normalized phases current values with suitable threshold value, the sensor fault (type and sensor number) is detected and located effectively. The proposed technique, can separate transient conditions such as starting from faulty cases which is the main advantage of the proposed technique related to the other diagnosis techniques. The simulation results for two different types of the BLDC motors under different loads and speed conditions, show the capability of the proposed technique in sensor fault diagnosis. Verification of the proposed technique is carried out by experimental results effectively.

6. REFERENCES

1. Procter, S. and Secco, E.L., "Design of a biomimetic bldc driven robotic arm for teleoperation & biomedical applications", *J Hum Earth Future. ISSN*, (2022), 2785-2997. doi: 10.28991/HEF-2021-02-04-03.

2. Morales, L.A., Fabara, P. and Pozo, D.F., "An intelligent controller based on lamda for speed control of a three-phase inductor motor", *Emerging Science Journal*, Vol. 7, No. 3, (2023), 676-690. doi: 10.28991/ESJ-2023-07-03-01.

3. Patel, A. and Suthar, B., "Cogging torque reduction of sandwiched stator axial flux permanent magnet brushless dc motor using magnet notching technique", *International Journal of Engineering, Transactions A: Basics* Vol. 32, No. 7, (2019), 940-946. doi: 10.5829/IJE.2019.32.07A.06.

4. Gol, S., Ardeshir, G., Zahabi, M. and Ale Ahmad, A., "The influence of dc-link voltage on commutation torque ripple of brushless dc motors with two-segment pulse-width modulation control method", *International Journal of Engineering,*

Transactions B: Applications Vol. 31, No. 2, (2018), 307-314. doi: 10.5829/ije.2018.31.02b.15.

5. Jain, C., Garg, P. and Jain, A.K., "Hall-effect sensor fault diagnosis, identification and remedial strategy in permanent magnet brushless dc drive", in 2018 IEEE International Conference on Power Electronics, Drives and Energy Systems (PEDES), IEEE. (2018), 1-5.

6. Zhang, Q. and Feng, M., "Fast fault diagnosis method for hall sensors in brushless dc motor drives", *IEEE Transactions on Power Electronics*, Vol. 34, No. 3, (2018), 2585-2596. doi: 10.1109/TPEL.2018.2844956.

7. Aqil, M. and Hur, J., "A direct redundancy approach to fault-tolerant control of bldc motor with a damaged hall-effect sensor", *IEEE Transactions on Power Electronics*, Vol. 35, No. 2, (2019), 1732-1741. doi: 10.1109/TPEL.2019.2917559.

8. Mitronikas, E., Papathanasopoulos, D., Athanasiou, G. and Tsotoulidis, S., "Hall-effect sensor fault identification in brushless dc motor drives using wavelets", in 2017 IEEE 11th International Symposium on Diagnostics for Electrical Machines, Power Electronics and Drives (SDEMPED), IEEE. (2017), 434-440.

9. Papathanasopoulos, D.A., Spyropoulos, D.V. and Mitronikas, E.D., "Fault diagnosis of misaligned hall-effect position sensors in brushless dc motor drives using a goertzel algorithm", in 2019 IEEE 12th international symposium on diagnostics for electrical machines, power electronics and drives (SDEMPED), IEEE. (2019), 167-173.

10. Skóra, M., "Operation of pm bldc motor drives with faulty rotor position sensor", in 2017 International Symposium on Electrical Machines (SME), IEEE. (2017), 1-6.

11. Papathanasopoulos, D.A., Spyropoulos, D.V., Mitronikas, E.D. and Karlis, A.D., "Commutation angle self-calibrating technique for brushless dc motor drives with defective hall-effect position sensors", in 2020 International Conference on Electrical Machines (ICEM), IEEE. (2020), 1301-1307.

12. Mehta, H., Thakar, U., Joshi, V., Rathod, K. and Kurulkar, P., "Hall sensor fault detection and fault tolerant control of pmsm drive system", in 2015 International Conference on Industrial Instrumentation and Control (ICIC), IEEE. (2015), 624-629.

13. Tashakori, A. and Ektesabi, M., "A simple fault tolerant control system for hall effect sensors failure of bldc motor", in 2013 IEEE 8th Conference on Industrial Electronics and Applications (ICIEA), IEEE. (2013), 1011-1016.

14. Dong, L., Jatskevich, J., Huang, Y., Chapariha, M. and Liu, J., "Fault diagnosis and signal reconstruction of hall sensors in brushless permanent magnet motor drives", *IEEE Transactions on Energy Conversion*, Vol. 31, No. 1, (2015), 118-131. doi: 10.1109/TEC.2015.2459072.

15. Scelba, G., De Donato, G., Pulvirenti, M., Capponi, F.G. and Scarcella, G., "Hall-effect sensor fault detection, identification, and compensation in brushless dc drives", *IEEE Transactions on Industry Applications*, Vol. 52, No. 2, (2015), 1542-1554. doi: 10.1109/TIA.2015.2506139.

16. Scelba, G., De Donato, G., Scarcella, G., Capponi, F.G. and Bonaccorso, F., "Fault-tolerant rotor position and velocity estimation using binary hall-effect sensors for low-cost vector control drives", *IEEE Transactions on Industry Applications*, Vol. 50, No. 5, (2014), 3403-3413. doi: 10.1109/TIA.2014.2304616.

17. Dong, L., Huang, Y., Jatskevich, J. and Liu, J., "Improved fault-tolerant control for brushless permanent magnet motor drives with defective hall sensors", *IEEE Transactions on Energy Conversion*, Vol. 31, No. 2, (2016), 789-799. doi: 10.1109/TEC.2016.2526621.

18. Mousmi, A., Abbou, A. and El Houm, Y., "Binary diagnosis of hall effect sensors in brushless dc motor drives", *IEEE*

Transactions on Power Electronics, Vol. 35, No. 4, (2019), 3859-3868. doi: 10.1109/TPEL.2019.2934794.

19. Gowtham, S., Keerthana, I. and Balaji, M., "Characterization and classification of hall sensor faults using s-transform analysis on bldc motor drive", in 2019 IEEE 1st International Conference on

Energy, Systems and Information Processing (ICESIP), IEEE. (2019), 1-6.
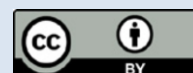
Persian Abstract

چکیده

در این مقاله یک روش برخط جدید برای تشخیص خطای سنسور اثر هال در موتور DC بدون جاروبک پیشنهاد شده است. در روش پیشنهادی تحلیل شکل موج جریان فاز جایگزین بررسی خروجی حسگرهای موقعیت شده است. مقادیر جریان فازهای نرمال شده قبل و بعد از خطا در هر سیکل تجزیه و تحلیل می شوند. با استفاده از تعریف شرایط و مقادیر آستانه مناسب ، همه انواع خطاهای حسگر می تواند به طور موثر و برخط شناسایی شده و محل خطا تعیین گیرند. مهمترین بخش مقاله تشخیص برخط خطای سنسور و مکان یابی آن در سرعت پایین است. نتایج شبیه‌سازی اثربخشی روش پیشنهادی را در تشخیص همه انواع خطاهای حسگر بدون استفاده مستقیم از مقدار خروجی سنسور نشان می‌دهد. دو نوع مختلف از موتورهای BLDC در شبیه سازی شده اند. نتایج شبیه سازی در شرایط کارکرد معمولی و سرعت پایین به خوبی توسط نتایج تجربی تایید شده اند.

International Journal of Engineering

Hierarchical Coverage Repair Policies Optimization by Dhouib-Matrix-4 Metaheuristic for Wireless Sensor Networks using Mobile Robot

S. Dhouib*

Department of Industrial Management, Higher Institute of Industrial Management, University of Sfax, Tunisia

A B S T R A C T

The wireless sensor networks represent a wide range of potential application, they are composed of a set of energy-constrained sensors used for detecting events and then sending information. In this paper, the novel metaheuristic Dhouib-Matrix-4 (DM4) is enhanced to optimize the coverage repair policies for wireless sensor networks using a mobile robot with different moving speeds. Hierarchically, two conflicted criteria are considered: at first the number of sensors to be visited in time is maximized, then at second, the trajectory distance of the mobile robot is minimized. Therefore, maximizing the lifetime of sensors and minimizing the path of the mobile robot is a challenging issue. DM4 is a multi-start method which uses at each start the novel greedy heuristic Dhouib-Matrix-TSP1 in order to generate an initial basic feasible solution which will be intensified by the new local search technique entitled Far-to-Near. DM4 is applied on several TSP-LIB standard instances from the literature where the moving speed (w) of a mobile actor varied from 0.4 to 1. The performance of DM4 is proven by comparing its results to those generated by the Evolutionary Algorithm (EA). DM4 is developed under Python programming language and a graphical representation of the generated solution is illustrated.

doi: 10.5829/ije.2023.36.12c.03

NOMENCLATURE

WSNs	Wireless Sensor Networks	TSP	Travelling Salsmen Problem
DM4	Dhouib-Matrix-4 metaheuristic	EA	Evolutionary Algorithm
w	Static moving speed	d_i	Distance
α_i	Residual survival	β_i	Requested time for mobile robot to join sensor i
r_i	Current remaining energy	x_{ij}	Binary decision
c_i	Consumption of energy by time		

1. INTRODUCTION

The Wireless Sensor Networks (WSNs) are composed of a set of sensors used for detecting, measuring and collecting information from real world environments in order to offer a virtual layer for physical world. Indeed, the performance of the WSNs depends on several device parameters such as transmission range, battery and memory which highly constrained the wireless sensors. For that, the use of mobile robots can nicely enhance the performance of the wireless sensor through simultaneously (or separately) collecting information form sensor nodes and (or) delivering energy to these sensor nodes.

The WSNs have many applications in different domains such as prolonging the network lifetime under probabilistic target coverage via localized algorithm based on mobile nodes introduced by Zorbas and Razafindralambo [1], restoring of physical layer failure in the wireless sensor and actor networks using the Grey Wolf metaheuristic with Lagrangian Relaxation [2]. Moreover, a review of the three techniques (collection,

Corresponding Author Email: souhail.dhouib@gmail.com
(S. Dhouib)

delivery and combination) related to mobile robots in order to enhance the wireless sensor networks performance is presented by Huang et al. [3]. A Bat Algorithm is designed by Kim and Yoo [4] to optimize the target coverage problem with sensor node activation method and a greedy algorithm was proposed by Li and Shen [5] to solve the barrier coverage problem. An integrated algorithm is developed to unravel the scalability problem of robot formation [6] and a biomimetic robotic arm is designed for Teleoperation & Biomedical Applications [7]. Also, Sinks and sensors placement were studied in order to improve the coverage of WSNs by Kabakulak [8] and an enhanced Genetic Algorithm was developed by Harizan and Kuila [9] to improve the coverage and the connectivity for WSNs. A review on several applications of WSNs was considered by Rashid and Rehmani [10] and a survey on WSNs lifetime maximization was studied by Yetgin et al. [11]. Furthermore, a state-of-the-art dedicated for wireless sensor networks with mobile robots summarized by Boukerche and Sun [12] and a survey for the coverage problem in wireless sensor networks under uncertain domain was addressed by Wang et al. [13] and Tian et al. [14].

In this paper, we mainly focus on adapting the novel Dhouib-Matrix-4 (DM4) metaheuristic in order to solve the coverage repair policies hierarchically for wireless sensor networks using a mobile robot with different moving speeds. Originally, DM4 was designed by Dhouib [15] to solve the Travelling Salesman Problem with single objective (only the distance criterion was considered). However, in this current research work DM4 is enhanced to solve hierarchically two criteria: The hierarchical resolution emphasis on the one hand to move the robot mobile to the sensor node and repairs it before its energy runs out (the first goal is to maximize the number of sensors to be visited in time: Therefore, maximizing the number of cover sets lifetime) and on the other hand to minimize the movement of the mobile robot (the second goal is to minimize the trajectory distance: Consequently, improve the performance of the mobile robot). The experiments show the superiority of the proposed DM4 method compared to the Evolutionary Algorithm (EA).

The rest of this manuscript is organized as follows. The second section introduces the coverage repair policies for wireless sensor networks using a mobile robot problem. The third section is the synopsis of basic knowledge related to the novel metaheuristic Dhouib-Matrix-4 (DM4). The experiment will be given to a standard case study developed in the literature with seven scenarios of changing the moving speed from 0.4 to 1 for mobile robot. Finally, the fifth section is the summary of this article.

2. PROBLEM DESCRIPTION

The coverage repair policies in wireless sensor networks using a mobile robot with different moving speeds is a famous combinatorial problem. It deals about a set of static sensors responsible for monitoring a specific area where their battery is reduced through the time and their network coverage will be degraded. For that, energy analysis is considered and every sensor reports its current energy left to the base station. Hence, each sensor with less survival time will be reached via a mobile robot (located at the base station) in order to replenish its energy. This problem is considered as a Travelling Salesman Problem where the sensors are the nodes and the mobile robot is the salesman: The Travelling Salesman Problem is composed of several cities to be visited by a salesman; in fact, the objective is to create a Hamiltonian cycle joining all nodes where each city is visited only once except the starting city which will be the ending one.

Moreover, two criteria are hierarchically considered: maximizing the active sensor (repair the sensor before that its node energy runs out) and minimizing the total trajectory distance. The mathematical formulation of this problem can be described as follows: the wireless sensor networks can be represented by a graph $G = (V, E)$ where V is the set $\{v_1, .., v_n\}$ of vertex (set of sensors) and E is the set $\{e_{ij}\}$ of edges (distances between two sensors i and j, $\forall i, j \in \{1, .., n\}$).

The first objective Equation (1) is to maximize the number of active sensors:

$$Max f_1(x) = \sum_{i \in V} (\delta_i)$$

where

$$\delta_i = \begin{cases} 1, & \text{if } (\alpha_i - \beta_i) > 0 \\ 0, & \text{if } (\alpha_i - \beta_i) \leq 0 \end{cases}$$

$$\alpha_i = \frac{r_i}{c_i}$$

$$\beta_i = \frac{d_i}{w}$$

α_i represents the residual survival time for node v_i: This node will die if its energy is not added after α_i time. Hence, α_i can be computed by r_i/c_i where r_i is its current remaining energy and c_i its consumption of energy by time.

β_i is the requested time for mobile robot to join sensor i from its current position. Indeed, the mobile actor

presents a static moving speed w and needs to cover the distance d_i to join the sensor i from its current position.

The second objective Equation (2) is to minimize the total trajectory distance:

$$Min f_2(x) = \sum_{i=1}^{n} \sum_{j}^{n} x_{ij} d_{ij}$$

$$\sum_{i=1}^{n} x_{ij} = 1, j = 1,..n \qquad (2)$$

$$\sum_{j=1}^{n} x_{ij} = 1, i = 1,..n$$

x_{ij} is the binary decision variable: if vertex j is visited from vertex i $(x_{ij} = 1)$ and if not $(x_{ij} = 0)$.

3. THE PROPOSED METHOD

In this paper, the new metaheuristic named Dhouib-Matrix-4 (DM4) is applied to hierarchically solve the coverage repair policies for WSNs. DM4 has been firstly invented by Dhouib [15] and performed to optimize the shortest path joining all nodes as reported in literature [16-18]. Hence, DM4 is a multi-start technique (see Figure 1) and for each start two independent methods are applied: At first, the novel column-row heuristic Dhouib-Matrix-TSP1 (DM-TSP1) is used to create several initial feasible solutions with different statistical metrics (Min, Max, Mean, Standard deviation etc.); at second, this solution will be used as a starting point by the second method namely the Far-to-Near (FtN). Essentially, DM-TSP1 and FtN are applied in a relay process where the output of the first method will be the input for the second one (For more information about DM-TSP1 and FtN see respectively Dhouib's work [19, 20]).

Hence, DM-TSP1 is a novel greedy method and its performance was tested on different standard problems under crisp, fuzzy, intuitionistic and neutrosophic

Figure 1. The proposed multi-start DM4 method

domains [21-26]. Basically, FtN is a local search method characterized by its organized perturbation process (for more details see literature [20]).

Besides, DM4, DM-TSP1 and FtN belong to the concept of Dhouib-Matrix where several other methods are developed such as: the greedy heuristic Dhouib-Matrix-TP1 designed to unravel the transportation problem [27, 28]; the constructive methods Dhouib-Matrix-AP1 [29-31] and Dhouib-Matrix-AP2 [32] which are dedicated to solve respectively the balanced and unbalanced assignment problem. Moreover, an iterative stochastic metaheuristic entitled Dhouib-Matrix-3 is designed and tested by Dhouib [33], Dhouib and Zouari [34, 35]. Lastly, an optimal technique called Dhouib-Matrix-SPP is invented to rapidly unravel the shortest path problem [36].

In this paper, the coverage repair policies for WSNs will be considered with two hierarchical criteria (f_1 and f_2) where the first criterion (see Equation (1)) aims to maximize the number of active sensors (repairing the sensor before that its node energy runs out) and the second criterion (see Equation (2)) targets to minimize the total trajectory distance. Thus, for hierarchical criteria the first criterion is considered first then only in the case of equality the second criterion will be considered: for example, for two realizable solutions (x_1 and x_2), the solution (x_1) is better than the solution (x_2) in two cases: on the one hand, if $f_1(x_1) > f_1(x_2)$ (nevertheless the value of $f_2(x_1)$ and $f_2(x_2)$); on the other hand, if $f_1(x_1) = f_1(x_2)$ and $f_2(x_1) < f_2(x_2)$. Figure 2 illustrates the pseudo-code of the proposed DM4 method for the hierarchical coverage repair policies for WSNs.

The novel greedy method DM-TSP1 is depicted in Figure 3.

Figure 4 represents the flowchart of the innovative local search FtN method.
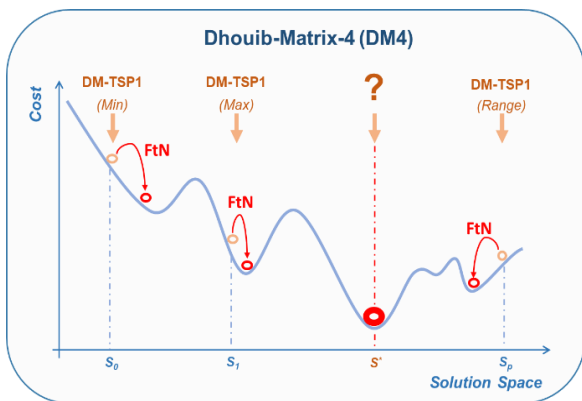
DM4 algorithm for Hierarchical Coverage Repair Policies for WSNs

Input: Distance matrix (*Matrix*), Residual survival time (α_i)
Output: Optimal solution
1. Set $S^*\_f_1$ and $S^*\_f_2$
2. *List-Metrics {Min, Max, Range, Mean, Mode, Sum, Q3, StDev}*
3. Set *Ctp-Start* (the number of metrics in the *List-Metrics*)
4. Set *Step* := 1
5. Repeat
    a. Select the metric number *Step* in the *List-Metrics*
    b. (S'_f_1, S'_f_2) := DM-TSP1 (*Matrix* , α_i , *List-Metrics[Step]*)
    c. (S''_f_1, S''_f_2) := FtN (*Matrix* , α_i , S'_f_1, S'_f_2)
    d. If $(S^*\_f_1 < S''\_f_1)$ or $((S^*\_f_1 = S''\_f_1)$ and $(S^*\_f_2 > S''\_f_2))$
        i. $S^*\_f_1 = S''\_f_1$
        ii. $S^*\_f_2 = S''\_f_2$
    e. *Step* := *Step* + 1
6. Until termination condition is met (*Step* = *Ctp-Start*)
7. Return $(S^*\_f_1 , S^*\_f_2)$

Figure 2. The pseudo-code of the proposed DM4 metaheuristic to optimize hierarchically the coverage repair policies for WSNs

Dhouib-Matrix-TSP1 (DM-TSP1) Algorithm

Input: Distance matrix, Residual survival time, Metric

Output: S'_f_1 and S'_f_2

1. Set $Path$ = {}
2. Compute the Metric (Min, Max, Average ... etc.) for each row, select the smallest generated value and find the minimal element d_{xy} for this row
3. $Path$ = {x,y}
4. Discard column x and column y
5. for i=1 to number of cities
6.   find the minimal element d_{xa} in row x
7.   find the minimal element d_{yb} in row y
8.   if ($d_{xa} < d_{yb}$) then
9.   insert a before x in the list $Path$
10. $x = a$
11.   else
12.   insert b after y in the list $Path$
13. $y = b$
14.   end
15. end
16. Compute S'_f_1 and S'_f_2 from $Path$
17. Return S'_f_1 and S'_f_2

Figure 3. The pseudo-code of the novel greedy DM-TSP1 method
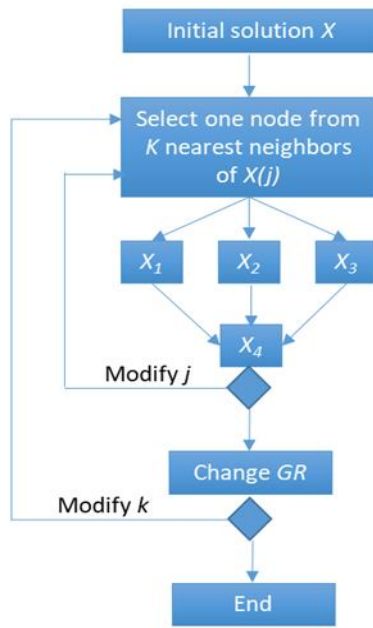
Figure 4. The flowchart of the FtN method [11]

4. EXPERIMENTAL RESULTS

The novel metaheuristic DM4 is applied to optimize the coverage repair policies for fourteen sensors using a moving actor with seven scenarios by changing the moving speed (w) from 0.4 to 1 (see Table 1). This is a standard instance originally taken from literature [37] where an Evolutionary Algorithm (EA) is performed in order to optimize the time and distance for the coverage repair strategy on behalf of the wireless network problem.

TABLE 1. The coordinates of 14 sensors with their residual survival times

Sensors	X	Y	Residual Survival Time (α_i)
1	16.47	96.10	39
2	16.47	94.44	27
3	20.09	92.54	36
4	22.39	93.37	23
5	25.23	97.24	39
6	22.00	96.05	37
7	20.47	97.02	35
8	17.20	96.29	37
9	16.30	97.38	39
10	14.05	98.12	35
11	16.53	97.38	36
12	21.52	95.59	33
13	19.41	97.13	23
14	20.09	94.55	24

No parameters are required for the metaheuristic DM4, just the stopping criterion which is fixed by no improvement of the current solution. Table 2 depicts the generated results and the performance of DM4 is computed for the two criteria using respectively Equation (3) (maximizing the number of active sensors) and Equation (4) (minimizing the total trajectory distance).

$$\% Perfomance_{f1} = \left(\frac{EA - DM4}{DM4} * 100 \right) \qquad (3)$$

$$\% Perfomance_{f2} = \left(\frac{DM4 - EA}{EA} * 100 \right) \qquad (4)$$

Obviously, DM4 generates four new better solutions than EA (respectively for instances with moving speed of 0.4, 0.5, 0.8 and 0.9) and finds the same results for the remaining three instances (thus, the improvement percentage is 19.96%). Besides, DM4 is developed under a Python programming language and a graphical representation of the generated solution are given.

Figure 5 illustrates the solution obtained by DM4 (after two seconds) with a moving speed varying from (w=0.4) to (w=1).

Figure 6 depicts the solutions generated by the two metaheuristics DM4 and EA for the two conflictual criteria. Obviously, DM4 outperforms EA on the first criterion (maximize f_1) for instances with speeds (w=0.4) and (w=0.8); concerning the second criterion (minimize f_2), DM4 outperforms EA especially for the instances with speeds (w=0.5) and (w=0.9).

TABLE 2. The generated results by DM4 and EA

W	The DM4 solutions	DM4		EA		% Performance	
		f_1	f_2	f_1	f_2	f_1	f_2
0.4	0-8-10-7-12-6-13-11-5-4-3-2-1-9-0	**10**	**33.4954**	9	31.2088	**10.00**	-
0.5	0-1-7-8-10-12-6-13-11-5-4-3-2-9-0	**11**	**36.2439**	11	36.4161	-	**0.47**
0.6	0-9-8-10-7-12-6-13-2-11-5-4-3-1-0	12	34.9211	12	34.9211	-	0.00
0.7	0-1-9-8-10-7-12-6-13-2-3-11-5-4-0	13	35.6519	13	35.6519	-	0.00
0.8	0-1-9-8-10-7-12-6-13-3-2-11-5-4-0	**14**	**37.2112**	13	30.8785	**7.14**	-
0.9	0-7-12-6-11-5-4-3-2-13-1-9-8-10-0	**14**	**31.2269**	14	31.9583	-	**2.34**
1.0	0-1-13-2-3-4-5-11-6-12-7-10-8-9-0	14	30.8785	14	30.8785	-	0.00
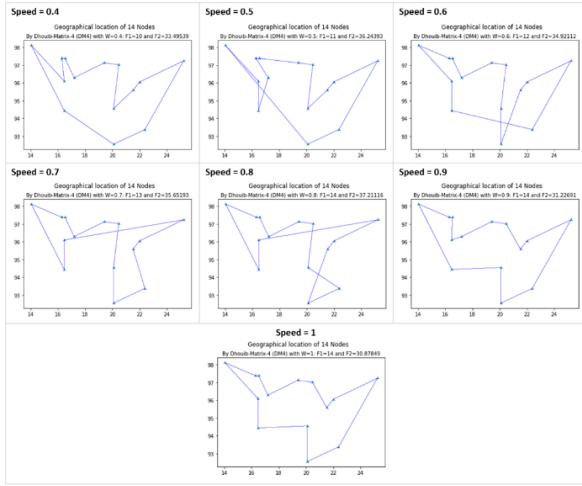
Figure 5. The solutions generated by DM4 with different moving speeds from (w=0.4) to (w=1)
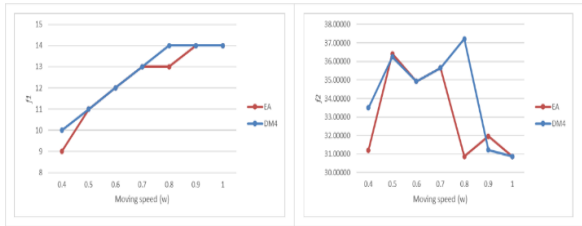
Figure 6. Comparing DM4 to EA with maximizing f_1 and minimizing f_2

Another example is considered from TSP-LIB entitled Berlin-52 where DM4 is applied to optimize the coverage repair policies for fifty one sensors using a moving actor with seven scenarios by changing the moving speed (*w*) from 0.4 to 1 (see Table 3).

Figure 7 illustrates the generated solutions by DM4 (after an average of 6 seconds) for Berlin-52 TSP-Lib instance with different moving speeds (from 0.4 to 1).

TABLE 3. The generated results by DM4 for Berlin-52 problem

W	The DM4 solutions	DM4	
		f_1	f_2
0.4	0-21-17-30-20-22-19-49-15-43-45-24-3-5-14-4-23-47-36-37-39-38-33-34-35-48-31-44-18-40-7-8-9-42-32-50-11-10-51-13-12-26-27-25-46-28-29-41-1-6-16-2-0	34	8104.01187
0.5	0-21-30-17-2-16-20-41-6-1-29-22-19-49-15-43-45-24-3-5-14-4-23-47-37-36-39-38-33-34-35-48-31-44-18-40-7-8-9-42-32-50-11-10-51-13-12-26-27-25-46-28-0	38	8070.62699
0.6	0-21-48-31-44-18-7-40-2-17-30-20-41-6-1-29-22-19-49-28-15-45-43-33-34-35-38-39-37-36-47-23-4-14-5-3-24-11-27-26-25-46-12-13-51-10-50-32-42-16-8-9-0	42	8948.94064
0.7	0-21-48-31-44-18-9-8-7-40-2-16-17-30-20-41-6-1-29-22-19-49-28-15-45-43-33-34-35-38-39-36-37-47-23-4-14-5-3-24-11-27-26-25-46-12-13-51-10-50-32-42-0	45	8105.87697
0.8	0-21-30-17-2-16-20-41-6-1-29-22-19-49-28-15-45-43-33-34-35-48-31-44-18-40-7-8-9-42-14-4-23-47-36-38-39-37-5-3-24-11-27-25-26-12-13-46-51-10-50-32-0	48	8654.12008
0.9	0-48-31-21-30-17-2-44-18-40-7-8-9-42-32-50-10-51-13-12-46-25-26-27-11-24-3-5-14-4-23-47-37-36-39-38-35-34-33-43-45-15-28-49-19-22-29-41-6-1-16-20-0	50	7863.03197
1.0	0-48-31-21-30-17-2-16-20-41-6-1-29-22-19-49-28-15-45-43-33-34-35-38-39-36-37-47-23-4-14-5-3-24-11-27-26-25-46-12-13-51-10-50-32-42-9-8-7-40-18-44-0	52	7684.23141
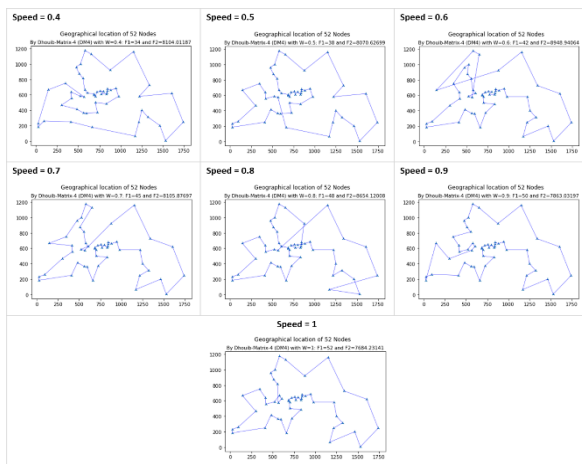
Figure 7. The solutions generated by DM4 for the Berlin-52 problem with different moving speeds from (w=0.4) to (w=1)

5. CONCLUSION

A Wireless Sensor Networks are mainly used to create a virtual layer from the physical world through exchanging information from a set of sensors. The purpose of the current study was to hierarchically optimize the coverage repair policies for wireless sensor networks using a mobile robot with different moving speeds by enhancing the novel Dhouib-Matrix-4 (DM4) metaheuristic. DM4 is improved to maximize at first the numbers of nodes to be visited in time and at second to minimize the trajectory distance.

This DM4 method is compared to the Evolutionary Algorithm on seven standard instances taken from the literature where the moving speed (*w*) of a mobile actor is varied from 0.4 to 1. The robustness of DM4 is proved by outperforming the Evolutionary Algorithm on four instances and finding the same results for the remaining three instances. Moreover, DM4 is simulated on other instances (dealing about 52 sensors) with diferent moving speeds.

As far as we know, no one in the literature generated the Pareto non dominated set solutions for the problem of coverage repair policies for wireless sensor networks using a mobile robot with different moving speeds. Despite this limitation, in future work we hope to use the proposed Dhouib-Matrix-4 metaheuristic to generate the Pareto non dominated set solutions for maximizing the numbers of nodes to be visited in time and in parallel (instead of hierarchical resolution) for minimizing the trajectory distance.

6. REFERENCES

1. Zorbas, D. and Razafindralambo, T., "Prolonging network lifetime under probabilistic target coverage in wireless mobile sensor networks", *Computer Communications*, Vol. 36, No. 9, (2013), 1039-1053. doi: 10.1016/j.comcom.2012.07.021.

2. Mohammadi, S. and Farahani, G., "Computational intelligence-based connectivity restoration in wireless sensor and actor networks", *EURASIP Journal on Wireless Communications and Networking*, Vol. 2020, (2020), 1-33. doi: 10.1186/s13638-020-01831-0.

3. Huang, H., Savkin, A.V., Ding, M. and Huang, C., "Mobile robots in wireless sensor networks: A survey on tasks", *Computer Networks*, Vol. 148, (2019), 1-19. doi: 10.1016/j.comnet.2018.10.018.

4. Kim, J. and Yoo, Y., "Sensor node activation using bat algorithm for connected target coverage in wsns", *Sensors*, Vol. 20, No. 13, (2020), 3733. doi: 10.3390/s20133733.

5. Li, S. and Shen, H., "Minimizing maximum movement of sensors for line barrier coverage in the plane", *Computer Networks*, Vol. 163, (2019), 106841. doi: 10.1016/j.comnet.2019.06.019.

6. Andaluz, G.M., Leica, P., Herrera, M., Morales, L. and Camacho, O., "Hybrid controller based on null space and consensus algorithms for mobile robot formation", *Emerging Science Journal*, Vol. 6, No. 3, (2022), 429-447.

7. Procter, S. and Secco, E.L., "Design of a biomimetic bldc driven robotic arm for teleoperation & biomedical applications", *J Hum Earth Future. ISSN*, (2022), 2785-2997. doi: 10.28991/HEF-2021-02-04-03.

8. Kabakulak, B., "Sensor and sink placement, scheduling and routing algorithms for connected coverage of wireless sensor networks", *Ad Hoc Networks*, Vol. 86, (2019), 83-102. https://doi.org/10.1016/j.adhoc.2018.11.005

9. Harizan, S. and Kuila, P., "Coverage and connectivity aware energy efficient scheduling in target based wireless sensor networks: An improved genetic algorithm based approach", *Wireless Networks*, Vol. 25, No. 4, (2019), 1995-2011.

10. Rashid, B. and Rehmani, M.H., "Applications of wireless sensor networks for urban areas: A survey", *Journal of Network and Computer Applications*, Vol. 60, (2016), 192-219. https://doi.org/10.1016/j.jnca.2015.09.008

11. Yetgin, H., Cheung, K.T.K., El-Hajjar, M. and Hanzo, L.H., "A survey of network lifetime maximization techniques in wireless sensor networks", *IEEE Communications Surveys & Tutorials*, Vol. 19, No. 2, (2017), 828-854. doi: 10.1109/COMST.2017.2650979.

12. Boukerche, A. and Sun, P., "Connectivity and coverage based protocols for wireless sensor networks", *Ad Hoc Networks*, Vol. 80, (2018), 54-69. doi: 10.1016/j.adhoc.2018.07.003.

13. Wang, Y., Wu, S., Chen, Z., Gao, X. and Chen, G., "Coverage problem with uncertain properties in wireless sensor networks: A survey", *Computer Networks*, Vol. 123, (2017), 200-232. doi: 10.1016/j.comnet.2017.05.008.

14. Tian, Y., Ou, Y., Reza Karimi, H., Liu, Y.T. and Han, J.Q., "Distributed multitarget probabilistic coverage control algorithm for wireless sensor networks", *Mathematical Problems in Engineering*, Vol. 2014, (2014).

15. Dhouib, S., "Multi-start constructive heuristic through descriptive statistical metrics: The dhouib-matrix-4 (DM4) metaheuristic", *International Journal of Operational Research*, (2022). doi: 10.1504/IJOR.2021.10045069.

16. Dhouib, S., "Finding the shortest holes drilling path in printed circuit board via the dhouib-matrix-4 technique", *Advances in Transdisciplinary Engineering, Mechatronics and Automation Technology*, Vol. 33, (2023), 396-401. doi: 10.3233/ATDE221192.

17. Dhouib, S. and Pezer, D., "A novel metaheuristic approach for drilling process planning optimization: Dhouib-matrix-4 (DM4)",

International Journal of Artificial Intelligence, Vol. 20, No. 2, (2022), 80-92.

18. Dhouib, S. and Pezer, D., "Increasing the performance of computer numerical control machine via the dhouib-matrix-4 metaheuristic: Metaheuristic for computer numerical control machine", *Inteligencia Artificial*, Vol. 26, No. 71, (2023), 142-152. doi: 10.4114/intartif.vol26iss71pp142-152.

19. Dhouib, S., "Novel heuristic for new pentagonal neutrosophic travelling salesman problem", *Neutrosophic Sets and Systems*, Vol. 51, (2022), 344-359. doi: 10.5281/zenodo.7135315.

20. Dhouib, S., "Hole drilling route optimization in printed circuit boards using far-to-near metaheuristics: Optimizing the hole drilling route via far-to-near metaheuristic", *International Journal of Strategic Engineering (IJoSE)*, Vol. 5, No. 1, (2022), 1-12. doi: 10.4018/IJoSE.301568.

21. Dhouib, S., "Novel heuristic for intuitionistic triangular fuzzy travelling salesman problem", *International Journal of Applied Evolutionary Computation (IJAEC)*, Vol. 12, No. 4, (2021), 39-55. doi: 10.4018/IJAEC.2021100104.

22. Dhouib, S., "Neutrosophic triangular fuzzy travelling salesman problem based on dhouib-matrix-tsp1 heuristic", *International Journal of Computer and Information Technology (2279-0764)*, Vol. 10, No. 5, (2021). doi: 10.24203/ijcit.v10i5.154.

23. Dhouib, S., "Optimization of travelling salesman problem on single valued triangular neutrosophic number using dhouib-matrix-tsp1 heuristic", *International Journal of Engineering, Transactions C: Aspects*, Vol. 34, No. 12, (2021), 2642-2647. doi: 10.5829/IJE.2021.34.12C.09.

24. S. Dhouib, "An application of the novel heuristic dhouib-matrix-tsp1", *International Journal on Engineering Technologies and Informatics*, Vol. 2, No. 5, (2021), 133-135. https://skeenapublishers.com/journal/ijeti/IJETI-02-00026.pdf

25. Dhouib, S., Broumi, S. and Lathamaheswari, M., "Single valued trapezoidal neutrosophic travelling salesman problem with novel greedy method: The dhouib-matrix-tsp1 (DM-TSP1)", *International Journal of Neutrosophic Science*, Vol. 17, No. 2, (2021), 144-157. doi: 10.54216/IJNS.170205.

26. Dhouib, S., Zouari, A., Dhouib, S. and Chabchoub, H., "Integrating the artificial bee colony metaheuristic with dhouib-matrix-tsp1 heuristic for holes drilling problems", *Journal of Industrial and Production Engineering*, Vol. 40, No. 3, (2023), 177-187. doi: 10.1080/21681015.2022.2158499.

27. Dhouib, S., "Solving the trapezoidal fuzzy transportation problems via new heuristic: The dhouib-matrix-tp1", *International Journal of Operations Research and Information Systems (IJORIS)*, Vol. 12, No. 4, (2021), 1-16. doi: 10.4018/IJORIS.294119.

28. Dhouib, S., "Solving the single-valued trapezoidal neutrosophic transportation problems through the novel dhouib-matrix-tp1 heuristic", *Mathematical Problems in Engineering*, Vol. 2021, (2021), 1-11. doi: 10.1155/2021/3945808.

29. Dhouib, S., "An intelligent assignment problem using novel heuristic: The dhouib-matrix-ap1 (dm-ap1): Novel method for assignment problem", *International Journal of Intelligent Systems and Applications in Engineering*, Vol. 10, No. 1, (2022), 135-141. doi: 10.18201/ijisae.2022.277.

30. Dhouib, S., "Unravelling the assignment problem under intuitionistic triangular fuzzy environment by the novel heuristic dhouib-matrix-ap1", *Yugoslav Journal of Operations Research*, (2023). doi: 10.2298/YJOR220915005D.

31. Dhouib, S. and Sutikno, T., "Solving the trapezoidal fuzzy assignment problem using the novel dhouib-matrix-ap1 heuristic", *Bulletin of Electrical Engineering and Informatics*, Vol. 12, No. 2, (2023), 950-957. doi: 10.11591/eei.v12i2.4855.

32. Dhouib, S., "Novel optimization method for unbalanced assignment problems with multiple jobs: The dhouib-matrix-ap2", *Intelligent Systems with Applications*, Vol. 17, (2023), 200179. doi: 10.1016/j.iswa.2023.200179.

33. Dhouib, S., "Novel metaheuristic based on iterated constructive stochastic heuristic: Dhouib-matrix-3 (DM3)", *Applied Computational Intelligence and Soft Computing*, Vol. 2021, (2021), 1-10. doi: 10.1155/2021/7761993.

34. Dhouib, S. and Zouari, A., "Optimising the non-productive time of robotic arm for drilling circular holes network patterns via the dhouib-matrix-3 metaheuristic", *International Journal of Mechatronics and Manufacturing Systems*, Vol. 16, No. 2-3, (2023), 320-338. doi: 10.1504/IJMMS.2023.10054319.

35. Dhouib, S. and Zouari, A., "Adaptive iterated stochastic metaheuristic to optimize holes drilling path in manufacturing industry: The adaptive-dhouib-matrix-3 (a-dm3)", *Engineering Applications of Artificial Intelligence*, Vol. 120, (2023), 105898. doi: 10.1016/j.engappai.2023.105898.

36. Dhouib, S., "An optimal method for the shortest path problem: The dhouib-matrix-spp (dm-spp)", *Results in Control and Optimization*, Vol. 12, (2023), 100269. doi: 10.1016/j.rico.2023.100269.

37. Miao, Y. and Yu-Ping, W., "Coverage repair strategies for wireless sensor networks using mobile actor based on evolutionary computing", *Bulletin of Electrical Engineering and Informatics*, Vol. 3, No. 3, (2014), 213-222.

Persian Abstract

چکیده

در این مقاله، فراابتکاری جدید (DM4) Dhouib-Matrix-4 برای بهینه‌سازی سیاست‌های تعمیر پوشش برای شبکه‌های حسگر بی‌سیم با استفاده از یک ربات متحرک با
سرعت‌های متحرک متفاوت، بهبود می‌یابد. به صورت سلسله مراتبی، دو معیار متناقض در نظر گرفته می شود: ابتدا تعداد گره هایی که باید در زمان بازدید شوند به حداکثر می
رسد، سپس در مرحله دوم، فاصله مسیر به حداقل می رسد. DM4 یک روش چند استارتی است که در هر شروع از اکتشافی حریصانه جدید Dhouib-Matrix-TSP1
استفاده می کند تا یک راه حل اولیه اولیه را ایجاد کند که توسط تکنیک جستجوی محلی جدید با عنوان Far-to-Near تشدید می شود. DM4 در هفت نمونه استاندارد از
ادبیات استفاده می شود که در آن سرعت حرکت (w) یک بازیگر متحرک از ۴.۰ تا ۱ متغیر است. عملکرد DM4 با مقایسه نتایج آن با نتایج ایجاد شده توسط الگوریتم تکاملی
(EA) که در آن DM4 عملکرد بهتری دارد اثبات می شود. EA در چهار نمونه و نتایج یکسانی را برای سه نمونه یادآوری می یابد. DM4 تحت زبان برنامه نویسی پایتون
توسعه یافته است و یک نمایش گرافیکی از راه حل تولید شده نشان داده شده است.

International Journal of Engineering

Journal Homepage: www.ije.ir

Development of a Wideband Bi-layered Mantle-Cloak for Perfect Electric Conductor Cylindrical Objects under Obliquely Incident Plane Wave

A. Moosaei, M. H. Neshati*

Department of Electrical Engineering, Faculty of Engineering, Ferdowsi University of Mashhad, Mashhad, Iran

PAPER INFO	*ABSTRACT*
	This paper presents a mantle cloak structure to provide a wideband capability to hide a metallic cylinder over a broad span of angles of obliquely impinging plane waves. A bi-layered dielectric structure and a sheet of metasurface are used to enclose the object to be hidden. At first, the scattered field, including co- and cross-polarized components, is analytically formulated using circumferential waves for a multi-layer wrap around the cylinder. A tensor description is also applied to model the impedance of the metasurface for TE and TM waves. Then, a metasurface made of rectangular patches is considered, and its related parameters are optimized to hide a perfect electric conductor (PEC) cylinder. Moreover, a double-layered mantle cloak is presented and numerically investigated using a software package to enhance its cloaking bandwidth. The numerical results show that the clocking bandwidth is enhanced by up to 33% compared to that of a single-layered structure.

1. INTRODUCTION

New advances in metamaterial technology propose the feasibility of electromagnetics invisibility, which mainly relies on the complex interaction between waves and artificial materials [1-3]. To this end, Pendry et al. [4] introduced the Coordinate Transform (CT) method, considered one of the most effective techniques to achieve invisibility [5], which relies on the concept of the curving electromagnetic waves around the object performed by employing a special coating to create an enclosed environment, which ensures that the illuminated waves move around the object to avoid reflecting, interpreting the interior space of the container as virtually invisible. By this method, an ideal conversion-based coating could completely separate the coated object, making it appear that the coating and inner area do not exist in terms of electromagnetic properties [6].

As of late, there have been significant improvements in making metamaterials. In this regard, experimental evidence has validated the application of the CT technique to microwave bands. Numerous efforts have been made to apply this method to visible light frequencies [1, 7, 8]. Plasmonic cloaking is another helpful technique to achieve invisibility using the property of scattering elimination using metamaterials with a low electrical permeability coefficient [9-13] which creates an anti-phase scattering wave, reducing the scattered fields and eventually concealing the object.

Other unconventional techniques have been investigated in the literature in covering a sphere to be invisible. The limited size of the applied metamaterial coating results in an inherent need for a certain thickness. However, increasing the thickness of the layer is not suitable due to reducing bandwidth and increasing sensitivity. The plasmonic cloaking method requires thinner layers than the conversion-based approach and typically requires a finite thickness to function correctly [14-16].

A new masking technique based on the concept of mantle cloak has been proposed to address this issue by decreasing the Radar Cross Section (RCS) for various shaped objects, including planar, cylindrical, elliptical, and spheroidal objects at microwave and lower band of terahertz (THz) frequencies [14, 15, 17-20]. This

Corresponding author email: neshat@um.ac.ir (M. H. Neshati)

technique relies on a patterned conductive thin surface coating, known as a metasurface, to diminish the scattered components appropriately. By calculating the parameters of the metasurface, an optimal surface reactance is obtained to effectively suppress the object's scattered fields, resulting in its invisibility.

Most published research on cylindrical objects focuses on obtaining cloaking for TE and TM plane waves illuminated perpendicular to the PEC cylinders. In contrast, electromagnetic cloaking in the case of obliquely illuminated waves is still a challenging topic, that demands further investigation [21]. Most investigations have examined the performance of isotropic mantle cloaks, designed to be inductive or capacitive in one or two dimensions. Nevertheless, in practical applications, reducing the scattered field by cylindrical objects with thicknesses comparable to the wavelength of the incident wave is often preferable. This reduction should be satisfied over a wide range of polarization states.

When an obliquely incident electromagnetic wave illuminates a PEC cylinder, coupling polarization occurs, leading to an increase in the total *RCS* of the structure, which is generally undesirable. In addition, the cloaking frequency range is slightly shifted, which is also a challenging task. It should be pointed out that while an obliquely incident wave exposes a bare PEC cylinder, the scattered fields are not coupled. In contrast, the cross-polarized coupling is introduced for a dielectric or coated PEC cylinder using dielectric layers [22]. As a result, scattering, and consequently acquiring invisibility is an exciting subject [23]. Moreover, covering these objects over a wide range of angles of the incident wave is another exciting issue due to existing of the cross-coupling.

In a few studies, graphene has been applied as a mantle-cloaked material for dielectric cylinders with low permittivity at lower frequencies of the tera-hertz band [24, 25]. Nonetheless, the authors facilitated their analytical explanation by bypassing the cross-polarized components of the scattered fields. This simplification is necessary due to the cylinder's small size and low permittivity. A comparable level of simplification was considered by Bilotti et al. [26]. Additionally, a single-layered mantle cloak, possessing specific surface reactance, simply suppresses one or, at most, a limited number of orders of the scattered field, whereas using multi-layered coating introduces a few benefits, including the ability to suppress higher orders of the scattered fields, facilitating multi-band and wideband invisibility. Moreover, the range of invisibility angle is widened, and more importantly, cloaking feasibility for TM and TE polarized waves.

In our previous study [21], we thoroughly addressed and validated the analytical formulation of the scattering issue for a metallic cylinder enlightened obliquely by TM and TE polarized wave. A single-layered mantle cloak is also designed and optimized to suppress the scattered components by considering the co- and cross-polarized terms.

In this paper, the preliminary step involves expressing the scattered fields concerning co- and cross-polarized components originating from the PEC cylinder coated with multiple layers of dielectric material and subjected to the oblique incidence of a plane wave. Afterward, a numerical study is accomplished using CST EM simulator [27] to evaluate the accuracy of the derived results for a bi-layered structure. Moreover, further investigations are directed to develop upon the findings for a bi-layered mantle cloak to lessen the *RCS* of the metallic cylinders over a wide frequency range.

2. SCATTERING FORMULATION

2. 1. Single-Layered Mantel Cloak   Figure 1 shows a single-layered mantel cloak, in which a metallic cylinder with a radius of a is covered by a dielectric layer with a thickness of between a and a_d. In addition, a metasurface is positioned directly on top of the spacer. The mantle cloak impedance is formulated by a tensor consisting of off-diagonal terms, in which the cross-polarized components are considered. These factors are mathematically represented by Equation (1) to model the metasurface impedance.

$$Z_s = \begin{bmatrix} Z_s^{\text{TM,TE}} & Z_s^{\text{TM,TE}} \\ Z_s^{\text{TM,TE}} & Z_s^{\text{TM,TE}} \end{bmatrix}, \tag{1}$$

An oblique incident wave is illuminated on the cylinder by the angle of φ_i and inclination angle of θ_i as shown in Figure 1. For a TM wave, the cylindrical harmonics of the electric field are given by Equation (2) [28].

$$\begin{aligned}
\mathbf{E}_i &= \mathbf{E}_1 e^{-j\mathbf{k}_i \cdot \mathbf{r}} \\
&= \mathbf{E}_1 e^{jk_1 \cos\theta_i z} \sum_{n=-\infty}^{\infty} j^n J_n(k_1 \rho \sin\theta_i) e^{jn(\varphi - \varphi_i)}
\end{aligned} \tag{2}$$

Using Jacobi-Anger expansion [28], electric fields inside the dielectric layer and its associated cross-polarized
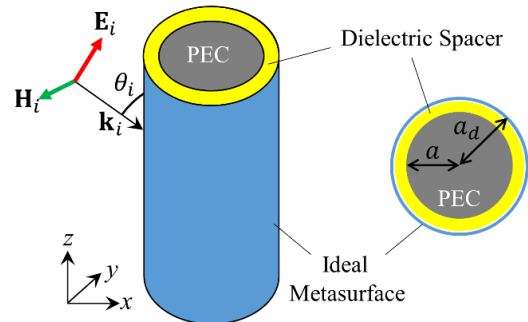
Figure 1. Single-layered mantel cloak using metasurface to cover the PEC cylinder illuminated obliquely by a plane wave

terms of the scattered fields are specified by Equations (3a) to (3c), in which $J_n(.)$ and $Y_n(.)$ represent ordinary Bessel functions of the first and second kind in cylindrical coordinates, respectively. $H_n^{(2)}(\cdot)$ denotes the second kind of Hankel function, to articulate an outward-traveling cylindrical wave.

$$E_i^z = \sin\theta_i\, e^{jk_1\cos\theta_i z} \sum_{n=-\infty}^{\infty} j^n J_n(k_1\sin\theta_i\rho\, e^{jn(\varphi-\varphi_i)} \tag{3a}$$

$$E_s^z = \sin\theta_i\, e^{jk_1\cos\theta_i z}$$
$$\sum_{n=-\infty}^{\infty} A_n^{co} H_n^{(2)}(k_1\sin\theta_i\rho)e^{jn(\varphi-\varphi_i)} \tag{3b}$$

$$E_d^z = \sin\theta_i\, e^{jk_2\cos\theta_i z}\sum_{n=-\infty}^{\infty}\Big[C_n^{co} J_n(k_2\sin\theta_t\rho)$$
$$+ D_n^{co} Y_n(k_2\sin\theta_t\rho)\Big]e^{jn(\varphi-\varphi_i)} \tag{3c}$$

Equations (4a) and (4b) also give the cross-polarized components.

$$H_s^z = \sin\theta_i\, e^{jk_1\cos\theta_i z}$$
$$\sum_{n=-\infty}^{\infty} B_n^{cr} H_n^{(2)}(k_1\sin\theta_i\rho)e^{jn(\varphi-\varphi_i)} \tag{4a}$$

$$H_d^z = \sin\theta_t\, e^{jk_2\cos\theta_t z}\sum_{n=-\infty}^{\infty} E_n^{cr} J_n(k_2\sin\theta_t\rho)$$
$$+ F_n^{cr} Y_n(k_2\sin\theta_t\rho)\Big]e^{jn(\varphi-\varphi_i)} \tag{4b}$$

Using impedance boundary conditions at the metasurface with a radius of $\rho = a_d$, the unknown coefficients of the mentioned equations are calculated. This is involved to satisfy the continuity of the tangential components of the electric fields. In addition, the discontinuity of the tangential terms of the magnetic field by the total induced current on the metasurface is the other condition. In addition, the continuity of the tangential components of electric and magnetic fields have to be satisfied on the planar surface, and the absence of tangential electric fields on the surface of the cylinder.

The σ_{2D}^{TM} of the structure is obtained by summation of the co- and cross-polarized terms of the scatted fields, calculated by the asymptotic forms of Hankel functions and their derivatives [22]. For a TM wave, σ_{2D}^{TM} is obtained using Equations (5a) to (5c).

$$\sigma_{2D}^{TM} = \sigma_{2D}^{TM,CO} + \sigma_{2D}^{TM,CR} \tag{5a}$$

$$\sigma_{2D}^{TM,CO} = \frac{4}{k_1\sin\theta_i^2}\left|\sum_{n=-\infty}^{\infty} A_n^{co}\, j^n e^{jn(\varphi-\varphi_i)}\right|^2 \tag{5b}$$

$$\sigma_{2D}^{TE,CR} = \frac{4\eta_1^2}{k_1\sin\theta_i^2}\left|\sum_{n=-\infty}^{\infty} B_n^{CR}\, j^{n+1} e^{jn(\varphi-\varphi_i)}\right|^2 \tag{5c}$$

2. 2. Multi-Layered Mantel Cloak   To develop the concept of a mantle cloak using a multi-layered structure,

the scattering formulation is extended for non-electrically small objects over a wide frequency range. In this instance, the focus is directed towards an arrangement featuring an infinitely extended cylinder of a radius of a, which is covered by N conformal anisotropic metasurfaces, which exhibit an effective surface impedance tensor equivalent to Z_S^1 and Z_S^N given by Equation (6a).

$$Z_S^i = \begin{bmatrix} Z_S^{TM,TM,i} & Z_S^{TM,TE,i} \\ Z_S^{TE,TM,i} & Z_S^{TE,TE,i} \end{bmatrix}, i = 1,2,\cdots N, \tag{6a}$$

The metasurfaces' radii are denoted by Equation (6b).

$$a_{d,i} = \gamma_i a, \quad i = 1,2,\cdots N, \tag{6b}$$

In addition, the object under consideration is subjected to an external obliquely incident plane wave, with the electric field oriented parallel to the cylinder axis, known as TM, or perpendicular to it, designated as TE wave. The electromagnetic formulation conducted in the case of mentioned scenario is comparable to that of the single-layered mantle cloak. The only difference is the existence of an additional spatial term (between two metasurfaces) in which the electric field E_z^d requires an accurate description. Equation (7a) is used for the co-polarized components.

$$E_d^z = \sum_{n=-\infty}^{\infty} e^{jn(\varphi-\varphi_i)} \times$$
$$\begin{cases} \sin\theta_{t1}\, e^{jk_1 z\cos\theta_{t1}} \times \\ [C1_n^{co}J_n(k_1'\rho) + D1_n^{co}Y_n(k_1'\rho)], a < \rho < a_{d1} \\ \sin\theta_{tN}\, e^{jk_N z\cos\theta_{tN}} \times \\ [CN_n^{co}J_n(k_N'\rho) + DN_n^{co}Y_n(k_N'\rho)], a_{d(N-1)} < \rho < a_{dN} \end{cases} \tag{7a}$$

Moreover, Equation (7b) is given for the cross-polarization terms.

$$H_d^z = \sum_{n=-\infty}^{\infty} e^{jn(\varphi-\varphi_i)} \times$$
$$\begin{cases} \sin\theta_{t1}\, e^{jk_1 z\cos\theta_{t1}} \times \\ [E1_n^{cr}J_n(k_1'\rho) + F1_n^{cr}Y_n(k_1'\rho)], a < \rho < a_{d1} \\ \sin\theta_{tN}\, e^{jk_N z\cos\theta_{tN}} \times \\ [EN_n^{cr}J_n(k_N'\rho) + FN_n^{cr}Y_n(k_N'\rho)], a_{d(N-1)} < \rho < a_{dN} \end{cases} \tag{7b}$$

Applying the boundary conditions at the surface between two adjacent layers, yields $4N+2$ mathematical statements. Therefore, $(4N+2)\times(4N+2)$ equations are obtained, and its solution determines the unknown coefficients, including A_n^{co}, B_n^{cr}, Ci_n^{co}, Di_n^{co}, Ei_n^{cr} and Fi_n^{cr}.

2. 3. Bi-Layered Mantel Cloak   As a specific example of a multi-layered mantel cloak, a bi-layered structure is considered in this section, which is shown in Figure 2. Considering a TM-polarized wave illuminates the object under investigation, the impinged, scattered, and transferred electric and magnetic fields are denoted by Equations (8a) to (8d).

$$E_i^z = \sin\theta_i\, e^{jk_1\cos\theta_i z} \sum_{n=-\infty}^{\infty} j^n J_n(k_1\sin\theta_i\rho\, e^{jn(\varphi-\varphi_i)} \tag{8a}$$

$$E_s^z = \sin\theta_i e^{jk_1\cos\theta_i z}$$
$$\sum_{n=-\infty}^{\infty} A_n^{co} H_n^{(2)}(k_1\sin\theta_i\rho)e^{jn(\varphi-\varphi_i)} \tag{8b}$$

$$E_{d1}^z = \sin\theta_{t1}e^{jk_3\cos\theta_{t1}z}\sum_{n=-\infty}^{\infty}\Big[C1_n^{co}J_n(k_3\sin\theta_{t1}\rho)$$
$$+D1_n^{co}Y_n(k_3\sin\theta_{t1}\rho)\Big]e^{jn(\varphi-\varphi_i)} \tag{8c}$$

$$E_{d2}^z = \sin\theta_{t2}e^{jk_2\cos\theta_{t2}z}\sum_{n=-\infty}^{\infty}\Big[C2_n^{co}J_n(k_2\sin\theta_{t2}\rho)$$
$$+D2_n^{co}Y_n(k_2\sin\theta_{t2}\rho)\Big]e^{jn(\varphi-\varphi_i)} \tag{8d}$$

The cross-polarized terms are also provided by Equations (9a) to (9c).

$$H_s^z = \sin\theta_i e^{jk_1\cos\theta_i z}$$
$$\sum_{n=-\infty}^{\infty} B_n^{cr} H_n^{(2)}(k_1\sin\theta_i\rho)e^{jn(\varphi-\varphi_i)} \tag{9a}$$

$$H_{d1}^z = \sin\theta_{t1}e^{jk_3\cos\theta_{t1}z}\sum_{n=-\infty}^{\infty}E1_n^{cr}J_n(k_3\sin\theta_{t1}\rho)$$
$$+F1_n^{cr}Y_n(k_3\sin\theta_{t1}\rho)\Big]e^{jn(\varphi-\varphi_i)} \tag{9b}$$

$$H_{d2}^z = \sin\theta_{t2}e^{jk_2\cos\theta_{t2}z}\sum_{n=-\infty}^{\infty}E2_n^{cr}J_n(k_2\sin\theta_{t2}\rho)$$
$$+F2_n^{cr}Y_n(k_3\sin\theta_{t2}\rho)\Big]e^{jn(\varphi-\varphi_i)} \tag{9c}$$

It should be noted that using the duality theorem, the scattered fields for a TE plane wave are derived using the same method as that of the TM one [21]. Accordinghly, ten equations are obtained, which can be solved by applying boundary conditions, leading to finding scattering coefficients at different boundaries. Then,
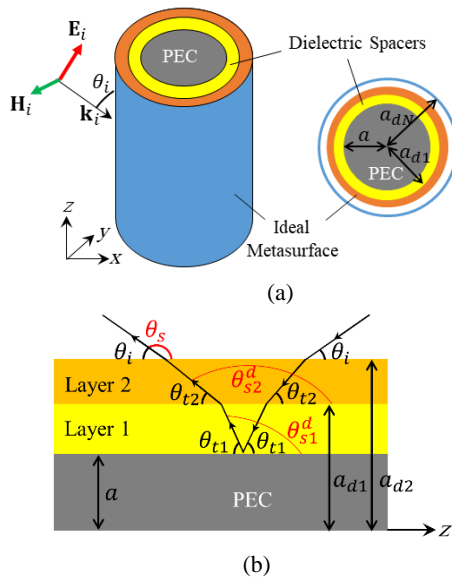
Figure 2. (a) bi-layered mantel cloak to invisible a dielectric-coated cylinder under oblique incidence wave, (b) side view and the definition of the incident and scattered angle

using the obtained coefficients, including A_n^{co} and B_n^{cr}, the total *RCS* of the object is calculated.

3. RESULTS AND DISCUSSION

3. 1. Single-layered Mantel Cloak   To design a single-layered cloak, a metallic cylinder is considered in our investigation with a length and radius of $10\lambda_o$ and $0.1\lambda_o$, respectively, and λ_o is the free space wavelength at 3 GHz. The cylinder is illuminated by an obliquely oriented TM wave at 3 GHz with $\theta_i = 60°$ and the polarization plane is perpendicular to the propagation direction.

Figure 3 depicts the simulated scattering width contours versus chromaticity based on a relative radius of a_d/a and the vital metasurface impedance, X_S^{TM}, for the dielectric constant of $\varepsilon_r = 4$. Moreover, it can be concluded that $X_S^{TM} = -50\,\Omega$ is required to achieve minimum scattering width, $\sigma_{2D} \pounds -7$ dB, corresponding to the thickness of $a_d = 1.2a$. So, depending on the covering radius, obtaining the minimum scattering width for a cylinder at a specific value of the surface reactance, denoted by *Xs*, is feasible. The aforementioned minimum scattering width significantly reducses the object's visibility, thereby establishing cloaking effectiveness. Figure 4 shows the required impedance of the applied metasurface for the mentioned metallic cylinder, whereas the dielectric constant of the spacer is $\varepsilon_r = 4$ and its thickness is $a_d = 1.2a$. It shows the scattering width versus X_S^{TM} and X_S^{TE}, obtained by assuming $\sigma_{2D} \gg -7$ dB, which indicates $X_S^{TM} = -47\Omega$ and $X_S^{TE} = -17\,\Omega$.

3. 2. Bi-Layered Mantel Cloak   To evaluate the impact of the radius cylinder on the scattered fields, a TM
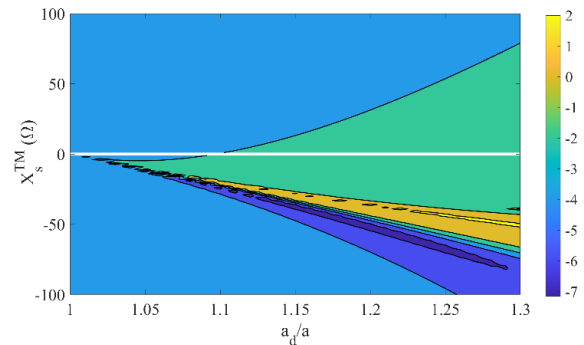
Figure 3. The surface impedance of metasurface for an obliquely incident TM wave and $\sigma_{2D} \gg -7$ dB versus relative radius of a_d/a
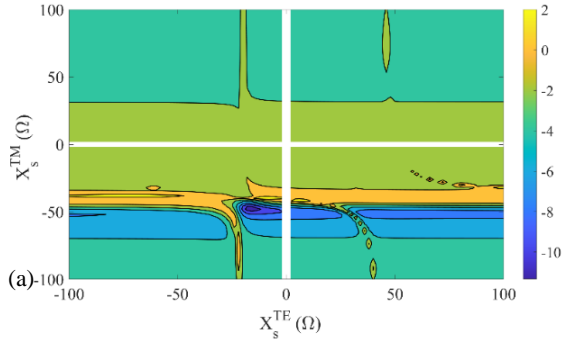
Figure 4. The required covering reactance of the metasurface for an oblique incident TM polarized wave on a dielectric-coated cylinder

wave at 3 GHz is obliquely illuminated by $\theta_i = 60°$ on a dielectric-coated metallic cylinder with relative permittivity of 15. Then, the magnitude of the co-polarized scattering coefficients A_n^{co}, in Equation (8b), are calculated. The results are illustrated in Figure 5 for two different cylinder radii of $a = 0.1\lambda_o$ and $a = \lambda_o$. The results confirm that for a PEC cylinder with a radius smaller than the operating wavelength, only the zeroth scattering mode contributes to the co-polarized scatter

(a)

(b)
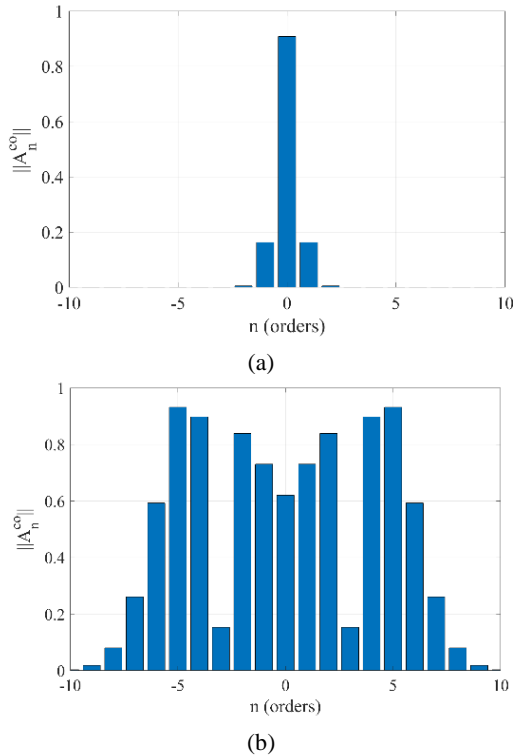
Figure 5. The radius-dependent scattering coefficients of a dielectric-covered metallic cylinder with relative permittivity of $\varepsilon_r = 15$ and cylinder radius of a) $a = 0.1\lambda_o$, b) $a = \lambda_o$.

fields, while for cylinders with a radius of nearly λ_o, free space wavelength, at least up to the eight order of the scattering modes affect the co-polarized terms.

Due to the ability of a metasurface to manipulate a single scattering mode, it is now possible to achieve cloaking for the objects that satisfy the quasi-static condition, in which the cylinder radius satisfies $r \leq \lambda_0 /10$ [Ergin, #1]. As can be appreciated from Figure 5, depending on the covering radius, there exists the possibility to obtain a minimum scattering width for a cylinder at a specific magnitude of the surface reactance of the cloak, denoted by X_s. The minimum scattering width is linked to significantly reducing the object's visibility. Nonetheless, dielectric objects require a positive surface reactance, which is an inductive surface, while in the case of metallic objects, they require a sheet of capacitive reactance.

It is worth saying that the application of the single-layered mantle cloaking in reducing the total *RCS* is only limited to small radius cylinders relative to the operating free-space wavelength over a narrow bandwidth. However, for large objects multi-layered covering structure is proposed to widen available bandwidth [18].

Because the examination of metallic cylinders is significantly more pronounced when interacting with a TM wave in comparison with that of a TE one, in this paper, a TM wave at 3 GHz illuminates a limited length of a cylinder with a radius of $a = 0.1\lambda_o$ and a length of $L = \lambda_o$ at $\theta_i = 60°$ and the required mantle cloak is designed to obtain low total *RCS*.

As discussed in section II, using a single- or bi-layered dielectric covering with a dielectric constant of 4, which provides capacitive reactance, the required reactance are $X_S^{TM} = -23 \, \Omega$ and $X_S^{TE} = -5 \, \Omega$. To design the required metasurface providing the mentioned values of reactance, a quadrilateral capacitive patch is applied as shown in Figure 6. This structure provides two distinct periodicity parameters including D_z and D_φ, which are optimized to satisfy the required situation. Initially, Equation (10) is used to estimate X_S^{TM}, in which c and η_o represent light speed and inherent impedance of free space, respectively. Table 1 summarizes the optimal parameters of the single- and bi-layered designed mantle cloaks. In this regard, in our optimization process, initially, we assume to have geometrical parameters obtained from analytical formula. Then, we run the optimizer in CST MWS to achieve a minimum total RCS.

$$X_S^{TM} = \frac{\eta_o \pi c}{2\pi f D(\varepsilon_r + 1) \ln\left[\csc\left(\frac{\pi g}{2D}\right)\right]}, \tag{10}$$

Figure 7 shows the total *RCS* of the single- and bi-layered mantel cloak. It can be seen that invisibility is obtained for a wide range of θ_i using the optimized values of the relative thickness a_d/a and spacer permittivity,
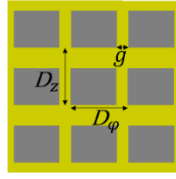
Figure 6. The rectangular-shaped metasurface coverings the PEC cylinder and its related parameters

TABLE 1. The calculated and refined optimal parameters for single- and bi-layered mantle cloaks

	Description	Param.	Values (mm)
PEC Cylinder	Cylinder radius	a	10
	Spacer thickness	a_d	11
Single-layered structure	Patch distance	g	1.5
	φ periodicity	D_φ	17.28
	z periodicity	D_z	24
		a_{d1}	11.2
	First layer	g_1	1.2
		$D_{\varphi1}$	17.28
bi-layered structure		D_{z1}	12.6
		a_{d2}	13
	Second layer	g_2	1.2
		$D_{\varphi2}$	8.64
		D_{z2}	12.1
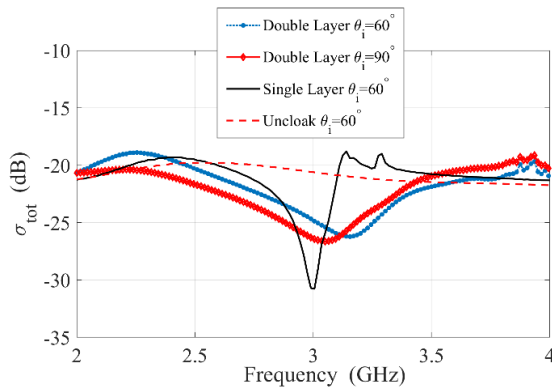
Figure 7. The total *RCS* for the single- and bi-layered mantel cloak versus frequency

resulting in acquiring the required surface impedance values using the rectangular-shaped metasurface. Notably, the frequency range in which the invisibility is achieved using the bi-layered structure is nearly doubled compared to that of the single-layered cloak. Figure 7 also confirms that, at 3 GHz, the bi-layered mantle cloak provides 1 GHz bandwidth, corresponding to a fractional

bandwidth of 33%. So, the bi-layered metasurface can significantly reduce scattered fields over a wideband frequency range, interpreting the object as invisible. The photos of the electric field for the cloaked- and bared cylinder are shown in Figure 8, which confirms that the field distribution is strongly disturbed in the case of the cloaked cylinder. However, by covering the metallic cylinder using the designed metasurface, the wavefronts for the cloaked- and bared-cylinder is illustrated in Figure 8. It can be concluded that field distribution is powerfully disturbed in the case of the cloaked cylinder. However, by covering the metallic cylinder using the designed metasurface, the wavefronts rotate around the object leading to become invisible.

The simulated patterns of the total *RCS* for the cloaked and uncloaked cylinder are depicted in Figure 9 versus φ in the observation angle of $\theta_s = 120°$, since the impinging angle is $\theta_i = 60°$ which confirms that the designed bi-layered metasurface as mantle cloak significantly reduces the scattered fields. Also, it indicates that in all observation angles the cloak is efficient.

Table 2. summarizes a comparison between published works in the literature and the proposed technique in terms of cloaking performance and bandwidth. As can be seen, the introduced bi-layeedr rectangular patch metasurfaces with 33% bandwidth at 3 GHz provides better performance than the other published works wich represent the robustness of the
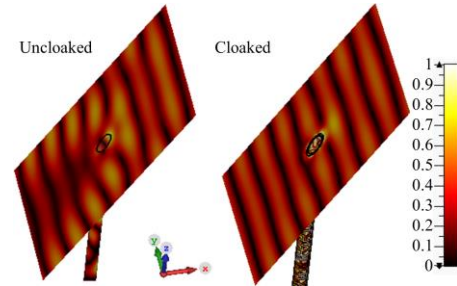
Figure 8. The snapshots of the normalized electric fields of the cloaked and uncloaked cylinder for $\theta_i = 60°$
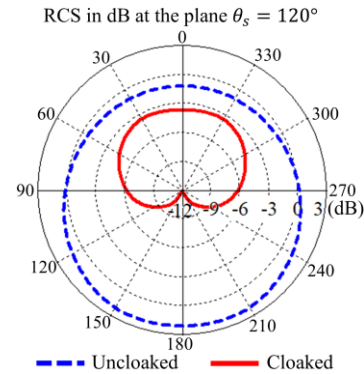
Figure 9. The simulated total *RCS* patterns of the bare and cloaked cylinder versus φ, for $\theta_i = 60°$ and $\theta_s = 120°$

TABLE 2. The comparsion of cloaking and bandwidth performaance with published works

Ref.	Metasurface	Frequncy (GHz)	Cloaking Perfomance (dB)	Cloaking BW (%)
[25]	Graphene Metasurface	4	5.2	30
[29]	Nonlinear Metasurface	3	30	10
[30]	Huygens' Metasurface	4	15	27.5
[31]	Metallic patches	9	6.2	16.6
[21]	Metallic patches	3	6	20
[32]	I-Shaped Metasurface	3	10	10
[18]	Metallic patches	3.3	8	30
This Work	Rectangular Patch	3	6	33

proposed methode to increase the cloaking bandwidth while an obliquely incident wave is impinged on a PEC cylinder.

4. CONCLUSION

This paper uses the established mantle cloak technique to study electromagnetic invisibility for a metallic cylinder illuminated by a broad range of obliquely incidence angles for both TM and TE waves. It is shown that the scattered fields provide co- and cross-polarized terms due to obliquely impinging waves. To settle the issue and consider these two components simultaneously, a metasurface sheet impedance is used, which is modeled by a tensor model for both waves. The metasurface is made by rectangular-patch, which provides capacitive reactance to diminish the scattered fields and significantly decrease the total *RCS* leading to hiding the object from the incoming wave. The systematic formulation is verified using numerical investigation by CST software. To widen the available bandwidth, a bi-layered mantle cloak is also designed, resulting in nearly 33% cloaking bandwidth, which is twice that of the single-layered mantle clock at 3 GHz for a PEC cylinder with a radius of 10 mm.

5. REFERENCES

1. Schurig, D., Mock, J.J., Justice, B., Cummer, S.A., Pendry, J.B., Starr, A.F. and Smith, D.R., "Metamaterial electromagnetic cloak at microwave frequencies", *Science*, Vol. 314, No. 5801, (2006), 977-980, DOI: 10.1126/science.1133628.

2. Alù, A. and Engheta, N., "Achieving transparency with plasmonic and metamaterial coatings", *Physical Review E*, Vol. 72, No. 1, (2005), 016623, DOI: 10.1103/ PhysRevE. 72.016623.

3. Alù, A. and Engheta, N., "Plasmonic cloaks", in Metamaterials and Plasmonics: Fundamentals, Modelling, Applications, Springer. (2009), 37-47, DOI: 10.1007/978-1-4020-9407-1_3.

4. Pendry, J. B., Schurig, D. and Smith, D. R., "Controlling electromagnetic fields", *Science*, Vol. 312, No. 5781, (2006), 1780-1782, DOI: 10.1126/science.1125907 10.1126/science.1125907.

5. Leonhardt, U., "Optical conformal mapping", *Science*, Vol. 312, No. 5781, (2006), 1777-1780, DOI: 10.1126/science.1126493.

6. Padooru, Y.R., Yakovlev, A.B., Chen, P.-Y. and Alu, A., "Analytical modeling of conformal mantle cloaks for cylindrical objects using sub-wavelength printed and slotted arrays", *Journal of Applied Physics*, Vol. 112, No. 3, (2012), 034907, DOI: 10.1063/1.4745888.

7. Ergin, T., Stenger, N., Brenner, P., Pendry, J.B. and Wegener, M., "Three-dimensional invisibility cloak at optical wavelengths", *Science*, Vol. 328, No. 5976, (2010), 337-339, DOI: 10.1126/science.1186351.

8. Valentine, J., Li, J., Zentgraf, T., Bartal, G. and Zhang, X., "An optical cloak made of dielectrics", *Nature Materials*, Vol. 8, No. 7, (2009), 568-571, DOI: 10.1038/nmat2461.

9. Alù, A. and Engheta, N., "Cloaking a sensor", *Physical Review letters*, Vol. 102, No. 23, (2009), 233901, DOI: 10.1103/PhysRevLett.102.233901.

10. Alù, A. and Engheta, N., "Multifrequency optical invisibility cloak with layered plasmonic shells", *Physical Review Letters*, Vol. 100, No. 11, (2008), 113901, DOI: 10.1103/PhysRevLett.100.113901.

11. Alu, A. and Engheta, N., "Plasmonic and metamaterial cloaking: Physical mechanisms and potentials", *Journal of Optics A: Pure and Applied Optics*, Vol. 10, No. 9, (2008), 093002, DOI: 10.1088/1464-4258/10/9/093002.

12. Milton, G.W. and Nicorovici, N.-A.P., "On the cloaking effects associated with anomalous localized resonance", *Proceedings of the Royal Society A: Mathematical, Physical and Engineering Sciences*, Vol. 462, No. 2074, (2006), 3027-3059, DOI: 10.1098/rspa.2006.1715.

13. Yuste, P., Rius, J. M., Romeu, J., Blanch, S., Heldring, A. and Ubeda, E., "A microwave invisibility cloak: The design, simulation, and measurement of a simple and effective frequency-selective surface-based mantle cloak", *IEEE Antennas and Propagation Magazine*, Vol. 60, No. 4, (2018), 49-59, DOI: 10.1109/MAP.2018.2839903.

14. Alù, A., "Mantle cloak: Invisibility induced by a surface", *Physical Review B*, Vol. 80, No. 24, (2009), 245115.

15. Chen, P.-Y. and Alu, A., "Mantle cloaking using thin patterned metasurfaces", *Physical Review B*, Vol. 84, No. 20, (2011), 205110, DOI: 10.1103/PhysRevB.80.245115.

16. Chen, P.-Y., Montione, F. and Alu, A., "Suppressing the electromagnetic scattering with a helical mantle cloak", *IEEE Antennas and Wireless Propagation Letters*, Vol. 10, (2011), 1598-1601, DOI: 10.1109/LAWP. 2011. 2179001.

17. Monti, A., Toscano, A. and Bilotti, F., "Metasurface mantle cloak for antenna applications", in Proceedings of the 2012 IEEE International Symposium on Antennas and Propagation, IEEE. (2012), 1-2, DOI: 10.1109/APS.2012. 6348711.

18. Soric, J.C., Alù, A., Kerkhoff, A. and Rainwater, D., "Experimental demonstration of a conformal mantle cloak for radio-waves", in Proceedings of the 2012 IEEE International Symposium on Antennas and Propagation, IEEE. (2012), 1-2, DOI: 10.1109/APS.2012.6349400.

19. Monti, A., Bilotti, F., Toscano, A., Soric, J. and Alù, A., "Mantle cloak devices for TE and TM polarizations", in 2013 IEEE Antennas and Propagation Society International Symposium (APSURSI), IEEE. (2013), 324-325, DOI: 10.1109/APS.2013.6710823.

20. Bernety, H. M. and Yakovlev, A. B., "Metasurface cloaks for dielectric and metallic elliptical cylinders and strips", in 2014 International Conference on Electromagnetics in Advanced Applications (ICEAA), IEEE. (2014), 496-499, DOI: 10.1109/ICEAA.2014.6903905.

21. Moosaei, A. and Neshati, Mohammad H., "Design investigation of mantle-cloak for a PEC cylindrical object under oblique incidence of TM and TE waves", *AEU-International Journal of Electronics and Communications*, Vol. 137, (2021), 153801, DOI: 10.1016/j.aeue.2021.153801.

22. Balanis, C., "Advanced engineering electromagnetics", John Wiley & Sons,, *NewYork*, 1989.

23. Moosaei, A. and Neshati, Mohammad H., "Wide-band cloaking of finite length pec cylindrical objects under oblique incidence using multi-layer mantle cloak", in 2021 29th Iranian Conference on Electrical Engineering (ICEE), IEEE. (2021), 886-890, DOI: 10.1109/ICEE52715.2021. 9544464.

24. Hamzavi-Zarghani, Z., Yahaghi, A. and Matekovits, L., "Electrically tunable mantle cloaking utilizing graphene metasurface for oblique incidence", *AEU-International Journal of Electronics and Communications*, Vol. 116, (2020), 153080, DOI: 10.1016/j.aeue.2020.153080.

25. Pawar, S., Bernety, H.M. and Yakovlev, A.B., "Cloaking of cylindrical objects with graphene-metasurface structures for low-terahertz applications", in 2022 IEEE International Symposium on Antennas and Propagation and USNC-URSI Radio Science

Meeting (AP-S/URSI), IEEE. (2022), 1366-1367, DOI: 10.1109/AP-S/USNC-URSI47032.2022. 9886308.

26. Bilotti, F., Tricarico, S. and Vegni, L., "Plasmonic metamaterial cloaking at optical frequencies", *IEEE Transactions on Nanotechnology*, Vol. 9, No. 1, (2009), 55-61, DOI: 10.1109/TNANO.2009.2025945.

27. Studio, C.M., "CST microwave studio", *CST Studio Suite*, (2020).

28. Osipov, A. V. and Tretyakov, S. A., "Modern electromagnetic scattering theory with applications", John Wiley & Sons, NewYork, 2017.

29. S. Vellucci et al., "On the use of nonlinear metasurfaces for circumventing fundamental limits of mantle cloaking for antennas," *IEEE Transactions on Antennas and Propagation*, Vol. 69, No. 8, (2021), 5048-5053, DOI: 10.1109/TAP.2021.3061010.

30. H. Younesiraad, Z. Hamzavi-Zarghani, and L. Matekovits, "Invisibility utilizing Huygens' metasurface based on mantle cloak and scattering suppression phenomen," *IEEE Transactions on Antennas and Propagation*, Vol. 69, No. 8, (2021), 5181-5186, DOI: 10.1109/TAP.2021.3060022.

31. V. Pratik, M. Singh Bisht, and K .Vaibhav Srivastava, "Improving performance of mantle cloak for electrically large PEC cylinders by reducing higher-order scattering coefficients," *Journal of Electromagnetic Waves and Applications,* Vol. 35, No. 9, (2021), 1176-1191, DOI: 10. 1080/09205071.2021.1872042.

32. M. Bisht, V. P. Vinubhai, and K. V. Srivastava, "Analysis and realization of a wideband mantle cloak with improved cloaking performance," *Journal of Electromagnetic Waves and Applications*, Vol. 34, No. 10, (2020), 1386-1399, DOI: 10.1080/09205071.2020.1726213

Persian Abstract

چکیده

در این مقاله، فراابتکاری جدید Dhouib-Matrix-4 (DM4) برای بهینه‌سازی سیاست‌های تعمیر پوشش برای شبکه‌های حسگر بی‌سیم با استفاده از یک ربات متحرک با سرعت‌های متحرک متفاوت، بهبود می‌یابد. به صورت سلسله مراتبی، دو معیار متناقض در نظر گرفته می شود: ابتدا تعداد گره هایی که باید در زمان بازدید شوند به حداکثر می رسد، سپس در مرحله دوم، فاصله مسیر به حداقل می رسد. DM4 یک روش چند استارتی است که در هر شروع از اکتشافی حریصانه جدید Dhouib-Matrix-TSP1 استفاده می کند تا یک راه حل اولیه را ایجاد کند که توسط تکنیک جستجوی محلی جدید با عنوان Far-to-Near تشدید می شود. DM4 در هفت نمونه استاندارد از ادبیات استفاده می شود که در آن سرعت حرکت (w) یک بازیگر متحرک آن از ۰.٤ تا ۱ متغیر است. عملکرد DM4 با مقایسه نتایج آن با نتایج ایجاد شده توسط الگوریتم تکاملی (EA) که در آن DM4 عملکرد بهتری دارد اثبات می شود. EA در چهار نمونه و نتایج یکسانی را برای سه نمونه یادآوری می یابد. DM4 تحت زبان برنامه نویسی پایتون توسعه یافته است و یک نمایش گرافیکی از راه حل تولید شده نشان داده شده است.

International Journal of Engineering

Prediction of the Efficiency of Hydraulic Fracturing Based on Reservoir Parameters

A. Dieng, G. P. Khiznyk, V. V. Poplygin*

Department of Oil and Gas Technologies, Perm National Research Polytechnic University (PNRPU), Russia

PAPER INFO

ABSTRACT

According to experts, the use of hydraulic fracturing can increase the oil and gas recovery factor by 10-15%. The Perm Territory belongs to the old oil-producing region of the Russian Federation. To date, more than 60% of the remaining recoverable oil reserves of the fields of the Perm region are concentrated in carbonate deposits. Most of the fields are currently in the late stages of development. These fields, as a rule, are characterized by the presence of undrained zones with residual reserves and low well flow rates. Most of the remaining reserves of the fields are concentrated in low-permeability reservoirs with a high degree of heterogeneity and difficult fluid filtration. Unfortunately, the results obtained in practice do not always correspond to preliminary calculations and do not reach the planned oil production rates. In connection with the above, the problem arises of predicting the effectiveness of hydraulic fracturing operations using mathematical methods of analysis. The effectiveness of hydraulic fracturing is undoubtedly influenced by both geological and technological parameters. In this paper, for the carbonate Kashirsky (K) and Podolsky (Pd) productive deposits of one of the oil fields in the Perm region, using step-by-step regression analysis based on geological and technological parameters, a forecast of the initial oil production rate after hydraulic fracturing was made. There was good agreement between model and experimental results obtained.

NOMENCLATURE

m	Porosity, %	q_p	Specific proppant consumption, t/m
q_o	Actual oil flow rate, t/day	C_r	Reservoir compartmentalization
S_o	Oil saturation, %	P_b	Bottom hole pressure, atm
K	Permeability, $10^{-3} \mu m^2$	q_l	Liquid flow rate pre-frac,m^3/day
h	Gross pay thickness, m	q_o^{Cal}	Oil production post-frac
S_X	Standard deviations of variables X	$a_0, a_1, ..., a_8$	Regression coefficients
S_Y	Standard deviations of variables Y	p	Levels of statistical significance
r	Correlation coefficients		

1. INTRODUCTION

During the development of oil and gas fields, there is a requirement to increase production efficiency. This goal, in particular is achieved by set of enhanced oil recovery measures, including a variety of technological method and special techniques. Existing technologies can be divided into 2 types: those that affect the entire oil reservoir and local reservoir stimulation methods that are directed to the area next to the well. Local

methods refer to the methods of intensification, which cover only a certain well with the specified condition [1, 2].

The development of oil fields with hard-to-recover oil reserves is a very important problem in the nearest future. The assessment of the prospects for using geological and technical measure is related to the creation of unconventional methods; the essence of which differs not only in high technological effectiveness, but also is energy consumption with a substantial improvement in geological criteria for their applicability [3]. Even after achieving the latest techniques, in primary and secondary recovery, only

Corresponding Author Institutional Email: poplygin@bk.ru
 (V. V. Poplygin)

one-third of the oil in the reservoir can be recovered. One of the most common local methods of stimulation is hydraulic fracturing. Recently, hydraulic fracturing has found wide application in wells, the effectiveness of which in most cases has been proven theoretically and practically, and it is difficult to find appropriate solutions [4-6].

Hydraulic fracturing is an effective method to enhance oil recovery. With the help of hydraulic fracturing technology, high well production rates are achieved by significantly expanding the drainage zone and the beginning of fluid filtration in tight areas of the reservoir [7, 8].

Hydraulic fracturing is a common method for producing oil or gas. Hydraulic fracturing technology consists of several steps: the first step is to pump the fracturing fluid at a high rate to create burst pressure and initiate a fracture in the formation. Next, proppant is pumped in to fix the crack and, at the third stage, the well is kept until the pressure at the wellhead is reduced. It is very important to choose the composition of the hydraulic fracturing fluid. The effect of many different chemicals on oil production must be determined in advance in the laboratory [9, 10].

In the absence of complete data, it is necessary to use integrated models to evaluate and improve the efficiency of hydraulic fracturing or reduce sand production of various operations and fluid modifications. For example, it is possible to use the Appach D model to simulate hydraulic fracturing and determine the duration of the effect, the change in sand and water content [11, 12].

Lolon et al. [13] used fracture modelling and multi-well simulation to evaluate down-spacing potential for horizontal well sand also examines the effectiveness oil permeability affect production profiles and oil recovery in the middle Bakken formation (North Dakota), proppant type, treatment volume. The study showed a significant infill drilling potential because of the low estimated effective oil permeability located between 0.002 and 0.04 mD.

The primary technology for developing tight gas is hydraulic fracturing of horizontal wells. After fracturing, the gas well exhibits the traits of a significant variation in production energy and a variety of parameters influencing production capacity [14, 15]. By using 10 fractured wells in a gas fields, Liu et al. [16] were able to fully count for the influence of geological and engineering factors. They were chosen 17 geological and engineering parameters then based on the statistical analysis of gas well productivity and used the gray correlation method. The findings demonstrate that tight gas fracturing horizontal wells can achieve high production which is influenced by both engineering and geological factors.

Predicting hydraulic fracturing efficiency, assessing the factors to one degree or another influencing the event, as detailed and justified selection of design wells for impacts are fundamental processes that need to be carried out and coordinated at the early stages of oil fields development. An early assessment of possible risks prior to the event and identification of the various factors influencing the potential for the projected event to be effective will minimize the probability of an unfavorable outcome [17, 18].

Identification of parameters that have a prevailing effect on the efficiency, and the subsequent formalization of the process based on statistical modelling, allow implementing a scientifically grounded choice of wells and selecting the optimal stimulation technology in order to increase hydraulic fracturing efficiency [19, 20].

2. METHODOLOGY

The research methodology consisted of several successive stages. The first step was to create a database of wells that were hydraulically fractured. Information was obtained on well productivity, reservoir permeability, bottom-hole and reservoir pressures before and after hydraulic fracturing. Information was also obtained on water saturation and oil saturation, reservoir thickness, porosity.

To create a model that would allow to quickly predicting the well flow rate after hydraulic fracturing, a regression analysis was performed on the parameters available in the database. During regression analysis, a correlation matrix was created.

A correlation matrix is a special type of covariance matrix. A correlation matrix is a covariance matrix that calculated on variables that have a mean of zero and standard deviation of one. The general formula for a correlation coefficient between variables X and Y is:

$$corr\ (X\ Y = \frac{cov(X\ Y)}{s_X s_Y} \tag{1}$$

Because a correlation is a specific form of a covariance, it has the same two properties magnitude and sign as a covariance. The sign indicates the direction of the relationship. Positive correlations imply a direct relationship, and negative correlation imply an inverse relationship. Similarly, correlation close to zero denote to statistical associations or predictability between the two variables. Correlations that deviates from 0 in either direction (positive or negative) indicate stronger statistical associations and predictability.

The correlation coefficient has one important property that distinguishes it from other types of covariance. The correlation coefficient has a mathematical lower boundary of -1.0 and an upper

bound 1.0. This property permits correlation coefficient to be compared, while ordinary covariance usually cannot be compared.

A linear statistical model for predicting oil production has been obtained, which has been verified against the original database. The use of the model will allow the engineer to predict the results of hydraulic fracturing with a minimal set of data.

3. RESULTS OF HYDRAULIC FRACTURING

Analysis of the hydraulic fracturing operation was carried out on the operating well stock of the investigated field in order to study the influence of geological and technological parameters on the success of hydraulic fracturing in the conditions of one of the oil fields in Perm region.

The regression model was built in order to identify the mathematical dependence of technological and geological parameters. Twenty wells, belonging to the K and Pd carbonate reservoir were identified on the basis of the production data on hydraulic fracturing treatment of the reservoir in the considered field.

The main geological and technological parameters were considered by wells for affecting the hydraulic fracturing efficiency of the actual rate oil production post-frac: geological- porosity, permeability, oil saturation and the pay thickness, technological- specific proppant consumption, reservoir compartmentalization, bottom-hole pressure and liquid production rate pre-frac (see Table 1).

The influence of various factors on the event success was defined by means of regression analysis.

The correlation matrix is presented in Table 2. The correlation coefficients and levels of statistical significance were determined for paired dependencies.

The correlation matrix demonstrated that the actual oil production rate post-frac (q_o), porosity and oil saturation correlate well with all others parameters. At the same time, there are statistically significant relationships between:
– Bottom-hole pressure with specific proppant consumption and reservoir compartmentalization;
– reservoir compartmentalization and specific proppant consumption;
– specific proppant consumption and the gross pay thickness

Correlation fields were built for the initial sample parameters with high correlation coefficients and low levels of statistical significance: according to geological factors - Figure 1, according to technological factors - Figure 2.

The initial oil production rate increases with increasing porosity and oil saturation of the formation.

TABLE 1. Results of hydraulic fracturing

q_o, t/day	m, %	S_o, %	K, $10^{-3}\mu m^2$	h, m	q_p, t/m	C_r	P_b, atm	q_l, m³/day
5.4	14.05	59.40	3.50	3.0	9.40	2	203.0	0.9
4.9	15.60	63.65	3.20	4.2	8.79	3	165.0	1.2
5.5	15.85	63.75	5.80	3.8	8.64	2	178.0	1.1
5.7	16.75	64.60	6.00	3.8	7.54	4	168.0	1.2
5.8	15.75	63.45	5.80	3.0	9.87	3	157.7	1.4
5.6	15.70	68.80	14.50	3.1	7.58	3	176.5	1.6
6.2	15.50	62.80	5.40	3.8	6.89	3	179.0	4.0
7.5	26.60	72.30	91.41	2.6	10.43	3	138.8	3.7
6.1	17.70	67.70	9.59	3.0	10.17	2	161.1	3.0
5.5	16.10	64.30	6.23	3.6	5.31	1	245.0	1.4
6.0	14.00	69.20	31.00	4.4	7.20	1	191.0	2.4
6.7	26.60	72.30	91.41	2.6	10.43	3	138.8	3.7
6.1	17.70	67.70	9.59	3.0	10.17	2	161.1	3.0
4.4	16.10	59.00	6.23	3.6	5.31	1	245.0	0.5
5.5	14.50	63.10	14.20	3.8	6.45	2	161.0	1.0
6.0	22.75	69.95	33.00	2.6	10.19	4	156.0	1.7
4.9	17.05	66.20	4.50	4.2	7.26	2	163.4	1.9
5.6	15.00	61.00	4.40	3.2	8.59	2	166.0	0.5
6.0	21.20	71.00	15.00	4.0	8.90	4	155.5	2.3
5.6	17.20	60.00	7.00	3.8	6.08	2	186.0	1.8
7.0	25.20	74.00	79.00	2.4	8.11	4	120.7	1.9
5.0	12.30	59.00	5.00	3.8	8.03	1	173.3	1.3

High reservoir permeability before hydraulic fracturing leads to a significant increase in initial production.

The greater the well flow rate before hydraulic fracturing, the greater it becomes after hydraulic fracturing. With an increase in the mass of injected proppant, the well flow rate after hydraulic fracturing increases.

4. REGRESSION ANALYSIS

According to the values of the correlation coefficients r of the dependences of the actual rate of the oil production q_o on geological and technological factors and the level of statistical significance p, the degree of influence of these factors on the calculated oil production rate post-frac is determined.

Further, the regression model is built by the method of multiple linear regression. The general of the regression equation and the equation obtained after calculations in statistical software (Statistics), in which

TABLE 2. Correlation matrix

	q_o	m	S_o	K	h	q_p	C_r	P_b	q_l
q_o	1	r= 0.759 p= 0.000	r= 0.760 p= 0.000	r= 0.799 p= 0.000	r= -0.617 p= 0.002	r= 0.521 p= 0.013	r= 0.501 p= 0.018	r= -0.638 p=0.001	r= 0.719 p= 0.000
m		1	r= 0.795 p= 0.000	r= 0.872 p= 0.000	r= -0.637 p= 0.001	r= 0.475 p= 0.025	r= 0.599 p= 0.003	r= -0.580 p= 0.005	r= 0.541 p= 0.009
S_o			1	r= 0.751 p= 0.000	r= -0.435 p= 0.043	r= 0.465 p= 0.029	r= 0.560 p= 0.007	r= -0.623 p= 0.002	r= 0.593 p= 0.004
K				1	r= -0.603 p=.003	r= 0.395 p= 0.069	r= 0.372 p=0.088	r= -0.552 p=0.008	r= 0.534 p= 0.010
h					1	r= -0.59 p= 0.004	r= -0.376 p= 0.084	r= 0.408 p=0.059	r= -0.253 p= 0.256
q_p						1	r= 0.440 p= 0.041	r= -0.665 p= 0.001	r= 0.391 p= 0.072
C_r							1	r= -0.670 p= 0.001	r= 0.245 p= 0.271
P_b								1	r= -0.420 p=0.052
q_l									1

Note: the cells in the numerator indicate the value of the correlation coefficient, in the denominator - the level of statistical significance (p); red highlighted statistically significant correlation coefficients, for which $p < 0.05$.
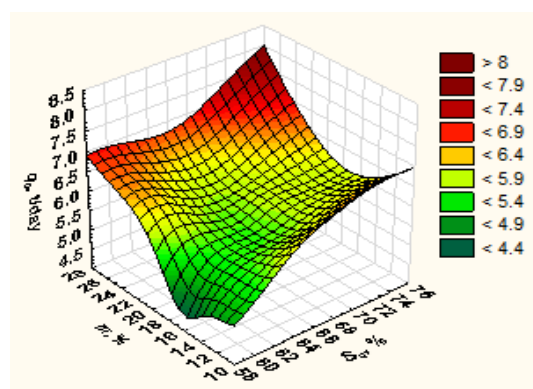
(a)
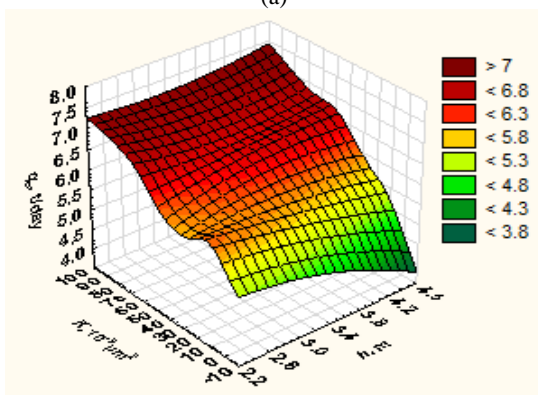
(b)

Figure 1. Dependences of the actual oil production rate after hydraulic fracturing with geological factors: a) porosity, oil saturation; b) permeability, gross pay thickness
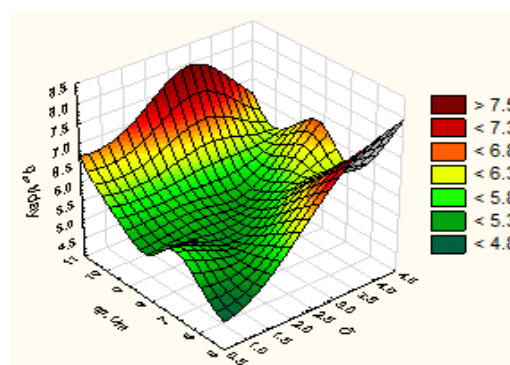
(a)
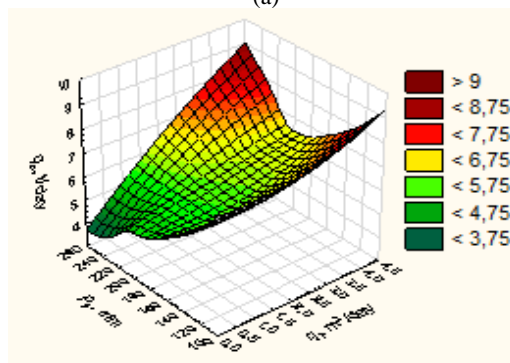
(b)

Figure 2. Dependences of the actual oil production rate after hydraulic fracturing with technological factors: a) specific proppant consumption, reservoir compartmentalization; b) bottom-hole pressure, liquid flow rate before hydraulic fracturing

the dependent variable is the calculated rate of the oil production post-frac q_o^{Cal}, and the independent variables are the sampling factors for which the level of statistical significance $p < 0.05$.

In general, the equation is written as follows:

$$q_o^{Cal} = a_o + a_1\, m + a_2\, So + a_3\, K + a_4\, h + a_5\, q_p + a_6\, C_r + a_7\, P_b + a_8\, q_l \quad (2)$$

General view identifying the coefficients of the regression equation and the obtained equation after simulation in software are presented in Table 3.

The future productivity of a well can be predicted using an exponential type well curve. The performance of wells with a very short production history can be modeled using aggregated analysis results as informative values.

Comparison of the calculated and actual rate of oil production increase after hydraulic fracturing is shown in Figure 3.

The absolute deviation of the calculated values of the oil production rate from its actual values in the field is in the range from 0.006 to 0.511 t/day, with an average of 0.219 t/day. The relative deviation is in the range of 0.11 to 10.90% with an average of 3.97%.

TABLE 3. Results of hydraulic fracturing

a_o	**5.857**
a_1	-0.054
a_2	0.025
a_3	0.011
a_4	-0.356
a_5	-0.028
a_6	0.126
a_7	-0.002
a_8	0.286
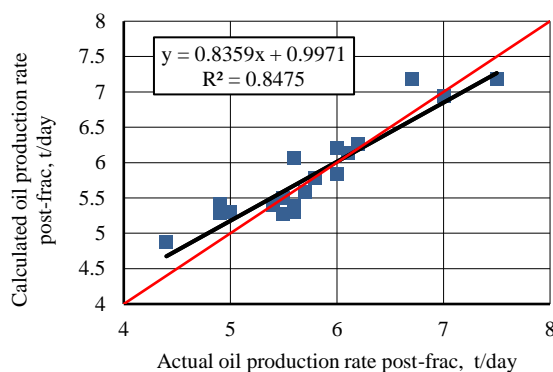
Figure 3. Correlation field of calculated (q_o^{Cal}) and actual (q_o) values of oil production rate post-frac for wells of the Kashirsky and Podolsk carbonate deposits of the Perm region field

4. CONCLUSIONS

As a result of the research carried out, it was established:

1. The value of the oil production rate after hydraulic fracturing in the Kashirsky and Podolsky carbonate deposits of one of the fields in the Perm Territory is mainly influenced by geological parameters-porosity, oil saturation, permeability, gross pay thickness and technological parameters- specific proppant consumption, compartmentalization, closure pressure at the bottom-hole and liquid production rate before hydraulic fracturing.

2. The proposed method allows, using the geological and technological parameters of the productive formation, to predict the value of the oil production rate after hydraulic fracturing.

5. FUNDING STATEMENT

6. REFERENCES

1. Poplygin, V. and Wiercigroch, M., "Research of efficiency of complex non-stationary impact on layer with high-quality oil", *Bulletin of Tomsk Polytechnic University. Geo Assets Engineering*, Vol. 331, No. 3, (2020), 7-12.

2. Poplygin, V.V., Poplygina, I.S. and Mordvinov, V.A., "Influence of reservoir properties on the velocity of water movement from injection to production well", *Energies*, Vol. 15, No. 20, (2022), 7797. https://doi.org/10.3390/en15207797

3. Poplygin, V. and Pavlovskaia, E., "Investigation of the influence of pressures and proppant mass on the well parameters after hydraulic fracturing", *International Journal of Engineering, Transactions A: Basic*, Vol. 34, No. 4, (2021), 1066-1073. doi: 10.5829/IJE.2021.34.04A.33.

4. Poplygin, V.V., Qi, C., Guzev, M., Riabokon, E., Turbakov, M. and Kozhevnikov, E., "Influence of frequency of wave action on oil production", *International Journal of Engineering, Transactions A: Basic*, Vol. 35, No. 11, (2022), 2072-2076. doi: 10.5829/IJE.2022.35.11B.02.

5. Guzev, M., Kozhevnikov, E., Turbakov, M., Riabokon, E. and Poplygin, V., "Experimental investigation of the change of elastic moduli of clastic rocks under nonlinear loading", *International Journal of Engineering, Transactions C: Aspects*, Vol. 34, No. 3, (2021), 750-755. doi: 10.5829/IJE.2021.34.03C.21.

6. POPLYGIN, V., "Well production after hydraulic fracturing in sandstone rocks in the north of the perm region", (2022).

7. Chen, J., Qu, Z., Zhou, L. and Su, X., "Numerical study on the hydraulic fracturing pattern in the hard roof in response to mining-induced stress", *Minerals*, Vol. 13, No. 3, (2023), 308. https://doi.org/10.3390/min13030308

8. Qu, H.-Y., Zhang, J.-L., Zhou, F.-J., Peng, Y., Pan, Z.-J. and Wu, X.-Y., "Evaluation of hydraulic fracturing of horizontal

wells in tight reservoirs based on the deep neural network with physical constraints", **Petroleum Science**, Vol. 20, No. 2, (2023), 1129-1141. https://doi.org/10.1016/j.petsci.2023.03.015

9. Alotaibi, N. and Dursun, S., "Optimizing the hydraulic fracturing fluid systems using the completion and production data in bakken shale", in SPE Middle East Oil and Gas Show and Conference, SPE. (2023), D021S084R006.

10. Hakimi, M.H., Hamed, T.E., Lotfy, N.M., Radwan, A.E., Lashin, A. and Rahim, A., "Hydraulic fracturing as unconventional production potential for the organic-rich carbonate reservoir rocks in the abu el gharadig field, north western desert (egypt): Evidence from combined organic geochemical, petrophysical and bulk kinetics modeling results", **Fuel**, Vol. 334, (2023), 126606. doi. https://doi.org/10.1016/j.fuel.2022.126606

11. Appah, D., "Application of the theory of diffuse set to optimize hydraulic fracturing", **Journal of Petroleum Science and Engineering**, Vol. 11, No. 4, (1994), 335-340. https://doi.org/10.1016/0920-4105(94)90051-5

12. Wu, R., "Some fundamental mechanisms of hydraulic fracturing, Georgia Institute of Technology, (2006).

13. Lolon, E., Cipolla, C., Weijers, L., Hesketh, R. and Grigg, M., "Evaluating horizontal well placement and hydraulic fracture spacing/conductivity in the bakken formation", in North Dakota. In SPE Annual Technical Conference and Exhibition. Society of Petroleum Engineers. (2009).

14. Chen, X., Zhao, L., Liu, P., Du, J., Wang, Q., An, Q., Chang, B., Luo, Z. and Zhang, N., "Experimental study and field verification of fracturing technique using a thermo-responsive diverting agent", **Journal of Natural Gas Science and Engineering**, Vol. 92, (2021), 103993. https://doi.org/10.1016/j.jngse.2021.103993

15. Lv, Z., Li, S., Liu, G., Zhang, Z. and Guo, X., "Factors affecting the productivity of a multifractured horizontal well", **Petroleum Science and Technology**, Vol. 31, No. 22, (2013), 2325-2334. https://doi.org/10.1080/10916466.2011.555338

16. Liu, L., Zhai, S., Li, H. and Wang, J., "Evaluation of main factors affecting fractured horizontal well productivity of tight sand gas reservoir in sichuan basin", in E3S Web of Conferences, EDP Sciences. Vol. 329, (2021), 01013.

17. Wang, D., Li, S., Zhang, D. and Pan, Z., "Understanding and predicting proppant bedload transport in hydraulic fracture via numerical simulation", **Powder Technology**, Vol. 417, (2023), 118232. https://doi.org/10.1016/j.powtec.2023.118232

18. Turbakov, M.S., Kozhevnikov, E.V., Riabokon, E.P., Gladkikh, E.A., Poplygin, V.V., Guzev, M.A. and Jing, H., "Permeability evolution of porous sandstone in the initial period of oil production: Comparison of well test and coreflooding data", **Energies**, Vol. 15, No. 17, (2022), 6137. https://doi.org/10.3390/en15176137

19. Guzev, M.A., Riabokon, E.P., Turbakov, M.S., Poplygin, V.V., Kozhevnikov, E.V. and Gladkikh, E.A., Classical and non-classical models of changes in the young modulus of geomaterials under alternating loads, in Sixty shades of generalized continua: Dedicated to the 60th birthday of prof. Victor a. Eremeyev. 2023, Springer.331-344.

20. Zhao, H., Li, Z., Zhu, C. and Ru, Z., "Reliability analysis models for hydraulic fracturing", **Journal of Petroleum Science and Engineering**, Vol. 162, (2018), 150-157. https://doi.org/10.1016/j.petrol.2017.12.048

Persian Abstract

چکیده

به گفته کارشناسان، استفاده از شکست هیدرولیک می تواند ضریب بازیافت نفت و گاز را 10تا 15درصد افزایش دهد .قلمرو پرم متعلق به منطقه قدیمی تولید نفت فدراسیون روسیه است .تا به امروز، بیش از 60درصد از ذخایر نفت قابل استحصال باقیمانده میادین منطقه پرم در ذخایر کربناته متمرکز شده است .اکثر رشته ها در حال حاضر در مراحل پایانی توسعه هستند .این میدان ها، به عنوان یک قاعده، با وجود مناطق زهکشی نشده با ذخایر باقیمانده و نرخ جریان چاه کم مشخص می شوند .بیشتر ذخایر باقیمانده میدان ها در مخازن با نفوذپذیری کم با درجه ناهمگنی بالا و فیلتراسیون سیال دشوار متمرکز شده است .متأسفانه، نتایج به دست آمده در عمل همیشه با محاسبات اولیه مطابقت ندارد و به نرخ های تولید نفت برنامه ریزی شده نمی رسد .در ارتباط با موارد فوق، مشکل پیش‌بینی اثربخشی عملیات شکست هیدرولیکی مطرح می‌شود .اثربخشی شکست هیدرولیکی بدون شک تحت تأثیر پارامترهای زمین‌شناسی و فناوری است .در این مقاله، برای ذخایر مولد کربنات کشیرسکی (K) و پودولسکی (Pd) یکی از میادین نفتی در منطقه پرم، با استفاده از تحلیل رگرسیون گام به گام بر اساس پارامترهای زمین‌شناسی و فناوری، پیش‌بینی نفت اولیه نرخ تولید پس از شکست هیدرولیک ساخته شد .توافق خوبی بین نتایج مدل و تجربی به دست آمده است

International Journal of Engineering

Optimal Capacity and Location for Renewable-based Microgrids Considering Economic Planning in Distribution Networks

R. Aazami*, S. Dabestani, M. Shirkhani

Smart Electric Distribution Network Lab, Department of Electrical Engineering, Ilam University, Ilam, Iran

P A P E R   I N F O

A B S T R A C T

By integrating distributed generation resources with the distribution network, the stability and reliability of the distribution network will increase. Due to the advantages of microgrids and the need to implement them, as well as the high cost of installation of distributed generation resources, the existence of a comprehensive and optimal method by considering various aspects of microgrid design is felt more than ever. In this paper, an optimal method for designing microgrids with various conditions is presented. In the first stage, the design of microgrids is discussed on a multi-purpose basis, considering its economic aspects. At this stage, to make a compromise between the economic aspects, the proposed problem is modeled as two-objective functions. In the second stage, the design of distributed generation sources is done in the first level and then in the second level, the optimal placement of switches is done to determine the electrical boundaries of microgrids. In this paper, the discussion of optimal microgrid location based on economic planning using a two-level particle swarm optimization (PSO) algorithm on the standard IEEE 33 Bus network in MATLAB software was performed and for this network, three microgrids with two keys were used.

1. INTRODUCTION

Today, due to the increasing need for electricity and environmental issue and economic issues, renewable energy sources (RES) are of particular importance and their use in different countries is increasing day by day. Although renewable energy sources have various challenges such as uncertainty, but due to many advantages, distributed generations (DGs) can become a suitable source of power supply [1-4]. According to the US Energy Agency, microgrids, consisting of DG units, are small-scale networks at low-pressure levels that have controllable and uncontrollable loads with distributed generation sources and energy storage systems that can be exploited in grid-connected or island mode [5, 6]. Due to the disadvantages of current distribution networks and the need to address these problems and restructure power systems, distribution networks are moving away from the traditional model and moving towards smart distribution networks. Accordingly, today's networks will be a cluster of microgrids in which each microgrid can function as a separate and independent unit. The high cost of constructing microgrids is one of the most important obstacles to the expansion of these networks. Therefore, the design of this network should be done optimally and taking into account the conditions of the system under study.

The design of microgrids involves two major steps. In the first step, distributed generation resources must be located at the distribution network level to convert the passive distribution network into an active distribution network. Then, with the optimal placement of the switches in the network lines obtained from the first step, the distribution network will become a set of interconnected microgrids. Researchers have examined the location of distributed generation sources from a variety of perspectives.

2. RELATED WORKS

Wang and Singh [7] provided an overview of the various methods used to design microgrids. Belfkira [8] proposed an optimal method for designing microgrids considering the reliability and security of the system. The main purpose of this study is to cluster the distribution network into a set of microgrids and only reliability indicators are used to design microgrids and the economic and technical aspects of the design are not discussed. Also, the location and capacity of distributed generation resources have not been done and the possible properties of resources and network load have not been seen in the design. Sharma et al. [9] also proposed a multi-objective economic method for the design of a single microgrid in which the uncertainty property of renewable distributed generation sources is considered but the load uncertainty property is not considered. Also, network design in terms of reliability and technical issues of the system, including voltage profile, system losses, and power quality has not been discussed. The design of microgrids based on self-healing against possible accidents in the distribution network has been investigated by Borhanazad et al. [10].

The design of multiple microgrids interconnected by the minimum cut set method was discussed by Wang and Nehrir [11]. Zou et al. [12], proposed an optimal model for the design of microgrids, taking into account the uncertainty in the production of distributed renewable sources such as wind turbines and photovoltaic systems. In this study, the objective function of the problem includes the cost of installation and operation of production units and energy storage resources and the aspects of reliability and environment are not considered. An optimal multi-objective economic method for locating distributed generation sources on the medium pressure side of the distribution network using a multi-objective harmonic search algorithm has been presented by Soroudi et al. [13]. The design of microgrids has been investigated by Soroudi and Afrasiab [14] considering the development of transmission lines and delaying the development of the upstream network.

The conflict between the optimal performance of the microgrids and the maximum amount of investment of the investor is one of the existing problems for the design of the microgrids, which has been solved by Fang et al. [15] by using game theory. This study proposes a two-layer game model that programs the output power of the allocated capacity of each microgrid. In the first layer, the effects of renewable energy power uncertainty are reduced, and in the second layer, the profit in the worst conditions is maximized. In this design, by repeating the process of the first and second layers, the microgrid capacity is optimized. By using the improved artificial bee colony (IABC) algorithm, an optimal structure for determining the optimal capacity of combined cooling, heating, and power (CCHP) microgrid is presented by

Zhang et al. [16]. One of the advantages of using this algorithm is that it takes into account the economic, energy, and environmental impacts.

There are many ways to calculate the optimal capacity and location of DGs. One of them is the use of the PSO algorithm. PSO is a meta-heuristic algorithm, developed in 1995 [17-19]. It should also be noted that the use of meta-heuristic algorithms can be a good solution to deal with nonlinear problems in the network. Also, to solve the sizing problems of renewable energy systems, meta-heuristic algorithms and especially PSO algorithm can be an effective solution [20-22]. Niazi and Lalwani [23] studied by using the objective function, the microgrid capacity and location optimization are performed using three algorithms, PSO, Genetic Algorithm (GA), and Imperialist Competitive Algorithm (ICA), for a 13 bus radial system. By comparing the optimization results obtained by these three algorithms, it was found that the use of the PSO algorithm has been faster and better than GA and ICA algorithms. A combined method of two algorithms PSO and GA is proposed by HassanzadehFard and Jalilian [24]. This method is proposed to determine the optimal location and size of DGs in the distribution network. This method can minimize network losses and improve voltage stability. In this study, the optimal size of DG is optimized in the first stage by the PSO algorithm, then in the second stage, with the help of the GA algorithm, the optimal location of the DG is determined. This method is performed on 33 and 69 bus systems. Optimizing the location and capacity of the DG, in addition to reducing losses, can improve the voltage profile in the system. Moradi and Abedini [25] designed a simulator by using the PSO algorithm to determine the optimal location and size of the DG. The Graphical User Interface (GUI), was used to design this simulator. The DG type on which this study was performed can supply active and reactive power and has a leading power factor between 0.8 and 0.9.

The use of fuzzy systems along with the PSO algorithm can also provide a way to optimally locate the DG. This method is performed on an IEEE 33 BUS radial distributed system [26]. Nagaballi et al. [27] simultaneously considered the heating, cooling, electric load, and variable load systems, a PSO algorithm is proposed to find the optimal location and size of DGs in the distribution system. This distribution system includes PVs, fuel cells, ESS, and wind turbines. A method for determining the optimal position and size of grid-connected DGs for one IEEE 33 BUS radial system, is presented by HassanzadehFard and Jalilian [28]. In this method, which is to reduce power losses and improve the voltage profile, the optimal size of dg is determined in the places predicted by the PSO algorithm.

Although the design of microgrids has been reported in previous references, the design of microgrids is multiple and interconnected and has not been considered

all economic, technical, environmental, and 24-hour load planning and sources and location of switches. In this paper, an optimal and comprehensive method considering economic, technical, environmental aspects and with the aim of economic planning for the operation of intelligent distribution networks is presented. Also in the proposed method, power exchanges between the microgrid and the upstream network are considered to increase the reliability of the system and reduce loading in the island mode. The proposed method has been implemented in standard distribution networks using MATLAB software and the results show the efficiency and effectiveness of the proposed method.

In the continuation of the contents, in section 2, the studied network and its details are introduced. In section 3, the proposed plan is introduced and the modeling and formulation of the problem are examined. Section 4 describes the research results and examines the numerical data resulting from the paper along with the simulations performed. A conclusion of the paper is given at the end. Table 1 shows a comparison between the methods presented in previous studies with the method presented in this paper.

3. PROPOSED METHOD

In this paper, a two-level planning method is proposed to determine the boundary, number, and optimal capacity of microgrids in a distribution network structure. In this method, considering that the goal is to determine the number and optimal capacity of microgrids, it is defined in two levels. In the first level, the objective function is determined based on determining the boundary, number, and optimal capacity of microgrids, and this first level function must be executed in sync with the second level function. In the second level, economic planning for a distribution network is introduced and the results of the two levels are combined and lead to determining the boundary, number, and optimal capacity of microgrids based on the economic planning of the distribution network.

The objective function of the first level is the problem of locating microgrids to reduce the cost of unsupplied energy, reducing the cost of installing switches and reducing the cost of formulated losses. In the second objective function, the economic planning model of the distribution network is presented. The purpose of operating a distribution network in economic planning is to minimize the cost of managing and operating a distribution network.

It can be said that the use of a bi-level PSO algorithm, in order to determine the boundary, number and capacity of microgrids, is the main difference between the method presented in this paper compared to similar works done in the past.

3. 1. Study System   The model proposed in this paper is applied to the IEEE 33 Bus system. The structure of this system is shown in Figure 1. Also, the data of this network is designed under the standard 33-bus system [14].

The network uses distributed generation resources including microturbines, diesel generators, fuel cells, photovoltaic systems, wind turbines, and batteries. The output power of microturbines, diesel generators, and fuel cells can be controlled and these sources are distributable. However, the power of renewable sources, namely PV and wind turbines, depends on weather conditions. The output power of PV and wind turbine sources depends on the intensity of sunlight and wind speed, respectively. To calculate the power of these sources, it is assumed that the average value of radiation intensity and wind speed is calculated based on historical data for daylight hours. The output power values of the sources and their installation locations are given in Table 2.

3. 2. Two-level Planning   The issue of two-level planning has been raised as an important issue in decision theory. Decision-makers usually make decisions in a hierarchical structure, and their decisions are likely to contradict each other. It should be noted that two-level models are a subset of multilevel planning problems. Two-level planning is a special mode of multi-level planning in which there are only two levels in the structure. In two-level planning, two decision-makers in a hierarchical structure try to optimize their goals in some cases that conflict with each other. The second-level decision maker optimizes his goals under the parameters taken from the first-level decision- maker.

TABLE 1. Comparison of the proposed method with previous works

Ref.	24-hour planning	Economic	Reliability	Technical	Optimization
Wang and Nehrir [11]. Zou et al. [12]	×	×	✓	×	Bi-level
Soroudi et al. [13]	×	✓	×	✓	Multi-objective
Soroudi and Afrasiab [14]	×	✓	✓	×	Single-objective
Zhang et al. [16]	×	×	×	✓	Single-objective
Proposed Method	✓	✓	✓	✓	Bi-level
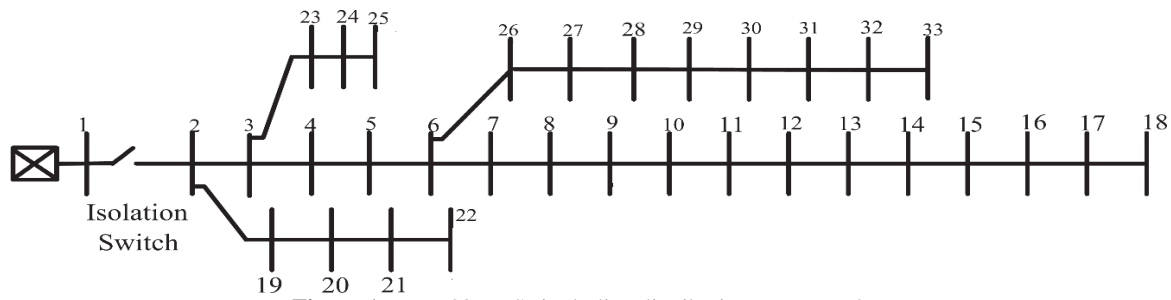
Figure 1. IEEE 33 BUS single-line distribution structure [29]

TABLE 2. Assumed locations and capacities for each power source in the 33 bus network

Resource capacity (KW)											
Battery		Wind Turbine		PV		Fuel Cell		Microturbine		Diesel Generator	
Shin installation	capacity	Shin installation	capacity	Shin installation	capacity	Shin installation	capacity	Shin installation	capacity	Shin installation	capacity
24	230	31	750	13	100	28	100	14	430	9	100
31	230	33	750	30	100	32	100	17	430	28	100

The problem of two-level planning is a non-convex problem and therefore, if the number of variables is large, it will not be possible to solve it with traditional and classical methods. Of course, it should be noted that two-level programming models have different types, such as linear, integer, nonlinear. Multilevel planning problems involve several target sets, which must be optimized over a given area. Although there is control over decision variables at different levels, it first allows him to influence the policies of other managers so that he can optimize his objective function.

3. 3. Two-level PSO Algorithm   The two-level PSO algorithm is a meta-innovative algorithm based on the PSO algorithm. This algorithm starts by assigning a batch of particles to the answer space of the problem of determining the capacity and optimal location of several microgrids and determining the initial values of these particles and continues until the condition of stopping the search process is established. The final values of the variable vector x^* as the location of the keys in the first level are two-level optimization. Also, the installation location of the keys resulting from the implementation of the first stage of the algorithm as an input parameter to the economic planning model (the second level of two-level planning). The allocation of a batch of particles to the answer space of the problem of determining the capacity and optimal location of several microgrids and determining the initial values of these particles continues the two-level PSO algorithm. The search process continues until the condition is stopped.

3. 4. Modeling the Proposed Method   The purpose of this work is to determine the capacity and optimal

location of several microgrids in a distribution network. For this network, the installation location of the distributed generation is assumed to be specific, to reduce active power losses as well as reduce the economic planning costs of the distribution network. Distributed generations have different technologies and can be renewable or non-renewable. By considering distributed generation sources whose capacity and installation location are known, a new problem is defined for the optimal location of remote-control switches that delimit the distribution network into several microgrids. This work is formulated to improve reliability, reduce losses, and minimizing the cost of keys. The variables of the first problem will be used as the data of the second problem and vice versa. The problem algorithm website is in Figure 2. In this figure, the proposed problem structure is presented to determine the boundary and the optimal capacity of the number of microgrids based on economic planning, and the two-level optimization algorithm is used accordingly.

3. 5. Problem Formulation

3. 5. 1. Formulation of Microgrid Location Problem   After determining the status of distributed generation sources, network load conditions, and power values in the distribution network, the resulting system is divided into several microgrids. As mentioned, the distribution network is divided into several microgrids through the optimal location of automatic switches. These switches act when a fault occurs in the distribution network and isolate the faulty parts of the system from the rest. Therefore, the number and position of the remote
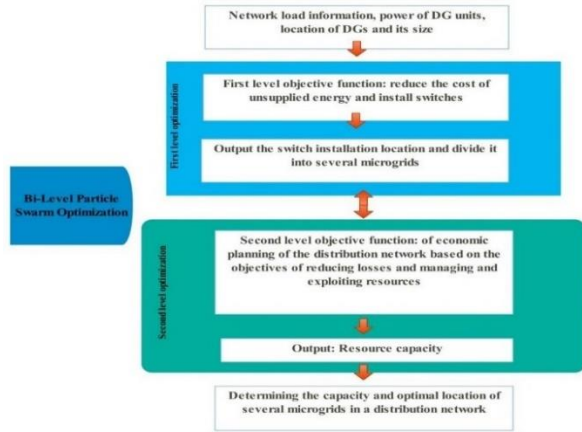
Figure 2. Modeling framework for determining the capacity and optimal location of multiple microgrids in a distribution network

control keys of the network are very important and directly affect the amount of load lost after an error in the network. These switches should be located in such a way that during the formation of the microgrid after the error occurs, the load of each microgrid is close to the value of the distributed generation resources of that microgrid to minimize the load lost in these conditions.

In this case, the installation or non-installation of keys on network lines is defined as a binary variable 'X' that has NBr (number of network lines) binary variable. For example, if a key is installed on the fifth line, X (5) is equal to one, otherwise, it is equal to zero. The problem of locating microgrids is formulated to reduce the cost of reliability and reduce the cost of installing switches, which is in the form of Equation (1).

$$F_1 = C_{ENS} + C_{SW} + C_3 \tag{1}$$

Equation (2) is used for the objective function of reducing reliability costs:

$$C_{ENS} = \left(\sum_{l=1}^{N_{br}} \sum_{n=1}^{N_b} \lambda_l \times L_1 \times P_{l,n} \times VOLL_n\right) \times \sum_{t=1}^{T} \left(\frac{1+InfR}{1+IntR}\right)^t \tag{2}$$

where $CENS$ is the present value of the total unladen load cost of the buses, $L1$ and $\lambda1$, respectively, the length and failure rate of line l, the amount of load lost in bus No. n due to fault in line l, Nb is the number of the bus in the system, $VOLLn$ is Value of unheated load in bus No. n, t is economic planning interval (5 years), InfR is inflation rate (2.1%), IntR is interest rate (0.75%) and 5% load growth for each year are considered. The cost of installing the keys can be calculated from Equation (3).

$$C_{SW} = \left(\sum_{l=1}^{N_{hr}} X_l \times C_{inv,SW}\right) \times \sum_{t=1}^{T} \left(\frac{1+InfR}{1+IntR}\right)^t \tag{3}$$

where CSW is the current value of the installation cost of all keys and Cinv, SW is the installation cost of each key. Now for the first level of constraints, the objective

function must be modeled. One of the most important constraints is the discussion of power balance in each microgrid. Because there must be balance in each microgrid, so the constraint of power balance and the maximum number of switches that can be installed (maximum number of acceptable microgrids) is presented as follows:

$$\sum_{i=1}^{Res} P_i = P_l \quad Each\ Microgrid\ With\ N_{SW}$$
$$N_{SW} \le N_a \tag{4}$$

Electrical losses are one of the most important technical and economic indicators of distribution networks. Losses include active and reactive power losses. Because the distribution network lines are more resistant, so only active power losses are considered here. Figure 3 shows a single-line diagram of a part of a distribution system.

Based on the explanations provided, the active power losses for the connecting line of bus i and i+1 can be calculated as Equation (4). Where the variables Pi and Qi represent the active and reactive power, respectively, passing through the interface of bus ain i and i 1. Also, Ri, Ii, and Vi are ohmic resistance, line current, and bus 'i' voltage, respectively.

$$P_{Loss}(i, i+1) = R_i \cdot \frac{(P_i^2 + Q_i^2)}{|V_i|^2} = R_i \cdot I^2_i \tag{5}$$

By calculating and adding the individual losses of distribution network lines, the total losses of network lines are obtained according to Equation (6).

$$P_{T,Loss} = \sum_{i=1}^{NB} P_{Loss}(i, i+1) \tag{6}$$

Where NB is the total number of bus networks of the desired distribution network and $PT,LOSS$ is the total active power loss of this network. Therefore, the cost of active power losses can be calculated from Equation (7).

$$C_3 = \sum_{T=1}^{T} P_{T,LOSS} \times C_{LOSS} \times \sum_{t=1}^{T} \left(\frac{1+InfR}{1+IntR}\right)^t \tag{7}$$

where $CLOSS$ is the cost of energy losses in dollars per kilowatt-hour (\$ / kWh) and T is the study period for the above problem. The period studied in the first level is considered to be five years.

3. 5. 2. Economic Planning Model   distribution network operator purpose is to minimize the cost of losses, management, and exploitation of the resources of the desired distributed generation. Equation (8) shows the
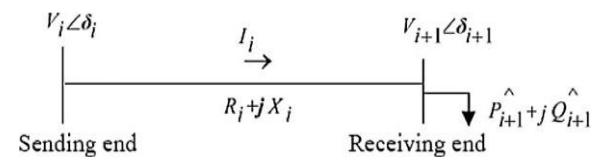
Figure 3. Single-line diagram of a part of a distribution network

mathematical formulation of the economic planning of the distribution network in a situation where all the distributed generation resources in the network are owned by the distribution operator.

$$F_2 = C_1 + C_2 \tag{8}$$

$$C_l = \int_0^t (C_G + C_{OM})dt \tag{9}$$

$$C_G = \sum_{i=1}^M K_{CFT} P_i(t) \tag{10}$$

$$C_{OM} = \sum_{i=1}^M K_{OMi} P_i(t) \tag{11}$$

$$C_2 = \int_0^t \sum_{i=1}^M C_K (P_{it})dt \tag{12}$$

Function F, which represents economic planning in a distribution network, includes function C_1, which is the cost of managing and operating distributed generation resources. CG is the cost of power generation by distributed generation and COM is the cost of managing distributed generation resources. KCFT is the Power generation cost factor for distributed generation resources, KOMi is the cost generation management factor for distributed generation resources. $PI(t)$ is the output power of distributed generation sources. M is the number and type of distributed generation sources. t is a 24-hour planning period for resource utilization and management. The C_2 function is a function of the cost of pollution disposal and CK is the cost of waste disposal of distributed generation units, which is equal to $ 0.136 per kilowatt-hour.

The equations for active and reactive power flux in the network as well as injectable active and reactive power developed by distributed generation sources are given below:

$$P_g - PD_i = \sum_j |V_i||V_j||Y_{ij}|cos(\theta_{ij} + \delta_j - \delta_i) \tag{12}$$

$$Q_g - QD_i = -\sum_j |V_i||V_j||Y_{ij}|sin(\theta_{ij} + \delta_j - \delta_i) \tag{13}$$

One of the most important constraints is the set of constraints that guaranteeing the maintenance of the voltage of the network bus in the acceptable range. . In particular, these constraints prevent the voltage across the network bus from falling below the allowable voltage limit as a problem in distribution networks. Also, similar to the conventional procedure in classical load distribution, the bus voltage in the distribution post is kept constant at a certain value, just like the slack bus.

$$|V_i| = Constant \qquad \forall io\ s$$
$$V_i^{Min} \le |V_i| \le V_i^{Max} \tag{14}$$

This set of constraints ensures that the amount of power intended for distributed generation resources is less than the maximum and more than the minimum allowed for their production.

$$P_i^{Min} \le |P_i| \le P_i^{Max} \forall io\ g \tag{15}$$

$$Q_i^{Min} \le |Q_i| \le Q_i^{Max}\ \forall io\ gC_l = \int_0^t (C_G + C_{OM})dt \tag{16}$$

Power transmission capability by distribution network feeders is limited by their current limit, which is expressed as their apparent power limit in the MVA unit.

$$\sqrt{P^2_k + Q^2_k} \le S_k^{Max} \qquad \forall k \tag{17}$$

4. SIMULATIONS AND NUMERICAL RESULTS

The proposed scheme is applied to the IEEE 33 Bus radial distribution network and some of its specifications are given in Figure 1 and Table 2. Based on the measures taken and the existing assumptions, the distribution network is demarcated into several microgrids. Also, the price purchase chart of energy from the upstream network in terms of daylight hours is shown in Figure 4.

Now, according to the implementation of the two-level algorithm for the 33-bus network, the following results have been obtained for this network as follows. At this stage, according to the assumed 33 bus network, the location of power generation sources, and existing microgrids, three scenarios are examined.

Scenario A. Operation and management in a traditional network

Scenario B. Operation and management in a traditional network with distributed generation resources

Scenario C. Operation and management in the network, which turned to several microgrids (proposed plan).

Table 3 shows the results of different scenarios. In the first scenario, since there is no key and distributed generation sources, the energy supply of the network is through the upper hand network. The cost of buying electricity from the above grid is considered to be 100
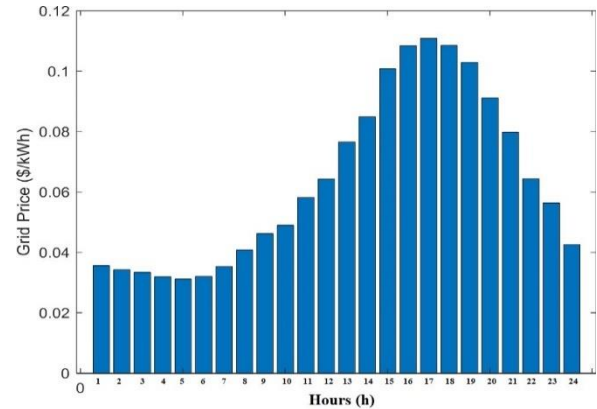
Figure 4. Cost of purchasing electricity from the upstream network

TABLE 3. Results of different scenarios

	Cost in dollars (percentage reduction compared to the initial state)				
Scenario	Unsupplied EnergyCost	Cost of losses	Cost of purchasingfrom the upstreamnetwork	Cost of operatingDGs	Cost of keys
A	6626	8653	173060	-	-
B	5300(20%)	6576(24%)	129800(11%)	23260	-
C (Proposed Scenario)	4638 (30%)	1000 (23%)	5797 (16%)	110297	35073

$/MWh. The cost of lost load value is also considered equal to 1000 $/MWh. In the second scenario, since distributed generation sources are used, in addition to supplying energy to the network through the upstream network, scattered production sources are used. The cost of buying electricity from the above grid is considered to be 100 dollars per megawatt hour. The cost of lost load value is also considered equal to 100 dollars per megawatt hour. Scenario C, which is proposed in this paper, is about operation and management in a network that has been converted to several microgrids, and the results are shown in Table 3. According to this table, it is clear that the answer related to the use of two keys is the best answer for the objective functions.In this case, the results of the two-level program are based on the use of two keys. Two switches in the specified feeders, which are embedded in Figure 5 for three optimal microgrids.

For the optimal response selected by the two-tier algorithm, the amount of resource generation power and the power purchased from the network is shown in Figure 6. Depending on the shape during peak hours, all sources have produced their maximum power to buy the minimum power from the network. This shows that the optimal use of distribution network resources has been achieved properly.

Figure 7 also shows the charging power as well as the total charge level of the two batteries. Based on this figure, it is also clear that the battery is charged during non-peak hours and discharged during peak hours. Figure 7 shows that the initial and final charge levels of the batteries are equal, which is one of the important constraints on the operation of batteries in a certain interval. The voltage profile of all distribution system busbars for 24 hours is shown in Figure 8. In this figure,
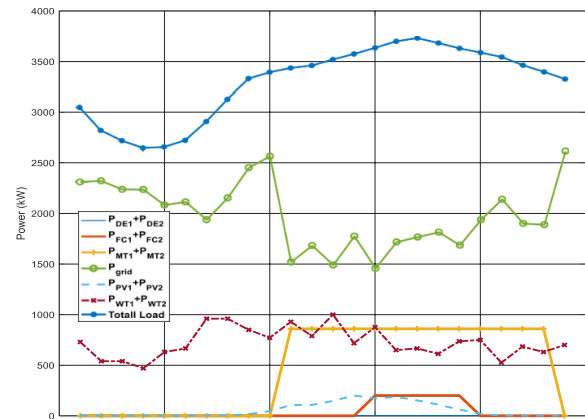
Figure 6. Production capacity of each network resource for 24-hour operation
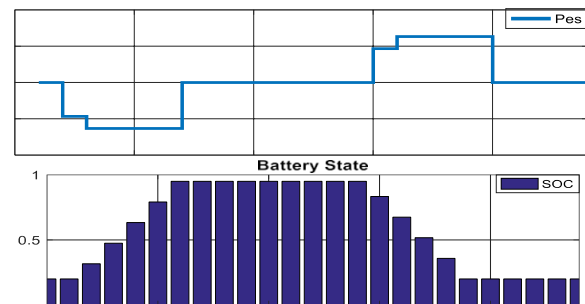
Figure 7. Total battery charge and discharge capacity and storage level of network batteries in the 24-hour operation
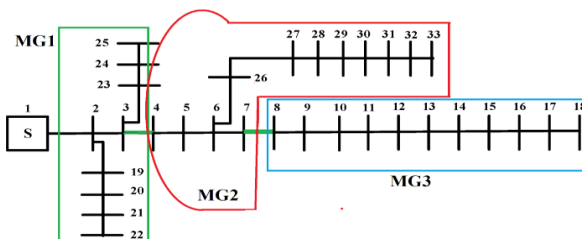
Figure 5. The optimal response obtained from the implementation of a two-level algorithm
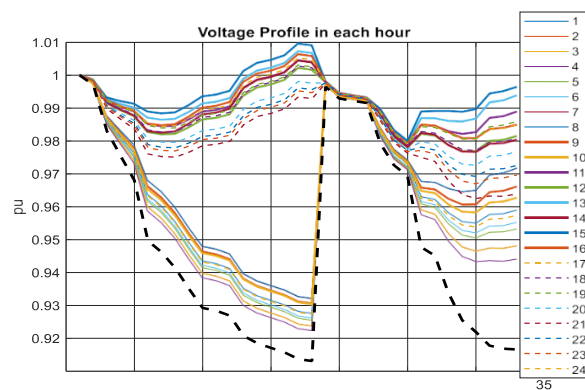
Figure 8. System bus voltage range in the 24-hour operation

the black curve is related to the voltage range of the system busbars in the absence of DG and microgrid, and for the other curves, the corresponding clock is specified.

5. CONCLUSION

In order to optimally exploit distribution networks and increase the reliability of these systems, they can be divided into several different microgrids. In this paper, the capacity and location of distributed generation and energy storage systems are assumed for a radial distribution network. In this paper, a programming-based method using the two-level PSO algorithm to determine the boundary, number, and optimal capacity of microgrids in a distribution network structure is presented. The objective function of the first level formulates the problem of locating microgrids to reduce the cost of unsupplied energy, reducing the cost of installing switches, and reducing the cost of losses. In the second objective function, the economic planning model of the distribution network is presented. The goal of the distribution network operator in economic planning is to minimize the costs of managing and operating the distribution network. The results of the three scenarios examined show that in the scenario in which the proposed plan has been implemented, the amount of unsupplied energy is reduced by 30% compared to the baseline, the cost of losses is reduced by 33% and energy purchases from the upstream network are reduced by 16% compared to other scenarios. Based on the general results, using the proposed algorithm in this work, it is possible to determine the unsupplied energy cost, losses, and installation cost of switches in such a way that a certain level of improvement in reducing operation and management costs, reducing voltage deviation and reducing load Lost to be realized. This leaves the system operator free to choose the answer and increases the flexibility of the problem. Considering that in this article, the location of microgrids is considered fixed, this work can be improved in the future by placing microgrids at the same time.

6. REFERENCES

1.   Tan, M., Chen, Y., Su, Y. and Duan, B., "Simulation planning of power supply capacity: An approach to optimal industrial microgrid operation with carbon emission permits", *International Journal of Sustainable Engineering*, Vol. 12, No. 5, (2019), 303-311. https://doi.org/10.1080/19397038.2018.1547331

2.   Aazami, R., Heydari, O., Tavoosi, J., Shirkhani, M., Mohammadzadeh, A. and Mosavi, A., "Optimal control of an energy-storage system in a microgrid for reducing wind-power fluctuations", *Sustainability*, Vol. 14, No. 10, (2022), 6183. https://doi.org/10.3390/su14106183

3.   Iranmehr, H., Aazami, R., Tavoosi, J., Shirkhani, M., Azizi, A.-R., Mohammadzadeh, A., Mosavi, A.H. and Guo, W., "Modeling the price of emergency power transmission lines in the reserve market due to the influence of renewable energies", *Frontiers in Energy Research*, Vol. 9, (2022), 792418. https://doi.org/10.3389/fenrg.2021.792418

4.   Tavoosi, J., Shirkhani, M., Azizi, A., Din, S.U., Mohammadzadeh, A. and Mobayen, S., "A hybrid approach for fault location in power distributed networks: Impedance-based and machine learning technique", *Electric Power Systems Research*, Vol. 210, (2022), 108073. https://doi.org/10.1016/j.epsr.2022.108073

5.   Mohammadi, F., Mohammadi-Ivatloo, B., Gharehpetian, G.B., Ali, M.H., Wei, W., Erdinç, O. and Shirkhani, M., "Robust control strategies for microgrids: A review", *IEEE Systems Journal*, (2021). doi: 10.1109/JSYST.2021.3077213.

6.   Danyali, S., Aghaei, O., Shirkhani, M., Aazami, R., Tavoosi, J., Mohammadzadeh, A. and Mosavi, A., "A new model predictive control method for buck-boost inverter-based photovoltaic systems", *Sustainability*, Vol. 14, No. 18, (2022), 11731. https://doi.org/10.3390/su141811731

7.   Wang, L. and Singh, C., "Pso-based multi-criteria optimum design of a grid-connected hybrid power system with multiple renewable sources of energy", in 2007 IEEE swarm intelligence symposium, IEEE. Vol., No. Issue, (2007), 250-257.

8.   Belfkira, R., "Modélisation et optimisation de centrales multi-sources de production d'énergies électrique: Application aux sites isolés", Ph. D. Thesis, University of Le Havre, (2009),

9.   Sharma, S., Bhattacharjee, S. and Bhattacharya, A., "Probabilistic operation cost minimization of micro-grid", *Energy*, Vol. 148, (2018), 1116-1139. https://doi.org/10.1016/j.energy.2018.01.164

10. Borhanazad, H., Mekhilef, S., Ganapathy, V.G., Modiri-Delshad, M. and Mirtaheri, A., "Optimization of micro-grid system using mopso", *Renewable Energy*, Vol. 71, (2014), 295-306. https://doi.org/10.1016/j.renene.2014.05.006

11. Wang, C. and Nehrir, M.H., "Analytical approaches for optimal placement of distributed generation sources in power systems", *IEEE Transactions on Power Systems*, Vol. 19, No. 4, (2004), 2068-2076.

12. Zou, K., Agalgaonkar, A.P., Muttaqi, K.M. and Perera, S., "Distribution system planning with incorporating dg reactive capability and system uncertainties", *IEEE Transactions on Sustainable Energy*, Vol. 3, No. 1, (2011), 112-123.

13. Soroudi, A., Caire, R., Hadjsaid, N. and Ehsan, M., "Probabilistic dynamic multi-objective model for renewable and non-renewable distributed generation planning", *IET Generation, Transmission & Distribution*, Vol. 5, No. 11, (2011), 1173-1182. doi: 10.1049/iet-gtd.2011.0173.

14. Soroudi, A. and Afrasiab, M., "Binary pso-based dynamic multi-objective model for distributed generation planning under uncertainty", *IET Renewable Power Generation*, Vol. 6, No. 2, (2012), 67-78. doi: 10.1049/iet-rpg.2011.0028.

15. Fang, F., Zhu, Z., Jin, S. and Hu, S., "Two-layer game theoretic microgrid capacity optimization considering uncertainty of renewable energy", *IEEE Systems Journal*, Vol. 15, No. 3, (2020), 4260-4271. doi: 10.1049/iet-rpg.2011.0028.

16. Zhang, H., Xie, Z., Lin, H.-C. and Li, S., "Power capacity optimization in a photovoltaics-based microgrid using the improved artificial bee colony algorithm", *Applied Sciences*, Vol. 10, No. 9, (2020), 2990. https://doi.org/10.3390/app10092990

17. Wazir, A. and Arbab, N., "Analysis and optimization of ieee 33 bus radial distributed system using optimization algorithm", *Journal of Emerging Trends in Applied Engineering*, Vol. 1, No. 2, (2016), 17-21.

18. Bagheri Tolabi, H. and Ayob, S., "Dynamic modeling and controller design of distribution static compensator in a microgrid based on combination of fuzzy set and galaxy-based search algorithm", *International Journal of Engineering, Transactions A: Basics*, Vol. 29, No. 10, (2016), 1392-1400. doi: 10.5829/idosi.ije.2016.29.10a.10.

19. Rashno, A., Shafipour, M. and Fadaei, S., "Particle ranking: An efficient method for multi-objective particle swarm optimization feature selection", *Knowledge-based Systems*, Vol. 245, (2022), 108640. https://doi.org/10.1016/j.knosys.2022.108640

20. Mansouri Kouhestani, F., Byrne, J., Johnson, D., Spencer, L., Brown, B., Hazendonk, P. and Scott, J., "Multi-criteria pso-based optimal design of grid-connected hybrid renewable energy systems", *International Journal of Green Energy*, Vol. 17, No. 11, (2020), 617-631. doi: 10.1080/15435075.2020.1779072.

21. Shafipour, M., Rashno, A. and Fadaei, S., "Particle distance rank feature selection by particle swarm optimization", *Expert Systems with Applications*, Vol. 185, (2021), 115620. https://doi.org/10.1016/j.eswa.2021.115620

22. Ahmadigorji, M. and Mehrasa, M., "A robust renewable energy source-oriented strategy for smart charging of plug-in electric vehicles considering diverse uncertainty resources", *International Journal of Engineering, Transactions A: Basics*, Vol. 36, No. 4, (2023), 709-719. doi: 10.5829/ije.2023.36.04a.10.

23. Niazi, G. and Lalwani, M., "Pso based optimal distributed generation placement and sizing in power distribution networks: A comprehensive review", in 2017 International Conference on Computer, Communications and Electronics (Comptelix), IEEE. (2017), 305-311.

24. HassanzadehFard, H. and Jalilian, A., "A novel objective function for optimal dg allocation in distribution systems using meta-heuristic algorithms", *International Journal of Green Energy*, Vol. 13, No. 15, (2016), 1615-1625. doi: 10.1080/15435075.2016.1212355.

25. Moradi, M. and Abedini, M., "A combination of genetic algorithm and particle swarm optimization for optimal distributed generation location and sizing in distribution systems with fuzzy optimal theory", *International Journal of Green Energy*, Vol. 9, No. 7, (2012), 641-660. doi: 10.1080/15435075.2011.625590.

26. Masrufun, M., "Optimization of dg placement and size using pso based on gui", in 2020 International Conference on Smart Technology and Applications (ICoSTA), IEEE. (2020), 1-6.

27. Nagaballi, S., Bhosale, R.R. and Kale, V., "A hybrid fuzzy and pso based optimum placement and sizing of dg in radial distribution system", in 2018 International Conference on Smart Electric Drives and Power System (ICSEDPS), IEEE. (2018), 272-275.

28. HassanzadehFard, H. and Jalilian, A., "Optimal sizing and siting of renewable energy resources in distribution systems considering time varying electrical/heating/cooling loads using pso algorithm", *International Journal of Green Energy*, Vol. 15, No. 2, (2018), 113-128. doi: 10.1080/15435075.2018.1423981.

29. Abdel-Salam, M., El-Mohandes, M.T. and Shaker, E., "Pso-based performance improvement of distribution systems using dg sources", in 2016 Eighteenth International Middle East Power Systems Conference (MEPCON), IEEE. (2016), 866-870.

Persian Abstract

چکیده

با ادغام منابع تولید پراکنده با شبکه توزیع، پایداری و قابلیت اطمینان شبکه توزیع افزایش می یابد. با توجه به مزایای ریزشبکه ها و لزوم اجرای آنها و همچنین هزینه بالای نصب منابع تولید پراکنده، وجود روشی جامع و بهینه با در نظر گرفتن جنبه های مختلف طراحی ریزشبکه بیش از پیش احساس می شود. در این مقاله روشی بهینه برای طراحی ریزشبکه با شرایط مختلف ارائه شده است. در مرحله اول، طراحی ریزشبکه ها با توجه به جنبه های اقتصادی آن به صورت چند منظوره مورد بحث قرار می گیرد. در این مرحله، برای ایجاد مصالحه بین جنبه‌های اقتصادی، مسئله پیشنهادی به‌عنوان توابع دو هدفه مدل‌سازی می‌شود. در مرحله دوم، طراحی منابع تولید پراکنده در سطح اول و سپس در سطح دوم، قرارگیری بهینه کلیدها برای تعیین مرزهای الکتریکی ریزشبکه ها انجام می شود. در این مقاله بحث مکان یابی بهینه ریزشبکه بر اساس برنامه ریزی اقتصادی با استفاده از الگوریتم بهینه سازی ازدحام ذرات دو سطحی (PSO) بر روی شبکه استاندارد IEEE 33 Bus در نرم افزار MATLAB انجام شده است و برای این ریزشبکه با دو کلید طراحی شده است.

International Journal of Engineering

Discrimination between Inrush and Internal Fault Currents in Power Transformers Using Hyperbolic S-Transform

L. A. Yaseen[a], A. Ebadi*[b], A. A. Abdoos[b]

[a] Department of Electrical Technology, Institute Technical-Anbar, Middle Technical University, Baghdad, Iraq
[b] Department of Electrical and Computer Engineering, Babol Noshirvani University of Technology, Babol, Iran

A B S T R A C T

Numerous methods exist to distinguish between inrush current and internal faults, but these approaches have not yet become practical due to their inherent limitations. As a result, conventional methods, despite their well-known drawbacks, continue to be widely used in practice. In this paper, a new method based on time-frequency analysis is presented for detecting inrush current situations. To do this, a diverse array of scenarios involving a power transformer switching ON and internal fault cases are simulated using the PSCAD/EMTDC software package. Then, a hyperbolic S-transformer is employed to extract a determining index from the simulation results. Finally, a suitable threshold value for this index is computed so that inrush current can be distinguished from fault current by comparing the index with its threshold. Evaluation of the efficiency of the proposed method using simulation and real data confirms its excellent accuracy. Therefore, it can be used in algorithms for power transformer differential protection to improve their stability during inrush current transients.

doi: 10.5829/ije.2023.36.12c.07

NOMENCLATURE

$w(t)$	Scalable Gaussian window	DI	Determining Index
γ_{HY}^{F}	Forward-taper parameter	i_a, i_b and i_c	Phase currents
γ_{HY}^{B}	Backward-taper parameter	f	Frequency

1. INTRODUCTION

Power transformers are vital and expensive equipment for any electrical power network. Hence, it is very important to equip this device with a dependable, secure, and fast protective system. Differential protection is the most important and most commonly used protection scheme, which is employed to protect the power transformer with a nominal power above 5 MVA [1]. However, it is prone to false operation in the presence of transformer magnetizing inrush current. Because this relay is designed for detecting transformer internal faults by comparing its primary- and secondary-side currents while inrush currents just appear on one side, which leads to the appearance of a false differential current [2]. Since the harmonic content of the inrush current is usually

different from the fault current, many harmonic restraining and harmonic blocking methods have been developed to prevent false operation of the differential relay during inrush current [3]. The use of new materials with better magnetic characteristics for producing transformer cores has decreased the effectiveness of these methods [4]. On the other hand, time-frequency analysis techniques can be used to discriminate between inrush current and fault current. For example, the wavelet transform is useful to analyze signals with non-stationary characteristics, so it is widely used to create new methods to discriminate inrush current from fault current [5]. However, how to choose the mother wavelet can have a great impact on the results, and it is necessary to use a denoizing algorithm along with it. The S-transform, as another time-frequency analysis technique that combines

*Corresponding Author Institutional Email: a.ebadi@nit.ac.ir
(A. Ebadi)

the advantages of both Fourier and wavelet transforms, has been employed by many researchers to distinguish inrush current from fault current [6]. The accuracy of the methods presented by these researchers completely depends on the features extracted and selected by them.

Pattern recognition algorithms or machine learning techniques are other methods that have been used in this field. For a power transformer, Khatib and Arar [7] proposed a differential protection technique based on random forest and boosting learning machines. Afrasiabi et al. [8] extracted statistical features from the normalized differential current gradient to train the robust soft learning vector quantization (RSLVQ) classifier for developing a new intelligent differential protection scheme. Jiao et al. [9] proposed a transformer intelligent protection algorithm with strong recognition ability and high recognition accuracy. To do this, image recognition has been used to supervise and study the equivalent magnetization curve by employing a convolutional neural network (CNN). Despite their high accuracy, these methods are complex and have a high computational burden.

In this paper, a time-frequency analysis-based method is proposed for the discrimination of inrush and internal fault currents. To do this, during inrush current and fault cases, differential current is analyzed using the hyperbolic S-transform. Then, an effective index is determined, and a suitable threshold value for this index is computed using analysis of the simulation results of many internal faults and inrush current cases in a real power transformer. Therefore, the condition for detecting an internal fault is that this index value is less than its threshold. It is worthy to say that all power transformer simulations are done by the PSCAD/EMTDC software package, and analysis of simulation results and implementation of the proposed method are done in the MATLAB environment.

The paper organization is as follows: In section 2, the hyperbolic S-transform is briefly described. The specifications of the power system under study are presented in section 3. The process of analyzing differential currents using the hyperbolic S-transform is described in section 4. Section 5 presents the proposed method. The simulation results and the method assessments can be found in section 6. Finally, the paper ends with the conclusion in section 7.

2. HYPERBOLIC S-TRANSFORM

The S-transform is a time-frequency analysis technique that combines the advantages of both short-time Fourier and wavelet transforms and can handle non-stationary signals. It uses a Gaussian window whose height scales linearly and whose width scales inversely with the

frequency. The expression of the S-Transform is given below [10]:

$$S(\tau, f) = \int_{-\infty}^{+\infty} h(t)\{w(\tau - t)\exp(-i2\pi ft)\}dt \qquad (1)$$

where, S is the S-transform of $h(t)$, f denotes frequency, and the parameter τ controls the position of scalable the Gaussian window ($w(t)$) on the t-axis.

There is no parameter in the Gaussian window to adjust its width in the time or frequency domain. Hence, the generalized S-transform has been introduced by Nandi et al. [11], which has more control over the window function. For a more detailed explanation, a more symmetrical window can be used at high frequencies, and a more asymmetrical window may be used at low frequencies. Therefore, the hyperbolic window is used instead of the Gaussian window. The discrete version of the hyperbolic S-Transform of $h(t)$ is calculated as follows:

$$S[(n, j)] = \sum_{m=0}^{N-1} H[m+n]G(m, n)\exp(i2\pi mj) \qquad (2)$$

where the total number of samples is denoted by N, $m = [0 \quad 1 \quad \ldots \quad N-1]$, $n = [0 \quad 1 \quad \ldots \quad N-1]$ and $j = [0 \quad 1 \quad \ldots \quad N-1]$. The frequency-shifted discrete Fourier transform of $h(t)$ is denoted by $H[m+n]$. The Fourier transform of the hyperbolic window is represented by $G(m, n)$ and can be expressed as follows:

$$G(m, n) = \frac{2|f|}{\sqrt{2\pi(\gamma_{HY}^F - \gamma_{HY}^B)}} exp\left(\frac{-f^2 X^2}{n^2}\right) \qquad (3)$$

In this expression, X is a hyperbola, γ_{HY}^F is a forward-taper parameter and γ_{HY}^B is a backward-taper parameter. it is assumed that $0 < \gamma_{HY}^F < \gamma_{HY}^B$.

3. EXPERIMENTAL STUDY

To evaluate the proposed method's performance, a part of a real high-voltage (HV) substation introduced by Bkhaitawi et al. [12], including a 160 MVA, 230/63 kV power transformer, a grounding transformer (GT), and both side current transformers (CTs), is simulated using the PSCAD/EMTDC program (see Figure 1). Tables 1 and 2 show some technical information about the power transformer and CTs, respectively. It should be noted that the simulation of the magnetic behavior of the core of current transformers is based on the Jiles-Atherton (JA) model. The JA model parameters used to simulate the CTs were introduced by Taghipour Gorji et al. [13]. In simulations, the sampling frequency is set to 2500 Hz. It means that each cycle contains 50 samples because the power system frequency is 50 Hz. According to Nyquist's theorem, the maximum frequency that can be accurately represented in a signal is half of the sampling frequency [14, 15], i.e., 1250 Hz.
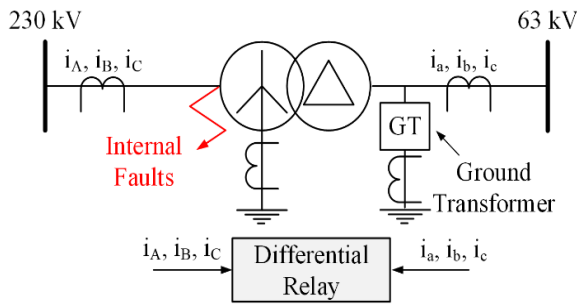
Figure 1. Power transformer protected by differential relay

TABLE 1. Technical information of the power transformer

Technical Data	Nominal Value
Power (MVA)	160
HV voltage (kV)	230
LV voltage (kV)	63
Short-circuit impedance (%)	14
No-load losses (%)	0.06
Ohmic losses (%)	0.2

TABLE 2. Technical information of CTs

Technical Data	HV side CTs	LV side CTs
Nominal primary current (A)	600	2000
Nominal secondary current (A)	1	1
Magnetic path length (cm)	84.8	54.8
Core cross section area (cm^2)	32.9	10.36
CT winding resistance (ohm)	4.3	7.77
Total burden (VA)	30	30

4. DIFFERENTIAL CURRENT SIGNAL ANALYSIS BASED ON HYPERBOLIC S-TRANSFORM

The hyperbolic S-transform is applied in this section to analyze differential current signals in two scenarios: one is a severe inrush current, and another is a severe internal fault. The goal is to extract the determining characteristics of the signals. It is worthy to say that the output of the S-transform is a complex matrix called the S-matrix, whose columns and rows pertain to the time and frequency domains, respectively.

In the first scenario, the unloaded transformer with a residual flux value of 80% (in phase *a*) is energized from the HV side winding at t=0.1 s. In this situation, the power transformer draws large magnetizing inrush currents from the power supply. Hence, differential currents appear in the relay. Figure 2 shows the phase *a* differential current. It is seen that the magnitude of this current is very high, so it may cause the relay to

malfunction. Figure 3 shows the 3D representation of the S-matrix element magnitudes obtained from the differential current signal. According to this figure, the elements of this matrix have the largest magnitudes in the fundamental frequency and the second harmonic, so the magnitude of the second harmonic is significant. For more detailed analysis, the ratios of the magnitude of the second harmonic to the magnitude of the fundamental harmonic are shown in Figure 4. It is seen that these ratios are high during inrush currents.

In the second scenario, a ground fault with a fault resistance of 2 Ω occurs at t=0.1 s on the phase *a* terminal of the Y winding. Figure 5 shows the phase *a* differential current in this situation, whose waveform is somewhat distorted due to saturation of CTs. The 3D representation of S-matrix element magnitudes obtained from the differential current signal is shown in Figure 6. As can be seen, the magnitudes of S-matrix elements in the second harmonic are not considerable in comparison with the fundamental frequency. For better understanding, the
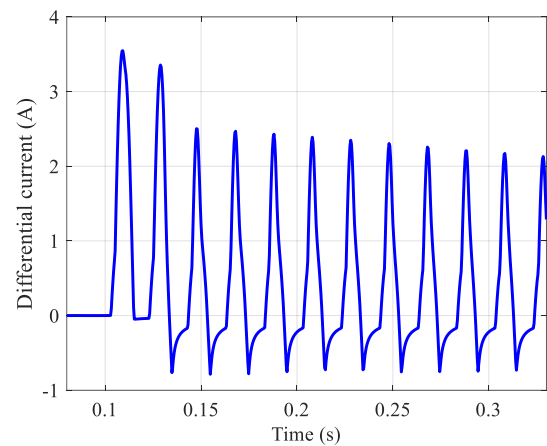
Figure 2. The Phase *a* differential current during unloaded power transformer energization at t=0.1 s
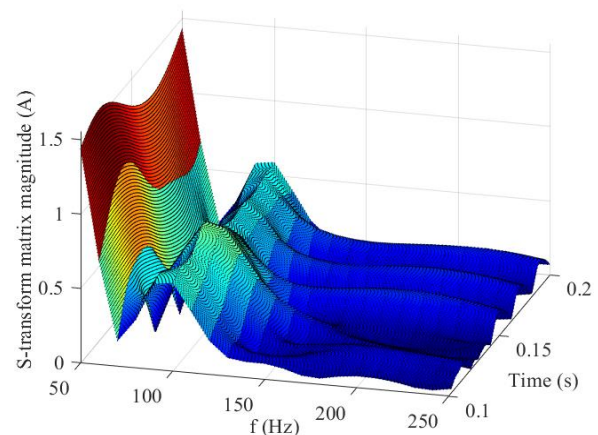
Figure 3. S-matrix elements magnitudes obtained from the differential current during inrush current
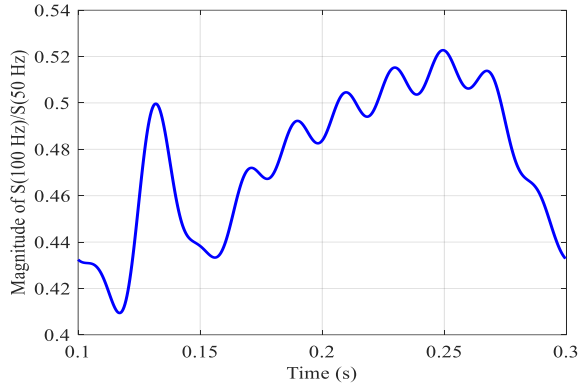
Figure 4. The ratios of the magnitude of the second harmonic to the magnitude of the fundamental harmonic of the differential current signal during inrush current

ratios of the magnitude of the second harmonic to the magnitude of the fundamental frequency are depicted in Figure 7.

According to the above explanation, the ratio of the magnitude of the S-matrix element at the second harmonic to the magnitude of its element at the

Figure 5. The phase *a* differential current internal fault occurs at t=0.1 s

Figure 6. S-matrix elements magnitudes obtained from the differential current during internal fault
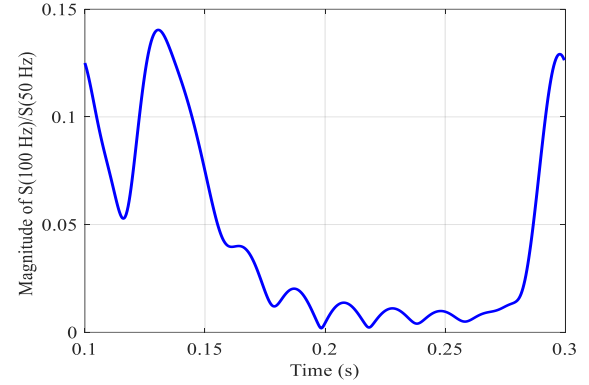
Figure 7. The ratios of the magnitude of the second harmonic to the magnitude of the fundamental frequency of the differential current signal during internal fault

fundamental frequency can be used as a determining index (DI) for the discrimination of inrush current from fault current. But to achieve this goal, it is necessary to first determine a suitable threshold value for this index.

5. PROPOSED METHOD

The new method is based on the parameter DI introduced in the previous section and can be implemented by the following steps:

Step 1: A large number of inrush current and internal fault cases in a power transformer must be simulated.

Step 2: For each internal fault, a one-cycle sliding window starts to move once the I_D is greater than 0.02 p.u. and it continues to one cycle later and DI will be calculated for all points. Then, the minimum DI is saved. It must be done for the differential current of all three phases. After doing this for all internal faults, the maximum of saved values (DI_{Mm}) is considered for finding the threshold value of DI. The use of DI_{Mm}, according to the above description, guarantees the detection and operation of the relay in the first cycle of the fault.

Step 3: By adding a safety margin to DI_{Mm}, the threshold value of DI^{TH} can be calculated. The condition for confirming the appropriateness of the obtained value for DI^{TH} is the accuracy of the method in detecting the inrush current. It is worth noting that the condition for detecting an inrush current is:

$$DI \geq DI^{TH} \qquad (4)$$

It should be mentioned that this condition should be checked for the differential currents of all three phases.

6. SIMULATION RESULTS

In this section, a wide range of internal faults are simulated, and DI^{TH} is computed using the obtained
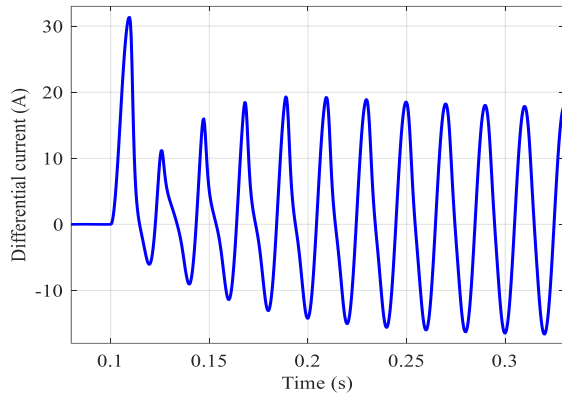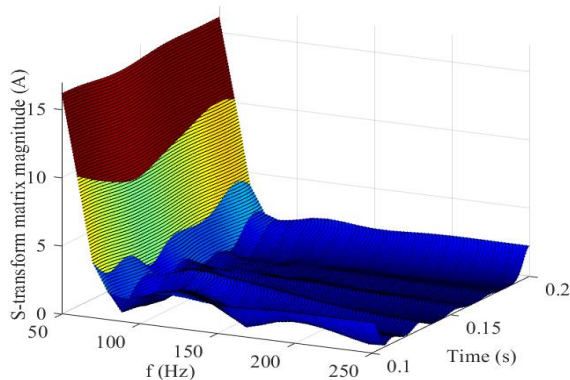
simulation results. Then, a large number of inrush current conditions are simulated and the accuracy of the proposed method in detecting the inrush current is evaluated using the mentioned condition.

6. 1. Calculation of DI^{TH}   Four types of internal faults on the HV side terminal of the power transformer are simulated. They are single-line-to-ground, line-to-line, line-to-line-to-ground and three-phase faults. Five values are considered for each fault resistance, including 0, 2.5, 5, 10, and 20 ohms. On the other hand, fault instants are 11 points of equal distance on the 6th time cycle. Therefore, 220 internal faults are simulated, and many of which are considered severe. Using simulation results, the value of DI_{Mm} is calculated as 0.136 and by adding a safety margin to it, the DI^{TH} value is set to 0.15.

6. 2. Accuracy Analysis of the Proposed Method To simulate inrush current cases, the no-load transformer is energized once from the HV side and again from the LV side. The switching-on instants are 51 points of equal distance on the 6th time cycle. On the other hand, when the transformer is energized from the LV side, the core residual flux is 0%, but for energizing from the HV side, it is assumed to be 0% and 80% in simulations. Thus, the number of simulated power transformer energization situations is 153. Using the DI^{TH}, the proposed method is implemented, and the obtained results are presented in Table 3. It is seen that all internal faults and inrush currents are truly detected by this new method. It means that the accuracy of the proposed method is 100%.

6. 3. Method Verification using Real Data Figures 8 show the inrush currents of a real 400/230 kV

TABLE 3. The proposed method implementation results

Method Setting	# of undetected cases of 220 faults	# of mis-operation during 153 inrush current cases	Accuracy (%)
$DI^{TH} = 0.15$	0	0	100

(a)

(b)

(c)
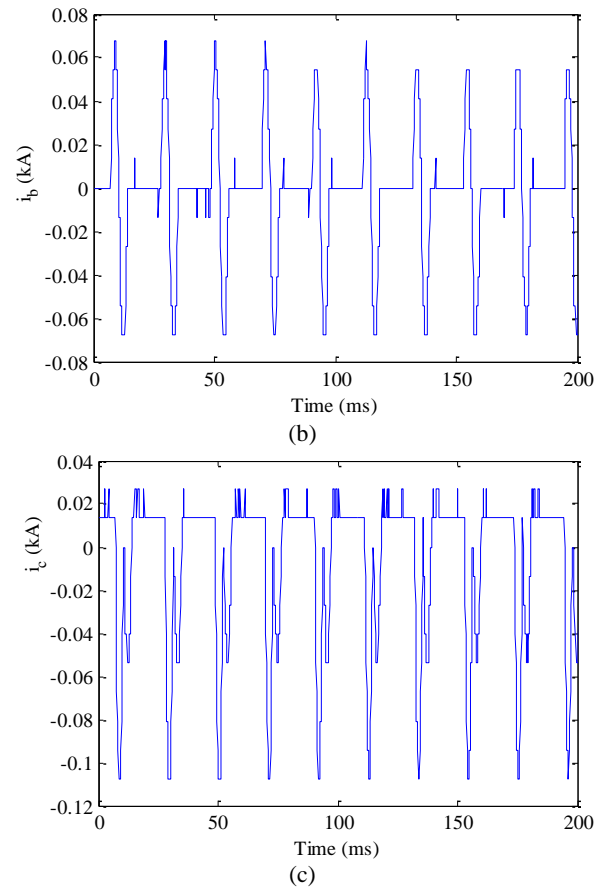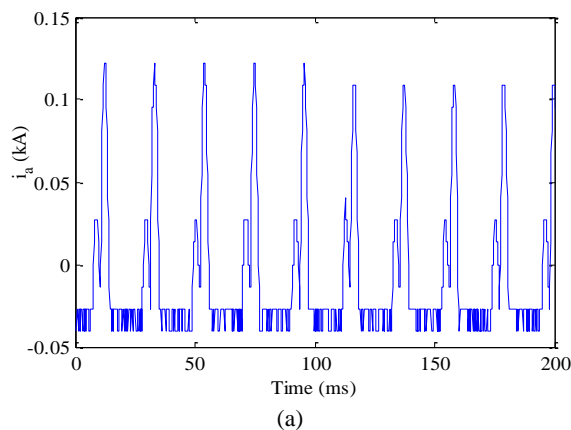
Figure 8. Phase *a*, phase *b*, and phase *c* inrush currents extracted from a differential relay of a 400/230 kV autotransformer

autotransformer extracted from a differential relay. It must be noted that the relay has malfunctioned because of these currents. But our proposed method remains stable in this situation. It means that this new method is suitable for use in practical conditions.

7. CONCLUSION

In this paper, the hyperbolic S-transform is used for discrimination between inrush and fault current in power transformers. To do this, a wide range of internal faults and energizing conditions of a power transformer are simulated using the PSCAD/EMTDC program. Then, differential currents are analyzed by the hyperbolic S-transform, and an effective determining index is extracted. Simulation results show that inrush current can be detected accurately using this index. Also, the accuracy of the new method has been verified using real data. Therefore, it is suitable for use in practical applications. The authors decided to extend this method for discriminating between internal and external faults in their next research.

8. REFERENCES

1. Ebadi, A., Hosseini, S. and Abdoos, A., "A new restricted earth fault relay based on artificial intelligence", *International Journal of Engineering, Transactions A: Basics*, Vol. 32, No. 1, (2019), 62-70. doi: 10.5829/ije.2019.32.01a.08.

2. Babaei-Roudi, F. and Abdoos, A., "Detection of internal fault from external fault and inrush current in power transformers based on combination of vmd and elm", *Computational Intelligence in Electrical Engineering*, Vol. 9, No. 1, (2018), 65-78. doi: 10.22108/ISEE.2018.110376.1115.

3. Li, Z., Jiao, Z., He, A. and Xu, N., "A denoising-classification neural network for power transformer protection", *Protection and Control of Modern Power Systems*, Vol. 7, No. 1, (2022), 1-14. doi: 10.1186/s41601-022-00273-8.

4. Ebadi, A., Hosseini, S. and Abdoos, A.A., "Designing of a new transformer ground differential relay based on probabilistic neural network", *Engineering and Energy Management*, Vol. 9, No. 4, (2023), 2-13. doi.

5. Tajani, A.H.N., Bamshad, A. and Ghaffarzadeh, N., "A novel differential protection scheme for ac microgrids based on discrete wavelet transform", *Electric Power Systems Research*, Vol. 220, (2023), 109292. doi: 10.1016/j.epsr.2023.109292.

6. Behvandi, A., Seifossadat, S.G. and Saffarian, A., "A new method for discrimination of internal fault from other transient states in power transformer using clarke's transform and modified hyperbolic s-transform", *Electric Power Systems Research*, Vol. 178, (2020), 106023. doi: 10.1016/j.epsr.2019.106023.

7. Khatib, T. and Arar, G., "Identification of power transformer currents by using random forest and boosting techniques", *Mathematical Problems in Engineering*, Vol. 2020, (2020), 1-12. doi: 10.1155/2020/1269367.

8. Afrasiabi, S., Behdani, B., Afrasiabi, M., Mohammadi, M., Asheralieva, A. and Gheisari, M., "Differential protection of power transformers based on rslvq-gradient approach considering sfcl", in 2021 IEEE Madrid PowerTech, IEEE. (2021), 1-6.

9. Jiao, W., Dong, K. and Zhao, J., "Intelligent transformer protection method based on convolutional neural network", in 2021 4th International Conference on Energy, Electrical and Power Engineering (CEEPE), IEEE. (2021), 698-703.

10. Ebadi, A., Hosseini, S.M. and Abdoos, A.A., "A new time-frequency analysis based supervision method for the transformer restricted ground fault relay", *International Journal of Electrical Power & Energy Systems*, Vol. 129, (2021), 106858. doi: 10.1016/j.ijepes.2021.106858.

11. Nandi, K., Das, A.K., Ghosh, R., Dalai, S. and Chatterjee, B., "Hyperbolic window s-transform aided deep neural network model-based power quality monitoring framework in electrical power system", *IEEE Sensors Journal*, Vol. 21, No. 12, (2021), 13695-13703. doi: 10.1109/JSEN.2021.3071935.

12. Bkhaitawi, A., Abdoos, A.A. and Ebadi, A., "Presenting an adaptive restraint method to improve performance of ground differential protection of power transformer", *International Journal of Engineering, Transactions B: Applications*, Vol. 35, No. 11, (2022), 2213-2219. doi: 10.5829/IJE.2022.35.11B.16.

13. Gorji, R.T., Hosseini, S.M., Abdoos, A.A. and Ebadi, A., "A hybrid intelligent method for compensation of current transformers saturation based on pso-svr", *Periodica Polytechnica Electrical Engineering and Computer Science*, Vol. 65, No. 1, (2021), 53-61. doi: 10.3311/PPee.16248.

14. Ebadi, A., Hosseini, S.M. and Abdoos, A.A., "Immunity improvement of a low-impedance restricted earth fault relay by making its mechanism intelligent based on support vector machine", *Computational Intelligence in Electrical Engineering*, Vol. 9, No. 2, (2018), 29-40. doi: 10.22108/ISEE.2018.111464.1132.

15. Yahiou, A., Mellah, H. and Bayadi, A., "Inrush current reduction by a point-on-wave energization strategy and sequential phase shifting in three-phase transformer", *International Journal of Engineering, Transactions C: Aspects*, Vol. 35, No. 12, (2022), 2321-2328. doi: 10.5829/IJE.2022.35.12C.07.
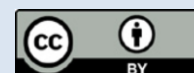
Persian Abstract

چکیده

روش‌های متعددی برای تمییز دادن بین جریان هجومی و خطاهای داخلی وجود دارند اما به دلیل محدودیت‌های ذاتی شان هنوز عملی نشده‌اند. در نتیجه، روش‌های مرسوم، علی رغم معایب شناخته شده‌شان، همچنان در عمل به طور گسترده مورد استفاده قرار می‌گیرند. در این مقاله، یک روش جدید مبتنی بر تحلیل زمان – فرکانس برای تشخیص وضعیت جریان هجومی ارائه شده است. برای انجام این کار، ابتدا موارد متنوعی از سناریوها شامل برق دار شدن یک ترانسفورماتور قدرت و موارد خطای داخلی با استفاده از بسته نرم‌افزاری PSCAD/EMTDC شبیه‌سازی می‌شوند. سپس، از تبدیل S هیپربولیکی برای استخراج یک شاخص متمایز کننده از نتایج شبیه‌سازی استفاده می‌شود. در نهایت، یک مقدار آستانه مناسب برای این شاخص محاسبه می‌شود تا بتوان جریان هجومی را از جریان خطا با مقایسه شاخص مذکور با آستانه آن متمایز کرد. ارزیابی کارایی روش پیشنهادی با استفاده از شبیه سازی و داده های واقعی دقت عالی آن را تایید می کند. بنابراین، این روش می تواند در الگوریتم های حفاظت دیفرانسیل ترانسفورماتور قدرت استفاده شود تا پایداری آن ها را در وضعیت گذرای جریان هجومی ارتقاء دهد.

International Journal of Engineering

J o u r n a l   H o m e p a g e :   w w w . i j e . i r

Algorithm of Predicting Heart Attack with using Sparse Coder

S. Mohamadzadeh*, M. Ghayedi, S. Pasban, A. K. Shafiei

Department of Electrical and Computer Engineering, University of Birjand, Birjand, Iran

A B S T R A C T

One of the most serious causes of disease in the world's population, which kills many people worldwide every year, is heart attack. Various factors are involved in this matter, such as high blood pressure, high cholesterol, abnormal pulse rate, diabetes, etc. Various methods have been proposed in this field, but in this article, by using sparse codes in the classification process, higher accuracy has been achieved in predicting heart attacks. The proposed method consists of two parts: preprocessing and sparse code processing. The proposed method is resistant to noise and data scattering because it uses a sparse representation for this purpose. The spars allow the signal to be displayed at its lowest value, which leads to improve computing speed and reduce storage requirements. To evaluate the proposed method, the Cleveland database has been used, which includes 303 samples and each sample has 76 features. Only 13 features are used in the proposed method. FISTA, AMP, DALM and PALM classifiers have been used for the classification process. The accuracy of the proposed method, especially with the PALM classifier, is the highest among other classifiers with 96.23%, and the other classifiers are 95.08%, 94.11% and 94.52% for DALM, AMP, FISTA, respectively.

doi: 10.5829/ije.2023.36.12c.08

1. INTRODUCTION

Numerous studies indicate that hospitals and medical centers possess a significant amount of patient information. However, this data is rarely utilized for decision-making, treatment, and patient services. Extracting and utilizing this information can greatly contribute to decision-making and the quality of healthcare services. Heart disease is especially critical due to its high sensitivity and potential for saving lives through early diagnosis and treatment. It is a well-known cause of death worldwide, resulting in significant financial and human losses. Implementing preventive methods plays a vital role in reducing the incidence of heart disease, such as clogged arteries. Angiography, the established method for diagnosing clogged arteries, is associated with numerous side effects and is costly. Therefore, researchers are seeking alternative non-invasive methods. Figure 1 demonstrates an example of an ECG signal, which is crucial for diagnosing heart disease [1].

The importance of predicting heart disease can be assessed from two perspectives: heart disease itself and machine vision methods. Machine vision methods, in terms of modeling, are more accurate than traditional approaches. By 2030, the estimated global death toll from heart disease is expected to reach 23 million. Based on these statistics, early and accurate prognosis of heart disease is crucial for saving countless lives worldwide [2].

In this paper, we proposed using sparse coding to extract generative features from input data that are robust to noise, diversity, and other factors. Our goal is to reconstruct the signal using the fewest number of signals. One of the advantages of using sparse codes is that it is resistant to noise and data dispersion. In other words, according to the sampling environment, most processed signals are associated with noise or dispersion. One of the best ways to deal with these two problems is to use L1-norm that is used in this paper. In the following, various classifiers have been used in the learning process, which achieved higher accuracy by using the PALM. To

Corresponding Author Email: s.mohamadzadeh@birjand.ac.ir (S. Mohamadzadeh)
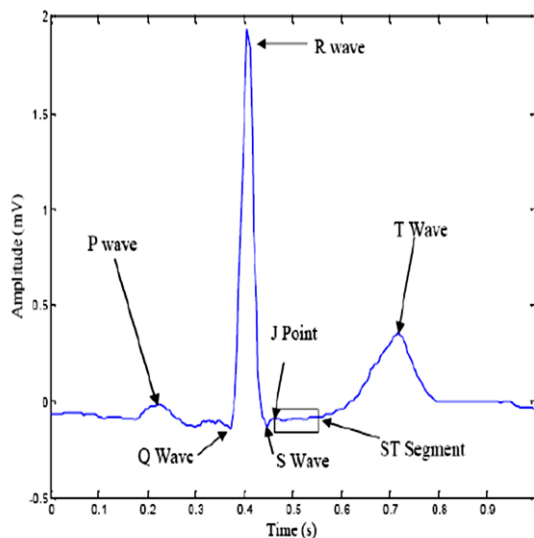
Figure 1. Electrical signal wave of the heart [1]

evaluate the proposed method, the Cleveland database has been used, which only 13 features are used in the proposed method. In order to select efficient features from the database, the influencing variables have an effect on the occurrence of heart disease. In this article, two methods are used to select the features, which are: using the opinions of experts and specialists, as well as existing articles in this field. After the investigations, 13 features were selected to evaluate the proposed method, the results of which are compared in section 4.

Details about the parameters related to our proposed method are provided in Section 2. In section 3, we explained the sparse coding-based method we have developed. We compared our proposed method with other techniques using evaluation metrics, which are presented in section 4 along with the results. Finally, we conclude our study in section 5.

2. RELATED WORKS

The section presents a review of previous methods for predicting heart attacks. Gheitasi et al. [3] used the C-Means fuzzy clustering method to predict heart disease. The study evaluated the proposed method with 270 samples and found that it was more accurate than the K-Means clustering method, with an accuracy of 92%. Mohan et al. [4] proposed a method based on the backpropagation neural network. All 13 features of the Cleveland dataset were used to train the neural network, which had a specific structure. The accuracy of this method was 92% for the learning data and 86% for the test data. Verma et al. [5] presented a combined model of heart disease prediction which uses the genetic algorithm to update weights in an artificial neural

network. This model has a higher speed in updating weights compared to the error back-propagation learning method. Finally, Mohamadzadeh et al. [6] utilized a hybrid model of the fuzzy-particle swarm system and decision tree to predict heart disease. The decision tree algorithm is used to select disease rules, the fuzzy system implements the selected rules, and the particle swarm algorithm optimizes the fuzzy system membership functions. The accuracy and sensitivity obtained from this model are 94.4% and 62%, respectively. Numerous methods have been proposed for predicting heart disease. Nazir wt al. [7] proposed an adaptive neural-fuzzy inference system to predict heart disease in the Cleveland Database. All 13 features are used for this purpose. Initially, a fuzzy inference system is formed. Then, the parameters of the fuzzy system are updated using an adaptive neural-fuzzy inference system and a combined training method to achieve the lowest possible error. The system is designed to have 9 rules and achieves an accuracy of 93.88%. Bahtiar et al. [8] presented a hybrid model based on the majority vote. This model uses three types of artificial neural networks: two multilayer perceptron neural networks and one radial base function network. The model uses a total of eight learning algorithms. The multilayer perceptron neural network achieves an accuracy of 93%, while the radial base neural network achieves 79.6%. Fooladi et al. [9] proposed the use of a hybrid model based on three simple Bayesian classification algorithms, decision trees, and support vector machines. The model uses the Cleveland Database and makes a final prediction of heart disease based on the majority vote of the results from the three categories. To predict heart attacks, previous studies have suggested using a combination of neural networks and genetic algorithms [10]. The genetic algorithm is used in this method to reduce the dimensions of the features, thereby increasing the accuracy of the prediction. Wadhawan and Maini [11] used the particle swarm optimization method based on fuzzy logic in order to classify patients in the prediction of cardiac patients. First, they fuzzified the rules in the patient data set by fuzzy logic and then optimized these rules by the particle swarm method. Many methods have used supervised data mining techniques to detect heart disease. Ahmed et al. [12] have used two algorithms for this purpose, which are: genetic algorithm and particle swarm algorithm. Patients are divided into two classes: disease and non-disease. The use of Bagging method to classify cardiac patients is suggested by Yuan et al. [13]. The authors of this article have used the Begin method, which is based on the decision tree base algorithm. The accuracy of the Bagging-based method has been higher than the conventional decision tree method.

The use of deep learning techniques based on neural networks has had a remarkable growth in the last several years, which have been used in many medical

applications, including the risk of heart failure. Choudhury and Akbar [14] suggested the use of Convolutional Neural Networks (CNN), which deals with the early identification of people at risk of heart failure. Adaptive multilayer networks are also introduced by Banu and Vanjerkhede [15] to predict the risk of heart failure. This method works better than classical neural networks.

Various perspectives can be considered in this regard, which can achieve higher efficiency in the field of heart attack prediction by using new technologies such as artificial intelligence. An example is an artificial intelligence (AI) model that can predict the risk of death from a heart attack or stroke over a 10-year period with just a chest X-ray. This risk is calculated using a score based on variables such as age, sex, race, blood pressure, high blood pressure treatment, smoking, type 2 diabetes and blood tests. In this method artificial intelligence researchers trained deep learning to search X-ray images for patterns associated with atherosclerosis, a leading cause of cardiovascular disease. Because chest X-ray imaging is more readily available than other imaging modalities, it helps to identify individuals at risk [16].

3. THEORETICAL BACKGROUND

Figure 2 shows a block diagram of the heart attack prediction algorithm using a sparse classifier. In this part, the features used are from the Cleveland Dataset, and each sample includes 13 features. Various sparse classifier methods have been employed for the learning process, such as Approximate Message Passing (AMP), Fast Iterative Soft-Thresholding Algorithm (FISTA), Primal Augmented Lagrangian Method (PALM), and Dual Augmented Lagrangian Method (DALM). The proposed method has two stopping conditions: reducing the error rate to the default threshold value and reaching the specified number of repetitions.

The algorithm presented in this section uses sparse representation and weighted elements to predict heart attacks. The flowchart for Algorithm 1, which outlines the steps of the proposed algorithm, is depicted below. Sparse coding, a powerful tool for analyzing various types of signals, is utilized in this method. The term "sparse" refers to a small number and is employed to represent non-zero values in vectors [17]. These methods require a learning process. A detailed explanation of sparse coding can be found in Algorithm 1.

In specific orthogonal transformations, the number of base signals is equal to the dimension of the processing signal. These transformations are suitable for representing a small number of signals. Specifically, it is not feasible to use a small number of signals to represent a signal, due to the limitations of unique orthogonal transformations. As a result, the use of sparse codes has
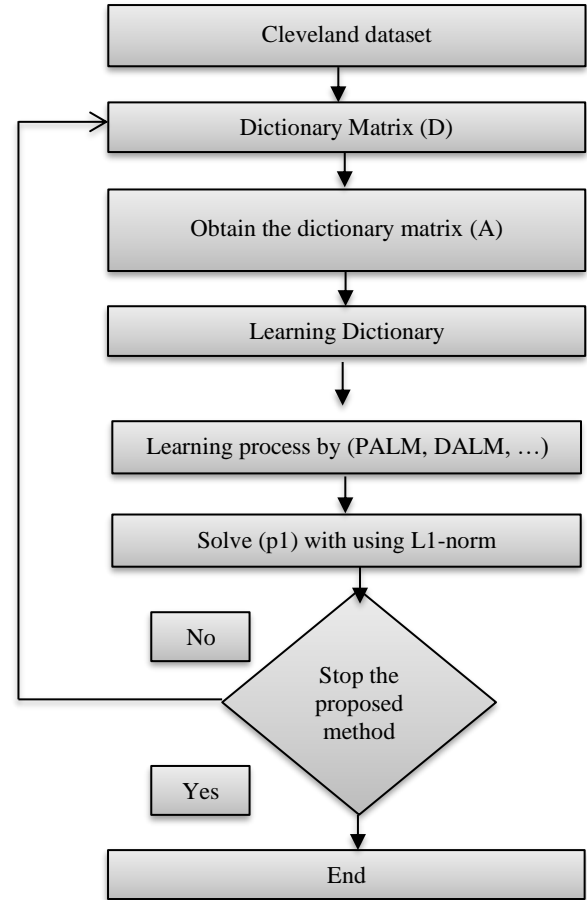
Figure 2. Schematic of the proposed method

Algorithm 1. Pseudo code of predicting heart attack algorithm method

1: Get data from new database;

2: Learning process by (PALM, Homotopy, …) algorithm;

3: solve $(p1)$: $\min\|x\|_1$ $subject\ to\ y = Dx$ and find x0:

$$E = \| b - Ax \|_F^2 = \| Y - \sum_{j=1}^{m} a_j x_j^T \|_F = \| (b - \sum_{j \neq j_0}^{m} a_j x_j^T) - a_{j0} x_{j0}^T \|_F^2$$

While stop condition is not satisfied, **do**:

4: Construct dictionary A:

$A_i = [v_{i,1}, v_{i,2}, ..., v_{i,m}] \in R^{m \times 1}$, $v_{i,j}$ denotes the jth feature of the ith image;

$A = [A_1, A_2, ..., A_n] \in R^{m \times n}$

5: Construct $b \in R^{m \times 1}$;

6: Seek sparse representation, $x_0 \epsilon R^n$ by solving Equation (1) and using SL0, DALM, PALM, homotopy, FISTA nd AMP techniques. Thus, some elements of x0 are zero except those associated with the kth column.

7: Separate elements of A and x0;

$$x_0 = [\underbrace{a_1, a_2, ..., a_j, ..., ..., a_n}_{1 \quad 2 \quad k}] = [x_{0,1}, x_{0,2}, ..., x_{0,k}]$$

$A = [A_1, A_2, ..., A_j, ..., ..., A_n]$
$\underbrace{\quad}_{1} \underbrace{\quad}_{2} \underbrace{\quad}_{k} = [D_1, D_2, ..., D_k]$

8: Define $C_k = D_k x_{o,k} \in R^m$;

9: Compute Euclidean Distance (ED);

$ED_k = \sqrt{\sum_{i=1}^{m} (b_i - C_i)^2}$

10: Compute the weighting elements;

$x_{weighted} = [\frac{|x_{o,1}|}{ED_1}, \frac{|x_{o,2}|}{ED_2}, ..., \frac{|x_{o,k}|}{ED_k}] \in R^m$

End

11: computed the accuracy query sample by using element of $x_{weighted}$.

been recommended. Sparse coding, which utilizes base signals instead of signal dimensions, provides a more straightforward representation of the signal by setting specific criteria for it.

The information in the input data has many repetitive structures that they are known as sparsity. Also, in many real-world applications, the input data is accompanied by noise. In this regard, sparse display has been used to solve these two problems. There are various reasons for the existence of these two problems, one of which is the sampling environment.

It is possible that most of the natural signals, taking into account personal bases, have a display sparse. Natural signals often do not cover the entire space and are placed on a manifold subspace. For this purpose, various methods such as Matching Pursuit and Orthogonal matching, can be used. In this paper, another criterion is used to measure thinness and stability against noise, which is confirmed as l_1-norm in the following.

In the sparse representation method, which is considered one of the best methods, a large signal can be represented using few non-zero coefficients. In the condition that k<< n, a 'k' non-zero coefficient presents a signal with the length of 'n'. This enables signal compression and reduction in the number of required measurements. Researchers in various fields, such as speech recognition and image processing, have therefore employed the sparse representation method:

$b = Ax = \sum_{i=1}^{n} a_i x_i$ (1)

If the main signal is $b \in R^m$, and the dictionary is defined as A in which $\alpha_i \in R^m$ $(1 \leq i \leq n)$ are named atoms. Clearly, Equation (1) solution is dependent on the relation between 'm' and 'n'. On the condition that 'm' is equal to 'n', the equation has one unique solution; and on the condition that 'm' is smaller than 'n', no unique solution is possible for the equation. Therefore, in order to achieve the specific solution, the following condition is considered for the equation [18]:

$P_j = \min J(x) \quad subject.to \quad b = Ax$ (2)

The problem can be classified into numerous forms based on J(x) function. Sezavar et al. [19] showed that the l_0-norm of x is found as follows:

$\|x\|_0 = \lim_{q \to 0} \sum_{i=1}^{n} |x_i|^q$ (3)

where

$P_0: \min\|x\|_0 \quad subject.to \quad b = Ax$ (4)

The output of this equation indicates the sum of non-zero components of the vector x. However solving this problem with the l_0-norm function can make results sparse; this is not a convex problem and is difficult to solve. Therefore, the closest solution to l_0 called l_1-norm is used instead. Therefore, the problem becomes a convex optimization problem [18-21]:

$P_1: min\|x\|_1 \quad subject.to \quad b = Ax$ (5)

Because, in fact, the signals are accompanied by noise, Equation (5) is rewritten as Equation (6) as follow:

$p_{1,2}: min\|x\|_1 \quad subject.to \quad \|b - Ax\|_2 \ll \varepsilon$ (6)

Finally, it can be displayed as the famous Equation (7) as follows [18, 21]:

$QP_\lambda: \min \frac{1}{2}\|b - Ax\|_2^2 + \lambda\|x\|_1$ (7)

Sezavar et al. [19] showed that PALM and DALM methods are more efficient than other methods. So PALM and DALM methods are used in this paper to solve the optimization problem (Equation (7)).

4. ANALYSIS OF EXPERIMENTAL RESULTS

In the sparse representation method, which is considered one of the best approaches, a large signal can be represented using only a few non-zero coefficients. This allows for efficient signal compression and reduces the number of required measurements. As a result, the sparse representation method has found applications in various fields, including speech recognition and image processing.

4. 1. Evaluation Metrics   In order to evaluate the proposed method with other existing methods, three evaluation criteria of sensitivity, specificity, and accuracy have been used [22]. In other words, the following terms are used for evaluation: TP (True Positive), TN (True Negative), FP (False Positive), FN (False Negative), PC= TP + FN, and NC= FP +TN. Also, the sensitivity, specificity, and accuracy are defined as follows:

$Sensitivity = \frac{TP}{TP + FN}$ (8)

$$Specificity = \frac{TN}{TN+FP} \tag{9}$$

$$Accuracy = \frac{TP+TN}{Pc+Nc} \tag{10}$$

4. 2. Dataset   The Cleveland database has been used to evaluate methods for predicting heart disease [16]. It is a collection of standardized and reliable data that is provided to researchers, who can use this data to compare their methods with others. Heart disease has many different symptoms, and analyzing patterns in heart data is important for diagnosing the condition. The Cleveland Database was compiled by the Cleveland Medical Center in 1998. It contains 303 samples, including 297 complete samples and 6 samples with missing values. The database includes 76 raw attributes, but experiments are only performed on 13 of these features. The data set is categorized, and Table 1 provides a description of the data [16].

4. 3. Simulation Details   To go to the details of implementation, it is noticed that codes are written using Matlab. The simulation was done on 8 GB of RAM and core i-5 Intel CPU. For training, data is randomly divided to training (70%), validation set (15%), and test (15%). Because the model performs the same in training and validation data, it is understood that it can be used generally for new data with high performance. The size of feature vector is 13 and the dataset has 297 signals. Regularization parameter is 0.5 and maximum iteration is 150 epochs.

4. 4. Experimental Results   In this section, the obtained results of the proposed method and state-of-the-art methods can be shown by computing the accuracy, the sensitivity, and the specificity measure. To solve Equation (1), the PALM algorithm is used. The results of the proposed method, ANNGA [23], TSB [24], FISGA [25], FISBFS [26], ANFIS1 [27], ANFIS2 [28] on Cleveland databases are presented. The index results on the Cleveland database are shown in Table 2.

TABLE 1. Cleveland Dataset

No	Features	Descriptions
1	Age	Age of patient (years)
2	Sex	1: male, 0: female
3	Chest pain (CP)	1 = typical angina 2 = atypical angina 3 = nonangina pain 4 = asymptomatic
4	Rest BP	Resting blood pressure
5	Chol	Serum cholesterol in mg/dl
6	FBS	Fasting blood sugar larger 120 mg/dl (1 true)
7	RestECG	Resting electrocardiographic result

8	Thalach	Maximum heart rate accomplished
9	Exang	Exercise-induce angina (1 yes)
10	Oldpeak	ST depression induce: exercise relative to rest
11	CA	Number of major vessels (0–3)
12	Slope	Slope of peak exercise ST
13	Thal	No explanation provided, but probably thalassemia
14	Num	Diagnosis of cardiac disease: 1: yes 0: no

TABLE 1. the evaluated metrics on Cleveland dataset

Method	The Accuracy %	The Sensitivity %	The Specificity %
ANNGA	89	--	--
TSB	82	74	93
FIGSA	86	80	90
FISBFS	81	81	82
ANFIS1	92.3	--	--
ANFIS2	83.8	--	--
The proposed method (PALM)	**96.23**	88.65	91.21

As observed in Table1, the best score has achieved Accuracy= 96.23%, Sensitivity= 88.65% and Specificity= 91.21% by the proposed method with using PALM classifier.

In the Cleveland database, we have compared the proposed model against state-of-the-art methods [23]. Saifudin et al. [23] proposed 6 classifiers, Logistic regression, K Neighbors, SVM, Random forest, Decision tree, DL. As an observer in Table 3, the accuracy rate by the proposed method, Logistic regression, K Neighbors, SVM, Random forest, Decision tree, DL classifier defined by Saifudin et al. [23] are 96.23%, 83.3%, 84.8%, 83.2%, 80.3%, 82.3% and 94.2%, respectively.

TABLE 3. Evaluated metrics for Cleveland dataset

Method	Accuracy %	Sensitivity %	Specificity %
Logistic regression	83.3	86.3	82.3
K Neighbors	84.8	85.0	77.7
SVM	83.2	78.2	78.7
Random forest	80.3	78.2	78.7
Decision tree	82.3	78.5	78.9
DL	94.2	82.3	83.1
The proposed method (PALM)	**96.23**	**88.65**	**91.21**

The performance of the proposed method on the Cleveland database is shown in Table 4, in which the proposed method has been achieved for FISTA, AMP, DALM, and PALM classifiers. The accuracy of the proposed approach using the PALM classifier is the best metric among the other classifiers.

The accuracy rate measures resulting from the proposed method and the methods reported in literture [29-34] on the Cleveland database are presented in Figure 3.

As an observer in Figure 3, the accuracy rate by the proposed method, and the data reported in literature [29-34] are 96.23%, 85.48%, 87%, 82.75%, 93%, 89.71%, and 93.44%, respectively. The proposed method provides the best performance in the Cleveland database.

As mentioned earlier, the sampling environment causes noise in the patients' data. In this regard, we have also evaluated the proposed method for the noise in the data, and the results of the accuracy evaluation criteria are shown in Figure 4. As an observer in Figure 4, the accuracy rate by PALM method is rather than other methods that is 91.87%.

TABLE 4. The proposed method on Cleveland dataset

Method	Accuracy %	Sensitivity %	Specificity %
The proposed method (FISTA)	94.52	87.62	84.76
The proposed method (AMP)	94.11	86.41	87.28
The proposed method (DALM)	95.08	87.19	91.04
The proposed method (PALM)	**96.23**	**88.65**	**91.21**
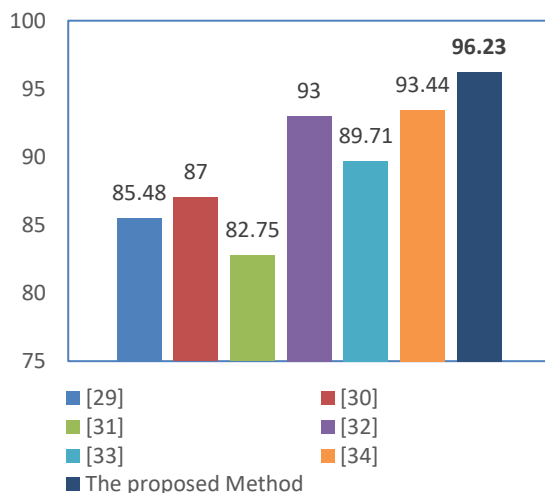
Figure 3. The Accuracy evaluated metrics for Cleveland dataset
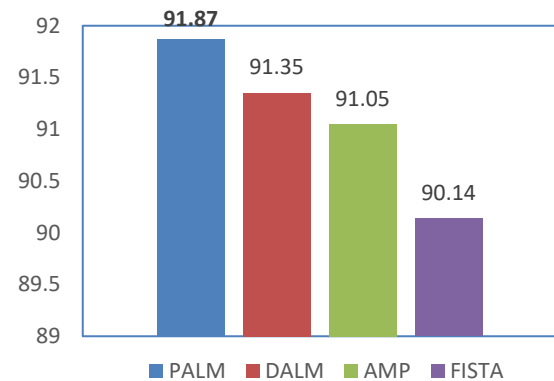
Figure 4. The Accuracy evaluated metrics of the proposed method with noisy data

5. CONCLUSION

In this paper, we proposed a novel method for predicting heart attacks based on sparse coding. Despite the extensive research conducted in this field, an efficient method has yet to be achieved. Most existing methods rely on extracting low-level features, which leads to low accuracy. The main difference between our proposed method and existing methods lies in the use of sparse classifiers. We modeled our method using FISTA, AMP, DALM, and PALM classifiers, which utilized sparse representation - a powerful method in this domain. Our proposed method for predicting heart attacks achieved better results compared to state-of-the-art methods. We evaluated the performance of our method on the Cleveland dataset, which is commonly used to assess prediction systems. As shown in the results section, our proposed method outperforms other methods in predicting heart attacks.

6. REFERENCES

1. Wang, M., Yao, X. and Chen, Y., "An imbalanced-data processing algorithm for the prediction of heart attack in stroke patients", *IEEE Access*, Vol. 9, (2021), 25394-25404. doi: 10.1109/ACCESS.2021.3057693.

2. Mehmood, A., Iqbal, M., Mehmood, Z., Irtaza, A., Nawaz, M., Nazir, T. and Masood, M., "Prediction of heart disease using deep convolutional neural networks", *Arabian Journal for Science and Engineering*, Vol. 46, No. 4, (2021), 3409-3422. https://doi.org/10.1007/s13369-020-05105-1

3. Gheitasi, A., Farsi, H. and Mohamadzadeh, S., "Estimation of hand skeletal postures by using deep convolutional neural networks", *International Journal of Engineering, Transactions A: Basics*, Vol. 33, No. 4, (2020), 552-559. https://doi.org/10.5829/IJE.2020.33.04A.06

4. Mohan, S., Thirumalai, C. and Srivastava, G., "Effective heart disease prediction using hybrid machine learning techniques", *IEEE Access*, Vol. 7, (2019), 81542-81554. doi: 10.1109/ACCESS.2019.2923707.

5. Verma, L., Srivastava, S. and Negi, P., "A hybrid data mining model to predict coronary artery disease cases using non-invasive

clinical data", *Journal of Medical Systems*, Vol. 40, (2016), 1-7. https://doi.org/10.1007/s10916-016-0536-z

6. Mohamadzadeh, S., Pasban, S., Zeraatkar-Moghadam, J. and Shafiei, A.K., "Parkinson's disease detection by using feature selection and sparse representation", *Journal of Medical and Biological Engineering*, Vol. 41, No. 4, (2021), 412-421. https://doi.org/10.1007/s40846-021-00626-y

7. Nazir, N., Rajab, S. and Sharma, V., "State-of-the-art artificial intelligence techniques in heart disease diagnosis", in Emerging Trends in Expert Applications and Security: Proceedings of ICETEAS 2018, Springer. (2019), 651-657.

8. Bahtiar, A., Dwilestari, G., Basysyar, F.M. and Suarna, N., "Data mining techniques with machine learning algorithm to predict patients of heart disease", in IOP Conference Series: Materials Science and Engineering, IOP Publishing. Vol. 1088, (2021), 012035.

9. Fooladi, S., Farsi, H. and Mohamadzadeh, S., "Segmenting the lesion area of brain tumor using convolutional neural networks and fuzzy k-means clustering", *International Journal of Engineering, Transaction B: Applications*, Vol. 36, No. 8, (2023), 1556-1568. doi: 10.5829/IJE.2023.36.08B.15.

10. Moameri, S. and Samadinai, N., "Diagnosis of coronary artery disease via a novel fuzzy expert system optimized by cuckoo search", *International Journal of Engineering, Transactions c: Aspects*, Vol. 31, No. 12, (2018), 2028-2036. doi: 10.5829/ije.2018.31.12c.06.

11. Wadhawan, S. and Maini, R., "Ebpso: Enhanced binary particle swarm optimization for cardiac disease classification with feature selection", *Expert Systems*, Vol. 39, No. 8, (2022), e13002. https://doi.org/10.1111/exsy.13002

12. Ahmed, R., Bibi, M. and Syed, S., "Improving heart disease prediction accuracy using a hybrid machine learning approach: A comparative study of svm and knn algorithms", *International Journal of Computations, Information and Manufacturing*, Vol.   3,   No.   1,   (2023),   49-54. https://doi.org/10.54489/ijcim.v3i1.223

13. Yuan, X., Wang, X., Han, J., Liu, J., Chen, H., Zhang, K. and Ye, Q., "A high accuracy integrated bagging-fuzzy-gbdt prediction algorithm for heart disease diagnosis", in 2019 IEEE/CIC International Conference on Communications in China (ICCC), IEEE. (2019), 467-471.

14. Choudhury, R.P. and Akbar, N., "Beyond diabetes: A relationship between cardiovascular outcomes and glycaemic index", *Cardiovascular Research*, Vol. 117, No. 8, (2021), e97-e98. https://doi.org/10.1093/cvr/cvab162

15. Banu, U. and Vanjerkhede, K., "Hybrid feature extraction and infinite feature selection based diagnosis for cardiovascular disease related to smoking habit", *International Journal on Advanced Science, Engineering & Information Technology*, Vol. 13, No. 2, (2023).

16. AL-Hawamleh, A.M., "Predictions of cybersecurity experts on future cyber-attacks and related cybersecurity measures", *International Journal of Advanced Computer Science and Applications*,   Vol.   14,   No.   2,   (2023).   doi: 10.14569/IJACSA.2023.0140292.

17. Sharma, H. and Rizvi, M., "Prediction of heart disease using machine learning algorithms: A survey", *International Journal on Recent and Innovation Trends in Computing and Communication*, Vol. 5, No. 8, (2017), 99-104.

18. Shahsavani, F., Nasiripour, R., Shakeri, R. and Gholamrezaee, A., "Arrhythmia detection based on the reduced features with k-svd sparse coding algorithm", *Multimedia Tools and Applications*, Vol.   82,   No.   8,   (2023),   12337-12350. https://doi.org/10.1007/s11042-022-13894-w

19. Sezavar, A., Farsi, H., Mohamadzadeh, S. and Radeva, P., "A new person re-identification method by defining cnn-based feature extractor and sparse representation", *Multimedia Tools and Applications*, (2023), 1-17. https://doi.org/10.1007/s11042-023-15718-x

20. Hamidi, H. and Daraee, A., "Analysis of pre-processing and post-processing methods and using data mining to diagnose heart diseases", *International Journal of Engineering, Transactions A: Basics*, Vol. 29, No. 7, (2016), 921-930. doi: 10.5829/idosi.ije.2016.29.07a.06.

21. Barati, A., Farsi, H. and Mohamadzadeh, S., "Integration of the latent variable knowledge into deep image captioning with bayesian modeling", *IET Image Processing*, Vol. 17, No. 7, (2023), 2256-2271. https://doi.org/10.1049/ipr2.12790

22. Nasiripour, R., Farsi, H. and Mohamadzadeh, S., "Saliency detection in eye gaze prediction by using deep learning", *Journal of Soft Computing and Information Technology*, Vol. 9, No. 3, (2020), 93-108.

23. Saifudin, A., Nabillah, U. and Desyani, T., "Bagging technique to reduce misclassification in coronary heart disease prediction based on random forest", in Journal of Physics: Conference Series, IOP Publishing. Vol. 1477, (2020), 032009.

24. Bashir, S., Qamar, U. and Javed, M.Y., "An ensemble based decision support framework for intelligent heart disease diagnosis", in International conference on information society (i-Society 2014), IEEE. (2014), 259-264.

25. Santhanam, T. and Ephzibah, E., "Heart disease prediction using hybrid genetic fuzzy model", *Indian Journal of Science and Technology*,   Vol.   8,   No.   9,   (2015),   797.   doi: 10.17485/ijst/2015/v8i9/52930.

26. Oad, K.K., DeZhi, X. and Butt, P.K., "A fuzzy rule based approach to predict risk level of heart", *Global Journal of Computer Science and Technology (C) Software & Data Engineering*, Vol. 14, No. 3, (2014).

27. Ziasabounchi, N. and Askerzade, I., "Anfis based classification model for heart disease prediction", *International Journal of Electrical & Computer Sciences IJECS-IJENS*, Vol. 14, No. 02, (2014), 7-12.

28. Kumar, A.S., "Diagnosis of heart disease using advanced fuzzy resolution mechanism", *International Journal of Science and Applied Information Technology*, Vol. 2, No. 2, (2013), 22-30.

29. Latha, C.B.C. and Jeeva, S.C., "Improving the accuracy of prediction of heart disease risk based on ensemble classification techniques", *Informatics in Medicine Unlocked*, Vol. 16, (2019), 100203. https://doi.org/10.1016/j.imu.2019.100203

30. Reddy, K.V.V., Elamvazuthi, I., Aziz, A.A., Paramasivam, S., Chua, H.N. and Pranavanand, S., "Heart disease risk prediction using machine learning classifiers with attribute evaluators", *Applied Sciences*,   Vol.   11,   No.   18,   (2021),   8352. https://doi.org/10.3390/app11188352

31. Ananey-Obiri, D. and Sarku, E., "Predicting the presence of heart diseases using comparative data mining and machine learning algorithms", *International Journal of Computer Applications*, Vol. 176, No. 11, (2020), 17-21.

32. Rustam, F., Ishaq, A., Munir, K., Almutairi, M., Aslam, N. and Ashraf, I., "Incorporating cnn features for optimizing performance of ensemble classifier for cardiovascular disease prediction", *Diagnostics*, Vol. 12, No. 6, (2022), 1474. https://doi.org/10.3390/diagnostics12061474

33. Ahamad, G.N., Shafiullah, Fatima, H., Imdadullah, Zakariya, S., Abbas, M., Alqahtani, M.S. and Usman, M., "Influence of optimal hyperparameters on the performance of machine learning algorithms for predicting heart disease", *Processes*, Vol. 11, No. 3, (2023), 734. https://doi.org/10.3390/pr11030734

34. Chandrasekhar, N. and Peddakrishna, S., "Enhancing heart disease prediction accuracy through machine learning techniques and optimization", *Processes*, Vol. 11, No. 4, (2023), 1210. https://doi.org/10.3390/pr11041210

Persian Abstract

چکیده

هر ساله بیماری های قلبی جان افراد بی شماری را در سراسر جهان می گیرد. میزان بروز این نوع بیماری در نقاط مختلف جهان متفاوت است. این امر منجر به عدم تعادل بین سوابق موجود افراد سالم و افراد مبتلا به بیماری قلبی شده است. به عبارت دیگر، عدم تعادل بین داده های موجود در تشخیص بیماری قلبی وجود دارد. استفاده از روش‌های پیشگیرانه نقش مهمی در پیشگیری از این بیماری ها دارد. مشکل پیش بینی بیماری قلبی یک موضوع تقسیم بندی است. در فرآیند بخش‌بندی، یک مجموعه داده جدید و ناشناخته با شناسایی دسته‌ها و مفاهیم بین آنها پیش‌بینی می‌شود. در این مقاله فرآیند طبقه بندی داده ها با استفاده از کدهای تنک انجام می شود. روش پیشنهادی از دو بخش تشکیل شده است: بخش اول پیش پردازش و بخش دوم پردازش کد تنک است. بخش پیش پردازش شامل قرار دادن داده‌های ناموجود و در بخش پردازش بیماری قلبی پیش بینی می‌شود. کدگذاری پراکنده به دنبال ساده ترین نمایش برای سیگنالی است که سیگنال را با استفاده از حداقل تعداد سیگنال بازسازی می‌کند. این امر باعث افزایش سرعت محاسبات و کاهش فضای مورد نیاز برای ذخیره داده‌ها می‌شود. در روش پیشنهادی از نمایش تنک استفاده می‌شود که توسط طبقه‌بندی‌کننده FISTA، AMP، DALM و PALM مدل‌سازی شده است که در مقایسه با روش‌های پیشرفته، روشی موفق بوده است. روش پیشنهادی با استفاده از طبقه‌بندی‌کننده PALM به عنوان بهترین متریک در بین طبقه‌بندی‌کننده‌های دیگر با دقت ۹۶/۲۳ درصد است.

International Journal of Engineering

Effect of Acidic Environments Containing Hydrochloric Acid on Rubberized Concrete

S. A. Hosseini*[a], F. A. Khankahdani[b], S. A. H. Moosavinezhad[c]

[a] *Faculty of Technology and Mining, Yasouj University, Choram, Iran*
[b] *Department of Civil Engineering, Shiraz Branch, Islamic Azad University, Shiraz, Iran*
[c] *Department of Engineering, Sepidan Branch, Islamic Azad University, Sepidan, Iran*

A B S T R A C T

Aggressive environment reduces the mechanical and durability-related properties of concrete. In this study, the effects of exposing the concrete containing crumbed tire rubber (CTR) to aggressive environmental conditions, including hydrochloric acid (HCl) is investigated. For this purpose, 5, 10, and 15% of the fine aggregate of the mixing design were partially replaced with the CTR, and then at the age of 7 days, when the concrete reached almost 70% of the initial strength, the samples were placed in water containing 2% HCl for 28 and 90 days. In this study, the effect of using Nano-SiO$_2$(NS) in the rubberized concrete and its behavior in acidic environments by replacing 5 and 10% by weight of cement with NS was also studied. Compressive strength and mass loss were evaluated at 28 and 90 days after casting. The results showed that the detrimental effects of HCl on the compressive strength of concrete significantly increased with an increasing in CTR content of concrete. The results also indicated that the impact of HCl acid on mass loss is improved by increasing the percentage of CTR so that the sample with the 15% crumbed tire showed a 7% lower weight reduction than the control sample.

doi: 10.5829/ije.2023.36.12c.09

1. INTRODUCTION

The decline in performance, as well as the deterioration of concrete structures during the service life due to durability issues, cause high costs. Durability-related parameters, especially in corrosive environmental conditions, have a great impact on the final design of concrete structures. Many factors affect the durability-related properties of concrete that harmful chemical reactions are known as one of the most important factors of the gradual deterioration and reduction of performance of concrete structures.

The most important factors that cause destructive chemical reactions in concrete include carbonation, chloride ion penetration, alkaline reaction, acid attack, and sulfate attack [1]. Due to the high alkalinity of the concrete, it is easily vulnerable under acidic conditions [2]. Acid rain, industrial environments, and some groundwater, as well as wastewater treatment systems, are conditions that expose concrete structures to acids [3]. Estimates show that in some countries, the cost of

repairing sewage systems that damaged by acid is higher than the cost of constructing new systems, which makes it necessary to study this effect on concrete structures more than ever [4].

Among the various acids, hydrochloric acid (HCl) and sulfuric acid are known as the most aggressive agents for concrete structure [5]. HCl is a staple and conventional acid in science laboratories and also it is one of the strong acids that can easily attack concrete. Physical and chemical reactions between acids and products due to the hydration of cement in concrete reduces the concrete performance [6]. The most important factors affecting the intensity of acid attack and the type of its mechanism are the coarse aggregate content, the type and composition of binder, the pH of the concrete environment, and the water to cement ratio [7, 8]. According to Chandra's [9] research, the HCl causes the formation of calcium-based salts soluble in water, and leaching out of these salts causes weakness in the structure of concrete. HCl accelerates the leaching process because of an increase in the

*Corresponding Author Email: *a.hosseini@yu.ac.ir* (S. A. Hosseini)

calcium concentration gradient in the attacking fluid phase.

The production of cement and the extraction of concrete aggregates from natural resources cause environmental pollution as well as the waste of many natural resources. The use of secondary cementitious materials (SCM) or alternatives to aggregates has attracted the attention of many researchers [10]. These materials replace with some ingredients of concrete in a way that causes less harmful effects on the environment and in addition; improves some properties of concrete. Meanwhile, the reuse of recycled materials such as waste tires has received more attention because which if not used it will increase environmental pollution. Estimates show that millions of tires are worn out every year, and the lack of a proper technical and environmental method to destroy or recycle these tires has led to the accumulation or release of these tires in nature .

Recently, the use of waste tires as a partial replacement of concrete aggregates or as filler has been considered by many researchers [11, 12]. In addition to environmental benefits, improving the ductility of concrete is one of the most important reasons for using CTR in concrete [13]. Marques et al. [14] reported that the mechanical properties of concrete, such as compressive strength, are reduced by replacing 12% of fine aggregate with CTR at all ages. Al-Tayeb et al. [15] reported an improvement in the ductility of concrete containing up to 20% of the tire under impact loads. Holmes et al. [16] reported an increase in flexural strength due to the ductile behavior of this type of concrete by replacing 7% aggregate with the CTR. Pham et al. [17] reported the replacement of up to 15% aggregate with the CTR has almost no significant reducing effect on compressive strength; While in 30% replacement, there is a 40% reduction in the maximum load-carrying capacity of concrete samples. Overall, in most studies, the replacement of up to 15% of aggregate with CTR has had no impressive reduction in concrete strength [18, 19]. The reduction of bond strength between concrete and rebar, as well as the severe reduction of compressive strength when large amounts of crumb tire rubbers are used, are the most important disadvantages of using waste tires in concrete. The durability-related properties of rubberized concrete are not also well investigated. There are not many studies on the effect of acidic environments on the properties of concrete containing waste CTR. Segre et al. [20] reported good resistance of concrete containing 10% CTR in 5% HCl medium. Rashad [21] reported better behavior of concrete containing CTR than the plain concrete against HCl attack.

In addition to mechanical properties, durability-related properties of concrete containing CTR under the influence of various environmental factors has also been studied by some researchers. Ganesan et al. [22]

investigated the effect of seawater and sulfuric acid solution on concrete samples containing 15% CTR and reported a greater mass loss of rubberized concrete than the control sample. By replacing different percentages of aggregates with crumb rubber obtained from PET bottles and storing samples in acidic environments, Shahini et al. [23] reported the appropriate behavior of samples containing crumb rubber. Avzedo et al. [24] reported an adverse effect under acidic conditions for concretes with different percentages of CTR but also concluded that water permeability properties remained constant for concrete containing up to 15% CTR. There has been a lot of research on the permeability of concrete containing CTR, and the results are very scattered. Pedro et al. [25] reported an approximately 9% reduction in water absorption in concrete mortars containing 5% CTR. Gesoglu et al. [26] reported a 44% reduction in the permeability of concrete containing 10% CTR. Hilal [27] has reported a 10% increase in water absorption for concretes containing 20% of CTR. Therefore, due to the dispersion in the results of previous research on the permeability of rubberized concrete, it is essential to study this issue.

Nano-SiO_2 (NS) is in the category of pozzolanic materials that adding it to concrete can improve the permeability properties as well as the strength of concrete [28, 29]. Pozzolans usually show their effects in improving concrete properties after a period of time due to their delayed reactions; However, due to the high intensity of NS pozzolanic reactions, concrete containing NS in the early days and during curing also has better strength and durability than conventional concrete [30]. NS improves strength by reacting with calcium hydroxide (CH) in concrete and producing calcium silicate hydrate (C-S-H), which is a more resistant material than calcium hydroxide [31]. Li et al. [32] reported the higher compressive and flexural strength of concrete containing NS than that of the control sample with the same w/b. Maghsoudi et al. [33] have reported a positive effect of adding NS against corrosion due to sulfate attack on concrete. Kumar et al. [8] replaced 2.5% of the cement with NS and cured concrete samples in a solution containing 5% HCl, reported that concrete containing NS was less corroded during 28 days of exposure to acidic conditions.

It is noteworthy that despite the extensive research done on concrete containing sub-tires, the available resources regarding the effect of corrosive environments, especially acidic conditions on this type of concrete are very limited. Considering that some investigations have considered the type of aggregate as effective on the performance of concrete against acid, replacing a part of aggregate with CTR can complement the study of the effect of concrete aggregate type in acidic conditions [34]. Additionally, it is desired to know more about this type of concrete for practical use in the road and

construction industries, as well as the lack of regulatory criteria for this type of concrete, has necessitated the need for further evaluations. Considering that a way to improve the durability of concrete against acid attack is to improve its permeability; in this research, NS, which has the property of reducing the permeability of concrete, has been used. The available resources for the simultaneous effect of using tire and NS under acidic conditions are very limited. The effect of NS on this type of concrete, especially in acidic conditions, needs further investigation. In this research, the effect of exposing concrete containing CTR to HCl on compressive strength and mass loss of concrete has been investigated. In this study, the maximum percentage of aggregate replacement with CTR was limited to 15% [35]. Compressive strength and water permeability tests have been used to evaluate the mechanical properties and durability of concrete.

2. MATERIALS AND METHODS

Local ordinary type II Portland cement (OPC) complying with ASTM C150 was used as the binding material [36]. The NS with specific gravity of 2.35 and specific surface area of 185.5 (m^2/g) was used. The chemical compositions of OPC and NS obtained from XRF analysis are presented in Table 1. The fine aggregate was prepared from local rivers and the dolomitic limestone coarse aggregate was obtained from local mountain mines. Some mechanical properties of aggregates are shown in Table 2.

CTR with a maximum size of 5 mm and a specific gravity of 1.1 were prepared from a local recycling plant were used to replace part of the fine aggregate. In this research, the CTR was used to replace part of the fine aggregates, so the size range of CTR was chosen between 0.8-5 mm because this range is the commone particle size distribution of fine aggregate. The CTR was washed with potable water till their pH reached about tap water. Tap water complying with ASTM C1602 was used for casting

TABLE 1. Chemical compositions of OPC and Nono-SiO₂ by XRF analysis (wt.%)

Chemical Composition	OPC	NS
CaO	63.2	0.11
SiO$_2$	22.6	98.73
Al$_2$O$_3$	4.1	0.028
Fe$_2$O$_3$	3.5	0.018
SO$_3$	1.5	0.011
MgO	2.6	0.01
Na$_2$O	0.2	0.2
K$_2$O	0.5	0.01

TABLE 2. Mechanical proprties of aggregates

Proprty	Fine	Coarse
Specific gravity	2.85	2.61
Water absorption	1.07%	2.36%
Fineness modulus	2.63	

and curing of specimens [37]. The chemical compositions and physical properties of water are given in Table 3. HCl with a concentration of 98% was used. HCl concentration was reduced to the desired concentration of 2% based on the volume of water used to cure the samples.

The particle size distributions of fine and coarse aggregates after modification according to the ASTM C33 are shown in Figure 1 [38].

The control mix design was based on ACI standard with the water-to-binder ratio (w/b) equal to 0.4. In this study, 5%, 10%, and 15% of the volume of fine aggregate were replaced with CTR. In some mix designs, 5% and 10% of the cement were replaced with NS. Table 4 shows the mix proportions of the investigated concretes.

Various methods have been proposed by researchers and standards to evaluate the effect of the acidic

TABLE 3. Chemical and physical properties of mixing water

Property	OPC	NS
SO$_4$	145	mg/L
Cl	62	mg/L
TDS	630	mg/L
CaCO$_3$	415	mg/L
NO$_3$	21	mg/L
Na	19	mg/L
K$_2$O	0.5	mg/L
Density	1000	Kg/m^3
pH	7.1	
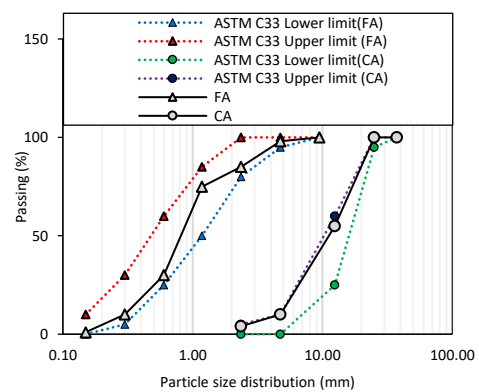
Figure 1. Particle size distribution of aggregates

environment on concrete. In most of the methods used by the researchers, the concentration of the acid has been different according to the purpose of the research. The concentration selected in this research was based on the conditions evaluated in the wastewater of an industrial complex.

By casting three samples for each experiment at each age, an appropriate number of 150 mm size cubes were cast for each mix design. To adjust the workability of concrete, its slump was kept within 10 cm by adding a carboxylate-based superplasticizer. After molding, the samples were kept at room temperature under plastic cover for 24 hours to retain moisture, and after demolding, they were cured with tap water for 7 days. After 7 days of standard curing, some samples were immersed in a solution with a concentration of 2% HCl and the rest were still kept under standard curing conditions.

For storage of samples, an anti-acid plastic tank with a volume of 500 liters, which contains 2% of HCl, was used. The tank water was changed every week to maintain the desired concentration of acid. Due to the errors caused by dissociating radicals on the pH value, the acid concentration was used to measure the acidity of the medium [39]. The temperature of water curing and acid solution was kept at level of 23°C ± 2°C [40]. After 28 and 90 days, the specimens were removed from the curing conditions and acid then the mass loss and compressive strength of the specimens were examined. The average of three specimens were used at every specified age and test.

TABLE 4. Concrete mix proportions per cubic meter of concrete

Mix ID	Cement (kg)	NS (%)	CTR (kg)	CTR (%)	Fine Agg (kg)
T0N0(control)	400	0	0	0	517
T0N5	400	0	0	0	517
T0N10	400	0	0	0	517
T5N0	400	0	15	5	448
T5N5	380	5	15	5	448
T5N10	360	10	15	5	448
T10N0	400	0	40	10	375
T10N5	380	5	40	10	375
T10N10	360	10	40	10	375
T15N0	400	0	66	15	316
T15N5	380	5	66	15	316
T15N10	360	10	66	15	316

3. RESULTS AND DISCUSSION

3. 1. Mass Loss   Mass loss of specimens was measured at 28 and 90 days after casting; for this purpose, at the desired age, the samples were removed from the solution and the corroded outer layer was separated with a soft brush. The specimens were stored in an oven at approximately 100°C and their weight was measured when the weight did not change with respect to time [41]. To obtain the mass ratio and evaluate the results, the weight of each specimen was divided by the weight of the 28-days water cured control specimen (without CTR and NS). Figure 2 shows the appearance of a specimen with CTR and the control specimen at the age of 28 days. The brown surface of the sample is attributed to the formation of ferric hydroxide [42].

Figures 3-5 show the mass ratios of samples at 28 and 90 days of curing and acid exposure conditions. Figure 3 shows the effect of different percentages of CTR on the weight of water-cured specimens; so that the effects of CTR and exposure conditions can be distinguished from the results presented in Figures 4 and 5. According to Figure 3, it is clear that NS has no effect on the weight ratio for water-cured specimens, and 5, 10 and 15% of

(a) Control specimen

(b) Specimen with 15% CTR

Figure 2. The appearance of samples after 28 days of exposure to HCl
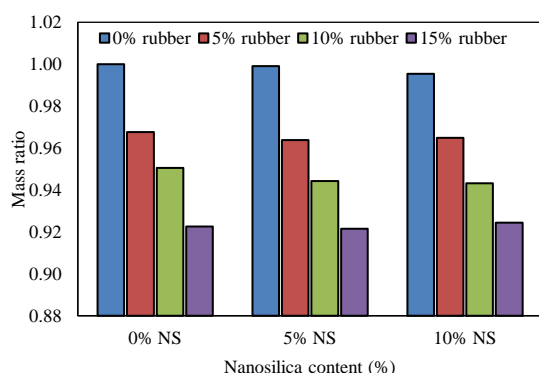
Figure 3. Mass ratio of water-cured specimens containing CTR and NS at 28 days
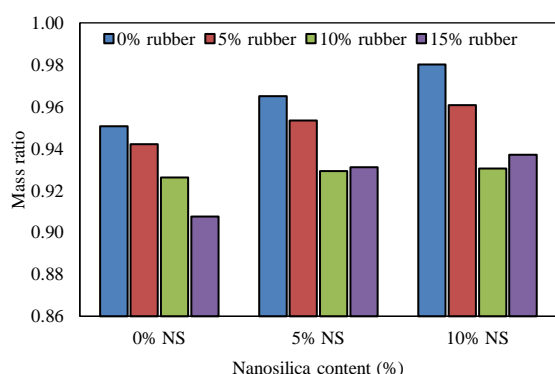
Figure 4. Mass ratio of specimens containing CTR and NS exposed to HCl at 28 days
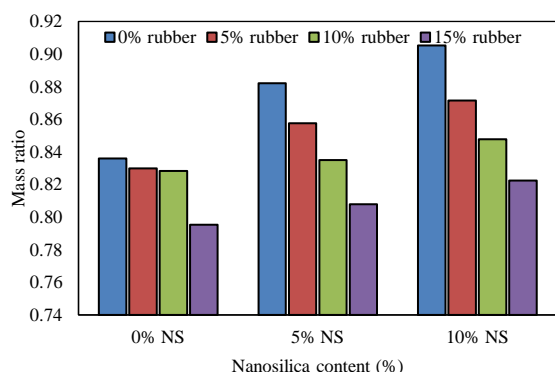
Figure 5. Mass ratio of specimens containing CTR and NS exposed to HCl at 90 days

the CTR has reduced the weight ratio to 0.97, 0.95, and 0.92 at the age of 28 days. As can be seen in Figure 4, for HCl exposure, the mass ratio for the T0N0 specimen reached 0.95 at 28 days, which means a 5% mass reduction of the control sample in an acidic environment. By adding 5 and 10% NS, the mass ratio has reached 0.96 and 0.98, which shows the positive effect of NS on weight loss values. For specimens with CTR in acidic

conditions, less amount of mass loss was observed. The reason for this is that the CTR particles prevent peeling off the corroded outer layer and consequently prevent the spread of acid attack in the depth of the specimen .

As the age of the samples increased to 90 days, a greater decrease in the mass of the samples occurred; For the T0N0 sample, the mass ratio was reached 0.84 and for the T0N5 and T0N10 samples, the mass ratio has reached 0.88 and 0.91, respectively. At this age, due to the development of pozzolanic reactions, the effect of NS was more than specimens with 28 days' age. The positive effect of pozzolanic materials such as NS in reducing the effect of acid attack, especially mass loss of concrete due to HCl is comply to the results of most previous researchers. Goyal et al. [39] reported an approximately 13% reduction in the mass of the control sample exposed to 1% HCl and 8% reduction for concrete containing silica fume.

Figure 6 shows the effect of CTR and curing conditions on compressive strength at 28 and 90 days of age. To evaluate the strength ratio, the compressive strength of each specimen was divided by the compressive strength of the 28-day water-cured control specimen (without CTR and NS). From the results, it is clear that the strength ratio for specimens containing 5%, 10%, and 15% of the CTR under standard curing conditions was 0.94, 0.85 and 0.67, respectively. Exposure to HCl has caused these strength ratios reach 0.90, 0.81 and 0.58, respectively, which indicates the greater effect of acidic conditions on compressive strength with increasing CTR content of concrete. The reduction in compressive strength of the specimen without CTR with HCl exposure at 28 days of age was approximately 3%. As the age of the concrete increased to 90 days, the effect of HCl on the specimens increased. The sample containing 15% of CTR had a strength ratio of 45%. To understand how much of this reduction was due to the effect of the acid attack, the strength ratio of this sample in water-curing conditions should be considered. At the age of 90 days, the effect of acid attack
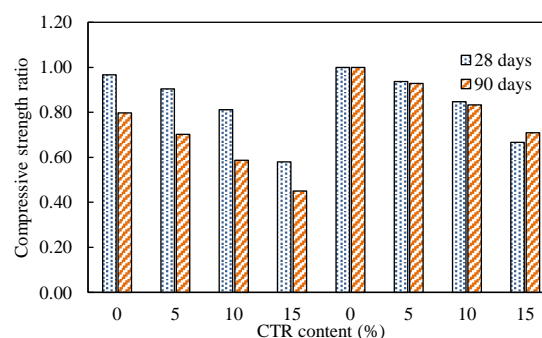
Figure 6. Strength ratio of specimens without NS at 28 and 90 days

has increased with increasing the percentage of CTR; for specimens containing 5%, 10% and 15% of CTR, the difference in resistance compared to water curing condition has reached to 23%, 25% and 27%, respectively.

The compressive strength of all specimens at age 28 days is illustrated in Figure7. Figures 8 and 9 show the
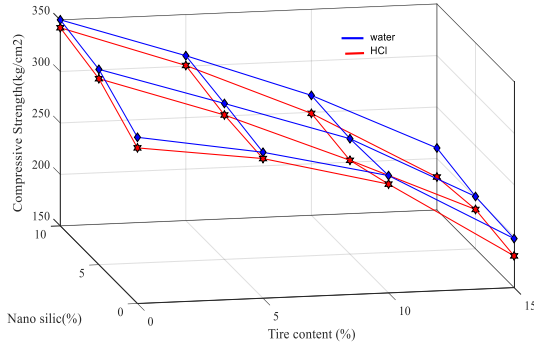
Figure 7. The compressive strength of the specimens at 28 days
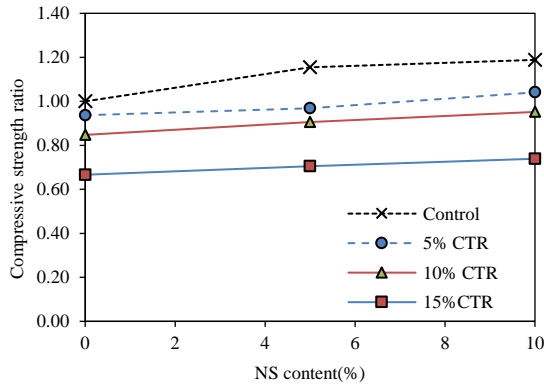
Figure 8. The compressive strength ratio based on CTR content and NS of water-cured specimens at 28 days
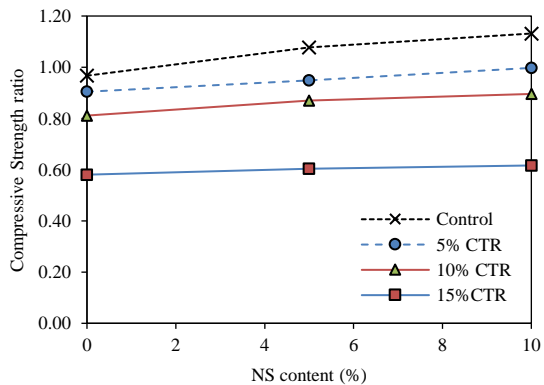
Figure 9. The compressive strength ratio based on CTR content and NS for HCl exposure conditions at 28 days

compressive strength ratio of the samples at 28 days for standard curing and exposure to HCl. The addition of NS in both conditions has improved the compressive strength. The compressive strength ratio for samples without CTR has reached 1.2 times that of the control sample by adding 10% NS at the age of 28 days. As can be seen from Figure 8 for the specimen, with 15% CTR, the strength ratio has increased from 0.67 to 0.74 with the addition of 10% NS. In any case, the addition of NS has improved the compressive strength, but the amount of this increase was less than the samples without CTR. In the case of exposure to hydrochloric acid, samples containing NS have reported more compressive strength, but with increasing the percentage of CTR, the effect of NS has been less.

As can be seen from Figure 10, with increasing the age of the samples to 90 days, the compressive strength of the T0N10 increased up to 20% compared to the control specimen at the same age. The compressive strength for this specimen, when exposed to HCl, was approximately equal to that of the Nano-free sample that was cured in water. T0N0 had a strength ratio of 0.8 and T0N10 had a strength ratio of 1.02, which shows the great effect of NS on improving the strength of samples exposed to HCl. In samples containing sub-tires at this age, the effect of adding NS was also positive, so that the strength ratio for samples containing 15% CTR increased by adding 10% NS from 0.45 to 0.57.

The effect of acids attack on concrete includes the dissolution of cement hydrates and calcium hydroxide and the formation of calcium salts [43]. HCl usually reacts with CH and has less effect on C-S-H. The resulting products react with calcium aluminate (C3A) in cement [44].

$$2HCl + Ca(OH)_2 \rightarrow CaCl_2 + 2H_2O \qquad (1)$$

$$CaCl_2 + CaO.Al_2O_3 + 10H_2O \\ \rightarrow 3CaO.Al_2O_3.CaCl_2.10H_2O \qquad (2)$$
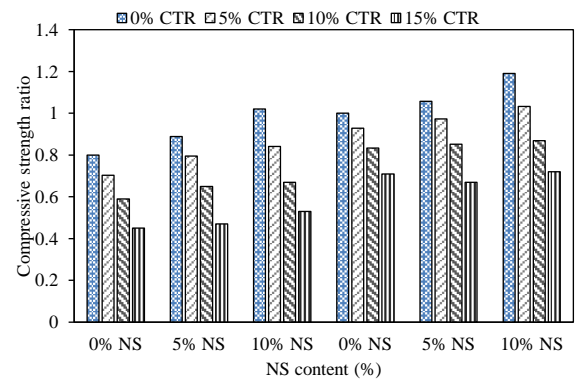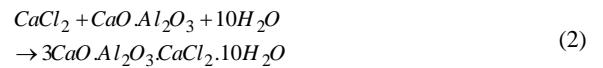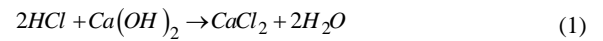
Figure 10. The compressive strength ratio based on CTR content and NS for HCl exposure conditions at 90 days

Products due to the effect of HCl on concrete include the formation of soluble and insoluble salts [9]. As shown in the reaction above, $CaCl_2$ is a water-soluble salt, and if, as in this experiment, the effect of acid on concrete was superficial, most of this salt will dissolve in water. Insoluble salts can reduce the permeability.

Concrete containing NS has a uniform and compact structure that reduces the permeability and increases the durability of concrete [45]. Due to their small size, NS fine particles play the role of filling effect well and therefore have a good effect in reducing permeability [43, 46]. The filler properties of nanoparticles also increase the strength of the final concrete structure. Pozzolanic reactions mostly involve the reaction of free hydrocalcium or CH, which is a hydration product, with NS [47]. These reactions result in the formation of C-S-H, which is a stronger substance in the concrete structure.

4. CONCLUSIONS

In this study, the effects of hydrochloric acid attack on the compressive strength and mass reduction of rubberized concrete with up to 15% of CTR were investigated, and based on the test results, the following conclusions can be drawn:

-Increasing the percentage of CTR increases the detrimental effects of hydrochloric acid on the compressive strength of the rubberized concrete so that for concrete with 15% CTR, the compressive strength at the age of 28 days is 10% and at the age of 90 days 26% less than concrete with the same percentage of CTR and cured with tap water.

- By increasing the percentage of crumbs, the effect of acid on weight loss is improved; The sample containing 15% of the tire had only 1.5% and the concrete without the CTR had 5% mass loss in 28 days compared to the equivalent sample cured in standard conditions.

- Adding NS improves compressive strength and decreases the samples' mass loss in aggressive environmental conditions containing HCl acid. Under hydrochloric acid attack conditions, the effect of NS on compressive strength is greater than mass loss such that for concrete, without CTR, up to 20% improves the strength of samples exposed to HCl.

- As a suggestion, concrete containing crumbed tire rubbers and also NS can be used in the flooring of industrial and laboratory environments containing hydrochloric acid.

5. ACKNOWLEDGMENTS

6. REFERENCES

1. Huo, R., Li, S. and Ding, Y., "Experimental study on physicochemical and mechanical properties of mortar subjected to acid corrosion", *Advances in Materials Science and Engineering*, Vol. 2018, Article ID 3283907, (2018). https://doi.org/10.1155/2018/3283907

2. Duchesne, J. and Bertron, A., Leaching of cementitious materials by pure water and strong acids (hcl and hno 3), in Performance of cement-based materials in aggressive aqueous environments. 2013, Springer.91-112. https://doi.org/10.1617/s11527-014-0433-1

3. Lavigne, M.P., Bertron, A., Botanch, C., Auer, L., Hernandez-Raquet, G., Cockx, A., Foussard, J.-N., Escadeillas, G. and Paul, E., "Innovative approach to simulating the biodeterioration of industrial cementitious products in sewer environment. Part ii: Validation on cac and bfsc linings", *Cement and Concrete Research*, Vol. 79, (2016), 409-418. https://doi.org/10.1016/j.cemconres.2015.10.002

4. O'Connell, M., McNally, C. and Richardson, M.G., "Performance of concrete incorporating ggbs in aggressive wastewater environments", *Construction and Building Materials*, Vol. 27, No. 1, (2012), 368-374. https://doi.org/10.1016/j.conbuildmat.2011.07.036

5. Hosseini, S.A. and Bagheri, M., "The effect of sulfuric acid on the strength and durability of concrete containing waste tire crumbs", *Journal of Structural and Construction Engineering*, Vol. 9, No. 7, (2022), 27-39. https://doi.org/10.22065/jsce.2021.298577.2605

6. Mehta, P.K., "Durability of concrete--fifty years of progress?", *Special Publication*, Vol. 126, No., (1991), 1-32. https://doi.org/10.14359/1998

7. Grandclerc, A., Dangla, P., Gueguen-Minerbe, M. and Chaussadent, T., "Modelling of the sulfuric acid attack on different types of cementitious materials", *Cement and Concrete Research*, Vol. 105, (2018), 126-133. https://doi.org/10.1016/j.cemconres.2018.01.014

8. Kumar, l.R., Roger, Q., Santhosh, P., Gowtham, K. and Rajan, E.D.J., "Durability study of concrete using nano-silica", *International Journal of Advanced Research in Civil,Structural,Environmental and Infrastructure Engineering and Developing*, Vol. 2, No. 2, (2016), 155-164

9. Chandra, S., "Hydrochloric acid attack on cement mortar—an analytical study", *Cement and Concrete Research*, Vol. 18, No. 2, (1988), 193-203. https://doi.org/10.1016/0008-8846(88)90004-x

10. Ferdous, W., Manalo, A., Siddique, R., Mendis, P., Zhuge, Y., Wong, H.S., Lokuge, W., Aravinthan, T. and Schubel, P., "Recycling of landfill wastes (tyres, plastics and glass) in construction – a review on global waste generation, performance, application and future opportunities", *Resources, Conservation and Recycling*, Vol. 173, (2021), 105745. https://doi.org/10.1016/j.resconrec.2021.105745

11. Nikkhah, H., Tavakoli, H.R. and Fallah, N., "Experimental investigation of the effects of using waste rubber ash on mechanical properties of plain concrete", *International Journal of Engineering, Transactions C: Aspects*, Vol. 36, No. 3, (2023), 450-456. https://doi.org/10.5829/ije.2023.36.03c.03

12. Hosseini, S.A., Moosavinezhad, S.A.H. and Behshad, A., "Effect of curing in acidic environments on the strength and permeability of concrete containing nano-silica and rubber", *Asas Journal*, Vol. 21, No. 57, (2020), 72-81

13. AbdelAleem, B.H. and Hassan, A.A., "Influence of rubber content on enhancing the structural behaviour of beam–column

joints", *Magazine of Concrete Research*,   Vol. 70, No. 19, (2018), 984-996. https://doi.org/10.1680/jmacr.17.00323

14. Marques, A.C., Akasaki, J., Trigo, A.M. and Marques, M., "Influence of the surface treatment of tire rubber residues added in mortars", *Revista IBRACON de Estruturas e Materiais*, Vol. 1, No. 2, (2008), 113-120. https://doi.org/10.1590/s1983-41952008000200001

15. Al-Tayeb, M.M., Bakar, B.A., Ismail, H. and Akil, H.M., "Effect of partial replacement of sand by fine crumb rubber on impact load behavior of concrete beam: Experiment and nonlinear dynamic analysis", *Materials and Structures*, Vol. 46, No. 8, (2013), 1299-1307. https://doi.org/10.1617/s11527-012-9974-3

16. Holmes, N., Dunne, K. and O'Donnell, J., "Longitudinal shear resistance of composite slabs containing crumb rubber in concrete toppings", *Construction and Building Materials*, Vol. 55, No., (2014),   365-378. https://doi.org/10.1016/j.conbuildmat.2014.01.046

17. Pham, T.M., Zhang, X., Elchalakani, M., Karrech, A., Hao, H. and Ryan, A., "Dynamic response of rubberized concrete columns with and without frp confinement subjected to lateral impact", *Construction and Building Materials*, Vol. 186, (2018), 207-218. https://doi.org/10.1016/j.conbuildmat.2018.07.146

18. Luhar, S., Chaudhary, S. and Luhar, I., "Development of rubberized geopolymer concrete: Strength and durability studies", *Construction and Building Materials*, Vol. 204, (2019), 740-753. https://doi.org/10.1016/j.conbuildmat.2019.01.185

19. Hassanli, R., Youssf, O. and Mills, J.E., "Experimental investigations of reinforced rubberized concrete structural members", *Journal of Building Engineering*, Vol. 10, (2017), 149-165. https://doi.org/10.1016/j.jobe.2017.03.006

20. Segre, N., Joekes, I., Galves, A. and Rodrigues, J., "Rubber-mortar composites: Effect of composition on properties", *Journal of Materials Science*, Vol. 39, No. 10, (2004), 3319-3327. https://doi.org/10.1023/b:jmsc.0000026932.06653.de

21. Rashad, A.M., "A comprehensive overview about recycling rubber as fine aggregate replacement in traditional cementitious materials", *International Journal of Sustainable Built Environment*, Vol. 5, No. 1, (2016), 46-82. https://doi.org/10.1016/j.ijsbe.2015.11.003

22. Ganesan, N., Raj, J.B. and Shashikala, A., "Flexural fatigue behavior of self compacting rubberized concrete", *Construction and Building Materials*, Vol. 44, (2013), 7-14. https://doi.org/10.1016/j.conbuildmat.2013.02.077

23. Shahini, A., Yaghobi, S.M. and Janfeshan, A.H., "Sulfuric acid effect on the mechanical properties of concrete containing crumb tires and pet", *Amirkabir Journal of Civil Engineering*, Vol. 50, No.   1,   (2018),   111-120. https://doi.org/10.22060/ceej.2017.11573.5036

24. Avzedo, F., Pacheco-Torgel, F., Jesus, C., Barroso de Aguiar, J.L. and Camoes, A.F., "Properties and durability of hpc with tyre rubber wastes", *Construction and Building Materials*, Vol. 34, (2012),   186-191. https://doi.org/10.1016/j.conbuildmat.2012.02.062

25. Pedro, D., De Brito, J. and Veiga, R., "Mortars made with fine granulate from shredded tires", *Journal of Materials in Civil Engineering*, Vol. 25, No. 4, (2012), 519-529. https://doi.org/10.1061/(asce)mt.1943-5533.0000606

26. Gesoğlu, M., Güneyisi, E., Khoshnaw, G. and İpek, S., "Investigating properties of pervious concretes containing waste tire rubbers", *Construction and Building Materials*, Vol. 63, (2014),   206-213. https://doi.org/10.1016/j.conbuildmat.2014.04.046

27. Hilal, A.A., "Effect of crumb tyres rubber on some properties of foamed concrete", *Anbar Journal for Engineering Sciences*, Vol.   4,   No.   2,   (2011),   1-17. https://doi.org/10.37649/aengs.2011.40699

28. Hendi, A., Rahmani, H., Mostofinejad, D., Tavakolinia, A. and Khosravi, M., "Simultaneous effects of microsilica and nanosilica on self-consolidating concrete in a sulfuric acid medium", *Construction and Building Materials*, Vol. 152, (2017), 192-205. https://doi.org/10.1016/j.conbuildmat.2017.06.165

29. Borzouyi Kutenayi, S., Kiahosseini, S.R. and Talebpour, M.H., "The effect of caspian sea water on corrosion resistance and compressive strength of reinforced concrete containing different sio2 pozzolan", *International Journal of EngineeringTransactions A: Basics*, Vol. 30, No. 10, (2017), 1464-1470. https://doi.org/10.5829/ije.2017.30.10a.06

30. Atewi, Y.R., Hasan, M.F. and Güneyisi, E., "Fracture and permeability properties of glass fiber reinforced self-compacting concrete with and without nanosilica", *Construction and Building Materials*,   Vol. 226, (2019), 993-1005. https://doi.org/10.1016/j.conbuildmat.2019.08.029

31. Sobolev, K., Flores, I., Torres-Martinez, L., Valdez, P., Zarazua, E. and Cuellar, E., Engineering of sio 2 nanoparticles for optimal performance in nano cement-based materials, in Nanotechnology in   construction   3.   2009,   Springer.139-148. https://doi.org/10.1007/978-3-642-00980-8_18

32. Li, H., Xiao, H.-g. and Yuan, J., "Ou., jinping," microstructure of cement mortar with nano particles", *Composites: Part B*, Vol. 35, No.,   (2004),   185-189.   https://doi.org/10.1016/s1359-8368(03)00052-0

33. Maghsoudi, A., Soheil, M. and Darbhenz, A., "Effect of the nano particles in the new generation of concretes, scc", *International Journal of Nanoscience and Nanotechnology*, Vol. 6, No. 3, (2010), 137-143

34. Zivica, V.r. and Bajza, A., "Acidic attack of cement based materials—a review.: Part 1. Principle of acidic attack", *Construction and Building Materials*, Vol. 15, No. 8, (2001), 331-340. https://doi.org/10.1016/s0950-0618(01)00012-5

35. Youssf, O., ElGawady, M.A. and Mills, J.E., "Experimental investigation of crumb rubber concrete columns under seismic loading", in Structures, Elsevier. Vol. 3, (2015), 13-27. https://doi.org/10.1016/j.istruc.2015.02.005

36. ASTM, *Standard specification for portland cement,astm c150*. 2017, ASTM: West Conshohocken, PA:

37. ASTM, *Astm c1602/c1602m-12: Standard specific cation for mixing water used in the production of hydraulic cement concrete*. 2018, ASTM International West Conshohocken, PA, USA

38. ASTM, *Astm c33/c33m:Standard specification for concrete aggregates*. 2018, ASTM international West Conshohocken, PA

39. Goyal, S., Kumar, M., Sidhu, D.S. and Bhattacharjee, B., "Resistance of mineral admixture concrete to acid attack", *Journal of Advanced Concrete Technology*, Vol. 7, No. 2, (2009), 273-283. https://doi.org/10.3151/jact.7.273

40. ASTM, *Astm c192/c192m: Standard practice for making and curing concrete test specimens in the laboratory*. 2018, West Conshohocken, PA: ASTM International

41. ASTM, I., "Astm c642: Standard test method for density, absorption, and voids in hardened concrete, ASTM Philadelphia^ ePA PA. (2001),

42. De Ceukelaire, L., "The effects of hydrochloric acid on mortar", *Cement and Concrete Research*, Vol. 22, No. 5, (1992), 903-914. https://doi.org/10.1016/0008-8846(92)90114-b

43. Diab, A.M., Elyamany, H.E., Abd Elmoaty, M. and Sreh, M.M., "Effect of nanomaterials additives on performance of concrete resistance against magnesium sulfate and acids", *Construction and Building Materials*, Vol. 210, (2019), 210-231. https://doi.org/10.1016/j.conbuildmat.2019.03.099

44. Monteny, J., Vincke, E., Beeldens, A., De Belie, N., Taerwe, L., Van Gemert, D. and Verstraete, W., "Chemical, microbiological, and in situ test methods for biogenic sulfuric acid corrosion of

concrete", ***Cement and Concrete Research***, Vol. 30, No. 4, (2000), 623-634. https://doi.org/10.1016/s0008-8846(00)00219-2

45. Ozyildirim, H.C. and Zegetosky, C., *Laboratory investigation of nanomaterials to improve the permeability and strength of concrete*. 2010, Virginia Transportation Research Council

46. Norhasri, M.M., Hamidah, M. and Fadzil, A.M., "Applications of using nano material in concrete: A review", ***Construction and Building Materials***, Vol. 133, (2017), 91-97. https://doi.org/10.1016/j.conbuildmat.2016.12.005

47. Emerson, M., "Mechanisms of water absorption by concrete. Protection of concrete. Proceedings of the international conference held at the university of dundee, september 11-13, 1990", ***Publication of: E and F Spon Limited***, (1990). https://doi.org/10.1201/9781482267037-214

Persian Abstract

چکیده

قرارگیری بتن در محیط‌های اسیدی موجب کاهش خواص مکانیکی و همچنین خواص مرتبط با دوام بتن می‌شود. در این مقاله اثر قرارگیری بتن حاوی خرده تایر در شرایط محیطی خورنده حاوی اسید هیدروکلریدریک مورد مطالعه قرارگرفته است. بدین منظور در طرح اختلاط‌های مختلف، مقدار ۵، ۱۰ و ۱۵ درصد از ریزدانه بتن با خرده تایر جایگزین شده و بعد از ۷ روز عمل آوری در شرایط استاندارد و رسیدن به ۷۰ درصد مقاومت طرح، نمونه‌ها در محیط حاوی ۲ درصد اسید هیدروکلریدریک قرار داده شدند. در برخی از نمونه‌ها برای بررسی اثر نانو سیلیس بر مقاومت بتن در برابر اسید، مقدار ۵ و ۱۰ درصد سیمان با ژل نانو سیلیس جایگزین گردید. بعد از ۲۸ و ۹۰ روز قرار گیری در شرایط اسیدی، مقاومت فشاری و کاهش وزن نمونه‌ها مورد بررسی قرار گرفت. نتایج نشان داد که در نمونه‌های با خرده تایر بیشتر، اثرات کاهشی اسید هیدروکلریدریک بیشتر بوده است. بر اساس نتایج بدست آمده همچنین مشخص شد که مقدار خوردگی (کاهش وزن نمونه‌ها) با افزایش درصد خرده تایر بهبود یافته است به طوریکه نمونه حاوی ۱۵ درصد خرده تایر تا ۷ درصد کاهش وزن کمتری نسبت به نمونه شاهد داشته است.

International Journal of Engineering

Study on Application of Arps Decline Curves for Gas Production Forecasting in Senegal

A. Dieng, V. V. Poplygin*

Department of Oil and Gas Technologies, Perm National Research Polytechnic University (PNRPU), Russia

P A P E R   I N F O

A B S T R A C T

The purpose of this study is to evaluate the feasibility of using methods for predicting the flow rates of gas wells in fields in Senegal. Accurate forecasting of natural gas production allows you to correctly set the operating mode of wells and design onshore infrastructure. One of the gas fields of Senegal was chosen as the object of study, where deposits were discovered within the exploitation perimeters in the Campanian and Santonian sandstone horizons. Gas formations have high porosity and permeability values, as well as high formation temperatures. Gas well flow rates can be predicted using hydrodynamic models, mathematical models (hyperbolic, etc.) and other methods. This study assessed the possibility of using Arps curves for long-term forecasting of gas flow rate and comparing the forecasting results with actual data. Comparison of Arps curves and actual gas flow rates for wells made it possible to note a discrepancy in the forecast results and actual values of more than 20%. These differences arose for two reasons. Deviations at the initial stage of well operation (6 months), which is associated with the adjustment of the technological operating mode of the well and the establishment of constant parameters of rocks near the wellbore. The second reason is well repairs, which change the properties of rocks near the wellbore. In general, Arps curves of exponential type showed high convergence between predicted and actual values, which makes it possible to use them in predicting the flow rate of gas wells in Senegal.

doi: 10.5829/ije.2023.36.12c.10

NOMENCLATURE

K	permeability		SW	water saturation
Φ	porosity		q (t)	gas flow rate at time t
t	time, days or month		qi	initial gas flow rate at time to
b	the Arps decline curve exponent		Di	the initial decline rate, 1/day
G_P	gas rate-cumulative production			

1. INTRODUCTION

One of the most difficult tasks of gas production engineers is to accurately predict production, which is necessary for proper investment planning [1, 2]. The largest natural gas deposits are concentrated in the Middle East, Russia and Africa. Natural gas reserves are found in sandstones and limestones. Currently, dense gas deposits are also being actively introduced into development [3, 4], for such fields, the issues of forecasting gas production are relevant [5, 6]. Natural gas production plays a major role in the global energy system. In addition to energy, natural gas is actively used as a raw material for the production of chemicals, polymers, as well as by the population for heating housing [7, 8]. Forecasting the dynamics of production plays an important role in the process of creating infrastructure and evaluating options for the development of natural gas deposits [9]. A predictive method, such as decline curve analysis, cannot be applied before the wells are put into operation because it depends heavily on historical production to estimate parameters. For this purpose, a reliable method called drop curve analysis is used to compare the flow rate related to an individual and

*Corresponding Author Institutional Email: poplygin@bk.ru
(V. V. Poplygin)

a group of wells or reservoirs using a mathematical function to predict productivity by extrapolating the drop function [10, 11]. A combined method for analyzing the characteristics of the fall of a multi-barrel horizontal well in shale gas reservoirs has been developed. They came to the conclusion that the composite model developed by them can give some idea of the mechanism of fluid movement in gas reservoirs and help analyze the decrease in productivity of such wells and reservoirs. A significant part of the models used to predict the gas well performance of the dip curve analysis models is based on the Arps equation models [12].

The Arps method was not originally intended to predict gas production [13]. There are several fall curve analysis models used for gas wells, including exponential fall, hyperbolic fall, harmonic fall [14], Duong model, Fetkovich analysis [15]. Comparison of typical curves is, in fact, a graphical method of visual comparison of production data using pre-constructed curves on a logging log.

Ultimately, the choice of the model depends on the specific characteristics of the gas well. Khanamiri [10] developed a method for forecasting production for oil and gas reservoirs based on the change in time and flow rate. The results showed that the output data of the oil reservoir model is the same as the results obtained using the hyperbolic equation, and moreover, the output data of the gas reservoir model is reliable compared to the Arps method.

It is shown by Can and Kabir [16] that the Arps method provides the smallest average error among the six methods for field data. Wells in the reservoir vault that have the highest reservoir capacity and have high b-factors, while wells in the periphery have low b-factors due to a thinner productive reservoir [17].

The Arps method can take into account the stratification of the formation, the properties of fluids, etc. Cheng et al. [18] proposed a diagnosis of the contribution of other layers. Ayala [19] also proposed methods for processing gas properties depending on pressure.

The data presented in the studies allows us to conclude that the use of gas production forecasting methods should be checked and tested in specific geological conditions. The purpose of this study is to examine the applicability of standard curves that can quantify the Arps b-factor for one of the gas fields of Senegal, revealing gas reservoirs along the production perimeter in the Campanian and Santonian sandstone horizons. To achieve the objectives of the study, a comparison was made of gas production forecasts using the Arps model with various values of the b factor and natural gas production from a real well. Finally, an analysis of the reasons for the deviation of the forecast and production data from a real well was performed and

the conditions for the practical application of the models were determined.

2. OVERVIEW OF THE STUDY AREA

The study of the field area is located in the western part of Senegal between the administrative regions of Dakar in the West and that of Thiès in the East. It represents Figure 1. The most explored area of Senegal and is of great interest to the country, for which it currently produces most of the hydrocarbons.

The study area is located with the deferred logging data from the fields wells, a geological model of the deposit showing the geometry and expansion of the natural gas producing horizons, which materialized by sand lenses with an average thickness of 20 m and are more pronounced in the north-east for the Santonian reservoir whereas the Campanian reservoir are more important in the west of the field with an average thickness of 6 m [20, 21]. The creation of the National Petroleum Company in 1981 led to the discovery of new natural gas and oil deposits exploited between 1986 and 2000 in the area of the southern block: approximately 218,000,000 Nm^3 were produced. In 1997, the national company discovered a new natural gas deposit with the drilling well. Since then, oil activity has experienced considerable growth, thanks in particular to the arrival of the American company which in synergy with the national company, will develop this deposit with the wells from W-1 to W-6., to this study using W-3 data to analyze the decline curve between the production flow, cumulative rate and the time. The annual cumulative production of W-3 from 2008 to 2012 is 1110 MMscf.

Using the petrophysicals characteristics represented by the model of porosity, saturation and permeability, we find that the East zone in Campanian and the West and

study area

Figure 1. Location of the study area

South - East zone in Santonian would be the most productive areas of the sector because of their porosity ($20\% \leq \Phi \leq 28\%$) and permeability (5 mD $\leq$ K $\leq$ 10mD), and their low water saturation ($30\% \leq SW \leq 50\%$). The characteristics of the reservoir parameters are shown in Table 1. In addition, the gas properties are stated in Table 2.

3. CURVE ANALYSIS METHODS

The possibility of using semi-analytical solutions and reduction curves to predict natural gas production on the example of a field in Senegal has been investigated.

Drop curves can be used as a direct and consistent approach to analysis. Analysis of the drop curve is much easier to perform than hydrodynamic modeling and there is no need to monitor the value of reservoir pressure, which greatly simplifies the forecasting process.

When analyzing the drop curves, I have analyzed both the accumulated gas production indicators and the flow rates of gas wells per day or month by changing the time scale in logarithmic coordinates. Based on the dynamics

TABLE 1. Characteristics of the Campanian production reservoir of W-3 gas well

General Formation Data	Values	
Top Gross Pay	4538.4 ft	1383.3 m
Bottom Gross pay	4564 ft	1391.1 m
Porosity	23.4 %	23.4 %
Initial Water Saturation	30 %	30 %
Initial Reservoir Pressure	196.3 psi	13534.4 KPa
Reservoir Temperature	154, °F	67.8°C
Compressibility Factor	0.8779	0.8779
Productive Area	158 acres	64 ha
Net Pay	6.9 ft	2.1 m
Initial Raw GIP	1.005, Bcf	28327, 10^6 m³
Recovery Factor	85 %	85 %
Initial Raw Recoverable	0.855 Bcf	24078,10^6 m³
Marketable Reserves	0.769 Bcf	21670,10^6 m³

TABLE 2. Gas properties of W-3 well

Data	Values
Gas Gravity	0.581
N_2 Concentration	0.140 %
CO_2 Concentration	0.150 %
Critical Pressure	4638 kPa
Critical temperature	196.8 K

of the actual flow rates of gas wells, a theoretical model is selected to predict the flow rate of gas wells for the future by extrapolation.

By using injection flows from the reservoir into the well for gas wells, the permeability or hydroconductivity of the reservoir can be obtained.

The theoretical foundations for forecasting gas well flow rates were laid at the beginning of the twentieth century. In 1921, the main results of that time were published in the Manual for the Oil and Gas Industry [22].

Further, the mathematical apparatus used to predict oil production was developed [23], and probably the most significant contribution to the development of the modern concept of the analysis of the decline curve is the classic article by Arps [11], written in 1944. In this work, a significant number of exponential and hyperbolic equations are proposed for the analysis of well production. It should be borne in mind that the functions were obtained experimentally, not mathematically. The good convergence of the predicted and actual results has led to the constant use of the "Arps equations".

The main types of gas production reduction curves are presented in the following ratios [11, 24]:

$$\frac{q(t)}{q_i} = \frac{1}{[1+bD_it]^{\frac{1}{b}}} \tag{1}$$

For b = 0 we can get the exponential reduction equation from the Equation (1):

$$\frac{q(t)}{q_i} = \frac{1}{(D_it)} \tag{2}$$

The rate-cumulative production relationship is:

$$G_P = \int_{t_1}^{t_2} q_t dt \tag{3}$$

Replacing the q_t flow rate in the above equation with three separate expressions describing the types of reduction curves, and integrating gives the following equation:

$$G_{P(t)} = \frac{q_i - q_t}{(D_i)} \tag{4}$$

For gas wells, there is a qualitative forecasting of well flow rates for a month from time to time or from secured gas production (Figure 2).

By extrapolating the production values in a gas well, we can determine the time of its cost-effective operation and the final production values.

Degree b must be selected at the stage of selecting a model to predict the flow rate of the well. At 0 <b <1, we get a hyperbolic equation as in Equation (2).

As for the hyperbolic logarithm of the decline (q) as a function of time, it is no longer a straight line on the semi-logarithm, as shown in Figure 3.

For the accumulated gas production from time, we can obtain the following function based on the Equation (2):

Figure 2. Exponential decline curve. (a) Rate-time curve; (b) Rate cumulative production curve

Figure 3. Hyperbolic decline curve. (a) rate-time curve; (b) Rate cumulative production

$$G_{P(t)} = \left[\frac{q_i}{D_i(1-b)}\right]\left[1 - \left(\frac{q_t}{q_i}\right)^{1-b}\right] \qquad (5)$$

In Equation (1), b = 1 corresponds to the harmonic decay and taking into account the following equation:

$$\frac{q(t)}{q_i} = \frac{1}{[1+bD_i t]} \qquad (6)$$

If Equation (6) is integrated, the cumulative ratio of production to time over a period of time can be obtained and determined as follows:

$$G_{P(t)} = \left[\frac{q_i}{D_i(1-b)}\right]\left[1 - \left(\frac{q_t}{q_i}\right)^{1-b}\right] \qquad (7)$$

The inverse dependence of the harmonic decay rate $1/q$ on time is linear, and the cumulative dependence on the $\log(q)$ (Figure 4).

4. DISCUSSION

From Figure 5 it can be seen that an increase in the value of b leads to a greater decrease in the predicted flow rates

of gas wells. With this, the harmonic decay is the fastest and the exponential decay is the slowest. For the considered reservoirs, the harmonic decay shows good convergence of the results. As shown in Figure 5, the deviation of the values calculated by the formula and the actual data in the first 25 months of forecasting was revealed. This is due to the establishment of the operating mode and optimization of well flow rates. Starting from the 25th month, the exponential Arps equation most accurately predicts the flow rate of a gas well in hyperbolic form. If 6 months of data is used for matching, excellent fit curves can be obtained, but there will be significant deviations in predicting the cumulative production trend. These phenomena are associated with well workovers and frequent shutdowns. Therefore, when the Arps method is used for analysis, the natural gas production time must be significant and must be sufficiently long. Using similar models by Guzev et al. [25], the error did not exceed 5%.

The studied equations take into account the state of rocks near the borehole wall in the initial state. During the operation of a well, various phenomena can occur in the reservoir that change the permeability [26-28].

$$q = 28/(1+0.0045t)$$

(a)

$$q = -0.0008Gp + 24.888$$

(b)
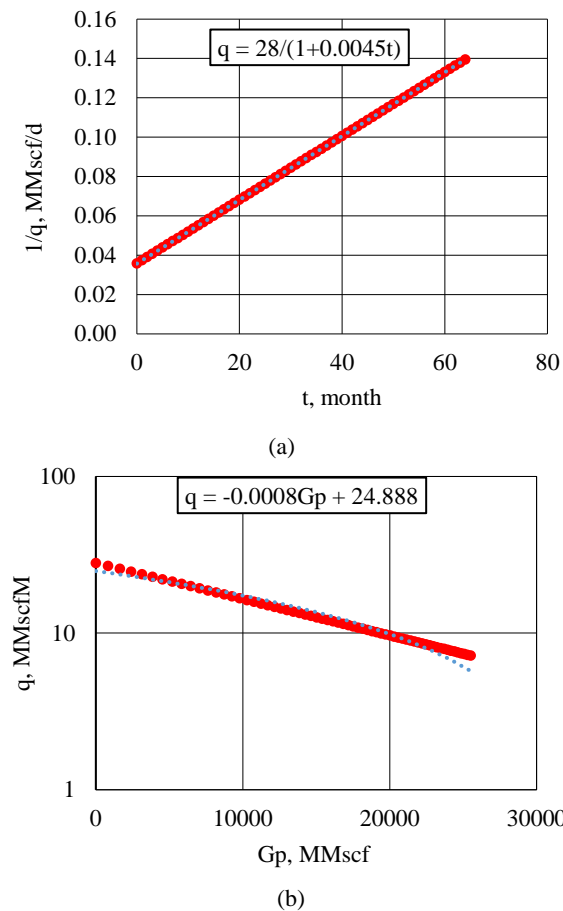
Figure 4. Harmonic decline curves. (a) Rate-time curve; (b) Rate-cumulative production curve

(a)

(b)

Figure 5. Arps decline curve shapes for a Cartesian rate-time (a) and cumulative-time (b) plot

The change in permeability in the initial period is associated with a decrease in pressure in the reservoir and rock deformations [29, 30]. If the field is large in area and has large reserves, then changes in permeability can lead to a significant deterioration in production [31] For more accurate forecasting of the natural gas flow rate, it is necessary to introduce refinements with the dependence of permeability on effective stresses. We state that there are significant changes in well operation and workovers associated with abrupt changes in gas production and the impossibility of using the Arps equation for wells W-3.

For wells without workovers, the equations make it possible to predict gas production with high accuracy (Figure 6). The greatest deviations occur in the first months of well operation, associated with the setting of the operating mode and the establishment of equilibrium conditions in the wellbore formation zone.

It was identifying some potential problems with Arps models: Arps models require accurate, reliable and sufficient input data to be effective. In some cases, the data may be incomplete, inaccurate or not adequately representative of the system. This can result in inaccurate projections and predictions. Arps models tend to be rigid and inflexible, meaning they may not be able to account for changes or new variables in the system. Arps models are based on certain assumptions and simplifications about the system being modeled. Assumptions about market behavior, for example, may not hold true in reality, or may change over time. Simplifications, such as aggregating data or assuming linear relationships, can also lead to inaccurate results. Inability to capture all factors: Arps models can only capture the factors that are included in the model. This means that some external factors or variables that may impact the system may not be accounted for, leading to incomplete or inaccurate predictions. But in gas wells, as a rule, the flow rate of wells monotony decreases and these models can show a good result. Deviations from the design parameters may occur during emergency situations at wells and well repairs. The results of a single well analysis can be combined to characterize the performance of the field. Future natural gas production can be predicted using a hyperbolic type curve. The operation of wells with a very short production history can be modeled using well data and similar geological parameters.
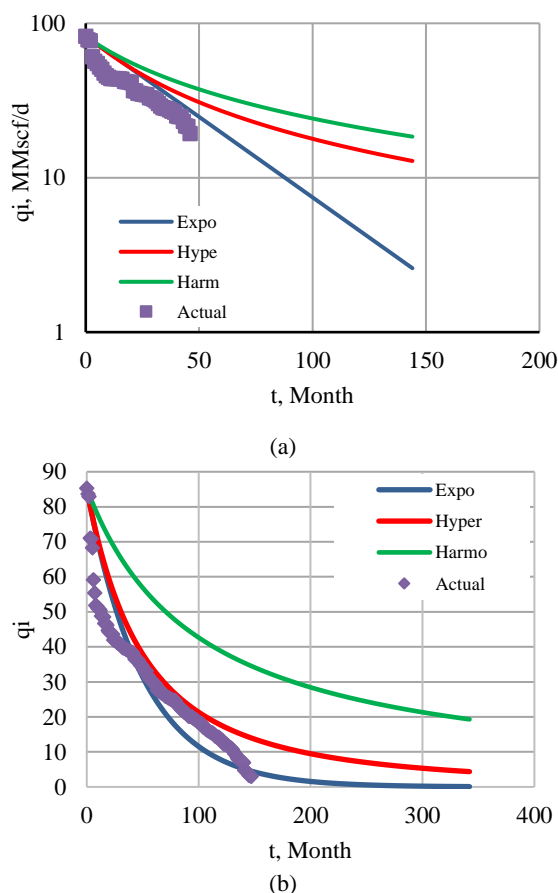
Figure 6. Arps decline curve shapes for a Cartesian rate-time (a) – well SA-2; (b) – well GD2)

4. CONCLUSIONS

This study tested the feasibility of using Arps curves to predict gas well production rates in a field in Senegal. Comparison of Arps models and actual well flow rates made it possible to note the presence of deviations. There were 2 types of deviations. The first type of deviation is associated with a change in the filtration parameters of the formation due to a change in the stress state when putting wells into operation. Deviations of this type can be observed in the first 6 months from the start of well operation. The second reason for deviations is well repair. During repairs, the filtration parameters of rocks near the well wall change. When excluding the above factors, exponential Arps curves can predict gas production in Senegal quite accurately.

5. FUNDING STATEMENT

6. REFERENCES

1. Kamari, A., Mohammadi, A.H., Lee, M. and Bahadori, A., "Decline curve based models for predicting natural gas well performance", *Petroleum*, Vol. 3, No. 2, (2017), 242-248. doi: 10.1016/j.petlm.2016.06.006.

2. Stroykov, G., Babyr, N., Ilin, I. and Marchenko, R., "System of comprehensive assessment of project risks in the energy industry", *International Journal of Engineering, Transactions A: Basics,* , Vol. 34, No. 7, (2021), 1778-1784. doi: 10.5829/IJE.2021.34.07A.22.

3. POPLYGIN, V., "Well production after hydraulic fracturing in sandstone rocks in the north of the perm region", (2022). doi: 10.17580/em.2022.02.09.

4. Benneche, J., "Natural gas projections from eia and six others", in EIA Energy Outlook, Modelling and Data Conference, Washington, DC. (2007).

5. Boswell, R., "Resource potential of methane hydrate coming into focus", *Journal of Petroleum Science and Engineering*, Vol. 56, No. 1-3, (2007), 9-13. doi: 10.1016/j.petrol.2006.09.002.

6. Chibura, P.E., Zhang, W., Luo, A. and Wang, J., "A review on gas hydrate production feasibility for permafrost and marine hydrates", *Journal of Natural Gas Science and Engineering*, Vol. 100, (2022), 104441. doi: 10.1016/j.jngse.2022.104441.

7. Boyer II, C.M. and Qingzhao, B., "Methodology of coalbed methane resource assessment", *International Journal of Coal Geology*, Vol. 35, No. 1-4, (1998), 349-368.

8. Mohr, S. and Evans, G., "Long term forecasting of natural gas production", *Energy Policy*, Vol. 39, No. 9, (2011), 5550-5560.

9. Adeyemi, T.S. and Rufus, D.O., "Analytical development of an improved inflow performance relationship (ipr) model for solution gas drive reservoirs", *Journal of Human, Earth, and Future*, Vol. 2, No. 2, (2021), 125-135. https://doi.org/10.28991/hef-2021-02-02-04

10. Khanamiri, H.H., "A non-iterative method of decline curve analysis", *Journal of Petroleum Science and Engineering*, Vol. 73, No. 1-2, (2010), 59-66.

11. Karpikov, A., Aliev, R. and Babyr, N., "An analysis of the effectiveness of hydraulic fracturing at ys1 of the northern field", in IOP Conference Series: Materials Science and Engineering, IOP Publishing. Vol. 952, (2020), 012036.

12. Arps, J.J., "Analysis of decline curves", *Transactions of the AIME*, Vol. 160, No. 01, (1945), 228-247. doi: 10.2118/945228-g.

13. Sharma, P., Salman, M., Reza, Z. and Kabir, C., "Probing the roots of arps hyperbolic relation and assessing variable-drive mechanisms for improved dca", *Journal of Petroleum Science and Engineering*, Vol. 182, (2019), 106288. doi: 10.1016/j.petrol.2019.106288.

14. Lijek, S., "Simple performance plots used in rate-time determination and waterflood analysis", in SPE Annual Technical Conference and Exhibition?, SPE. (1989), SPE-19847-MS.

15. Fetkovich, M.J., "Decline curve analysis using type curves", in SPE Annual Technical Conference and Exhibition?, SPE. (1973), SPE-4629-MS.

16. Can, B. and Kabir, C.S., "Simple tools for forecasting waterflood performance", *Journal of Petroleum Science and Engineering*, Vol. 120, (2014), 111-118. doi: 10.1016/j.petrol.2014.05.028.

17. Kabir, C., Haftbaradaran, R., Asghari, R. and Sastre, J., "Understanding variable well performance in a chalk reservoir", *SPE Reservoir Evaluation & Engineering*, Vol. 19, No. 01, (2016), 083-094. doi: 10.2118/175436-pa.

18. Cheng, Y., Lee, W.J. and McVay, D.A., "Improving reserves estimates from decline-curve analysis of tight and multilayer gas

wells", *SPE Reservoir Evaluation & Engineering*, Vol. 11, No. 05, (2008), 912-920. doi: 10.2118/108176-pa.

19. Ayala, L.F. and Peng, Y., "Unified decline type-curve analysis for natural gas wells in boundary-dominated flow", *SPE Journal*, Vol. 18, No. 1, (2013), 97-113. doi: 10.2118/161095-pa.

20. Lehner, P. and De Ruiter, P., "Structural history of atlantic margin of africa", *AAPG Bulletin*, Vol. 61, No. 7, (1977), 961-981.

21. Nzoussi-Mbassani, P., "Le cénomano-turonien de l'atlantique nord (bassin du sénégal): Environnement de dépôt et évolution diagénétique", Université d'Orléans, (2003),

22. Darnell, J.L. and Arnold, R., "Manual for the oil and gas industry under the revenue act of 1918, J. Wiley, (1920).

23. Gentry, R.W., "Decline-curve analysis", *Journal of Petroleum Technology*, Vol. 24, No. 01, (1972), 38-41.

24. Lu, H., Ma, X. and Azimi, M., "Us natural gas consumption prediction using an improved kernel-based nonlinear extension of the arps decline model", *Energy*, Vol. 194, (2020), 116905. doi: 10.1016/j.energy.2020.116905.

25. Guzev, M., Kozhevnikov, E., Turbakov, M., Riabokon, E. and Poplygin, V., "Experimental investigation of the change of elastic moduli of clastic rocks under nonlinear loading", *International Journal of Engineering, Transactions C: Aspects*, Vol. 34, No. 3, (2021), 750-755. doi: 10.5829/IJE.2021.34.03C.21.

26. Poplygin, V. and Wiercigroch, M., "Research of efficiency of complex non-stationary impact on layer with high-quality oil",

Bulletin of Tomsk Polytechnic University. Geo Assets Engineering, Vol. 331, No. 3, (2020), 7-12.

27. Poplygin, V. and Pavlovskaia, E., "Investigation of the influence of pressures and proppant mass on the well parameters after hydraulic fracturing", *International Journal of Engineering, Transactions A: Basics,*, Vol. 34, No. 4, (2021), 1066-1073. doi: 10.5829/IJE.2021.34.04A.33.

28. Poplygin, V.V., Qi, C., Guzev, M., Riabokon, E., Turbakov, M. and Kozhevnikov, E., "Influence of frequency of wave action on oil production", *International Journal of Engineering, Transactions A: Basics,*, Vol. 35, No. 11, (2022), 2072-2076. doi: 10.5829/IJE.2022.35.11B.02.

29. Poplygin, V.V., Poplygina, I.S. and Mordvinov, V.A., "Influence of reservoir properties on the velocity of water movement from injection to production well", *Energies*, Vol. 15, No. 20, (2022), 7797.

30. Talebkeikhah, M., Sadeghtabaghi, Z. and Shabani, M., "A comparison of machine learning approaches for prediction of permeability using well log data in the hydrocarbon reservoirs", *Journal of Human, Earth, and Future*, Vol. 2, No. 2, (2021), 82-99. doi: 10.28991/hef-2021-02-02-01.

31. Elmabrouk, S.K. and Mahmud, W.M., "Production data analysis techniques for the evaluation of the estimated ultimate recovery (eur) in oil and gas reservoirs", *HighTech and Innovation Journal*, Vol. 3, No. 1, (2022), 85-101. doi: 10.28991/hij-2022-03-01-09.

Persian Abstract

چکیده

هدف از این مطالعه ارزیابی امکان سنجی استفاده از روش‌هایی برای پیش‌بینی نرخ جریان چاه‌های گاز در میادین سنگال است. پیش بینی دقیق تولید گاز طبیعی به شما امکان می دهد تا به درستی حالت عملیات چاه ها را تنظیم کنید و زیرساخت های خشکی را طراحی کنید. یکی از میادین گازی سنگال به عنوان هدف مطالعه انتخاب شد که در آن ذخایر در محدوده بهره برداری در افق های ماسه سنگی کامپانین و سانتونین کشف شد. سازندهای گازی دارای مقادیر تخلخل و نفوذپذیری بالا و همچنین دمای سازند بالا هستند. نرخ جریان چاه گاز را می توان با استفاده از مدل های هیدرودینامیکی، مدل های ریاضی) هذلولی و غیره (و روش های دیگر پیش بینی کرد. این مطالعه امکان استفاده از منحنی‌های آرپس را برای پیش‌بینی بلندمدت نرخ جریان گاز و مقایسه نتایج پیش‌بینی با داده‌های واقعی ارزیابی کرد. مقایسه منحنی‌های Arps و نرخ جریان گاز واقعی برای چاه‌ها، نشان دادن اختلاف در نتایج پیش‌بینی‌شده و مقادیر واقعی بیش از 20 درصد را ممکن کرد. این اختلافات به دو دلیل به وجود آمد. انحراف در مرحله اولیه بهره برداری چاه 6) ماه (که با تنظیم حالت عملیات فن آوری چاه و ایجاد پارامترهای ثابت سنگ ها در نزدیکی چاه همراه است. دلیل دوم تعمیرات چاه است که خواص سنگ های نزدیک چاه را تغییر می دهد. به طور کلی، منحنی‌های آرپس از نوع نمایی همگرایی بالایی بین مقادیر پیش‌بینی‌شده و واقعی نشان دادند که استفاده از آن‌ها را در پیش‌بینی نرخ جریان چاه‌های گاز در سنگال ممکن می‌سازد.

Partial Enzymatic Hydrolysis of Glucomannan and Its Mathematical Model

D. H. Wardhani*, H. Cahyono, H. N. Ulya, A. C. Kumoro, N. Aryanti

Chemical Engineering Department, Faculty of Engineering, Diponegoro University, Semarang, Indonesia

P A P E R   I N F O

A B S T R A C T

The study of enzymatic hydrolysis of glucomannan (GM) was currently limited to obtain low molecular weight glucomannan, and was not specifically studied for spray drying feed applications. This research aimed to investigate the effect of enzyme concentration and duration of enzymatic hydrolysis of GM on the characteristics of hydrolyzed glucomannan (HGM). Moreover, the kinetic models of viscosity reduction in enzymatic hydrolysis of glucomannan were also studied. To achieve the goal, the GM was hydrolyzed using various enzyme concentrations (5 to 20 mg/l) for 300 min. Profiles of viscosity, average molecular weight (Mw), degree of polymerization, and antioxidant activity of HGM were observed. The kinetics of viscosity reduction was modeled with 1st-order kinetics, 2nd-order model, and Mahammad's order. An enzyme concentration of 20 mg/l (1% GM solution) was the fastest to reach the desired viscosity for spray drying feed purposes. The model of nth-order was the best fitted to the viscosity reduction with R^2 equal to 0.9935, so the constants k = 1.1842 (Pa.s n^{-1}.t)$^{-1}$ and n = 0.6328 are obtained. The hydrolysis improved the antioxidant activity of HGM as the enzyme concentration increases. This antioxidant result highlighted the advantage of using HGM for coating and encapsulating the active compound which also offers oxidation protection.

doi: 10.5829/ije.2023.36.12c.11

NOMENCLATURE

[Ez]	Enzyme concentration (mg/l)	k_n	n^{th}-order model constant [(Pa.s n^{-1} .t) $^{-1}$]
DNS	3,5-Dinitrosalicylic acid	k_m	Mahammad model constant (s^{-1})
DP	Degree of polymerization	Mw	Molecular weight (Da)
DPPH	2,2-Diphenyl-1-picrylhydrazyl	RS	Reducing sugar (ppm)
DRS	Drect reducing sugar	R^2	Coefficient of determination
EE	Encapsulation efficiency	t	Time (min)
$Fe_{initially\ added}$	Initial iron weight added to the solution (g)	TS	Total sugar (ppm)
Fe_{sample}	Measured iron content in powder (g)	W	Dried sample weight (g)
GM	Glucomannan	**Greek Symbols**	
HGM	Hydrolyzed glucomannan	α	Mark-Houwink constant
K	Mark-Houwink constant	$α_M$	Mahammad model constant
k_1	First-order model constant (s^{-1})	η	Viscosity (Pa-s)
k_2	Second-order model constant [(Pa.s.T)$^{-1}$]		

1. INTRODUCTION

Glucomannan (GM) is a neutral polysaccharide consisting of D-mannose and D-glucose bonding by β-1,4 linkage [1] with 5-10% of this polysaccharide is acetyl groups [2]. This amorphous polymer becomes the highest viscosity among various gum types with an average molecular weight (Mw) of 200 to 2000 kDa [3]. One percent of this heteropolysaccharide has apparent viscosity and average Mw up to 10,000 centipoise and 2.7×10^5 Da, respectively. The molecular structure of GM is shown in Figure 1.

As natural polysaccharides, GM is preferable for environmental purposes as it is biodegradable [4]. Its

Corresponding Author Email: dhwardhani@che.undip.ac.id
(D. H. Wardhani)
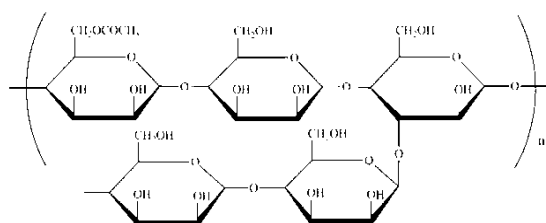
Figure 1. Molecular structure of glucomannan [5]

high viscosity provides a benefit in encapsulation applications by trapping more concentrations of active substances. However, this property leads to a challenge in its application as a matrix in spray drying encapsulation since the feed is required to be flowable [6, 7]. High viscosity prevents the formation of feed atomization in the drying chamber, resulting in drying to be insufficient because of the particle size is too large and even could block the atomizer nozzle. Sosnik and Seremeta [8] reported that approximately 0.3 Pa-s is the maximum viscosity of the feed solution for Büchi Mini Spray Dryer B-290. Hence, the viscosity of GM needs to be adjusted before spray drying application, without neglecting to obtain a high-yield product. Hydrolysis had successfully decreased GM viscosity and produced hydrolyzed glucomannan (HGM) [9, 10]. In addition, GM hydrolysis has been reported to improve the antioxidant activity of HGM [11].

Attempts to reduce average Mw of GM were reported using acids such as H_2SO_4 [12] and citric acid [13]. These processes require special specifications of the equipment to avoid oxidation. In addition, they generate acid waste, and are difficult to control the average Mw of the product. Li et al. [14] conducted a mechanical hydrolysis technique for GM using ultrasound. This method requires specific equipment to produce ultrasonic waves, which is costly for large capacity applications. Using the enzymatic method, hydrolysis offers mild reaction conditions, is easily controlled reaction, and environmentally friendly [15]. Wattanaprasert et al. [6] successfully applied β-mannanase to hydrolyze GM. Unfortunately, this enzyme is not widely available. Cellulase or 4-beta-D-glucan 4-glucanohydrolase is a specific enzyme that hydrolyzes β-1,4-glycosidic bonds of polysaccharides and produces oligosaccharides and/or monosaccharides [16]. Considering β-1,4 glycosidic as the primary linkage of GM, this commonly available enzyme is an excellent candidate to cleavage the linkage. Although this enzyme has been applied in GM hydrolysis for iron and flavour encapsulant [9, 15, 17], the combined effect of enzyme concentration and its kinetic in preparing spray drying feed is still less explored [18].

Hence, this work aims to examine the effect of cellulase concentration and hydrolysis period on the characteristics of HGM, including the viscosity, average Mw, degree of polymerization, and antioxidant capacity. The kinetic of the GM hydrolysis was also studied to predict a suitable pretreatment on GM prior to spray dryer application.

2. MATERIALS AND METHOD

2. 1. Materials   The materials used in this study were Now Food® Glucomannan powder, cellulase enzyme (4-beta-D-glucan 4-glucanohydrolase) (EC 3.2.14) from Sigma-Aldrich with 0.3 U/mg from Sigma-Aldrich, and other chemicals obtained from Merck KGaA used without purification.

2. 2. Glucomannan Hydrolysis   Visual diagram of glucomannan hydrolysis process is shown in Figure 2. One liter of GM solution (1% w/v) was hydrolyzed with cellulase (5, 10, 15, 20 mg/l) under 350 rpm constant stirring (Hightech Mixer IKA RW 20 Digital) at room temperature. After 300 min, the enzyme was inactivated by heating up the solution at 80°C for 10 min to stop the reaction.

2. 3. Total Sugar and Reducing Sugar   Total sugar (TS) was defined as the amount of sugar in the sample, while Direct Reducing Sugar (DRS) was the amount of reducing sugar. The degree of polymerization (DP) was the ratio of TS to DRS as calculated by Equation (1).

$$DP = \frac{TS}{DRS} \tag{1}$$

The method of TS was conducted based on method developed by Nakasaki et al. [19], while the method of DRS was determined using the 3.5-dinitrosalicylic acid (DNS) [20]. Basically, the DNS method was based on reducing DNS in alkaline atmosphere which was identified by the absorbance at 550 nm wavelength.

2. 4. Viscosity and Its Kinetic Model   GM or HGM solution (500 ml) was placed in beaker glass for viscosity measurements using spindle number 7 of Brookfield viscometer (Model RVTDV II, Brookfield Engineering Laboratories, Inc., Stoughton, MA) at 28±1°C at 100 rpm. Triple measurements were carried out for each sample.

The rheokinetic model was developed to estimate the reaction rate of the experimental data. Four mathematical models, i.e., order 1 (Equation (2)), order 2 (Equation (3)), order-n (Equation (4)), and Mahammad's model (Equation (5)) [21], were fitted to the viscosity of experimental data. The one with the coefficient of determination (R^2) close to 1 was the fittest model representing the glucomannan hydrolysis.

$$\eta = \eta_o e^{-k_1 \times t} \tag{2}$$

$$\frac{1}{\eta} = \frac{1}{\eta_o} + k_2 \times t \tag{3}$$

$$\eta = (\eta_o^{1-n} - (1-n) \times k_n \times t)^{\frac{1}{(1-n)}} \tag{4}$$

$$\ln(\frac{\eta 0}{\eta}) = \frac{\alpha_M}{3} \times \ln(1 + k_m \times t) \tag{5}$$

2. 5. Average Molecular Weight   The intrinsic viscosity of the solutions was conducted using Cannon Fenske Viscometer size 100. Various HGM concentration solutions (0.01, 0.02, 0.03, 0.04, and 0.05 g/l) were prepared for each sample. Average molecular weight was calculated by Mark Houwink using Equation (6), with the specific constant value K and a was 5.9610 x10^{-4} and 0.7317, respectively [22].

$$\eta = 5.9610 \times 10^{-4} \times Mw^{0.7317} \tag{6}$$

2. 6. Hydroxyl and DPPH Radical Scavenging Activity Determination   Hydroxyl radical and DPPH scavenging activity was measured using the method of Ding et al. [23] for HGM solution after 300 min hydrolysis. The sample (1.0 ml) was mixed with 1.0 ml of phosphate buffer (0.4 mM, pH 7.4), 1.0 ml 1.10-phenanthroline hydrate (2.5 mM), 1.0 ml $FeSO_4$ (20.5 mM), and 0.5 ml H_2O_2 (20 mM, 1%, v/v). The mixture was incubated for 60 min at 37°C, the absorbance of the mixture was measured at 536 nm (A_s). In addition, the blank mixture without sample addition also measured for its absorbance (A_0).

Freshly-prepared DPPH in 95% ethanol solution (0.1 mM, 4.0 ml) was incubated with the test sample (1.0 ml). After mixing for 1 min, the solution was incubated for 30 min at room temperature in dark conditions. The absorbance of the solution was read at a wavelength of 517 nm.

The inhibition activity (IA) was calculated using Equation (7), while IC_{50} showed the sample concentration which prevented 50% of total oxidation.

$$IA\ (\%) = \frac{A_0 - A_s}{A_0} \times 100\% \tag{7}$$

3. RESULTS AND DISCUSSIONS

β-mannanase has commonly been applied in GM hydrolysis [24]. However, this enzyme is not broadly available. Cellulase or 4-beta-D-glucan 4-glucanohydrolase, the more commonly found enzyme, is a typical specific enzyme to break β-1,4-glycosidic, the linkage between D-mannose and D-glucose of GM. The effectivity of this enzyme to hydrolyzed GM, specifically to fulfill characteristics for spray dryer feed, was studied

at various enzyme concentrations. Degradation of viscosity was modeled subsequently.

3. 1. Viscosity and Average Molecular Weight
Figure 3 shows a decrease in HGM viscosity during hydrolysis at all enzyme concentrations. All viscosity of the samples dropped significantly in the first 50 min, followed by a moderate decrease. Indeed, only a slight viscosity change was observed at higher enzyme concentrations after 90 min. Increasing enzyme concentration allowed more contact with GM and cleaved more GM linkages at the same duration reaction. As a result, an insignificant change of the viscosity was observed afterward. All samples achieved 300 cPs in different hydrolysis periods, in which the highest enzymatic concentration reached the viscosity in the shortest time, only 45 min. Meanwhile, the lowest enzyme concentration (5 mg/ml) reached the viscosity target after 300 min hydrolysis. These conditions which allow to reduce GM viscosity to about 300 cPs and fulfill the viscosity requirement for spray dryer feed [8] were recommended for GM pretreatment prior to spray dryer application. A similar trend in viscosity reduction of HGM after enzymatic hydrolysis was also reported by Liu et al. [11]. Using β-mannanase, Bhaturiwala et al. [25] also obtained 320 cPs viscosity of hydrolyzed glucomannan after 24 h incubation time. However, a shorter duration of hydrolysis (<5 h) should be conducted to prevent the growth of other unwanted microorganisms [26].

Viscosity reduction was modeled to predict the HGM viscosity in a certain hydrolysis time. Four mathematical models were fitted to the viscosity reduction. The constants of all models fitting are presented in Table 1.

Most of the model fittings showed R^2 above 0.9 for all enzyme concentrations, except the 2nd order model. Model of nth order was superior to describe viscosity decrease of all enzyme concentrations than other models
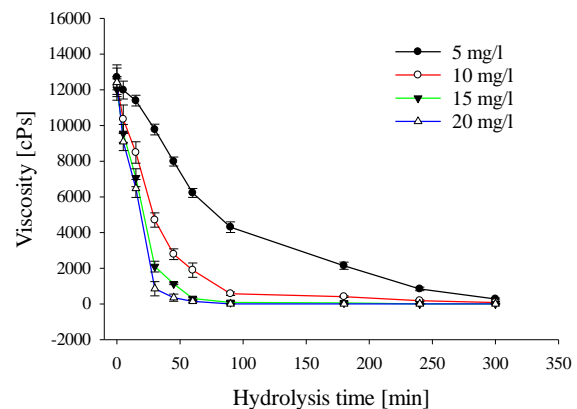
Figure 3. Effect of enzyme concentration on glucomannan viscosity

TABLE 1. The constants of the kinetics models in decreasing profile of the viscosity of HGM at various enzyme concentrations

Constants	[Ez] = 5 mg/l	[Ez] = 10 mg/l	[Ez] = 15 mg/l	[Ez] = 20 mg/l
1st order				
k_1 [s^{-1}]	0.0108	0.0307	0.0474	0.0595
R^2	0.9933	0.9951	0.9878	0.9806
2nd order				
k_2 [(Pa.s.T)$^{-1}$]	0.0000	0.0000	0.0028	0.0038
R^2	0.6775	0.7859	0.6973	0.8801
nth order				
k_n [(Pa.s n^{-1}.t)$^{-1}$]	0.0191	0.1341	1.1842	22.6446
n	0.9364	0.8329	0.6328	0.3268
R^2	0.9936	0.9960	0.9935	0.9910
Mahammad model				
α_M	9.0800	8.0700	8.0699	10.0899
k_m [s^{-1}]	0.0061	0.0168	0.0608	0.0599
R^2	0.9380	0.9786	0.8876	0.9398

TABLE 2. Effect of enzyme concentration on average molecular weight (Mw) of HGM after 300 min hydrolysis

Enzyme concentrations (mg/l)	Average molecular weight		Percentage of decrease (%)
	Initial GM (Da)	HGM (Da)	
5		120,550	83.96
10	751,628	118,564	84.23
15		112,190	85.07
20		107,611	85.68

in, in which the lowest R^2 is 0.9910. Plot of all models to viscosity decrease of HGM using 15 ppm cellulase is presented in Figure 4. This fitting profile supported the R^2 values of TABLE 1. The model of 2nd order was the worst with R^2=0.697, while nth order (R^2=0.993) showed the best fit one. The goodness of nth order suggested that the model is suitable to predict the viscosity profile during GM hydrolysis under various enzyme concentrations.

The relationship between viscosity and average Mw is determined based on the Mark-Houwink equation. The increase in viscosity positively correlates with average Mw [27]. The work of cellulase in cleaving β,1-4 linkage led to average Mw reduction of HGM, as shown in Table 2. Since all samples have similar viscosity after 300 min hydrolysis (Figure 3), the average Mw of all samples showed similar values ranging from 83.96-85.68% reduction compared to the initial average Mw of GM. Bhaturiwala et al. [25] found a similar value of average Mw decrease after glucomannan hydrolysis using β-mannanase, which had ~86.5% reduction after 24 h of hydrolysis.

3. 2. Reducing Sugar and Degree of Polymerization   Viscosity modifications were parallel with the change of DRS and DP (Figure 5). During GM hydrolysis, oligosaccharides and reducing sugars were released concerning the enzyme work. The high enzyme concentration provided more active sites to

cleave the GM linkages, resulting in more reducing sugars. The highest enzyme concentration (20 mg/l) sharply increased DRS from 1.2 to 78.1 mg/g sample in the first 30 min, followed by an insignificant change of reducing sugar afterward and reached 85.1 mg/g sample after 300 min. Meanwhile, the lowest enzyme (5 mg/l) produced 78.81 mg/g sample after 300 min hydrolysis and released the lowest reducing sugar concentration than other enzyme concentrations even after 300 min. Hydrolysis did not have an impact on the TS of HGM. Hence DP of samples was only influenced by DRS. As DP is a ratio between TS and DRS, an increase of DRS led to an opposite value of DP. DP HGM decreased from 7.64 to 1.67 within 15 min hydrolysis using 20 mg/l. The lowest concentration required 180 min to obtain a similar DP value. Jian et al. [28] produced 2-9 DP values of HGM in 10 h after a treatment combination of radiation and endo-1, 4-β-D-glucanase under incubator condition. Our study needed a shorter time to reach the range DP than that of Jian et al. [28] due to differences in the hydrolysis method. Our hydrolysis was conducted under continuous stirring, allowing more intensive collision between the enzyme and substrate, which reduced the reaction time.
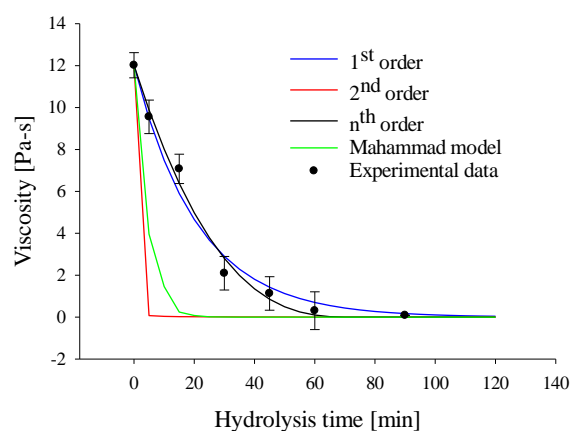
Figure 4. Plot of the kinetic models on HGM viscosity reduction using 15 ppm cellulase

(a)

(b)
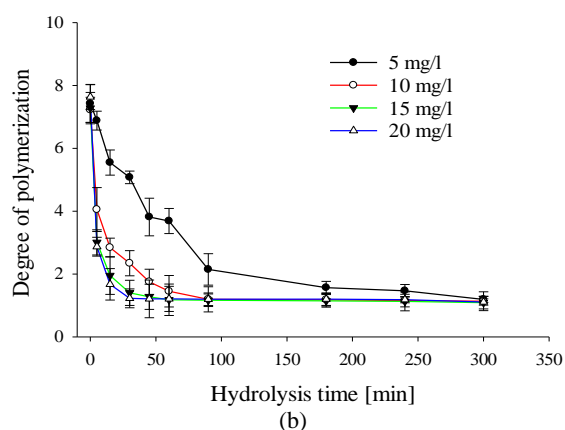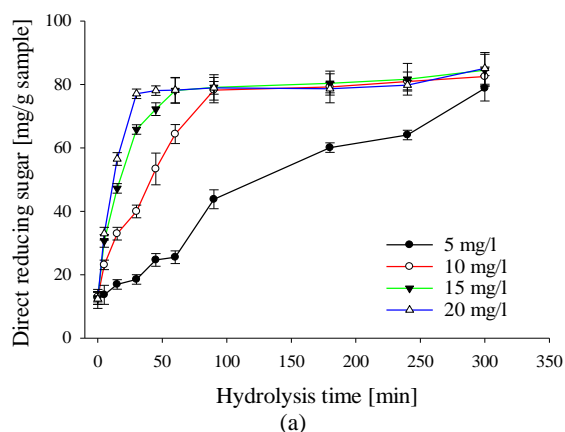
Figure 5. Effect of enzyme concentration on (a) direct reducing sugar and (b) degree of polymerization of HGM

(a)

(b)
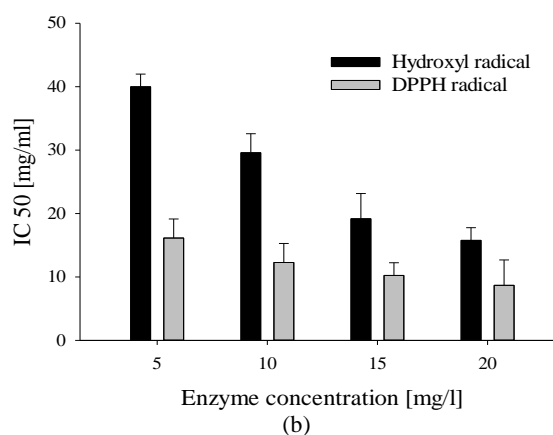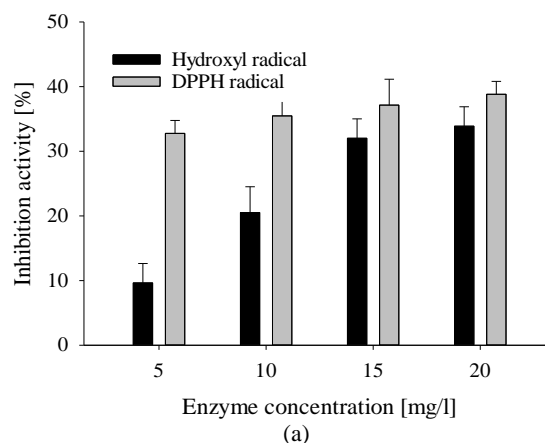
Figure 6. Effect of enzyme concentration on (a) HGM inhibitory activity and (b) IC$_{50}$ HGM

3. 3. Antioxidant Activity   Encapsulation using the spray drying method involves high-temperature treatment to obtain final dry powders containing active substances. The use of a matrix that can protect the active compounds from heat degradation helped suppress oxidation during the mixing of ingredients and the spray drying process. Antioxidant activities of HGM after 300 min hydrolysis using various enzyme concentrations are presented in Figure 6. The activities of HGM were presented as inhibition activity toward DPPH radical and hydroxyl radical. In both antioxidant determinations, scavenging activities of radicals increased with enzyme concentration. Higher enzyme concentration led to produce more numbers of shorter HGM molecules. The DRS of HGM ranged 78.81±2.01–85.10±4.98 mg/g sample, in line with enzyme concentration. Wardhani et al. [29]and Tripetch et al. [30] reported an increase in antioxidant activity after GM hydrolysis. A similar effect of enzyme concentration on the inhibition activity of HGM was reported by Liu et al. [11] using β-mannanase. The study of Cui et al. [24] confirmed that converting polysaccharides to oligosaccharides supports the increase of antioxidant activity.

HGM performed different sensitivity to respond to the inhibition activity and IC$_{50}$ of DPPH and hydroxyl radicals. HGM showed stronger as the DPPH radical scavenger than as the hydroxyl radicals. HGM allows more significant inhibition of DPPH than hydroxyl radical [11]. Interestingly, the HGM hydroxyl activity rose triple from 9.63±3.12% to 33.88±3.01% while DPPH scavenging inhibition was slightly improved from 32.77±1.99% to 38.82±2.11% under 5 to 20 mg/l enzyme treatment at 300 min. The slight difference in responses between the two antioxidant activity methods could be due to different mechanisms of the methods. DPPH proton-free radicals will be reduced when exposed to antioxidants that act as proton radical acceptors. Hence, the DPPH assay is based on the ability of an antioxidant compound to reduce an odd electron of the nitrogen atom in DPPH by receiving a hydrogen atom to the corresponding hydrazine [31]. Meanwhile, hydroxyl radical as the most reactive free radical could form hydrogen peroxide in the presence of metal ions such as iron [32, 33].

Apart from oligosaccharides, some researchers reported the contribution of phenolics compounds on supporting antioxidant properties of polysaccharides [34-36]. Hu et al. [37] reported a GM native of 98% purity contains 0.26% total phenolic and 0.97% total protein which both contribute to the scavenging activities against hydroxyl. In natural sources, most phenolics exist in a form bound to sugars, proteins, or lipids. Releasing total phenolic content and increasing DPPH scavenging activity on soybeans through fermentation was reported by Wardhani et al. [38]. Alrahmany et al. [39] succeeded in releasing the phenolics in rice bran and oat using cellulase, which improved the total phenolic and antioxidant activity. Moreover, some reports also demonstrated a relationship between the structures of the phenolic and their efficacy on antioxidant activity [40]. We argued that a similar phenomenon occurred in the HGM of this study. The more enzymes involved in the hydrolysis, the more phenolic compounds are released which increases the ability of HGM to scavenge the radicals. Since reports on exploring the relationship between enzymatic hydrolysis of GM and their phenolic antioxidant activity are still rarely available, therefore, an integrated study on this topic needs to be conducted in the future. Overall, this antioxidant result highlighted the advantage of using HGM for coating and encapsulating the active compound which also offers oxidation protection.

4. CONCLUSION

In general, viscosity, DP, and average Mw of HGM decreased over the hydrolysis treatment. Conversely, the hydrolysis increased the antioxidant activity of HGM which showed its potential in protecting bioactive from oxidation. Hydrolysis of 1% GM using 20 mg/l cellulase allowed to reach 300 cPs in a shorter time of hydrolysis, hence, fulfilling the viscosity of HGM for spray dryer feed. The reduction viscosity of GM during hydrolysis was best represented by n^{th} order ($R^2 \geq 0.991$).

5. ACKNOWLEDGMENT

6. REFERENCES

1. Wardhani, D.H. and Cahyono, H., "The effect of alcohol on bead performance of encapsulated iron using deacetylated glucomannan", in MATEC Web of Conferences, EDP Sciences. Vol. 156, (2018), 01005. https://doi.org/10.1051/matecconf/201815601005

2. Gao, S. and Nishinari, K., "Effect of degree of acetylation on gelation of konjac glucomannan", *Biomacromolecules*, Vol. 5, No. 1, (2004), 175-185, https://doi.org/10.1021/bm034302f

3. Zhang, C., Yang, X., Hu, W., Han, X., Fan, L. and Tao, S., "Preparation and characterization of carboxymethyl chitosan/collagen peptide/oxidized konjac composite hydrogel", *International Journal of Biological Macromolecules*, Vol. 149, (2020), 31-40, https://doi.org/10.1016/j.ijbiomac.2020.01.127

4. Asadpour, R., Sapari, N., Hasnain Isa, M. and Kakooei, S., "Further study of adsorption of crude oils onto acetylated corn silk and its kinetics and equilibrium isotherm", *International Journal of Engineering, Transactions B: Applications*, Vol. 32, No. 2, (2019), 229-235, https://doi.org/10.5829/ije.2019.32.02b.07

5. Yaseen, E., Herald, T., Aramouni, F. and Alavi, S., "Rheological properties of selected gum solutions", *Food Research International*, Vol. 38, No. 2, (2005), 111-119, https://doi.org/10.1016/j.foodres.2004.01.013

6. Wattanaprasert, S., Borompichaichartkul, C., Vaithanomsat, P. and Srzednicki, G., "Konjac glucomannan hydrolysate: A potential natural coating material for bioactive compounds in spray drying encapsulation", *Engineering in Life Sciences*, Vol. 17, No. 2, (2017), 145-152, https://doi.org/10.1002/elsc.201600016

7. Alemzadeh, I., Hajiabbas, M., Pakzad, H., Sajadi Dehkordi, S. and Vossoughi, A., "Encapsulation of food components and bioactive ingredients and targeted release", *International Journal of Engineering, Transactions A: Basics*, Vol. 33, No. 1, (2020), 1-11, https://doi.org/10.5829/ije.2020.33.01a.01

8. Sosnik, A. and Seremeta, K.P., "Advantages and challenges of the spray-drying technology for the production of pure drug particles and drug-loaded polymeric carriers", *Advances in Colloid and Interface Science*, Vol. 223, (2015), 40-54, https://doi.org/10.1016/j.cis.2015.05.003

9. Chen, C.-Y., Huang, Y.-C., Yang, T.-Y., Jian, J.-Y., Chen, W.-L. and Yang, C.-H., "Degradation of konjac glucomannan by thermobifida fusca thermostable β-mannanase from yeast transformant", *International Journal of Biological Macromolecules*, Vol. 82, (2016), 1-6, https://doi.org/10.1016/j.ijbiomac.2015.10.008

10. Zhu, F., "Modifications of konjac glucomannan for diverse applications", *Food Chemistry*, Vol. 256, (2018), 419-426, https://doi.org/10.1016/j.foodchem.2018.02.151

11. Liu, J., Xu, Q., Zhang, J., Zhou, X., Lyu, F., Zhao, P. and Ding, Y., "Preparation, composition analysis and antioxidant activities of konjac oligo-glucomannan", *Carbohydrate Polymers*, Vol. 130, (2015), 398-404, https://doi.org/10.1016/j.carbpol.2015.05.025

12. Wang, S., Zhou, B., Wang, Y. and Li, B., "Preparation and characterization of konjac glucomannan microcrystals through acid hydrolysis", *Food Research International*, Vol. 67, (2015), 111-116, https://doi.org/10.1016/j.foodres.2014.11.008

13. Ojima, R., Makabe, T., Prawitwong, P., Takahashi, R., Takigami, M. and Takigami, S., "Rheological property of hydrolyzed konjac glucomannan", *Transactions of the Materials Research Society of Japan*, Vol. 34, No. 3, (2009), 477-480, https://doi.org/10.14723/tmrsj.34.477

14. Li, J., Li, B., Geng, P., Song, A.-X. and Wu, J.-Y., "Ultrasonic degradation kinetics and rheological profiles of a food polysaccharide (konjac glucomannan) in water", *Food Hydrocolloids*, Vol. 70, (2017), 14-19, https://doi.org/10.1016/j.foodhyd.2017.03.022

15. Wardhani, D.H., Wardana, I.N., Ulya, H.N., Cahyono, H., Kumoro, A.C. and Aryanti, N., "The effect of spray-drying inlet conditions on iron encapsulation using hydrolysed glucomannan

as a matrix", ***Food and Bioproducts Processing***, Vol. 123, (2020), 72-79, https://doi.org/10.1016/j.fbp.2020.05.013

16. Afsahi, B., KHEYR, A.A., Nejati, S. and Kazemi, A., "Immobilization of cellulase on non-porous ultrafine silica particles", (2007).

17. Yang, J., Xiao, J.-x. and Ding, L.-z., "An investigation into the application of konjac glucomannan as a flavor encapsulant", ***European Food Research and Technology***, Vol. 229, (2009), 467-474, https://doi.org/10.1007/s00217-009-1084-2

18. Nikzad, M., Movagharnejad, K., Najafpour, G.D. and Talebnia, F., "Comparative studies on effect of pretreatment of rice husk for enzymatic digestibility and bioethanol production", ***International Journal of Engineering, Transactions B: Applications***, Vol. 26, No. 5, (2013), 455-464, https://doi.org/10.5829/idosi.ije.2013.26.05b.01

19. Nakasaki, K., Kato, J., Akiyama, T. and Kubota, H., "Transformations of water soluble organic materials during thermophilic composting of sewage sludge", ***Journal of Fermentation Technology***, Vol. 65, No. 6, (1987), 675-681, https://doi.org/10.1016/0385-6380(87)90010-0

20. Miller, G.L., "Use of dinitrosalicylic acid reagent for determination of reducing sugar", ***Analytical Chemistry***, Vol. 31, No. 3, (1959), 426-428, https://doi.org/10.1021/ac60147a030

21. Mahammad, S., Comfort, D.A., Kelly, R.M. and Khan, S.A., "Rheological properties of guar galactomannan solutions during hydrolysis with galactomannanase and α-galactosidase enzyme mixtures", ***Biomacromolecules***, Vol. 8, No. 3, (2007), 949-956, https://doi.org/10.1021/bm0608232

22. Li, B. and Xie, B., "Synthesis and characterization of konjac glucomannan/poly (vinyl alcohol) interpenetrating polymer networks", ***Journal of Applied Polymer Science***, Vol. 93, No. 6, (2004), 2775-2780, https://doi.org/10.1002/app.20769

23. Ding, L., Zhang, X. and Zhang, J., "Antioxidant activity in vitro guided screening and identification of flavonoids antioxidants in the extract from tetrastigma hemsleyanum diels et gilg", ***International Journal of Analytical Chemistry***, Vol. 2021, (2021), https://doi.org/10.1155/2021/7195125

24. Cui, S., Wu, Y. and Ding, H., "The range of dietary fibre ingredients and a comparison of their technical functionality", ***Fibre-rich and Wholegrain Foods: Improving Quality***, (2013), 96-119, https://doi.org/10.1533/9780857095787.1.96

25. Bhaturiwala, R., Bagban, M., Singh, T.A. and Modi, H., "Partial purification and application of β-mannanase for the preparation of low molecular weight galacto and glucomannan", ***Biocatalysis and Agricultural Biotechnology***, Vol. 36, (2021), 102155, https://doi.org/10.1016/j.bcab.2021.102155

26. Akesowan, A., "Syneresis and texture stability of hydrogel complexes containing konjac flour over multiple freeze-thaw cycles", ***Life Science Journal***, Vol. 9, No. 3, (2012), 1363-1367.

27. Jian, W., Tu, L., Wu, L., Xiong, H., Pang, J. and Sun, Y.-m., "Physicochemical properties and cellular protection against oxidation of degraded konjac glucomannan prepared by γ-irradiation", ***Food Chemistry***, Vol. 231, (2017), 42-50, https://doi.org/10.1016/j.foodchem.2017.03.121

28. Jian, W., Chen, Y.-H., Wang, L., Tu, L., Xiong, H. and Sun, Y.-m., "Preparation and cellular protection against oxidation of konjac oligosaccharides obtained by combination of γ-irradiation and enzymatic hydrolysis", ***Food Research International***, Vol. 107, (2018), 93-101, https://doi.org/10.1016/j.foodres.2018.02.014

29. Wardhani, D.H., Wardana, I.N., Tajuddin, C.A. and Abdillah, M.A., "Antioxidant and physicochemical properties of acid degraded glucomannan", in AIP Conference Proceedings, AIP Publishing. Vol. 2197, No. 1, (2020). https://doi.org/10.1063/1.5140937

30. Tripetch, P., Lekhavat, S., Devahastin, S., Chiewchan, N. and Borompichaichartkul, C., "Antioxidant activities of konjac glucomannan hydrolysates of different molecular weights at different values of ph", ***Foods***, Vol. 12, No. 18, (2023), 3406, https://doi.org/10.3390/foods12183406

31. Kedare, S.B. and Singh, R., "Genesis and development of dpph method of antioxidant assay", ***Journal of Food Science and Technology***, Vol. 48, (2011), 412-422, https://doi.org/10.1007/s13197-011-0251-1

32. Lee, J., Koo, N. and Min, D.B., "Reactive oxygen species, aging, and antioxidative nutraceuticals", ***Comprehensive Reviews in Food Science and Food Safety***, Vol. 3, No. 1, (2004), 21-33, https://doi.org/10.1111/j.1541-4337.2004.tb00058.x

33. Jin, M., Cai, Y.-X., Li, J.-R. and Zhao, H., "1, 10-phenanthroline-Fe^{2+} oxidative assay of hydroxyl radical produced by H_2O_2/ Fe^{2+}", ***Progress in Biochemistry and Biophysics***, Vol. 23, No. 6, (1996), 553-555.:

34. Fernandes, P.A. and Coimbra, M.A., "The antioxidant activity of polysaccharides: A structure-function relationship overview", ***Carbohydrate Polymers***, (2023), 120965, https://doi.org/10.1016/j.carbpol.2023.120965

35. Siu, K.-C., Xu, L., Chen, X. and Wu, J.-Y., "Molecular properties and antioxidant activities of polysaccharides isolated from alkaline extract of wild armillaria ostoyae mushrooms", ***Carbohydrate Polymers***, Vol. 137, (2016), 739-746, https://doi.org/10.1016/j.carbpol.2015.05.061

36. Xu, X.-Q., Su, B.-M., Xie, J.-S., Li, R.-K., Yang, J., Lin, J. and Ye, X.-Y., "Preparation of bioactive neoagarooligosaccharides through hydrolysis of gracilaria lemaneiformis agar: A comparative study", ***Food Chemistry***, Vol. 240, (2018), 330-337, https://doi.org/10.1016/j.foodchem.2017.07.036

37. Hu, S., Yin, J., Nie, S., Wang, J., Phillips, G.O., Xie, M. and Cui, S.W., "In vitro evaluation of the antioxidant activities of carbohydrates", ***Bioactive Carbohydrates and Dietary Fibre***, Vol. 7, No. 2, (2016), 19-27, https://doi.org/10.1016/j.bcdf.2016.04.001

38. Wardhani, D.H., Vázquez, J.A. and Pandiella, S.S., "Mathematical modeling of the development of antioxidant activity in soybeans fermented with aspergillus oryzae and aspergillus awamori in the solid state", ***Journal of Agricultural and Food Chemistry***, Vol. 57, No. 2, (2009), 540-544, https://doi.org/10.1021/jf802492s

39. Alrahmany, R. and Tsopmo, A., "Role of carbohydrases on the release of reducing sugar, total phenolics and on antioxidant properties of oat bran", ***Food Chemistry***, Vol. 132, No. 1, (2012), 413-418, https://doi.org/10.1016/j.foodchem.2011.11.014

40. Alrahmany, R., Avis, T.J. and Tsopmo, A., "Treatment of oat bran with carbohydrases increases soluble phenolic acid content and influences antioxidant and antimicrobial activities", ***Food Research International***, Vol. 52, No. 2, (2013), 568-574, https://doi.org/10.1016/j.foodres.2013.03.037
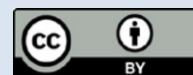
Persian Abstract

چکیده

مطالعه هیدرولیز آنزیمی گلوکومانان (GM) در حال حاضر محدود به تلاش برای به دست آوردن گلوکومانان با وزن مولکولی کم بود و به طور خاص برای کاربردهای خوراک خشک کردن اسپری مورد مطالعه قرار نگرفت. این تحقیق با هدف بررسی اثر غلظت آنزیم و مدت زمان هیدرولیز آنزیمی GM بر ویژگی‌های گلوکومانان هیدرولیز شده (HGM) انجام شد. علاوه بر این، مدل‌های جنبشی کاهش ویسکوزیته در هیدرولیز آنزیمی گلوکومانان نیز مورد مطالعه قرار گرفت. برای دستیابی به هدف، GM با استفاده از غلظت های مختلف آنزیم (5) تا 20 میلی گرم در لیتر (به مدت 300 دقیقه هیدرولیز شد. مشخصات ویسکوزیته، میانگین وزن مولکولی(Mw) ، درجه پلیمریزاسیون و فعالیت آنتی اکسیدانی HGM مشاهده شد. سینتیک کاهش ویسکوزیته با سینتیک مرتبه1، مدل مرتبه 2 و دستور محمد مدل‌سازی شد. غلظت آنزیم 20 میلی گرم در لیتر محلول 1 ٪ (GM) سریع ترین برای رسیدن به ویسکوزیته مورد نظر برای اهداف خوراک خشک کردن اسپری بود. مدل مرتبه n بهترین برازش را برای کاهش ویسکوزیته با R2 برابر با 0.9935 داشت، بنابراین ثابت‌های 1-(Pa.s n-1.t) k = 1.1842 و n = 0.6328 به دست می‌آیند. هیدرولیز فعالیت آنتی اکسیدانی HGM را با افزایش غلظت آنزیم بهبود بخشید. این نتیجه آنتی اکسیدانی مزیت استفاده از HGM را برای پوشش و محصور کردن ترکیب فعال که همچنین محافظت در برابر اکسیداسیون را ارائه می دهد برجسته کرد..

International Journal of Engineering

Utilizing Semi-Variograms and Geostatistical Approach for Land Value Model in Urban Region

N. T. Sugito*[a], I. Gumilar[b], A. Hernandi[b], A. P. Handayani[b], M. Dede[a,c,d]

[a] Faculty of Social Sciences Education, Universitas Pendidikan Indonesia, Bandung City, West Java, Indonesia
[b] Faculty of Earth Sciences and Technology, Institut Teknologi Bandung, Bandung City, West Java, Indonesia
[c] Environmental Science Program, Graduate School, Universitas Padjadjaran, Bandung City, West Java, Indonesia
[d] Cakrabuana Institute for Geoinformation, Environment and Social Studies, Cirebon Regency, West Java, Indonesia

P A P E R   I N F O

A B S T R A C T

The availability of land in Bandung City become a challenge for urban development. Bandung has long been an urbanization destination for Indonesians besides Jakarta, Surabaya, Medan, and Makassar. Currently there was still limited research that explores land values and spatial planning for urban areas. This study aims to develop spatial modeling for land values using a semi-variogram and geostatistical approach in urban areas. Our research was conducted in Bandung City, West Java (Indonesia). Data was selected based on purposive sampling involving 50 land price and 95 building price samples throughout the city. The collected data were then analyzed using 4 semi-variogram models and Ordinary Kriging to derive the spatial distribution of land values. Land value referred to spatial modeling from the geographic information system. The results of the analysis indicated that the semi-variogram stable type was the most suitable model, exhibiting the minimum error by root mean square, mean standardized, root mean square standardized, and average standard error. According to our model, the areas with the highest land values are located close to the city square "Alun-alun", which is closely associated with government offices, trading areas, defense and security facilities, service areas, education, cultural tourism, and high-density housing. These areas are well known since the Dutch East Indies era. Interestingly, despite the growth pole in Gedebage, the western part of Bandung has higher land values compared to the eastern part. This could be attributed to historical and actual aspects which have had a greater impact on land values than regional plans implemented by the government. Land values management is necessary to guarantee living space as well as to achieve a sustainable city.

Graphical Abstract
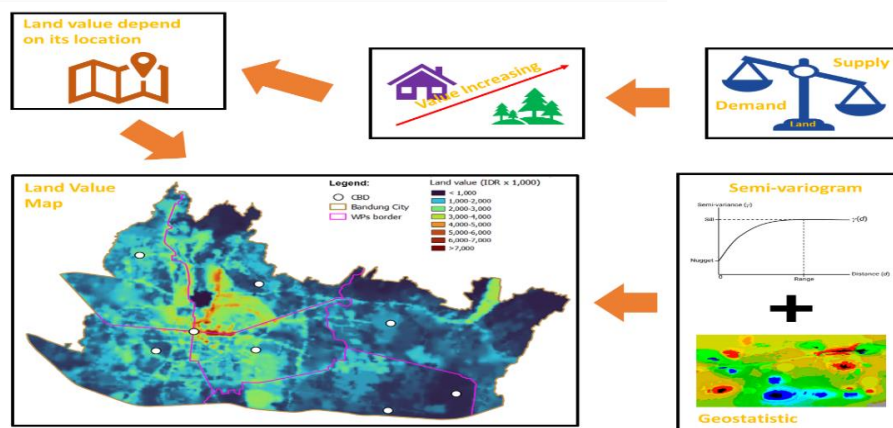
*Corresponding author email: naninsugito0403@gmail.com (N. T. Sugito)

1. INTRODUCTION

Land serves as a natural resource for various purposes in development and human activities [1]. It is important to note that land encompasses not just soil or ground, but also includes all objects on the earth's surface, making it a vital component of the geosphere [2]. With the growth of the human population, the demand for land and its resources has increased, while its availability is relatively constant [3, 4]. This heightened competitive land use leads to scarcity and encourages landscape changes from vegetated areas to built-up areas [5].

The demand for land remains high in urban areas, driven by a growing population, even market equilibrium is not ideal when the development pace is difficult to stop [6]. The availability and allocation of land in urban areas are increasingly limited, particularly in meeting the needs of settlements, public infrastructure, and commercial areas [7]. This limited availability of land leads to the formation of urbanized landscapes and peri-urban areas, which in turn drives up land values that become uncontrollable [8]. Human dependence on land has caused it to become an invaluable object, and this is reflected in its price [9].

The value of land in urban areas is heavily influenced by spatial structure. Many countries have implemented spatial planning that integrates registration and valuation of land objects as important considerations [10]. Accessibility plays a crucial role in determining land value, with infrastructure and the built environment being key factors that contribute to high prices, as observed in Arizona (The United States) [11]. The spatial configuration and development pressure as seen in spatial configuration caused land values in Central Strip, Israel to always be dynamic, even though historical aspects influence the values to be a reference for settlement development [12]. In Australia, spatial zoning had increased land and house prices by up to 73% [13]. Moreover, rising land values have also been observed in emerging industrialized countries such as China [14], Pakistan [15], Turkey [16], Vietnam [17], and Indonesia [18].

Previous studies on land values primarily focused on non-spatial economic analyses. However, in some research, the geospatial approach has started to be used to reveal the complexity involved [19-21]. The geospatial approach for assessing land values should include geostatistical analyses, as the value of land shares the same concept with elevation, water depth, groundwater exploitation, and environmental pollution which are not constrained by formal boundaries [22-24]. Previous studies have also not been able to link land values with urban development patterns. In fact, urban planning and development is multidisciplinary and multi-aspect management that combines knowledge about engineering, economic, socio-cultural, environmental as well as human behavior [25-28]. Therefore, the objective of this study is to develop spatial modeling for land values using a geostatistical approach in Bandung City. Our findings can contribute to the integration of spatial planning activities with land registration, which are currently separate, especially in Indonesia. This research would reveal the phenomenon between land values, urban planning, and other aspects that rationalize price differences in Bandung City. This article presents land value modeling compared to Bandung City's spatial planning, starting from introduction, materials and methods, results and discussion as well as conclusion.

2. MATERIALS AND METHOD

Our study takes place in Bandung City, West Java (Indonesia). Bandung serves as the provincial capital and the center of Bandung Raya Metropolitan Area (Figure 1). The city is home to over 2.5 million people, including thousands of commuters from neighboring areas such as Cimahi City, West Bandung Regency, Bandung Regency, Sumedang Regency, Subang Regency, Cianjur Regency, and Garut Regency [29]. Administratively, Bandung City is divided into 30 districts and 153 urban villages. It has emerged as a significant metropolis alongside Jakarta, Surabaya, Medan and Makassar [30]. Bandung City has problems related to land availability and its high price. Provisioning public facilities and low-cost housing become a big challenge in the development, coupled with Bandung's natural landscape as a basin surrounded by mountains.

Bandung City features two primary centers, 1) the square also known as "Alun-alun" and 2) Gedebage. Additionally, the city has 6 secondary centers serving development areas or WP, namely Setrasari (WP Bojonagara), Sadang Serang (WP Cibeunying), Kopo Kencana (WP Tegallega), Turangga (WP Karees), Arcamanik (WP Ujungberung), and Margasari (WP Gedebage) [31]. These centers are designated as central business districts (CBD) which have a significant impact on land values. Urbanization has resulted in urban sprawl, particularly in the eastern and southern parts of the city, leading to the emergence of new built-up areas [32].

2. 1. Data Preparation The data of this study were obtained through purposive sampling, which involved collecting information on 50 land prices and 95 building prices across the city (Figure 2). The sampling process followed specific criteria that were chosen to align with the research objectives [33]. Two key criteria were used in this study: 1) representing property sales, and 2) containing property rental information. It is important to consider income capitalization rates when assessing land values, as they form the basis for property valuation [34-

36]. We determined the capitalization rates based on 5 categories: vacant land (0.5-2%), rental houses (3-5%), shop houses and office houses (6-9%), kiosks and shops (5-10%), and apartments and condominiums (7-2%).

The land data used in this study consisted of geospatial polygons with various attributes, such as price, property type, building area, and site area. To facilitate the analysis, the data were converted into centroids using the Universal Transverse Mercator (UTM) coordinate system with the World Geodetic System (WGS) 1984 as datum [33, 34]. In addition to land values, we also incorporated other relevant information related to development, such as the city-level regional spatial plans (RTRW). These plans were sourced from the Bandung City Government and were obtained from the respective Regional Work Unit (SKPD) as person in charge [39].

2. 2. Data Analysis Land values are determined by comparing market prices with income capitalization. To assess land values accurately, data on property sales and rentals (supply) must be converted into land prices per square meter according to Equations (1)-(3). The geostatistical analysis is used in this study as it provides a stochastic model that allows optimal estimation at random points within the study area [36, 37]. The geostatistical analysis involves measuring variograms or semi-variograms, which include methods such as Circular, Spherical, Tetraspherical, Pentaspherical, Exponential, Gaussian, Rational Quadratic, Hole Effect, K-Bessel, J-Bessel, and Stable [42]. In this study, we utilized 4 semi-variogram models, namely Stable, Gaussian, Spherical, and Exponential, as the basis for Kriging interpolation. Kriging is a spatial interpolation
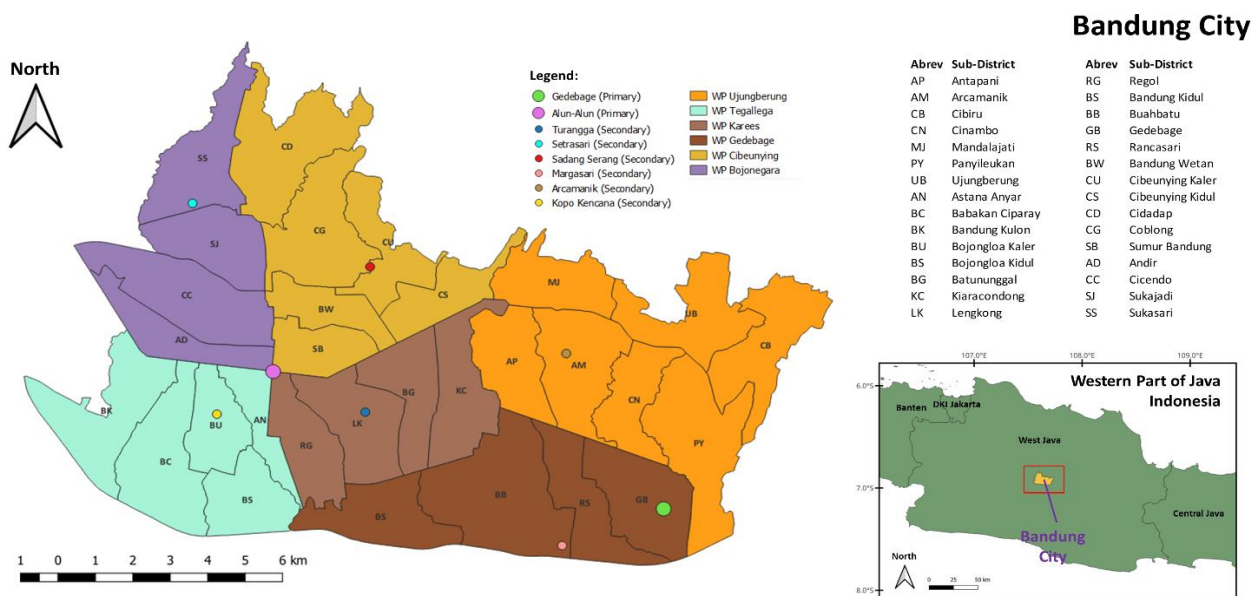
Figure 1. The research location in Bandung City, highlighting its 8 CBDs, 6 WPs, and 30 districts
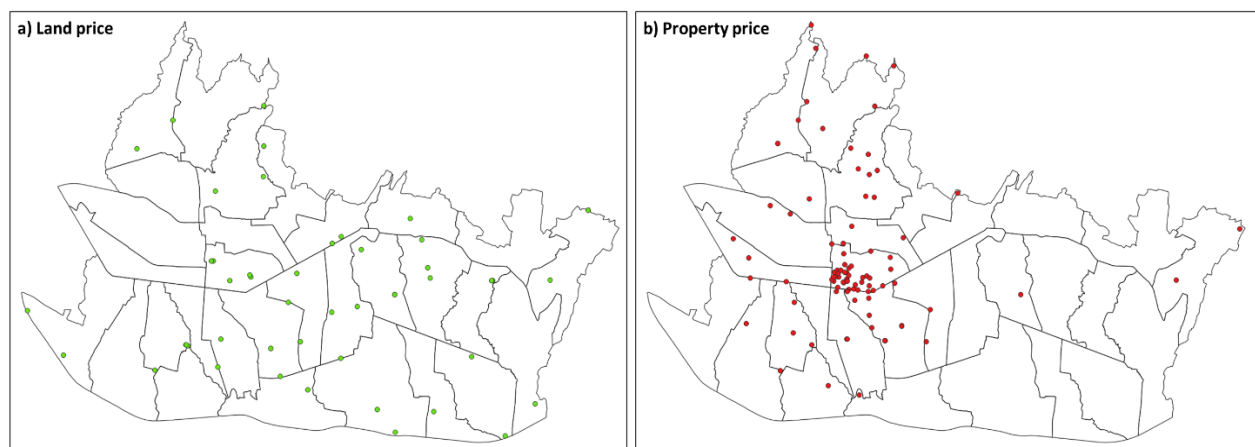
Figure 2. Sample distribution for measuring land values, a) land prices, and b) building prices

technique that provides accurate estimates with lower mean error (ME), root mean square error (RMSE), and R-square (R^2) as shown in Equation (4) [43]. Figure 3 presents the research process for a land value model in Bandung City.

$$LV = \frac{SP}{LA} \tag{1}$$

$$LV = \frac{PP - (BP \times BA)}{LA} \tag{2}$$

$$PP = \frac{ONI}{CL} \tag{3}$$

In the equations used, several variables are defined as follows: LV represents the land value, SP denotes the selling price, LA refers to the land area, PP represents the property price, BP denotes the building price, BA refers to the building area, ONI represents the annual net operating income, and CL represents the capitalization level. The value and price are expressed in units of local currency, while area refers to units per square meter.

$$Z(s) = \mu(s) + \varepsilon(s) \tag{4}$$

$$y(h) = \frac{1}{2\,N(h)}\,[Zi - Zj]^2 \tag{5}$$

In the equations used, the variables are defined as follows: Z(s) represents the expected value of the variable, μ(s) denotes the deterministic trend, ε(s) represents the random error, s indicates the position in a particular space, γ(h) is the semi-variance that describes the expected value between sample values, Z represents the sample value at i and j locations, N(h) represents the number of samples, and H represents the distance between data points (lag).

The semi-variogram is a tool used to assess the correlation between two points in space, and it can be likened to a least squares regression [44]. It quantifies the

Figure 3. Data processing to produce the land value map

expected value of the difference in sample values based on the distance (h) between pairs of sample points (Equation (5)). The semi-variogram is characterized by nuggets, sills, and ranges (spatial trend boundaries) [45]. The nugget represents the variability at zero distance and reflects both sampling and analytical errors, while the sill represents the variability at zero distance and reflects both sampling and analytical error, while still representing the variability of spatially independent samples and acts as the maximum limit of value [46]. To develop a reliable land value model, it is important to ensure that the estimation closely aligns with reality. This can be evaluated using metrics such as root mean square (RMS), mean standardized (MS), root mean square standardized (RMSS), and average standard error (ASE) [43, 44].

3. RESULTS AND DISCUSSION

Land values are attached to each centroid, with x and y coordinates, while the z coordinate serves as the main input for geostatistical analysis. Among the tested semi-variograms, the Stable model performed the best based on the testing of 4 semi-variograms. Figure 4 shows this model accurately estimates the actual land value conditions in Bandung City. The Stable model adjusts the distributions of land values, exhibiting exponential growth that gradually slows down after reaching the saturation phase. Regarding accuracy, the Stable model demonstrates the lowest value as summarized in Table 1. Its positive values for all four error parameters indicate a robust estimation reference for explaining the phenomenon [49-51]. The Stable semi-variogram as the best model has also been proven by researchers in agriculture and geophysics [52, 53].

The Stable semi-variogram and Ordinary Kriging were used to determine the distribution of land values and generate isoline-based classifications, as shown in Figure 5. Ordinary Kriging is an estimation method based on stationary data and BLUE - the best linear unbiased estimator [54]. The combination of precise semi-variogram and Ordinary Kriging would be the best option for numerical variables spatially [55]. In this case, the fit combination produced a land value model in Bandung City. High land values are concentrated around Alun-alun and its surroundings. Alun-alun has served as the primary growth center and has existed since the Dutch East Indies era [56-58]. In the western part of the city, which includes WP Bojonagara, WP Cibeunying, WP Tegallega, and WP Karees, the land values closely follow the pattern established by Alun-alun. In addition to its historical factors, Alun-alun attracts economic activities, such as office areas, businesses, star hotels, and tourism destinations [59, 60].
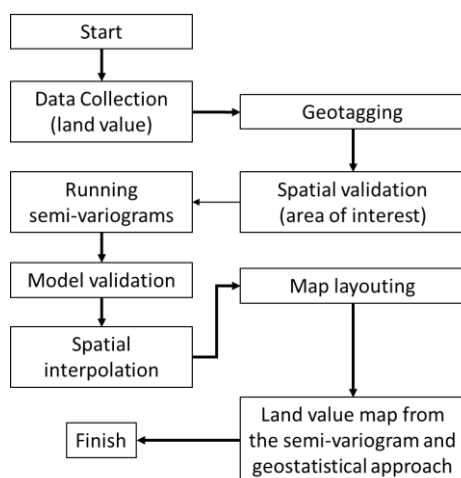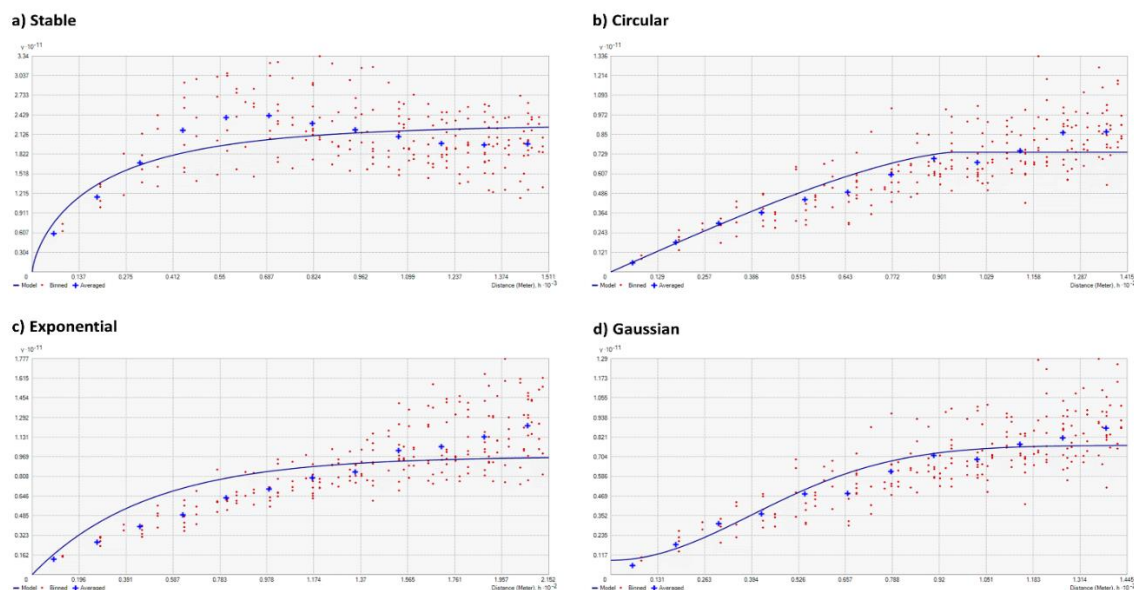
Figure 4. Land values' semi-variogram curves. Where "+" represents the actual values and the line represents an estimated model

TABLE 1. Error comparison for 4 types of semi-variogram in IDR currency unit

Type	RMS	MS	RMSS	ASE
Stable	106,201	0.001	0.790	105,662
Circular	104,958	-0.002	0.694	113,883
Exponential	104,172	-0.003	0.615	126,061
Gaussian	157,840	0.011	0.768	202,135

Different scenarios can be observed in Gedebage and its surroundings. Despite being the second primary center, Gedebage has not experienced an increase in land values. Currently, the area mainly consists of vegetated rice fields. Interestingly, the land value around Arcamanik is higher compared to Gedebage and Margasari. In the eastern part of the city, land values actually increase in the southeastern area, which directly borders Bandung Regency. This area is in close proximity to industrial centers such as Rancaekek and Majalaya, where large textile factories operate. Furthermore, new settlements for workers have emerged on formerly paddy fields, swamps, and brushes [61]. On the other hand, the Jatinangor Education Area, a new growth center, has not been able to significantly increase land values in the east due to its separation from the city by Cileunyi District (Bandung Regency) [62-64]. New
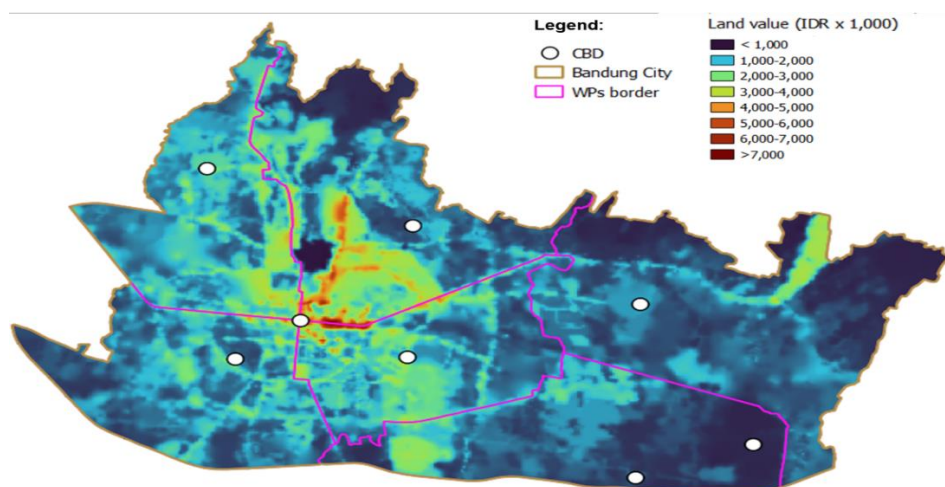
Figure 5. Land price model for Bandung City based on the Stable semi-variogram

growth centers that have not had a significant impact quickly on development often occur in Indonesia because there was still a lack of accessibility, promotion, and community stigma to these projects [65]. West Java itself, not only Gedebage, a similar phenomenon can be seen in Meikarta (Bekasi Regency) and Kertajati (Majalengka Regency) [66-68].

High land values in the city are closely associated with specific spatial patterns, such as government offices, trading areas, defense and security installations, service areas, education institutions, cultural tourism sites, and high-density housing, all forming a cohesive unit (Figure 6). This area serves as the core area as well as the administrative center for the West Java Provincial Government. Zhang et al. [69] revealed that the combination of adaptive expectations and the area's role as a cross-hierarchical government center can significantly impact land values, leading to continuous growth. Interestingly, if the money polarity is not fulfilled, for example only in high-density housing, the land value will not be high as in the southwestern (WP Tegallega). In other areas with lower land values, such as WP Gedebage, the government's effort to develop public infrastructures have not had a significant impact on land prices. Despite the establishment of an internationally renowned sports center (Gelora Bandung Lautan Api Stadium) and the introduction of elite housing projects by national developers [32]. However, these lands do not quickly change land values because

of the political situation at the local to national level which could be changing spatial planning policies every 5-10 years [5, 70]. The influence of historical factors and the existing socioeconomic landscape appears to be more dominant in shaping land values, as they offer a sense of profit certainty [71].

Land values have been increasing in the northern regions of WP Ujung Berung and WP Cibeunying, which are located adjacent to the conservation area. Real-estate developers are tempted to construct housing near these green open spaces, as they provide various ecosystem services to its residents, including fresh air, beautiful scenery, adequate accessibility, and free traffic jam [72-77]. This phenomenon has led to a significant surge in land values, particularly in areas previously dominated by traditional-style housing [78]. Green areas offer cooler temperatures amid the urban heat island in big cities [79]. An imbalance between land value with environment and socio-economic situation and natural factors would threaten urban sustainability [80, 81]. The rise in land prices can be attributed to factors such as accessibility including the presence of arterial or collector roads, as well as the growth rate of land transactions [82-84]. To regulate land values and ensure planned development, the city has implemented a spatial planning document, Bandung City's Regional Regulation Number 18 of 2011, which includes maps outlining the city's development plans from 2011-2031.
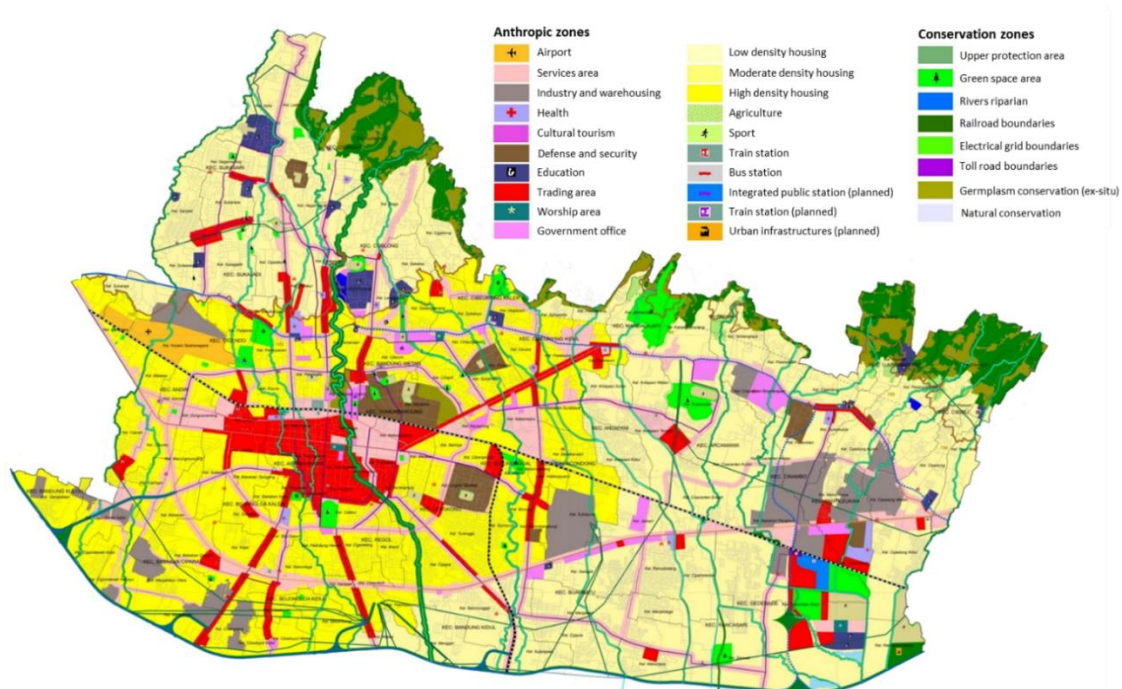
Figure 6. Spatial pattern of Bandung City in 2011-2031. The map is part of a spatial planning document based on Bandung City's Regional Regulation Number 18 of 2011

However, it is worth noting that this document has been revised with the introduction of Bandung City's Regional Regulation Number 05 of 2022. Although, the updated maps are not yet available. These regulatory measures play a vital role in shaping land values, promoting equitable development, and preventing unplanned growth [85-87]. Affordable land and housing for urban communities is a necessity, besides security, rule of law, transportation, communications and basic needs availabilities [88].

4. CONCLUSION

The spatial modeling used semi-variogram (Stable) and geostatistical (Ordinary Kriging) shows that the highest land values are concentrated in the western part of the city, particularly around Alun-Alun. Other growth centers in Bandung city do not affect the land value. Among the four WPs, namely Bojonegara, Cibeunying, Karees, and Tegallega, the highest land value is observed in the area between these areas. The high land values are associated with government offices, trading areas, defense and security installations, service areas, education institutions, cultural tourism sites, and high-density housing. The model also reveals the presence of land values ranging from IDR 3-4 million in proximity to conservation areas located in WP Cibeunying and WP Ujungberung. Densely populated areas have higher land values compared to sparsely populated areas that are dominated by agricultural lands. Despite the existence of spatial patterns and development plans for socio-economic purposes as stated in the document, it appears that new growth centers have no significant impact on the increase in land values. The new growth centers were unable to replicate the same impact as Alun-alun (circa 1810 AD). The high land values observed in Alun-alun highlight those historical aspects and ongoing socio-economic activities carry more impact than planning aspects. Efforts to maintain Alun-alun as a growth center can be seen from the improvement of this site by the government as a center for cultural tourism. This study has limitations because it has not included various other variables. To reveal land values due to new spatial patterns and detailed development plans in Bandung City, further studies are needed that incorporate various urban physical, environmental, social and cultural variables.

5. REFERENCES

1.   Lourenço, I. B., Guimarães, L. F., Alves, M. B., and Miguez, M. G. "Land as a sustainable resource in city planning: The use of open spaces and drainage systems to structure environmental and urban needs." *Journal of Cleaner Production*, Vol. 276, (2020), 123096. https://doi.org/10.1016/j.jclepro.2020.123096

2.   Metternicht, G. Land use and spatial planning: Enabling sustainable management of land resources. Cham: Springer International Publishing. https://doi.org/10.1007/978-3-319-71861-3

3.   Seter, H., Theisen, O. M., and Schilling, J. "All about water and land? Resource-related conflicts in East and West Africa revisited." *GeoJournal*, Vol. 83, No. 1, (2018), 169-187. https://doi.org/10.1007/s10708-016-9762-7

4.   Tong, S., Zhiming, F., Yanzhao, Y., Yumei, L., and Yanjuan, W. "Research on land resource carrying capacity: Progress and prospects." *Journal of Resources and Ecology*, Vol. 9, No. 4, (2018), 331-340. https://doi.org/10.5814/j.issn.1674-764x.2018.04.001

5.   Dede, M., Asdak, C., and Setiawan, I. "Spatial dynamics model of land use and land cover changes: A comparison of CA, ANN, and ANN-CA." *Register: Jurnal Ilmiah Teknologi Sistem Informasi*, Vol. 8, No. 1, (2022), 38–49. https://doi.org/10.26594/register.v8i1.2339

6.   Tsai, Y., Guan, J., and Huang, Y.-H. "Do degradation of urban greenery and increasing land prices often come along with urbanization?" In *Urban Agglomeration*. IntechOpen. https://doi.org/10.5772/intechopen.71651

7.   Ismail, A., Dede, M., and Widiawaty, M. "Urbanisation and HIV in Bandung City (health geography perspectives)." *Buletin Penelitian Kesehatan*, Vol. 48, (2020), 139-146. https://doi.org/10.22435/bpk.v48i2.2921

8.   Dede, M., Asdak, C., and Setiawan, I. "Spatial-ecological approach in cirebon's peri-urban regionalization." *IOP Conference Series: Earth and Environmental Science*, Vol. 1089, No. 1, (2022), 012080. https://doi.org/10.1088/1755-1315/1089/1/012080

9.   Deac, V. "Land valuation in Romania: Challenges and difficulties." *Procedia Economics and Finance*, Vol. 15, (2014), 792-799. https://doi.org/10.1016/S2212-5671(14)00518-8

10.   Abdulla, H., and Ibrahim, M. "The impact of urban spatial plan on land value: an approach system to relating space syntax premises to the land price." *Sustainability*, Vol. 15, No. 9, (2023), 7239. https://doi.org/10.3390/su15097239

11.   Clapp, J. M., Cohen, J. P., and Lindenthal, T. "Are estimates of rapid growth in urban land values an artifact of the land residual model?" *The Journal of Real Estate Finance and Economics*, Vol. 66, No. 2, (2023), 373-421. https://doi.org/10.1007/s11146-021-09834-4

12.   Buda, E., Broitman, D., and Czamanski, D. "Land value dynamics and the spatial evolution of cities following COVID 19 using big data analytics." *The Annals of Regional Science*, Vol. 70, No. 2, (2023), 429-445.

13.   Kendall, R., and Tulip, P. "The effect of zoning on housing prices." SSRN Scholarly Paper, Rochester, NY. https://doi.org/10.2139/ssrn.3149272

14.   Bo, X., Zhicui, L., and Ning, X. "The interactive influence of urbanization, land price and industrial structure adjustment-the empirical analysis from China." *Journal of Business*, Vol. 2, No. 3, (2015).

15.   Aziz, A., Anwar, M. M., and Dawood, M. "The impact of neighborhood services on land values: an estimation through the hedonic pricing model." *GeoJournal*, Vol. 86, No. 4, (2021), 1915-1925. https://doi.org/10.1007/s10708-019-10127-w

16.   Kılıç, O., Baser, U., and Gulser, C. "Factors explaining urban land value variability: A case study in Atakum District, Samsun-Turkey," (2019).

17. Ha, P. T., Tuan, N. T., Quan, N. V., and Trung, N. V. "Land Price Regression Model and Land Value Region Map to Support Residential Land Price Management: A Study in Nghe an Province, Vietnam." *Real Estate Management and Valuation*, Vol. 30, No. 1, (2022), 71-83. https://doi.org/10.2478/remav-2022-0007

18. Elmanisa, A. M., Kartiva, A. A., Fernando, A., Arianto, R., Winarso, H., and Zulkaidi, D. "Land price mapping of Jabodetabek, Indonesia." *Geoplanning: Journal of Geomatics and Planning*, Vol. 4, No. 1, (2016), 53. https://doi.org/10.14710/geoplanning.4.1.53-62

19. Bateman, I. J. "Bringing the real world into economic analyses of land use value: Incorporating spatial complexity." *Land Use Policy*, Vol. 26, (2009), S30-S42. https://doi.org/10.1016/j.landusepol.2009.09.010

20. Krause, A., and Bitter, C. "Spatial econometrics, land values and sustainability: Trends in real estate valuation research." *Cities*, Vol. 29, (2012), S19-S25. https://doi.org/10.1016/j.cities.2012.06.006

21. Duke, J., and Gao, T. "Land value taxation: A spatially explicit economic experiment with endogenous institutions." *The Journal of Real Estate Finance and Economics*, (2021). https://doi.org/10.1007/s11146-021-09875-9

22. Khordadi, M. J., Alizadeh, A., Nassiri-Mahallati, M., Ansari, H., and Sanaeinejad, S. H. "Climate change impact on precipitation extreme events in uncertainty situation; Passing from global scale to regional scale." *International Journal of Engineering, Transactions B: Applications*, Vol. 28, (2015), 1151-1158. DOI: 10.5829/idosi.ije.2015.28.08b.05

23. Widiawaty, M., Dede, M., and Ismail, A. "Kajian komparatif pemodelan air tanah menggunakan sistem informasi geografis di Desa Kayuambon, Kabupaten Bandung Barat." *Jurnal Geografi Gea*, Vol. 18, No. 1, (2018), 63-71. https://doi.org/10.17509/gea.v18i1.10397

24. Dede, Moh., Susiati, H., Widiawaty, M. A., Ismail, A., and Suntoko, H. "Depth estimation model of shallow-tropical seawaters based on remote sensing data and BatNas" (p. 050070). Presented at the Proceedings of the Symposium on Advance of Sustainable Engineering 2021 (SIMASE 2021): Post Covid-19 Pandemic (Challenges and Opportunities in Environment, Science, and Engineering Research), Bandung, Indonesia. https://doi.org/10.1063/5.0112639

25. Bohner, C. "Decision-support systems for sustainable urban planning." *International Journal of Environmental Technology and Management*, Vol. 6, No. 1-2, (2006), 193-205. https://doi.org/10.1504/IJETM.2006.008261

26. Anguillari, E., and Dimitrijević, B. Integrated urban planning: Directions, resources and territories. Delft: TU Delft Open. Retrieved from https://books.bk.tudelft.nl/index.php/press/catalog/book/624

27. Milojević, B. "Integrated urban planning in theory and practice" (Vol. 13, pp. 323-337). Presented at the International conference on Contemporary Theory and Practice in Construction, Sarajevo: National and University Library of Bosnia and Herzegovina.

28. Yigitcanlar, T., Li, R. Y. M., Inkinen, T., and Paz, A. "Public Perceptions on Application Areas and Adoption Challenges of AI in Urban Services." *Emerging Science Journal*, Vol. 6, No. 6, (2022), 1199-1236.

29. Rizki, M., Joewono, T. B., Dharmowijoyo, D. B. E., and Belgiawan, P. F. "Does multitasking improve the travel experience of public transport users? Investigating the activities during commuter travels in the Bandung Metropolitan Area, Indonesia." *Public Transport*, Vol. 13, No. 2, (2021), 429-454.

30. Firman, T. "The continuity and change in mega-urbanization in Indonesia: A survey of Jakarta-Bandung Region (JBR)

development." *Habitat International*, Vol. 33, No. 4, (2009), 327-339. https://doi.org/10.1016/j.habitatint.2008.08.005

31. Putri, P., and Zain, A. F. "Analisis spasial dan temporal perubahan luas ruang terbuka hijau di Kota Bandung." *Jurnal Lanskap Indonesia*, Vol. 2, No. 2, (2010). https://doi.org/10.29244/jli.2010.2.2.%p

32. Widiawaty, M., Dede, M., and Ismail, A. "Analisis tipologi urban sprawl di Kota Bandung." In *Seminar Nasional Geomatika* (Vol. 3, pp. 547-554). Bogor: Badan Informasi Geospasial. https://doi.org/10.24895/SNG.2018.3-0.1007

33. Campbell, S., Greenwood, M., Prior, S., Shearer, T., Walkem, K., Young, S., Bywaters, D., and Walker, K. "Purposive sampling: complex or simple? Research case examples." *Journal of Research in Nursing*, Vol. 25, No. 8, (2020), 652-661. https://doi.org/10.1177/1744987120927206

34. Rianto, R. E., and Jaya, W. K. "Pendekatan penilaian properti untuk estimasi nilai sewa tanah dan bangunan PT. KA (Persero) DAOP IV guna Peningkatan Pendapatan Asli Daerah (PAD) Pemerintah Daerah Istimewa Yogyakarta." *Jurnal Ekonomi dan Bisnis Indonesia*, Vol. 15, No. 3, (2000), 332-338.

35. Bokhari, S., and Geltner, D. "Characteristics of depreciation in commercial and multifamily property: An investment perspective." *Real Estate Economics*, Vol. 46, No. 4, (2018), 745-782. https://doi.org/10.1111/1540-6229.12156

36. Propheter, G. "Estimating the effect of sports facilities on local area commercial rents: Evidence from Brooklyn's Barclays Center." *Journal of Sports Economics*, Vol. 20, No. 1, (2019), 91-114.

37. Widiawaty, M. A. Mari mengenal sains informasi geografis. Bandung: Aria Mandiri Group. Retrieved from https://zenodo.org/record/3263711

38. Susiati, H., Dede, M., Widiawaty, M. A., Ismail, A., and Udiyani, P. M. "Site suitability-based spatial-weighted multicriteria analysis for nuclear power plants in Indonesia." *Heliyon*, Vol. 8, No. 3, (2022), e09088. https://doi.org/10.1016/j.heliyon.2022.e09088

39. Ismail, A., Widiawaty, M. A., Jupri, J., Setiawan, I., Sugito, N. T., and Dede, M. "The influence of Free and Open-Source Software-Geographic Information System online training on spatial habits, knowledge and skills." *Geografia - Malaysian Journal of Society and Space*, Vol. 18, No. 1, (2022), 118-130. https://doi.org/10.17576/geo-2022-1801-09

40. Uyan, M., and Cay, T. "Spatial analyses of groundwater level differences using geostatistical modeling." *Environmental and Ecological Statistics*, Vol. 20, No. 4, (2013), 633-646. https://doi.org/10.1007/s10651-013-0238-3

41. Mulyadi, A., Dede, M., and Widiawaty, M. A. "Spatial interaction of groundwater and surface topographic using geographically weighted regression in built-up area." *IOP Conference Series: Earth and Environmental Science*, Vol. 477, No. 1, (2020), 012023. https://doi.org/10.1088/1755-1315/477/1/012023

42. Uyan, M. "Determination of agricultural soil index using geostatistical analysis and GIS on land consolidation projects: A case study in Konya/Turkey." *Computers and Electronics in Agriculture*, Vol. 123, (2016), 402-409. https://doi.org/10.1016/j.compag.2016.03.019

43. Dede, M., Widiawaty, M., Pramulatsih, G., Ismail, A., Ati, A., and Murtianto, H. "Integration of participatory mapping, crowdsourcing and geographic information system in flood disaster management (case study Ciledug Lor, Cirebon)," Vol. 2, , (2019), 44-50. https://doi.org/10.30818/jitu.2.2.2555

44. Del Giudice, V., and De Paola, P. "Spatial analysis of residential real estate rental market with geoadditive models." In M. d'Amato & T. Kauko (Eds.), Advances in Automated Valuation Modeling: AVM After the Non-Agency Mortgage Crisis (pp.

155-162). Cham: Springer International Publishing. https://doi.org/10.1007/978-3-319-49746-4_8

45. Desassis, N., and Renard, D. "Automatic variogram modeling by iterative least squares: univariate and multivariate cases." *Mathematical Geosciences*, Vol. 45, No. 4, (2013), 453-470. https://doi.org/10.1007/s11004-012-9434-1

46. Legleiter, C. J. "A geostatistical framework for quantifying the reach-scale spatial structure of river morphology: 1. Variogram models, related metrics, and relation to channel form." *Geomorphology*, Vol. 205, (2014), 65-84. https://doi.org/10.1016/j.geomorph.2012.01.016

47. Xie, D., Liu, Y., and Chen, J. "Mapping urban environmental noise: A land use regression method." *Environmental Science & Technology*, Vol. 45, No. 17, (2011), 7358-7364. https://doi.org/10.1021/es200785x

48. Emenike, P. C., Nnaji, C. C., Tenebe, I. T., and Agunwamba, J. C. "Hydrogeochemical imprints and spatio-temporal health risk assessment of lead in drinking water sources of Abeokuta, south-western Nigeria." *International Journal of Environmental Science and Technology*, Vol. 17, No. 1, (2020), 343-360. https://doi.org/10.1007/s13762-019-02506-0

49. Staudte, R. G., and Sheather, S. J. Robust estimation and testing. Hoboken, NJ, USA: John Wiley & Sons, Inc. https://doi.org/10.1002/9781118165485

50. Oliver, M. A., and Webster, R. "A tutorial guide to geostatistics: Computing and modelling variograms and kriging." *Catena*, Vol. 113, (2014), 56-69. https://doi.org/10.1016/j.catena.2013.09.006

51. Dede, Moh., Susiati, H., Widiawaty, M. A., Kuok-Choy, L., Aiyub, K., and Asnawi, N. H. "Multivariate analysis and modeling of shoreline changes using geospatial data." *Geocarto International*, Vol. 38, No. 1, (2023), 2159070. https://doi.org/10.1080/10106049.2022.2159070

52. Pasini, M. P. B., Engel, E., Lúcio, A. D., and Bortolotto, R. P. "Semivariogram models for rice stem bug population densities estimated by ordinary kriging." *Acta Scientiarum. Agronomy*, Vol. 43, (2020), e48310. https://doi.org/10.4025/actasciagron.v43i1.48310

53. Wicaksono, T., Haris, A., Riyanto, A., and Riyadi, P. "Reservoir characterization using stochastic seismic inversion in 'K' gas field, Bonaparte Basin." AIP Conference Proceedings, Vol. 2320, No. 1, (2021), 040001. https://doi.org/10.1063/5.0037688

54. Alfiana, A. N. *Metode Ordinary Kriging pada geostatistika*. Universitas Negeri Yogyakarta.

55. Samui, P., and Sitharam, T. G. "Application of geostatistical models for estimating spatial variability of rock depth." *Engineering*, Vol. 3, No. 9, (2011), 886-894. https://doi.org/10.4236/eng.2011.39108

56. Lim, M., and Padawangi, R. "Contesting alun-alun : Power relations, identities and the production of urban space in Bandung, Indonesia." *International Development Planning Review - INT DEV PLAN REV*, Vol. 30, , (2008), 307-326. https://doi.org/10.3828/idpr.30.3.7

57. Tarigan, A. K. M., Sagala, S., Samsura, D. A. A., Fiisabiilillah, D. F., Simarmata, H. A., and Nababan, M. "Bandung City, Indonesia." *Cities*, Vol. 50, (2016), 100-110. https://doi.org/10.1016/j.cities.2015.09.005

58. Rukayah, R., Juwono, S., S, E., and Puguh, D. "Post office and traditional city square as city linkage in Java." *Environment-Behaviour Proceedings Journal*, Vol. 4, (2019). https://doi.org/10.21834/e-bpj.v4i10.1624

59. Gunawan, S. R., Nindyo, S., Ikaputra, I., and Bakti, S. "Colonial and traditional urban space in Java: a morphological study of ten cities." *Dimensi: Journal of Architecture and Built Environment*, Vol. 40, No. 2, (2013), 77-88.

60. Jones, P. "Formalizing the informal: Understanding the position of informal settlements and slums in sustainable urbanization policies and strategies in Bandung, Indonesia." *Sustainability*, Vol. 9, (2017), 1436. https://doi.org/10.3390/su9081436

61. Megantara, E. N., Husodo, T., Iskandar, J., Nurjaman, D., Suroso, U., Aminuddin, S. F., Atsaury, Z. I. A., Wulandari, I., and Shanida, S. S. "Population and distribution of some herons in Babakan Rancabayawak, Bandung city, Indonesia." *Biodiversitas*, Vol. 22, No. 12, (2021), 5389-5396. https://doi.org/10.13057/biodiv/d221221

62. Salim, W. "Development of the Jatinangor university area, Indonesia." In Global Universities and Urban Development: Case Studies and Analysis. Routledge.

63. Budiyantini, Y., and Pratiwi, V. "Peri-urban typology of Bandung Metropolitan area." *Procedia - Social and Behavioral Sciences*, Vol. 227, (2016), 833-837. https://doi.org/10.1016/j.sbspro.2016.06.152

64. Dachi, C. R. I., Labolo, M., and Suprayitno, D. "Implementation of the General Spatial Planning Policy for the Jatinangor Urban Area, Sumedang Regency, West Java Province." *Publica: Jurnal Pemikiran Administrasi Negara*, Vol. 15, No. 1, (2023), 1-11. https://doi.org/10.15575/jpan.v15i1.24550

65. Prihadi, T. H., Saputra, A., Taufik, I., and Ardi, I. "The application of life cycle assessment to evaluate water quality condition around fish cages in Cirata Reservoir, Indonesia." *Indonesian Aquaculture Journal*, Vol. 12, No. 2, (2017), undefined-undefined. https://doi.org/10.15578/iaj.12.2.2017.83-91

66. Donandi, S. "The legal consequences of incomplete building license to the sales and purchase agreement of apartments (case study of Meikarta's incomplete building license)." *Profit: Jurnal Kajian Ekonomi dan Perbankan Syariah*, Vol. 1, No. 1, (2017). https://doi.org/10.33650/profit.v1i1.317

67. Tjahjono, T., and Yuliawati, E. "Bandar Udara Internasional Jawa Barat (BIJB) dan potensi Kertajati sebagai aerocity." *Warta Ardhia*, Vol. 43, No. 1, (2017), 43-50. https://doi.org/10.25104/wa.v43i1.274.43-50

68. Ricardianto, P., Martagani, M., Teweng, N. M., Maemunah, S., and Kurniawan, J. S. "Strategy to increase passenger attractiveness at Kertajati International Airport, West Java." *Journal of Research in Humanities and Social Science*, Vol. 9, No. 9, (2021), 31-37.

69. Zhang, Y., Zhou, R., and Chen, N. "Identification and correction of ratchet effect of residential land price: empirical study on urban agglomeration in China." *Applied Economics*, (2022), 1-17. https://doi.org/10.1080/00036846.2022.2140768

70. Margono, R. B., and Zuraida, S. "Public space as an urban acupuncture: Learning from Bandung, Indonesia." *Journal of Applied Science*, Vol. 1, No. 1, (2019), 022-033. https://doi.org/10.36870/japps.v1i1.5

71. Binoy, B. V., Naseer, M. A., and Anil Kumar, P. P. "Factors affecting land value in an Indian city." *Journal of Property Research*, Vol. 39, No. 3, (2022), 268-292.

72. Dede, M., Sunardi, S., Lam, K. C., and Withaningsih, S. "Relationship between landscape and river ecosystem services." *Global Journal of Environmental Science and Management*, Vol. 9, (2023), 637-652. https://doi.org/10.22035/gjesm.2023.03.18

73. Ignasia, H. Transformations and conservation of the ex-colonial dwelling settlements in North Bandung - Indonesia : a historical and urban architectural review for the search of city identity and conservation strategy approaches (doctoralThesis). Retrieved from http://elib.uni-stuttgart.de/handle/11682/83

74. Alam, Md. J. "Rapid urbanization and changing land values in mega cities: implications for housing development projects in Dhaka, Bangladesh." *Bandung: Journal of the Global South*,

Vol. 5, No. 1, (2018), https://doi.org/10.1186/s40728-018-0046-0

75. Ali, M., Hasim, A., and Abidin, M. "Monitoring the built-up area transformation using urban index and normalized difference built-up index analysis." *International Journal of Engineering, Transactions B: Applications*, Vol. 32, (2019), 647-653. https://doi.org/10.5829/ije.2019.32.05b.04

76. Hafram, M., Valery, S., and Hasim, A. "Calibrating and validation microscopic traffic simulation models vissim for enhanced highway capacity planning." *International Journal of Engineering, Transactions B: Applications*, Vol. 36, No. 8, (2023), 1509-1519. https://doi.org/10.5829/IJE.2023.36.08B.11

77. Ergin, M., and Tezcan, H. "Joint Logit Model Approach to Analyze Soccer Spectators' Arrival Time and Location Preferences for Interim Activities in Istanbul." *International Journal of Engineering, Transactions A: Basics*, Vol. 35, No. 4, (2022), 613-625. https://doi.org/10.5829/ije.2022.35.04a.01

78. Zhang, P. "The dynamics of housing price and land price in urban versus rural contexts" (Vol. 108, pp. 1-40). Presented at the Annual Conference on Taxation and Minutes of the Annual Meeting of the National Tax Association, National Tax Association. Retrieved from https://www.semanticscholar.org/paper/The-Dynamics-of-Housing-Price-and-Land-Price-in-Zhang/709d44e78481ba67a098fa1244cf5015f974f492

79. Doi, R. "Are New Residential Areas Cooler than Older Ones?" *Emerging Science Journal*, Vol. 6, No. 6, (2022), 1346-1357. https://doi.org/10.28991/ESJ-2022-06-06-08

80. Mazzocchi, C., Orsi, L., and Sali, G. "Environmental, climate and socio-economic factors in large-scale land acquisitions (LSLAs)." *Climate Risk Management*, Vol. 32, (2021), 100316-. https://doi.org/10.1016/j.crm.2021.100316

81. Alaskary, A., and Alrobaee, T. "Identifying and measuring biophilic planning indicators in Riverside neighborhoods." *Civil Engineering Journal*, Vol. 8, No. 1, (2022), 33-44. https://doi.org/10.28991/CEJ-2022-08-01-03

82. An, P., Li, C., Duan, Y., Ge, J., and Feng, X. "Inter-metropolitan land price characteristics and pattern in the Beijing-Tianjin-Hebei urban agglomeration, China." *Plos One*, Vol. 16, No. 9, (2021), e0256710. https://doi.org/10.1371/journal.pone.0256710

83. Bencure, J. C., Tripathi, N. K., Miyazaki, H., Ninsawat, S., and Kim, S. M. "Factors affecting decision-making in land valuation process using AHP: A case in the Philippines." *International Journal of Housing Markets and Analysis*, Vol. 15, No. 1, (2021), 188-202. https://doi.org/10.1108/IJHMA-11-2020-0136

84. Shah, P. B., and Patel, C. R. "Remote sensing and big data to study spatial distribution of urban heat island for cities with different terrain." *International Journal of Engineering, Transactions A: Basics*, Vol. 36, No. 1, (2023), 71-77. https://doi.org/10.5829/ije.2023.36.01a.09

85. Yang, S., Hu, S., Wang, S., and Zou, L. "Effects of rapid urban land expansion on the spatial direction of residential land prices: Evidence from Wuhan, China." *Habitat International*, Vol. 101, (2020), 102186. https://doi.org/10.1016/j.habitatint.2020.102186

86. De Souza, F. F. Land readjustment in Denpasar, Indonesia: Effects on land management, the spatial distribution of land prices, and the sustainable development goals. Asian Development Bank. Retrieved from https://www.adb.org/publications/land-readjustment-denpasar-indonesia

87. Tutuko, P., Bonifacius, N., Yuniawan, D., and Jati, R. M. B. "Measuring spatial arrangement of Indonesian colonial cities using depth and connectivity calculations: Ratio study on master plans using space syntax." *International Review for Spatial Planning and Sustainable Development*, Vol. 9, No. 4, (2021), 67-81. https://doi.org/10.14246/irspsd.9.4_67

88. Al-Jawari, S. M., Hasach Albasri, N. A., and Al-Mosherefawi, O. J. "Using CRF tool for analyzing the resilience of cities." *Civil Engineering Journal*, Vol. 8, No. 10, (2022), 2220-2234. https://doi.org/10.28991/CEJ-2022-08-10-013

Persian Abstract

چکیده

در دسترس بودن زمین در شهر باندونگ به چالشی برای توسعه شهری تبدیل شده است .باندونگ علاوه بر جاکارتا، سورابایا، مدان و ماکاسار مدت‌هاست مقصد شهرنشینی اندونزیایی‌ها بوده است .در حال حاضر هنوز تحقیقات محدودی وجود دارد که ارزش زمین و برنامه ریزی فضایی را برای مناطق شهری بررسی می کند .این مطالعه با هدف توسعه مدل‌سازی فضایی برای ارزش‌های زمین با استفاده از رویکرد نیمه متغیری و زمین‌آماری در مناطق شهری انجام شده است .تحقیق ما در شهر باندونگ، جاوای غربی، اندونزی انجام شد .داده‌ها بر اساس نمونه‌گیری هدفمند شامل 50 نمونه قیمت زمین و 95 نمونه قیمت ساختمان در سراسر شهر انتخاب شدند .سپس داده‌های جمع‌آوری‌شده با استفاده از 4 مدل نیمه‌واریوگرام و کریجینگ معمولی برای استخراج توزیع فضایی ارزش‌های زمین مورد تجزیه و تحلیل قرار گرفت .ارزش زمین به مدل سازی فضایی از سیستم اطلاعات جغرافیایی اشاره دارد .نتایج تجزیه و تحلیل نشان داد که نوع پایدار نیمه متغیری مناسب ترین مدل است که کمترین خطا را بر اساس ریشه میانگین مربعات استاندارد شده، ریشه میانگین مربع استاندارد شده و میانگین خطای استاندارد نشان می دهد .طبق مدل ما، مناطق با بالاترین ارزش زمین در نزدیکی میدان شهر «alun-alun» قرار دارند که ارتباط نزدیکی با ادارات دولتی، مناطق تجاری، تأسیسات دفاعی و امنیتی، مناطق خدماتی، آموزش، گردشگری فرهنگی و مسکن با تراکم بالا این مناطق از دوران هند شرقی هلند به خوبی شناخته شده است .جالب اینجاست که علیرغم قطب رشد در گدباج، قسمت غربی باندونگ در مقایسه با قسمت شرقی ارزش زمین بالاتری دارد .این را می توان به جنبه های تاریخی و واقعی نسبت داد که تأثیر بیشتری بر ارزش زمین نسبت به طرح های منطقه ای اجرا شده توسط دولت داشته است .مدیریت ارزش زمین برای تضمین فضای زندگی و همچنین دستیابی به یک شهر پایدار ضروری است.

International Journal of Engineering

Effective Blended Learning Model Selection Based on Student Learning Style using Analytic Hierarchy Process for an Undergraduate Engineering Course

S. Maidin*, M. A. Shahrum, L. Y. Qian, T. K. Rajendran, S. Ismail

Faculty of Manufacturing Engineering, Universiti Teknikal Malaysia Melaka, Hang Tuah Jaya, 76100 Durian Tunggal, Melaka, Malaysia

P A P E R   I N F O

A B S T R A C T

Blended learning is a flexible method conducted through face-to-face and online learning. It requires students to learn by attempting the classes physically and allows them to learn virtually at different times and places. It has become more evident and common after the Movement Control Order (MCO) as most of the lectures at the university are carried out in hybrid mode. The blended learning models create problems and opportunities for students as they need to explore and adapt to different lecturers' different blended learning methods in terms of teaching styles, planning, and timing. Therefore, the objective of this research is to investigate the best-blended learning models for an undergraduate engineering course based on student learning style by using the Analytic Hierarchy Process (AHP) method, as it is a big challenge to select the most effective approach for universities to educate, tutor and bring out quality students according to their learning styles. The AHP method is used to aid the students in finding the best-blended learning model based on their learning style. AHP analysis is then conducted to validate and verify its accuracy by comparing it with Visual, Auditory, Read/write, and Kinesthetic (VARK) models. As a result, most students are kinaesthetic learners (72%) based on VARK results, and the face-to-face driver model is the most preferred blended learning model with the priority vector at 31.33% through the AHP analysis. The accuracy of the AHP result is 74% by comparing it with the VARK result. In summary, the data can be deployed in the UTeM blended learning system to improve the course design and student learning experience.

Graphical Abstract
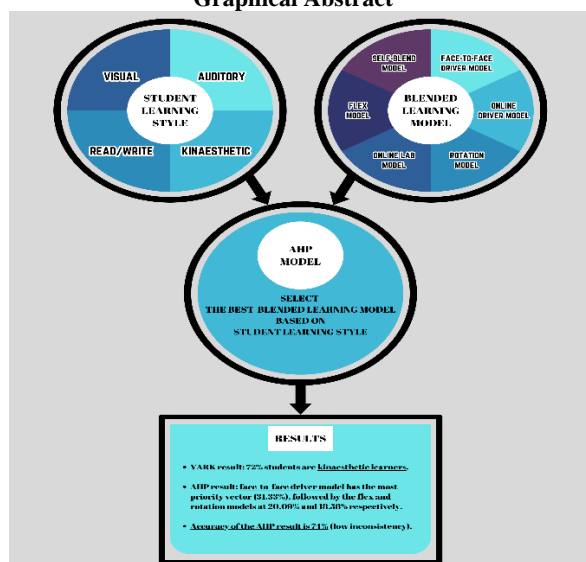
NOMENCLATURE

AHP	Analytic Hierarchy Process	MCO	Movement Control Order
AR	Augmented Reality	MODM	Multi-objective Decision-making
C.I.	Consistency Index	PCM	Pairwise Comparison Matrix
COVID-19	CoronavirusDisease 2019	R.I.	Random Index
C.R.	Consistency Ratio	TOPSIS	Technique for Order of Preference by Similarity to Ideal Solution
FKP	Fakulti Kejuruteraan Pembuatan (Faculty of Manufacturing Engineering)	UTeM	Universiti Teknikal Malaysia Melaka
HCI	Human-Computer Interaction	VARK	Visual, Auditory, Read/Write, Kinaesthetic
MADM	Multi-attribute Decision-making	VIKOR	VIseKriterijumska Optimizacija I Kompromisno Resenje
MCDM	Multi-criteria Decision-making		

Corresponding Author Email: shajahan@utem.edu.my (S. Maidin)

1. INTRODUCTION

Blended learning is a new educational methodology in 21st-century education. Its primary purpose is to create and provide an integrated classroom involving all learners from different places. There are six main blended learning models to explore and choose from face-to-face driver, online driver, rotation, flex, online lab, and self-blend to stimulate and engage students to have more significant gains innovatively. Students are more likely to succeed when face-to-face learning is combined with online learning options [1]. Blended learning can be an effective learning method as it enhances the teaching-learning experiences, especially for students facing various blended learning models [2]. Also, the students can identify their learning needs in terms of knowledge and skills through blended learning [3]. It improves students' brainstorming outcomes by exposing them to a more flexible environment that can propose more ideas and solutions [4].

However, blended learning comes with several limitations. Various types of blended learning models have been designed due to no standard for integrating the blended learning concept [5]. As different lecturers have designed different blended learning models based on their understanding of the concept, it challenges students to habituate to the blended learning style and its planning [6]. For example, learning technology and technology for teaching and training are the challenges that need to be faced by the students and lecturers, respectively [7]. Each model has its concept and characteristics that may affect the student's understanding and learning outcome [8]. Compared to fully online learning, blended learning is ineffective due to external factors like environment, knowledge, and skills [9]. To ensure that engineering students can stand a chance in competing in the industrial fields with the knowledge and skills required in management, planning, problem-solving and decision-making, blended learning models in the universities significantly impact the students. By referring to the available blended learning models, universities face the challenges of selecting the appropriate ones as it impacts the student's learning effectiveness and the university's reputation.

The COVID-19 pandemic forced most education institutions worldwide to switch to online learning as a substitute method of ensuring that the offered content is workable for student growth. As a result of this situation, a significant quantity of online education began. To offer knowledge, this utilized a variety of formats and interfaces and a misperception that students should be responsible for their learning results. Although most students concur that online learning offers a positive learning environment and better professional prospects through improved teamwork, students with special needs and budgetary constraints face technical difficulties and may not be given equal access to technology [10]. Also, online-based learning would lead to social isolation as it decreases engagement between the lecturer and friends. Several technical and communication skills can only develop effectively during face-to-face interaction [11].

As one of the core elements of multimedia applications is education technology, the teaching and learning process in the education system is greatly improved by interactive multimedia [12]. Numerous alternative e-learning options are available nowadays, some of which are free. Design preservation and utilization can be accelerated using Human-Computer Interaction (HCI) design rationales as a learning resource [13]. Due to students in the higher education field differing in age, it is crucial to consider all of the HCI principles to ensure that the proper e-learning solution is integrated with a suitable interface design, especially in an HCI classroom [14].

The education system has undergone significant change due to technology's rapidly expanding use, and students and lecturers now have better digital abilities [15]. The metaverse has been designed as a learning environment with immense potential. As a result, compared to existing approaches that currently use technology, such as flipped learning and e-learning, the metaverse's immersion possibilities grow [16]. Additionally, technology can affect how people think, learn, and communicate. Technological improvements push lecturers and students to comprehend and apply technology in teaching and learning activities to provide a flexible learning environment. The aspects that increase student analytical thinking skills are studied by flipping the classroom and combining digital storytelling and inquiry-based learning (IBL) [17]. The students agreed with the development of augmented reality (AR) in blended learning since it provided students freedom in learning time and period [18]. It also improved their self-discipline, integrity, and accountability.

Moreover, student learning styles in terms of personalities and characteristics are also crucial in leading the blended learning model to succession [19]. It cannot develop students' communication skills to interact with others during the online seminar if they hide behind the screen [20]. Students who cannot provide instant and concrete responses during blended learning will become passive participants [21]. Besides, technical issues related to the devices' hardware and software, like weak internet connection and bad sound delivery, will affect the quality of blended learning models that require online seminars [22]. Hence, educators need to learn a new skill in understanding blended learning models and select a suitable model to implement a delivery system that works well for their students.

There are four main student learning styles in the VARK model: Visual, Auditory, Reading/Writing, and Kinaesthetic. The VARK inventory provides metrics in

each of the four perceptual modes, with individuals having preferences for anywhere from one to all four. The students have relative preferences along the four perceptual modes but can learn to function in the other modes. It focuses on classifying how the students receive and gather the information [23]. It helps the students identify their learning styles and understand their personalities [24]. A study compares the impact of the conceptual map and conventional lecture approaches on students' learning based on the VARK learning styles model [8]. The results have shown that implementing the VARK model can effectively identify the student's preferred learning styles to enhance the standard of education and promote deeper learning. Through the VARK models, the students can improve their performance and enhance their study skills precisely as they understand their strengths in learning style and habit. There are also differences in learning approaches for the four VARK learning styles. Visual learners prefer videos, pictures, graphs and colours as they can remember what they have seen the most [25]. Auditory learners like to explain new ideas to others; hence, open discussion to discuss topics with others will suit them well [19]. Read/Write learners have a habit of taking notes based on reading materials like essays, reports, textbooks, printed handouts, readings, manuals, and web pages to improve their learning [26]. Kinaesthetic learners prefer hands-on approaches that link the material to reality, like doing things to understand them and finding solutions to problems [27].

Nevertheless, there are several limitations to the VARK models. The model does not consider external factors or other variables like student aspiration and abnormalities in learning. The models can be inaccurate as the student may apply different learning styles depending on different situations. Students are not limited to one learning style only in their studies [28]. Most students may have multimodal learning styles depending on the course and subject. Besides, the result data collected from VARK questionnaires can also be inaccurate if students answer them dishonestly. Students may expect their learning style and lead the VARK questionnaire into the results they would like to see. Hence, applying the VARK models to the students may be a dilemma. A good strategy for behaviours and development can be planned for the students so that their learning process and experiences can be benefited to the maximum.

Next, the multi-criteria decision-making (MCDM) method is a decision-making process with multiple criteria to consider. These methods can help decision-makers choose between different options, rank options or allocate resources [29]. In MCDM, many tools and methods can be used, ranging from simple methods like weighted sum models to more complex methods such as Analytic Hierarchy Process (AHP), VIseKriterijumska

Optimizacija I Kompromisno Resenje (VIKOR) and Technique for Order of Preference by Similarity to Ideal Solution (TOPSIS). The MCDM method of choice is determined by the specific decision-making problem. Some factors included are the number of criteria, the type of data available, and the decision maker's preferences. MCDM is widely implemented in various fields, including finance, engineering design, agriculture, and environmental management. MCDM is an effective decision-making method that may result in more information and better conclusions by properly organizing complicated situations and openly evaluating many factors [29]. MCDM methods can be classified into two main categories. The first is multi-attribute decision making (MADM), used to choose a single option from various possibilities. The options are scored against a set of criteria, and the option with the greatest overall rating is picked. The second one is multi-objective decision-making (MODM), which is used to identify the approach that provides the best potential trade-off among the objectives.

In this research, the AHP model is focused as the engineering tool to conduct multi-criteria decision-making. It is categorized as a MADM method and helps analyse complex decisions to identify the best decision using math and psychology knowledge [30]. It is an inclusive system as it can quickly structure problems from different aspects and backgrounds into a hierarchy to represent them [31]. The AHP method can be used for highly diversified input data [32]. Also, the AHP method can handle the bigger issues and make it ideal for planning, analysis, and decision-making purposes among many alternatives [33]. The AHP evaluates the outcomes of each pairwise comparison using linear algebra. Linear algebra is a mathematical concept that aids in using matrices to determine the weight of criteria. Each criterion is given its weight in terms of importance. The more significant a criterion is to the final judgement, the larger its weight. Numerous decisions can be made using this comparing technique [34]. However, AHP only allows use in triangular fuzzy numbers and not all linear equations will come with a solution [35]. As the handling issues become more extensive, the level number of hierarchy increases [36]. This led to the number of pairs increasing and more effort and time are required for analysis. AHP can be applied in various fields like engineering, science, and mathematics for analysis purposes, but the final decision made from the modeling method is not pledged.

This research will explore the student learning styles for undergraduate manufacturing engineering course students by using VARK models at the Faculty of Manufacturing Engineering at Universiti Teknikal Malaysia Melaka (UTeM). VARK questionnaire will be used for data collection. From the VARK questionnaire results, students' preferred blended learning models are

classified. Then, the AHP model is developed to select the best blended learning model based on student learning style. The generated AHP model is compared with the VARK model results to validate its accuracy. It is essential to investigate in terms of theoretical preparation and experimental expertise with blended learning to identify the suitable blended learning model for universities to educate, tutor and bring out quality students.

2. METHODOLOGY

2. 1. Overview of the Study   The research is focused on exploring the students' preferred blended learning model based on their learning style with the application of VARK and AHP models. Figure 1 shows the research process flow chart procedure. The methods and equipment used are also listed for data collection and analysis.

2. 2. Data Collection   A total of fifty year-four students have been chosen from the Faculty of Manufacturing Engineering at UTeM to be involved in the data collection as they have experienced all six types of blended learning models throughout their university life in UTeM. UTeM has implemented these six types of models in the blended learning system for the degree courses. So, their feedback is more practical and accurate than students from the other years and whoever only theoretically knows the blended learning models.

Figure 1. Research Process Flow Chart

Specifically, these students are selected from the undergraduate engineering course. The faculty has nearly 1000 students, meaning 5% of the sample population is randomly picked to participate in the survey. A simple random sample is applied in this research as this technique is the easiest probability sampling technique to use. Based on the literature review, the sample population is between 3 – 10%. Since randomization is included, this method has high internal and external validity and is less likely to be biased by factors like sampling and selection bias. There are several other feasible alternatives to simple random sampling, such as stratified sampling, cluster sampling and systematic sampling. These methods might introduce more variability compared to simple random sampling.

There are several tools and equipment are used to complete the research. To conduct the literature review, the research is done through journals, research papers and articles from physical and online publications. The main websites used for research included Google Scholar, Scopus and ScienceDirect. The reviewed topics are related to the research in terms of VARK, blended learning and AHP models. Besides, an online questionnaire is used to collect data from the 50 selected students in UTeM via Google Forms. The contents are a VARK questionnaire retrieved from VARK Learn Limited 2023, version 8.01, and a short survey on the students' preferred blended learning model. To conduct quantitative analysis for complex data, the software program Microsoft Excel is utilized for statistical analysis purposes. The Excel framework, fundamental data presentation and management, descriptive statistics, and common statistical analysis are all provided in Excel.
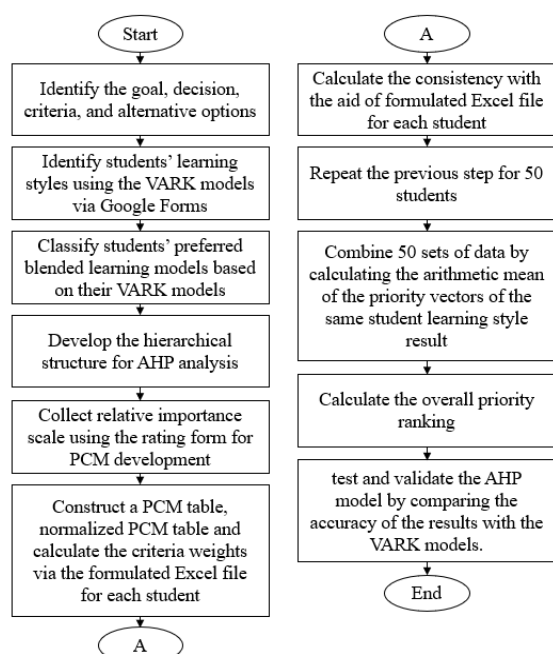
2. 3. AHP Model Development   The AHP model is used to identify the best-blended learning model based on student learning style. The AHP relate the student learning styles determined by VARK models with the six blended learning models to form 24 possible combinations. The following steps show the procedure of applying AHP for decision-making in this research.
1. The problem and objective are defined. The problem is that various types of blended learning models have been designed because there is no standard for integrating the blended learning concept and each model has its concept and characteristics that may affect the student's understanding and learning outcome. So, the objective is to identify the best blended learning model based on student learning style.
2. The hierarchical structure is developed by identifying the criteria and alternative options for this research as shown in Figure 2. The top tier is the objective, the second tier is the criteria and the third tier is the alternative options. In this research , the VARK model is the criteria while the blended learning models are the alternative options.

3. A pairwise comparison matrix is constructed. The pairwise comparison matrix is used to determine the relative importance of different criteria with respect to the objective. The value can be determined by comparing two elements based on the relative importance scale (row element divided by column element). Table 1 shows the relative importance scale used for rating the PCM. Then, the normalized pairwise comparison matrix is calculated by summing the total value for each column element, and then each column value is divided by the total value for each column element. Next, the criteria weights are calculated. Equation (1) shows the formula for calculating the priority vectors from the normalized pairwise comparison matrix. Figure 3 shows the formulated Excel template used to develop the AHP model. The relative importance scale is keyed into the green column, and it will calculate the priority vectors for the blended learning models.

$$\text{Priority vector for each row} = \frac{\text{Sum of row elements}}{\text{Number of criteria}} \quad (1)$$

4. The consistency is calculated. The weighted value is calculated by multiplying the not normalized pairwise matrix value with the criteria weights in column sequence. Then, the weighted sum value is calculated by summing up the weighted value in the row sequence. The weighted sum value and criteria weights ratio are calculated for each row. After that, the average ratio of weighted sum value and criteria weights, λ_{max} is calculated as shown in Equation (2). After λ_{max} is determined, the consistency index (C.I.) and consistency ratio (C.R.) are determined as shown in Equations (3) and (4). When calculating C.R., the random index (R.I.) is involved and its value is determined based on the number of compared elements. Table 2 shows the random index.
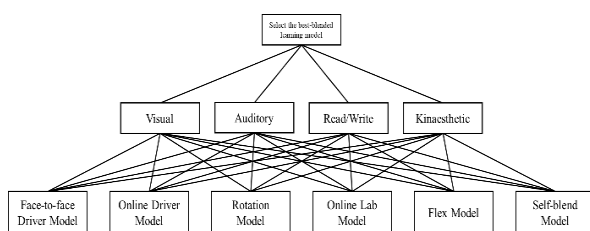
Figure 2. Hierarchical Structure of the AHP Model

TABLE 1. Relative Importance Scale

Verbal Judgement of Preference	Numerical Rating
Extremely Preferred	9
Very Strongly Preferred	7
Strongly Preferred	5
Moderately Preferred	3
Equally Preferred	1
Intermediate Values	2, 4, 6, 8

Pairwise Comparison Matrix	Face-to-face Driver	Online Driver	Rotation	Online Lab	Flex	Self-Blend		
Face-to-face Driver	1	3	7	8	5	9		
Online Driver	1/3	1	5	7	3	7		
Rotation	1/7	1/5	1	3	0.333	4		
Online Lab	1/8	1/7	1/3	1	0.2	3		
Flex	1/5	1/3	3	5	1	5		
Self-Blend	1/9	1/7	1/4	1/3	1/5	1		
SUM	1.9123	4.8190	16.5863	24.3333	9.7330	29.0000		

Normalized PCM	Face-to-face Driver	Online Driver	Rotation	Online Lab	Flex	Self-Blend	Criteria Weights	Priority Vector
Face-to-face Driver	0.5229	0.6225	0.4220	0.3288	0.5137	0.3103	0.4534	45.34%
Online Driver	0.1743	0.2075	0.3015	0.2877	0.3082	0.2414	0.2534	25.34%
Rotation	0.0747	0.0415	0.0603	0.1233	0.0342	0.1379	0.0787	7.87%
Online Lab	0.0654	0.0296	0.0201	0.0411	0.0205	0.1034	0.0467	4.67%
Flex	0.1046	0.0692	0.1811	0.2055	0.1027	0.1724	0.1392	13.92%
Self-Blend	0.0581	0.0296	0.0151	0.0137	0.0205	0.0345	0.0286	2.86%
SUM	1	1	1	1	1	1		

Figure 3. PCM and Normalized PCM Tables in the Formulated Excel

If C.R. is less than 0.1 (10%), the system is considered standard and reasonably consistent. Instead, the system is considered as not consistent and the criteria weights have to be recalculated to get it consistent. Figure 4 shows the consistency analysis tables used in the formulated Excel. If C.R. is less than 0.1, the indicator column will show VALID in green. Instead, it will show INVALID in red.

$$\lambda_{max} = \frac{\text{Sum of the ratio of weighted sum value and criteria weights}}{\text{Number of criteria}} \quad (2)$$

$$C.I. = \frac{\lambda_{max} - n}{n - 1} \quad (3)$$

$$C.R. = \frac{C.I.}{R.I.} \quad (4)$$

5. Steps 3 to 4 are repeated to develop the pairwise comparison matrix, priority vectors, and consistency ratio for the 50 sets of data collected from the students.
6. The overall priority vector is calculated by calculating the arithmetic mean of the priority vectors of the same student learning style result, as shown in Equation (5).

TABLE 2. Random Index

n	1	2	3	4	5	6	7	8	9	10
R.I.	0.00	0.00	0.58	0.90	1.12	1.24	1.32	1.41	1.45	1.49

Consistency Analysis	Face-to-face Driver	Online Driver	Rotation	Online Lab	Flex	Self-Blend	Weighted Sum Value	WSV/CW
Face-to-face Driver	0.4534	0.7603	0.5506	0.3736	0.6962	0.2573	3.0914	6.818
Online Driver	0.1511	0.2534	0.3933	0.3269	0.4177	0.2001	1.7426	6.876
Rotation	0.0648	0.0507	0.0787	0.1401	0.0464	0.1144	0.4949	6.293
Online Lab	0.0567	0.0362	0.0262	0.0467	0.0278	0.0858	0.2794	5.983
Flex	0.0907	0.0845	0.2362	0.2335	0.1392	0.1430	0.9271	6.658
Self-Blend	0.0504	0.0362	0.0197	0.0156	0.0278	0.0286	0.1783	6.234

λmax	6.4771	
Consistency Index (C.I.)	0.0954	
Random Index (R.I.)	1.24	
Consistency Ratio	0.0770	VALID

Figure 4. Consistency Analysis Table in the Formulated Excel

Then, the overall priority vectors are ranked by the combination of multiplication between weight and priority vector from each student's learning style result. The AHP ranking of alternative options is finalized by sorting the overall priority ranking result calculated from the previous step based on a higher priority in table format. The alternative option with the highest priority vector will be selected as the best option.

$$Arithmetic\ mean = \frac{N_1 + N_2 + N_3 + \cdots + N_n}{n} \qquad (5)$$

7. The AHP result is compared with the VARK result from the questionnaire to test and validate its accuracy regarding the number of students correctly identified in the AHP model based on the VARK model. Only the number of students correctly identified in the AHP model based on the VARK model is included.

3. RESULTS AND DISCUSSION

3. 1. VARK Model Analysis   The first objective of this research is to identify students learning styles by using the VARK models. Hence, the VARK questionnaire determines a person's preferred learning style. After the data is collected, it is analyzed via the formulated Excel by pasting the results of each student into specific columns to show the students' learning styles. However, cases are being found that several students have multimodal learning styles in which they get the same highest number for two or more learning styles in the VARK questionnaire. This demonstrates that these students can remember more information when learning through various senses. Interviews with the specific students are made to identify their most dominant learning style in the manufacturing engineering course to prevent miscellaneous results in the VARK model. Table 3 shows the number of students based on their learning styles. The majority of engineering students are kinaesthetic learners.

Next, VARK analysis proceeded to achieve this research's second objective: to classify students' preferred blended learning models based on their VARK models. The VARK questionnaire created in Google Forms is used to identify students' preferred blended

TABLE 3. Number of Students Based on Their Learning Style in the VARK Model

Student Learning Style	Number of Students
Visual	5
Auditory	8
Read/Write	1
Kinaesthetic	36
TOTAL	**50**

learning models. Six types of models are explained in short and the students must select the most preferred blended learning model. Then, they must also mention the reason for preferring that model. Table 4 shows the number of students with their preferred blended learning models, while Figure 5 shows the stacked bar graph of students' preferred blended learning models based on their VARK models.

Based on the results, 50% of the students preferred the face-to-face driver model. Most students mentioned that the face-to-face driver model is easier to understand the lesson during the learning process than other learning models. They can directly communicate with the lecturer face-to-face when they find questions in learning. It is an easier and more effective model, especially in engineering courses that require lots of practice and skills development. This has shown that these students prefer a blended learning model that can learn affordably in terms of efficiency and effectiveness, although more time and energy are required compared to other models.

Then, 12 students preferred the rotation model. They believed this model can reduce the frequency of attending classes physically. They claimed that the theoretical lesson can be conducted online, and they would like to attend physical classes only when there is a requirement

TABLE 4. Number of Students with Their Preferred Blended Learning Models

Blended Learning Models	Number of Students				TOTAL
	V	**A**	**R**	**K**	
Face-to-face Driver Model	4	4	1	16	25
Online Driver Model	0	0	0	1	1
Rotation Model	0	3	0	9	12
Online Lab Model	0	0	0	0	0
Flex Model	1	1	0	9	11
Self-blend Model	0	0	0	1	1
TOTAL	**5**	**8**	**1**	**36**	**50**
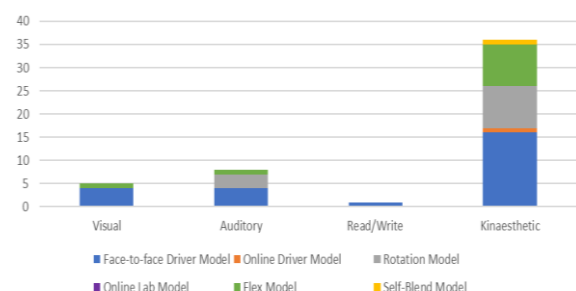
Figure 5. Students Preferred Blended Learning Models Based on Their VARK Models

for hands-on activities such as skill practices and lab sessions. It is an efficient model for students and lecturers as it reduces the time wasted in preparing themselves to attend a physical class for simple theoretical lessons. Furthermore, 11 students preferred the flex model. The students indicated that the flex model is better as it provides options for them to attend the class physically or remotely. It is a flexible learning model for the students because it allows them to manage at their own pace and time to study and brings comfort to them in terms of mood. However, several of them mentioned that this model depends on the subject. If the subject is required hands-on practice, then face-to-face is required. Instead, online learning is enough for them to study theoretical lessons.

Besides, only one student prefers the online driver model and the self-blend model. The student who preferred the online driver model stated that it is a simple and easy blended learning model for him, while the student who preferred the self-blend model stated that it enables him to study anytime and anywhere. Although both of these blended learning models get only 1 student preferred, they have provided essential data and feedback for the research as it shows that some students have their own thoughts and styles to prefer these blended learning models in their learning.

However, no students preferred the online lab model in their learning. Based on the literature review, students may not prefer this blended learning model due to limited interaction and communication between students and lecturers [37]. It might also provide poor learning experiences for the students as they are only guided and supervised by the paraprofessionali. Students are free to explore themselves in this blended learning model and sometimes they might be lost in the learning process if the guidance provided is not clear enough [38]. This blended learning model is only suitable in some specific cases like pandemics or severe cases, as several limitations are implemented in terms of quota accepted in the physical class. Hence, these possible reasons lead to no students preferring it as a practicable blended learning model in their learning.

3. 2. AHP Analysis   To achieve objective three of this research, the AHP model is designed and developed to select the best blended learning model based on student learning style. As mentioned in the methodology, several steps are required to get the final result in ranking based on the priority vectors to identify the best-blended learning model. Consistency analysis is required to ensure the data collected are valid and consistent. After developing the priority vector for 50 students, the data are combined based on the VARK model using Equation (5). Table 5 shows the priority vector for the blended learning models in terms of VARK.

TABLE 5. Priority Vector for the Blended Learning Models in terms of VARK

Blended Learning Models	Priority Vector			
	V	A	R	K
Face-to-face Driver Model	37.62%	28.65%	41.16%	30.07%
Online Driver Model	15.42%	15.65%	17.44%	15.46%
Rotation Model	10.81%	28.51%	5.01%	17.84%
Online Lab Model	9.04%	6.75%	9.68%	6.30%
Flex Model	18.44%	13.51%	24.01%	22.60%
Self-blend Model	8.66%	6.93%	2.71%	7.73%
TOTAL	100.00%	100.00%	100.00%	100.00%

Later, the VARK criteria in the second tier of the hierarchical structure are also required to construct PCM to get its priority vector to complete the AHP results. To get the importance relative scale for the VARK PCM, the answers from the VARK questionnaire are referred. There are 16 questions in a VARK questionnaire and 800 answers for the 50 sets of the VARK questionnaires. The percentage difference is calculated in terms of VARK for the different VARK combinations. The values are 90% normalized to get the relative importance scale for VARK PCM. Figure 6 shows the VARK PCM, normalized VARK PCM and consistency analysis for VARK PCM in formulated Excel. The priority vector for visual, auditory, read/write and kinaesthetic are 14.41%, 21.65%, 4.31% and 59.63%, respectively. The C.R. is 0.0594, which is less than 0.1 (valid).

VARK PCM	Visual	Auditory	Read/Write	Kinaesthetic		
Visual	1	0.50	5.00	0.20		
Auditory	2.00	1	6.00	0.25		
Read/Write	0.20	0.17	1	0.11		
Kinaesthetic	5.00	4.00	9.01	1		
SUM	8.200	5.667	21.009	1.561		

Normalized PCM	Visual	Auditory	Read/Write	Kinaesthetic	Criteria Weights	Priority Vector
Visual	0.1220	0.0882	0.2380	0.1281	0.1441	14.41%
Auditory	0.2439	0.1765	0.2856	0.1602	0.2165	21.65%
Read/Write	0.0244	0.0294	0.0476	0.0711	0.0431	4.31%
Kinaesthetic	0.6098	0.7059	0.4288	0.6406	0.5963	59.63%
SUM	1	1	1	1		

Consistency Analysis	Visual	Auditory	Read/Write	Kinaesthetic	Weighted Sum Value	WSV/CW
Visual	0.1441	0.1083	0.2156	0.1193	0.5872	4.076
Auditory	0.2882	0.2165	0.2588	0.1491	0.9125	4.214
Read/Write	0.0288	0.0361	0.0431	0.0662	0.1742	4.040
Kinaesthetic	0.7204	0.8661	0.3885	0.5963	2.5713	4.312

λmax	4.1605					
Consistency Index (C.I.)	0.0535					
Random Index (R.I.)	0.9					
Consistency Ratio	0.0594	VALID				

Figure 6. VARK PCM, Normalized VARK PCM and Consistency Analysis for VARK PCM in Formulated Excel

Then, the combination of the priority vectors calculated from Table 5 and Figure 6 is done to get the overall priority ranking for the blended learning model. Table 6 shows the overall priority ranking of the AHP model.

According to Table 6, the face-to-face driver model is engineering students' most preferred blended learning model. It is tallied with the finding of Zafirah et al. [39], as most students are interested in the face-to-face driver model due to its effectiveness. Students can get a better understanding through the lecture in the physical class and be able to discuss the questions they found with the lecturers directly. So, two-way communication via face-to-face sessions is an effective learning method as the students feel stable enough to have a learning session at a fixed time and place.

For the online lab model which is the least preferred blended learning model by the engineering students. There are a few possible reasons why students have not preferred it. First, the students are limited to interacting with the virtual environment [38]. This led to students having difficulty observing and manipulating physical objects and limiting their development of practical skills to connect theoretical knowledge. Also, the online lab model is less effective as the students might be isolated due to the difficulty of getting the lecturer's support [11]. This can also cause the loss of learning time and interest. Thus, this model becomes the least preferred model is reasonable. For the same possible reasons, the online driver model is not what many students prefer. Although a more flexible model allows students to learn at their own pace, it depends on their motivation to learn. Sometimes, the equipment required for online learning is more expensive, creating difficulty for students with limited budgets [40].

Besides, the self-blend model is not preferred by many students. Other than the student isolation issue, it lacks structure as it allows students to learn whatever they want [41]. It is effective for highly self-motivated students who can manage their time properly, while less effective for students who need support and guidance. Moreover, this model makes it difficult to track student progress if they apply for many online courses from different providers [42]. It leads to lecturers taking time to evaluate the student learning progress.

TABLE 6. Overall Priority Ranking of the AHP Model

Blended Learning Models	Priority Vector
Face-to-face Driver Model	31.33%
Online Driver Model	15.58%
Rotation Model	18.58%
Online Lab Model	6.94%
Flex Model	20.09%
Self-blend Model	7.47%

3. 3. Comparison Accuracy   To achieve objective four of this research, the AHP results are compared with the VARK results in accuracy to test and validate the AHP model. The VARK results are defined as the actual results, while the AHP results are defined as the calculated results. The overall VARK and AHP results are converted from the percentage values into the number of students for evaluation to calculate the accuracy. Table 7 shows the number of students who preferred the blended learning models in terms of VARK and AHP. The number of students correctly identified for the face-to-face driver model, online driver model, rotation model, online lab model, flex model, and self-blend model are 16, 1, 9, 0, 10, and 1, respectively. The accuracy of the AHP result is 74%.

It is believed that from the analysis, 74% accuracy is considered a good result due to the AHP model being good at consistency (low inconsistency). This can be justified through the method in the AHP model as it has ensured the C.R. is less than 0.1 during the consistency analysis. However, there might be inconsistent results that occurred due to the judgment of the decision-maker and it led to the accuracy dropping [43]. Besides, the factor that might affect the accuracy is the students' personality. The students do not understand their preference for the blended learning model. For example, the student claimed that the most preferred blended learning model for him is the face-to-face driver model, but after evaluating through the AHP analysis, his preferred blended learning model is the flex model. This can lead to the accuracy dropped as VARK results are directly applied and assumed as the actual result.

TABLE 7. Number of Students that Preferred the Blended Learning Models in terms of VARK and AHP Results

Blended Learning Models	Number of Students	
	VARK	AHP
Face-to-face Driver Model	25	16
Online Driver Model	1	8
Rotation Model	12	9
Online Lab Model	0	3
Flex Model	11	10
Self-blend Model	1	4

4. CONCLUSION

In summary, this research has aimed to utilize the AHP model to aid in identifying the best blended learning model for engineering students based on their learning styles. Blended learning, VARK, and AHP models are studied in this research. Based on the VARK result, most students are kinaesthetic learners (72%). After

classifying the students for the blended learning model based on the VARK model, 50% of the students prefer the face-to-face driver model as the top blended learning model. Then, the AHP model is designed and developed to identify the best blended learning model. According to the AHP result, the face-to-face driver model has the highest priority vector (31.33%), followed by the flex and rotation models at 20.09% and 18.58%, respectively. AHP analysis is conducted to the results in terms of consistency to ensure the data is valid and consistent. Afterward, the AHP results are compared with the VARK results to test and validate in terms of accuracy. The accuracy of the AHP result is 74%, which is considered as low inconsistency.

5. ACKNOWLEDGEMENT

6. REFERENCES

1. Hrastinski, S., "What do we mean by blended learning?", *TechTrends*, Vol. 63, No. 5, (2019), 564-569, https://doi.org/10.1007/S11528-019-00375-5

2. Deeva, G., De Smedt, J., Saint-Pierre, C., Weber, R. and De Weerdt, J., "Predicting student performance using sequence classification with time-based windows", *Expert Systems with Applications*, Vol. 209, (2022), 118182, https://doi.org/10.1016/J.ESWA.2022.118182

3. Cevikbas, M. and Kaiser, G., "Promoting personalized learning in flipped classrooms: A systematic review study", *Sustainability*, Vol. 14, No. 18, (2022), 11393, https://doi.org/10.3390/SU141811393

4. Sharma, D., Sood, A.K., Darius, P.S., Gundabattini, E., Darius Gnanaraj, S. and Joseph Jeyapaul, A., "A study on the online-offline and blended learning methods", *Journal of The Institution of Engineers (India): Series B*, Vol. 103, No. 4, (2022), 1373-1382, https://doi.org/10.1007/S40031-022-00766-Y

5. Kaur, M., "Blended learning-its challenges and future", *Procedia-Social and Behavioral Sciences*, Vol. 93, (2013), 612-617, https://doi.org/10.1016/J.SBSPRO.2013.09.248

6. Perwitasari, F., Astuti, N.B. and Atmojo, S., "Online learning and assessment: Challenges and opportunities during pandemic covid-19", in International Conference on Educational Assessment and Policy (ICEAP 2020), Atlantis Press. (2021), 133-137. https://doi.org/10.2991/ASSEHR.K.210423.077

7. Rasheed, R.A., Kamsin, A. and Abdullah, N.A., "Challenges in the online component of blended learning: A systematic review", *Computers & Education*, Vol. 144, (2020), 103701, https://doi.org/10.1016/J.COMPEDU.2019.103701

8. Amaniyan, S., Pouyesh, V., Bashiri, Y., Snelgrove, S. and Vaismoradi, M., "Comparison of the conceptual map and traditional lecture methods on students' learning based on the vark learning style model: A randomized controlled trial", *SAGE Open Nursing*, Vol. 6, (2020), 2377960820940550,

9. Kurniawan, Y., Karuh, C.S.Y., Ampow, M.K., Prahastuti, M., Anwar, N. and Cabezas, D., "Evaluation of hybrid learning in the university: A case study approach", *HighTech and Innovation Journal*, Vol. 3, No. 4, (2022), 394-410, https://doi.org/10.28991/HIJ-2022-03-04-03

10. Ahmed, S.A., Hegazy, N.N., Abdel Malak, H.W., Cliff Kayser, W., Elrafie, N.M., Hassanien, M., Al-Hayani, A.A., El Saadany, S.A., Ai-Youbi, A.O. and Shehata, M.H., "Model for utilizing distance learning post covid-19 using (pact)™ a cross sectional qualitative study", *BMC Medical Education*, Vol. 20, No., (2020), 1-13, https://doi.org/10.1186/S12909-020-02311-1/TABLES/3

11. Akuratiya, D. and Meddage, D., "Students' perception of online learning during covid-19 pandemic: A survey study of it students", *Tablet*, Vol. 57, No. 48, (2020), 23.

12. Al Mahdi, Z., Rao Naidu, V. and Kurian, P., "Analyzing the role of human computer interaction principles for e-learning solution design", in Smart Technologies and Innovation for a Sustainable Future: Proceedings of the 1st American University in the Emirates International Research Conference—Dubai, UAE 2017, Springer. (2019), 41-44. https://doi.org/10.1007/978-3-030-01659-3_6/COVER

13. Carey, T., McKerlie, D. and Wilson, J., "Hci design rationales as a learning resource", *Design Rationale: Concepts, Techniques, and Use*, (1996), 373-392, https://doi.org/10.1201/9781003064053-17

14. Wilcox, L., DiSalvo, B., Henneman, D. and Wang, Q., "Design in the hci classroom: Setting a research agenda", in Proceedings of the 2019 on Designing Interactive Systems Conference. (2019), 871-883. https://doi.org/10.1145/3322276.3322381

15. Dakhi, O., JAMA, J. and IRFAN, D., "Blended learning: A 21st century learning model at college", *International Journal of Multi Science*, Vol. 1, No. 08, (2020), 50-65, https://multisciencejournal.com/index.php/ijm/article/view/92

16. López-Belmonte, J., Pozo-Sánchez, S., Carmona-Serrano, N. and Moreno-Guerrero, A.-J., "Flipped learning and e-learning as training models focused on the metaverse", *Emerging Science Journal*, Vol. 6, (2022), 188-198, https://doi.org/10.28991/ESJ-2022-SIED-013

17. Phurikultong, N. and Kantathanawat, T., "Flipping the undergraduate classroom to develop student analytical thinking skills", *Emerging Science Journal*, Vol. 6, No. 4, (2022), 739-757, https://doi.org/10.28991/ESJ-2022-06-04-06

18. Risdianto, E., "Development of blended learning based on web and augmented reality", in International Conference on Educational Sciences and Teacher Profession (ICETeP 2018), Atlantis Press. (2019), 144-147. https://doi.org/10.2991/ICETEP-18.2019.35

19. Halif, M.M., Hassan, N., Sumardi, N.A., Omar, A.S., Ali, S., Aziz, R.A., Majid, A.A. and Salleh, N.F., "Moderating effects of student motivation on the relationship between learning styles and student engagement", *Asian Journal of University Education*, Vol. 16, No. 2, (2020), 93-103, https://doi.org/10.24191/AJUE.V16I2.10301

20. Aydogdu, O. and Winder, M., "Teachers' perspectives on improving online seminars in pharmacology: A quantitative and qualitative study on lessons learned during the covid-19 pandemic", *Medical Science Educator*, Vol. 32, No. 5, (2022), 1131-1142, https://doi.org/10.1007/S40670-022-01634-6

21. Burcă-Voicu, M.I., Cramarenco, R.E. and Dabija, D.-C., "Investigating learners' teaching format preferences during the covid-19 pandemic: An empirical investigation on an emerging market", *International Journal of Environmental Research and*

https://doi.org/10.1177/2377960820940550/ASSET/IMAGES/LARGE/10.1177_2377960820940550-FIG2.JPEG

Public Health,   Vol. 19, No. 18, (2022), 11563, https://doi.org/10.3390/IJERPH191811563

22. Kadirbayeva, R., Pardala, A., Alimkulova, B., Adylbekova, E., Zhetpisbayeva, G. and Jamankarayeva, M., "Methodology of application of blended learning technology in mathematics education", *Cypriot Journal of Educational Sciences*, Vol. 17, No.   4,   (2022),   1117-1129, https://doi.org/10.18844/CJES.V17I4.7159

23. Rojas-Palacio, C.V., Arango-Zuluaga, E.I. and Botero-Castro, H.A., "Teaching control theory: A selection of methodology based on learning styles", *Dyna*, Vol. 89, No. 222, (2022), 9-17, https://doi.org/10.15446/DYNA.V89N222.100547

24. Li, J., Han, S.-h. and Fu, S., "Exploring the relationship between students' learning styles and learning outcome in engineering laboratory education", *Journal of Further and Higher Education*,   Vol.   43,   No.   8,   (2019),   1064-1078, https://doi.org/10.1080/0309877X.2018.1449818

25. Majidova, G., "Organizing the classes consideri organizing the classes considering the students' learning styles", *Мактабгача Таълим Журнали*,   Vol.   3,   No.   3,   (2022), https://ruslit.jdpu.uz/index.php/presedu/article/view/5554

26. Taheri, M., Falahchai, M., Javanak, M., Hemmati, Y.B. and Bozorgi, M.D., "Analyzing the relationship between learning styles (kolb and vark) and creativity with the academic achievement of dental students", *Journal of Education and Health   Promotion*,   Vol.   10,   (2021), https://doi.org/10.4103/JEHP.JEHP_1492_20

27. Hernandez, J.E., Vasan, N., Huff, S. and Melovitz-Vasan, C., "Learning   styles/preferences   among   medical   students: Kinesthetic learner's multimodal approach to learning anatomy", *Medical Science Educator*,   Vol. 30, (2020), 1633-1638, https://doi.org/10.1007/S40670-020-01049-1/FIGURES/3

28. Espinoza-Poves, J.L., Miranda-Vílchez, W.A. and Chafloque-Céspedes, R., "The vark learning styles among university students of business schools", *Journal of Educational Psychology-Propositos y Representaciones*, Vol. 7, No. 2, (2019), 401-415, https://doi.org/10.20511/pyr2019.v7n2.254

29. Taherdoost, H. and Madanchian, M., "Multi-criteria decision making (mcdm) methods and concepts", *Encyclopedia*, Vol. 3, No.   1,   (2023),   77-87, https://doi.org/10.3390/ENCYCLOPEDIA3010006

30. Dewi, N.K. and Putra, A.S., "Decision support system for head of warehouse selection recommendation using analytic hierarchy process (ahp) method", in International Conference Universitas Pekalongan 2021. Vol. 1, No. 1, (2021), 43-50. https://proceeding.unikal.ac.id/index.php/icunikal2021/article/view/647

31. Fattoruso, G. and Marcarelli, G., "A multi-criteria approach for public tenders. Electre iii and parsimonious ahp: A comparative study", *Soft Computing*, Vol. 26, No. 21, (2022), 11771-11781, https://doi.org/10.1007/S00500-022-07426-9

32. Wolnowska, A.E. and Konicki, W., "Multi-criterial analysis of oversize cargo transport through the city, using the ahp method", *Transportation Research Procedia*, Vol. 39, No., (2019), 614-623, https://doi.org/10.1016/J.TRPRO.2019.06.063

33. De Guzman, K.J. and Robielos, R.A.C., "Ahp approach for determining category in social media content creation in order to maximize revenue per mille (rpm)", *HighTech and Innovation Journal*,   Vol.   3,   No.   1,   (2022),   65-72, https://doi.org/10.28991/HIJ-2022-03-01-07

34. Ho, W. and Ma, X., "The state-of-the-art integrations and applications of the analytic hierarchy process", *European Journal of Operational Research*, Vol. 267, No. 2, (2018), 399-414, https://doi.org/10.1016/J.EJOR.2017.09.007

35. Zhang, J., Bai, J., Zhang, Z. and Feng, W., "Operation state assessment of wind power system based on pso+ ahp—fce", *Frontiers in Energy Research*,   Vol. 10, (2022), 916852, https://doi.org/10.3389/FENRG.2022.916852

36. Huo, X., Gu, Y. and Zhang, Y., "The discovery of multi-target compounds with anti-inflammation activity from traditional chinese medicine by tcm-target effects relationship spectrum", *Journal of Ethnopharmacology*,   Vol. 293, (2022), 115289, https://doi.org/10.1016/J.JEP.2022.115289

37. Cornelius, S., Calder, C. and Mtika, P., "Understanding learner engagement on a blended course including a mooc", *Research in Learning   Technology*,   (2019), https://doi.org/10.25304/RLT.V27.2097

38. Kumar, V. and Tamilarasan, P., A comparative analysis of blended models at tertiary level, in Machine learning approaches for improvising modern learning systems. 2021, IGI Global.248-271. https://doi.org/10.4018/978-1-7998-5009-0.CH010

39. Zafirah, H.A., Basori, B. and Maryono, D., "The influence of blended learning face to face driver model type learning on learning interests and learning outcomes in simulation digital", *Journal of Informatics and Vocational Education*, Vol. 4, No. 1, (2021), https://doi.org/10.20961/JOIVE.V4I1.48630

40. Amemado, D., "Covid-19: An unexpected and unusual driver to online education", *International Higher Education*, No. 102, (2020),   12-14, https://ejournals.bc.edu/index.php/ihe/article/view/14599

41. Krismadinata, U.V., Jalinus, N., Rizal, F., Sukardi, P.S., Ramadhani, D., Lubis, A.L., Friadi, J., Arifin, A.S.R. and Novaliendry, D., "Blended learning as instructional model in vocational education: Literature review", *Universal Journal of Educational Research*, Vol. 8, No. 11B, (2020), 5801-5815, https://doi.org/10.13189/UJER.2020.082214

42. Rachmadtullah, R., Marianus Subandowo, R., Humaira, M.A., Aliyyah, R.R., Samsudin, A. and Nurtanto, M., "Use of blended learning with moodle: Study effectiveness in elementary school teacher education students during the covid-19 pandemic", *International Journal of Advanced Science and Technology*, Vol.   29,   No.   7,   (2020),   3272-3277, https://www.researchgate.net/publication/341724918

43. Grzybowski, A.Z. and Starczewski, T., "New look at the inconsistency   analysis   in   the   pairwise-comparisons-based prioritization problems", *Expert Systems with Applications*, Vol. 159,   (2020),   113549, https://doi.org/10.1016/J.ESWA.2020.113549

Persian Abstract

چکیده

یادگیری ترکیبی روشی انعطاف‌پذیر است که از طریق یادگیری حضوری و آنلاین انجام می‌شود. دانش آموزان را ملزم به یادگیری با تلاش فیزیکی در کلاس ها می کند و به
آنها امکان می دهد در زمان ها و مکان های مختلف به طور مجازی یاد بگیرند. این امر پس از دستور کنترل حرکت (MCO) مشهودتر و رایج‌تر شده است زیرا اکثر سخنرانی‌ها
در دانشگاه به صورت ترکیبی انجام می‌شوند. مدل‌های یادگیری ترکیبی مشکلات و فرصت‌هایی را برای دانش‌آموزان ایجاد می‌کنند، زیرا آنها باید روش‌های مختلف یادگیری
ترکیبی اساتید مختلف را از نظر سبک‌های تدریس، برنامه‌ریزی و زمان‌بندی کشف و سازگار کنند. بنابراین، هدف این تحقیق بررسی بهترین مدل‌های یادگیری ترکیبی برای
دوره کارشناسی مهندسی بر اساس سبک یادگیری دانشجویان با استفاده از روش فرآیند تحلیل سلسله مراتبی (AHP) است، زیرا انتخاب مؤثرترین رویکرد برای آن چالش
بزرگی است. دانشگاه ها برای آموزش، تعلیم و تربیت دانش آموزان با کیفیت با توجه به سبک های یادگیری آنها. روش AHP برای کمک به دانش آموزان در یافتن بهترین
مدل یادگیری تلفیقی بر اساس سبک یادگیری استفاده می شود. سپس تجزیه و تحلیل AHP برای اعتبارسنجی و تأیید صحت آن با مقایسه آن با مدل‌های دیداری، شنیداری،
خواندن/نوشتن و جنبشی (VARK) انجام می‌شود. در نتیجه، بیشتر دانش‌آموزان بر اساس نتایج VARK، یادگیرنده‌های حرکتی هستند (۷۲٪)، و مدل محرک چهره به چهره
ترجیح داده‌شده‌ترین مدل یادگیری ترکیبی با بردار اولویت در ۳۱.۳۳٪ از طریق تحلیل AHP است. دقت نتیجه AHP با مقایسه آن با نتیجه VARK 74 درصد است. به طور
خلاصه، داده ها را می توان در سیستم یادگیری ترکیبی UTeM برای بهبود طراحی دوره و تجربه یادگیری دانش آموز مستقر کرد.

International Journal of Engineering

Predicting Service Life of Polyethylene Pipes under Crack Expansion using "Random Forest" Method

P. Aleksander G., T. Yifan*, Z. Fuming

Department of Petroleum Engineering, Saint Petersburg Mining University, 2, 21st line, Saint Petersburg, Russian Federation

PAPER INFO	ABSTRACT
	The study of factors influencing the performance of PE pipe against rapid crack expansion is of great significance for the safe use of PE pipe. This paper analyzes the role of each step in the algorithm based on the theoretical basis of random forest, and proposes an improved random forest method based on recursive feature elimination by changing the node splitting rules to address the shortcomings of the random forest classification accuracy. The method is used to analyze the effect of rapid crack expansion of PE pipe in terms of pipe size and wall thickness, impact knife speed, and notched impact strength of simply supported beams. Under the same conditions, the extended crack lengths of DN260, DN150 and DN65 pipes are 197, 164 and 128 mm, respectively, while the crack lengths of PE80 pipes are 24, 210 and 239 mm at impact knife speeds of 10, 15 and 20 m/s, respectively. The higher the notched impact strength of the simple beam, the higher the critical pressure value and the better the RCP resistance. The study of rapid crack expansion of PE pipe based on deep learning algorithm can identify the main internal and external factors affecting the RCP resistance of PE pipe and provide a solid basis for PE pipe life prediction.

1. INTRODUCTION

Polyethylene pipes have many advantages over traditional metal pipes and have become the best choice for urban pipeline networks [1, 2]. Polyethylene pipes have excellent toughness, with a minimum elongation at break of 350% required for tensile testing. Therefore, it can usually undergo a large deformation and is very adaptable to foundation settlement as well as pipeline deflections [3-5]. In impact tests, brittle fracture occurs only when the specimen is sharply notched within the service temperature range [6-8]. Polyethylene is an inert material, and at 20°C, polyethylene is resistant to strong acid and alkali corrosion candles [9], solving the problem of the need to strictly consider corrosion protection when laying traditional pipelines [10]. Polyethylene pipes are easy to install and have good welding properties, which is due to the solubility of polyethylene pipes [11-13].

With the improvement of raw material performance, the resistance of PE pipes to crack sprouting and to rapid crack expansion has dramatically increased. Most of the methods for rapid crack evaluation of PE pipes [14-16]

generally suffer from complex experimental conditions and poor reproducibility, which seriously restrict the development process of PE pipes [17-19]. There are still many blank areas for research exploration in various aspects of PE pipe manufacturing, welding and laying, testing and maintenance. The study of material resistance to rapid crack growth of PE pipes can provide scientific guidance for the selection of materials, welding, inspection and evaluation, life prediction and other key issues of PE pipes and promote the safe, standardized and stable development of PE pipes by exploring in depth the performance of PE pipes.

With an increase in the usage of polyethylene pipes, more and more researchers have investigated their rapid crack expansion. Nikolaev and Zaripova [20] Baktizin et al. [21] and Vasiliev et al. [22] tested the resistance to rapid crack expansion of different types of single-peaked MDPE pipes and indicated that single-peaked MDPE pipes have sufficient RCP resistance to be used in gas distribution systems. A small-scale accelerated and reliable testing method was proposed by Liu and Kleiner [23], Naseri and Barabady [24] Rajeev and Kodikara

---

Corresponding Author Email: 75829472@qq.com (T. Yifan)

[25] for the S4 test of conventional plastic pipes against rapid crack expansion using a large amount of material and time consuming, and was experimentally verified for double-peaked MDPE pipes. Thaduri et al. [26], Transport [27], Sepideh et al. [28] proposed a new method for evaluating the resistance of PE pipes to rapid crack expansion at low temperatures to optimize the problem that the traditional evaluation method is not comprehensive enough.

Also, Enrico [29] Kim et al. [30] Mohamed and Jawhar [31] proposed a method for the evaluation of rapid crack expansion in PE pipes by analyzing the main causes of rapid crack expansion in PE pipes. On the other hand, Narayanan and Sankaranarayanan [32] Gafarova [33] investigated the effect of fatigue crack extension in HDPE pipes from the point of view of molecular weight distribution and proposed a possible link between the potential failure mechanism of cracked primary fibers and feed-back kinetics. Mohamed and Jawhar [34] Shammazov et al. [35] Jin and Eydgahi [36] analyzed the rapid crack expansion of polyethylene pressure pipes using simulation methods and proposed a test experiment method for testing the resistance of polyethylene pipes to rapid crack expansion.

In this paper, we investigate the fast crack extension life prediction of PE pipe based on deep learning. Firstly, the theoretical basis of random forest is studied, decision trees are constructed based on Bagging idea, and results are derived by systematic voting using a classification model composed of multiple decision trees. Secondly, the method of using recursive feature elimination is proposed to improve for the defects of random forest, and the accuracy of random forest is im-proved by changing the node fracture rule. Then, fast crack expansion experiments are designed for different PE pipe sizes in different environments, where the special material is divided into PE80 and PE100, and the pipe sizes are divided into DN160, DN63 and DN315, and the SDR is fixed at 11. Finally, the experimental data were analyzed based on random forest with recursive feature elimination to study the effects of pipe size and wall thickness, impact knife speed and simply supported beam. The effects of notch impact strength on the RCP resistance of PE pipe were investigated.

2. MATERIALS AND METHODS

2. 1. Improved Random Forest Algorithm   The random forest algorithm selects CART trees as the base classifier, uses the Bagging algorithm to randomly select a subset from the original data set samples as training samples, and then randomly selects a subset of features from multiple features in the training samples, on which a decision tree is generated, and the classification results of the random forest were obtained by decision tree voting. In the construction of the random forest, the

sample selection and attribute selection were obtained by random sampling, so it had better generalization ability.

Random Forest (RF) is an integrated learning algorithm, which is essentially a combinatorial classifier composed by a large number of decision trees [37, 38]. The actual class of the random forest is obtained by voting from Vasiliev et al. [22] Liu et al. [39] Palaev et al. [40] a large number of decision trees. The random forest algorithm combines the random subspace idea and the best partitioning idea, without many restrictions in terms of hyperparameters, with a simple and easy to understand structure not easy to overfit, and can handle missing and unbalanced data sets very well [41-44]. Its model training and prediction are efficient and stable, so it is widely used in clustering and regression classification. The principle of random forest algorithm is shown in Figure 1.

Random forest algorithm is a common integrated algorithm, which is combined by a large number of decision trees. The decision tree itself has poor classification accuracy and is a typical representative of weak classifiers [45-47]. The integration of weak classifiers together can significantly improve the accuracy of the overall classifier. Each decision tree of random forest is computed separately from different self-help samples, and multiple decision trees are generated and clustered together to form a forest. The classification error of a decision tree is determined by the classification effect of different trees and the degree of correlation between trees [48-50]. The random forest is improved by splitting the nodes based on the decision tree, which usually selects the best feature attribute among all the feature attributes as the base for splitting when the nodes are split [51, 52], but the random forest generally selects some feature attributes randomly for a higher degree of generalization, and then performs the selection of the best feature attribute on this basis [53, 54]. A simple voting operation is applied to all the decision tree classification results of the random forest to derive the category results
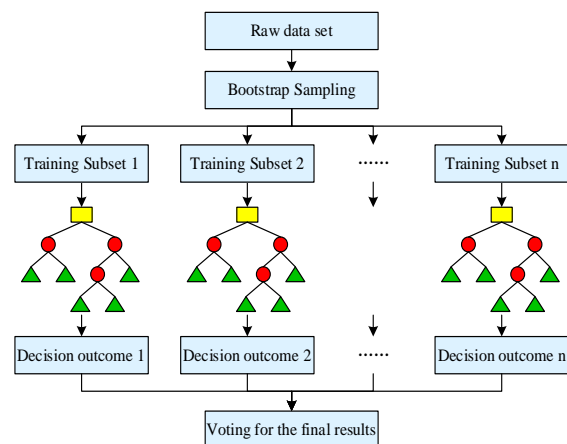
Figure 1. Random Forest algorithm principle

of the overall random forest, so the random forest classification accuracy is higher.

The composition of the random forest follows the following idea:

(1) Bagging idea: The random forest algorithm is able to randomly draw $\frac{2}{3}$ samples from the original sample set T to build a training subset. Each of these subsets builds a decision tree. Assume that to form a random forest with decision trees, self-help sample sets are first obtained by the Bagging algorithm. The data that are not drawn are recorded as out-of-bag data (OOB), and the generalization ability of the random forest is measured by the error. The error can reflect the classification accuracy and can also judge the feature importance (VIM). The OOB error is calculated for each decision tree, and the error is calculated again after randomly disrupting the out-of-bag data for variable x_i , and the average of the two differences is the VIM value of the current variable. Variable Xi in the j tree of VIM is:

$$VIM(x_i) = \frac{1}{N}\sum_{n=1}^{N}(I(Y_m = Y_m^j) - I(Y_m = Y_m^{j'})) \qquad (1)$$

Variable x_i in the random forest VIM is:

$$VIM = \frac{1}{N}\sum_{p=1}^{N} VIM(x_i) \qquad (2)$$

where N represents the amount of observed data for the J tree OOB, OOB the m th observation, Y_m^j and the estimated results of m observation of the J tree OOB before and after random swapping, and I the two values are equal to 1 and unequal to 0.

(2) Constructing decision trees. n self-help sample sets generate n classification trees each. The sample feature vector is M. The traditional decision tree selects the best features from M feature vectors, while the random forest first randomly selects m $(m\cdot M)$ features from M. Each decision tree is split by selecting the m optimal features from the feature vectors, and the classification trees are fully grown without pruning.

(3) Voting for the final classification result. The random forest algorithm helps to improve the diversity of decision trees by constructing different training subsets, which in turn improves the accuracy of the random forest as a whole n decision tree models will eventually produce n classification results:

$$\{y_1(x), y_2(x), \ldots, y_n(x)\} \qquad (3)$$

Equation (3) is a classification model system consisting of n decision tree model.

Combined classification model voting yields overall classification categories:

$$T(x) = \arg\max \sum_{i=1}^{n} Z(y_i(x) = A) \qquad (4)$$

In Equation (4), A represents the blockage fault category, $y_i(x)$ represents the individual decision tree classification model, $T(x)$ represents the combined classification model, and $Z(x)$ represents the schematic function.

A random forest can be viewed as a collection of classification models $H(x) = \{h(x)\}$ formed by combining $m(m > 1)$ classification models $h_1(x), h_2(x), \ldots, h_m(x)$. The classification models are trained by randomly selecting subsample sets from sample sets $D(X,Y)$, and vectors Y are obtained by classifying attribute features X. The edge function is defined as:

$$\arg\min(X,Y) = av_m I(h_m(X) = Y) - \max_{j \neq Y} av_m I(h_m(x) = j) \qquad (5)$$

where $I(func)$ is the indicator function, j represents the vector of classification errors, and $av_m(func)$ represents the mean value. $\arg\min(X,Y)$ is the ability of the classifier to accurately categorize the next classified sample (X,Y) by analyzing the difference between the average number of votes that were correctly classified and the maximum number of votes for classification deviation. A higher value of $\arg\min(X,Y)$ indicates a higher confidence level of the classifier and more reliable classification of the classification model.

We expect the edge function of the classification model set H to be high, which means that the number of correctly classified base classifiers is higher than the number of incorrectly classified base classifiers, i.e., $\arg\min(X,Y) > 0$. However, there are situations where incorrect classification results are obtained. Such misclassified results are usually presented by the generalization error. The generalization error for the set of classification models is calculated as:

$$PE^* = P_{X,Y}(\arg\min(X,Y) < 0) \qquad (6)$$

where $\arg\min(X,Y) < 0$ denotes that the test sample is misclassified in the whole combined classifier and represents the probability that the sample is misclassified in the combined classifier. Therefore a low value of generalization error means that the model classifies better.

According to the large number theorem and the structure of the decision tree itself, it is proved that the generalization error converges to a certain value when the size of the decision tree in the random forest is larger, satisfying Equation (7):

$$\lim_{m \to \infty} PE^* = P_{X,Y}(P_\theta(h(X,\theta) = Y) - \max_{j \neq Y} P_\theta(h(x,\theta) = j) < 0) \qquad (7)$$

where m is the random forest size, θ is the random vector of individual classification models, and $h(X,\theta)$ is

the output of the classification models based on attribute features X as well as θ.

As the random forest grows in size, it will gradually converge to a certain value without overfitting due to excessive increase in the decision tree.

Definition of RF edge function:

The classification ability of classification model set H is influenced by the individual classification models, and the combined value of the classification results of the individual classification models is the classification performance of the entire classification model set H. The classification ability of classification model set H can be described as the expected value of $mr(X,Y)$:

$$S = E(mr(X,Y)) \tag{8}$$

$$\hat{j}(X,Y) = \arg\max_{j \neq Y} P_\theta(h(X,\theta) = j) \tag{9}$$

$$mr(X,Y) = E_\theta(I(h(X,\theta) = Y) - I(h(X,\theta) = \hat{j}(X,Y))) \tag{10}$$

$$rmg(\theta,x,y) = \Gamma(h(X,\theta) = Y) - I(h(X,\theta) = \hat{j}(X,Y)) \tag{11}$$

From the above equation we can derive:

$$mr(X,Y)^2 = (E_\theta rmg(\theta,X,Y))^2 = E_{\theta\theta'} rmg(\theta,X,Y) rmg(\theta',X,Y) \tag{12}$$

The variance of the edge function is derived from the above equation:

$$\text{var}(mr) = E_{\theta\theta'} \text{cov}_{X,Y}(rmg(\theta,X,Y)rmg(\theta',X,Y)) \tag{13}$$

$\rho(\theta,\theta')$ is the correlation between the two. represents the standard deviation. Therefore $\text{var}(mr)$ simplifies to Equation:

$$\text{var}(mr) E_{\theta\theta'}(\rho(\theta,\theta')sd(\theta)sd(\theta')) = \bar{\rho}(E_\theta sd(\theta))^2 \leq \bar{\rho}(E_\theta \text{var}(\theta)) \tag{14}$$

where $\bar{\rho}$ is the mean value of base classifier correlation. S is the average intensity of the base classifier. The upper bound of generalization error PE^* can be obtained as:

$$PE^* \leq \bar{\rho}(1 - S^2)/S^2 \tag{15}$$

PE^* A larger upper bound value indicates that more samples are misclassified and the overall classification of the combined classifier is not good. It can be seen that the classification accuracy of the combined classifier is related to the correlation between each classifier and the classification ability of the individual classifier itself. Therefore, the classification accuracy of random forest can be improved by reducing the correlation of decision trees and improving the classification accuracy of each decision tree.

The classification accuracy of random forest is the most reliable way to verify its performance. The classification accuracy characterizes how well the actual labeled categories match the algorithm's classification

categories. Random forest is a high-precision algorithm among classification algorithms, and although its performance varies in different datasets, it basically maintains in the range of 70% to 90%.

2. 2. Improved Random Forest based on Recursive Feature Elimination

In this section, we perform the combination of RFE and random forest. First, the combination of random forest and RFE forms RF-RFE, which is able to decide the size of the final feature subset more rationally and avoid the influence caused by human factors. Recursive feature elimination (RFE) is a strategy to deal with the problem by combining machine learning methods with it in the process of each iteration to construct a model using the current set of features and evaluate the importance of the current features with the performance of the model.

RF-RFE algorithm is used for feature selection, first use random forest algorithm to get the importance ranking of features, according to the principle of backward iteration first delete the features with the smallest feature importance, then the remaining features again use random forest algorithm to get the importance ranking of new features, in turn delete the features with small feature importance, RF-RFE feature selection method in the process of each iteration, will re-evaluate the current set of remaining features, and the score of each feature is adjusted during repeated iterations, overcoming the drawback that the feature selection result of single random forest needs repeated trials to get the feature subset, making the feature subset not only reliable, but also of better quality.

When applying the RF-RFE algorithm for feature selection, the first is the process of random forest, using the bootstrap resampling method to draw multiple samples from the original sample, constructing a decision tree for each bootstrap sample, all the decision trees constitute a random forest, calculating the feature importance in the regression model, at this time, the backward iterative feature evaluation is introduced, and the features with small feature importance are removed. After using the random forest algorithm again to calculate the remaining feature importance until finally only one feature is left, the most feature set is selected according to the correlation coefficient and root mean square error, and the flow chart of RF-RFE algorithm is shown in Figure 2.

The process of RF-RFE algorithm for feature selection is:

Step 1: Assuming that the original number of data samples is n, bootstrap sampling is applied to randomly select b subsets of samples with release, and b regression trees are constructed based on these subsets of samples, and the samples that are not drawn during each bootstrap sampling form b out-of-bag data, which form the test sample of the random forest.
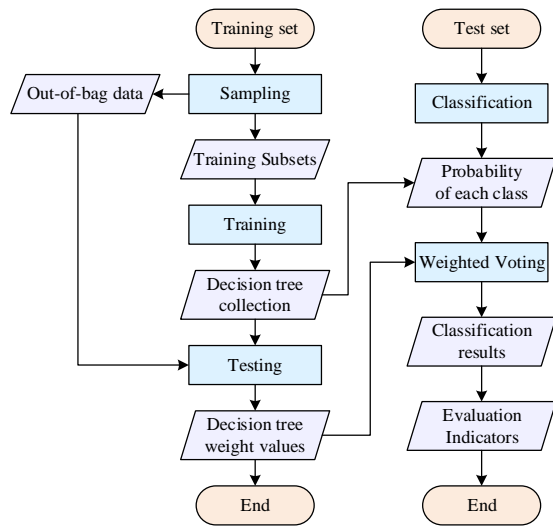
Figure 2. The RF-RFE algorithm flow chart

Step 2: Let the number of variables in the original sample set be, select a randomly selected variable at each node of each regression tree as an alternative variable, and then select the optimal branch in it according to certain criteria, so that each decision tree grows to the maximum.

Step 3: The set of 1 regression trees generated in step b becomes a random forest regression model, and the effect of the random forest regression model is evaluated using the mean square MSE_{OOB} of the residuals predicted using out-of-bag data, MSE_{OOB} which is calculated as:

$$MSE_{OOB} = n^{-1} \sum_{i=1}^{n} (y_i - y_i^{OOB})^2 \qquad (16)$$

where, y_i is the actual value of the dependent variable in the out-of-bag data. y_i^{OOB} is the predicted value of the random forest for the out-of-bag data.

Step 4: The mean decline MSE value is calculated from the mean square of the residuals predicted by out-of-bag data. The importance of the variables in the random forest regression can be measured by the mean decline MSE value, where a larger value indicates a more important feature.

Step 5: After calculating the average decline MSE value, the features with the smallest importance are firstly deleted according to the principle of backward iteration, and then the remaining features are repeated from steps 1-4, and the features with small importance are gradually deleted until the last feature is left, and after the results are output, the number of features with the smallest root mean square error and the largest correlation coefficient is selected as the result of feature selection for remote sensing estimation of forest biomass.

The RF-RFE algorithm for feature selection reevaluates the current set of remaining features during each iteration, and the score of each feature is adjusted during repeated iterations, overcoming the drawback that the feature selection results of a single random forest require repeated trials to obtain a subset of features.

3. RESULTS

3. 1. PE Pipe Rapid Crack Expansion Test   Rapid crack propagation (RCP) of polyethylene (PE) pipes refers to the phenomenon of PE pipes being subjected to external forces (e.g., building construction, irregular welding, etc.) during use and the formation of cracks generated by stress under the pressure of the medium inside the pipe (e.g., tap water, natural gas, etc.), which expand at a rate of several hundred meters per second along the length of the pipe [55, 56].

The fluid pressure inside the tube induces stress in the tube wall. The tube wall stores strain energy because it is in a stress-acting state. When rapid crack growth occurs in the light tube wall, the tube wall changes from a stress-acting state to a stress-free state. The original strain energy stored in the tube wall is released for the production of new crack area. This means that the released strain energy of the tube wall acts as a crack driving force [44, 57]. This released energy is transported to the crack tip by the stress wave of the tube wall material. The stress wave velocity is the velocity of the acoustic wave within the tube wall material.

In this paper, we obtained the influence factors affecting the service life of PE pipes through rapid extension cracking experiments, and then analyzed the obtained data based on RF-RFE algorithm to establish the life prediction method. The description of the samples of PE pipe special material is shown in Table 1.

In this paper, pipe series with larger outside diameters and thicker walls were selected for testing, while pipe series Dn160 (SDR11), Dn63 (SDR11) and Dn 315 (SDR11) were selected for comparative testing in order to compare the effect of different wall thicknesses and sizes on the rapid crack expansion of PE pipe. The finished pipe samples are shown in Table 2.

Experimental steps:

Step 1: Process the tubes in a cryogenic cabinet at $(0\pm2)°C$ for the appropriate time according to the standard requirements for different thicknesses of tubes.

TABLE 1. Samples of special materials for polyethylene pipes

Number	Special materials	Molecular weight distribution
1	PE80-1	Bimodal
2	PE80-2	Unimodal
3	PE100-1	Bimodal
4	PE100-2	Unimodal
5	PE100-3	Bimodal

TABLE 2. Tube samples for main test purposes

Tube	Raw material number	Tube specifications	
		Nominal diameter	Standard Dimension Ratio
number			
GS-001	1#	DN65	SDR11
GS-002	2#	DN65	SDR11
GS-003	3#	DN65	SDR11
GS-004	4#	DN65	SDR11
GS-005	5#	DN65	SDR11
GS-006	1#	DN150	SDR11
GS-007	2#	DN150	SDR11
GS-008	3#	DN150	SDR11
GS-009	4#	DN150	SDR11
GS-010	5#	DN150	SDR11
GS-011	1#	DN260	SDR11
GS-012	2#	DN260	SDR11
GS-013	3#	DN260	SDR11
GS-014	4#	DN260	SDR11
GS-015	5#	DN260	SDR11

Step 2: Fill the pipe sample with fluid (air or water, usually air).

Step 3: Given test temperature and pressure.

Step 4: An impact is made at one end of the pipe to initiate a rapidly propagating longitudinal crack.

Step 5: Use the internal baffle and external locating ring of the test setup to limit edge expansion after cracking and rapid decompression before expansion (uncracked portion) of the sample.

Step 6: Keep the temperature constant and change the pressure to find the critical point (4.7 times the OD length) for stopping and cracking. The higher the critical pressure Pcs_4, the better the resistance of the material to crack expansion.

3. 2. Determination of Critical Pressure　　When the test pressure value was less than 0.8 MPa, the crack length increased very slowly with an increase in the test pressure, and the curve was relatively flat, and the crack length at each pressure point did not exceed 500 mm. After that, with an increase in the pressure, the increase of crack length tends to slow down again and the curve tends to be horizontal. This phenomenon indicates that there is a sudden change in the crack extension of the material as the pressure increases, i.e., there is a critical value of RCP Pc, which is the result of the tough-brittle transformation of the internal structure of the pipe. The critical pressure determination is shown in Figure 3.

The critical pressure values for tubes GS-002 to GS-015 can be obtained in the same way.

The RF-RFE algorithm was used to analyze the experimentally obtained data, and the main factors influencing the RCP of PE pipe were pipe size and wall thickness, impact knife speed, and notched impact strength of the simple beam. The effect of pipe size and wall thickness on rapid crack expansion is shown in Figure 4. Under the same experimental conditions, the extended crack length for PE100-3 pipe is 203 mm for size DN260, 170 mm for size DN150 and 136 mm for size DN65. For PE100-2 pipe, the extended crack lengths for sizes DN260, DN150 and DN65 are 197, 164 and 128 mm in that order. For different pipe specialties, the average crack length is 189 mm for DN260 size, 156 mm for DN150 size and 122 mm for DN65 size.

The results of RCP experiments with different pipe sizes using the same PE pipe material show that the critical pressure values of the different materials differ greatly and the results are not related to the basic physical parameters such as density and melt flow rate of the PE pipe material. The critical pressure values of the same pipe material extruded with different pipe diameters increase as the pipe OD decreases and the wall thickness becomes thinner, and no RCP damage occurs at 0°C
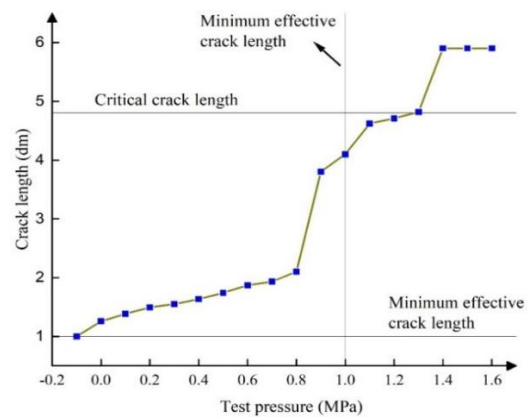
Figure 3. Critical pressure determination
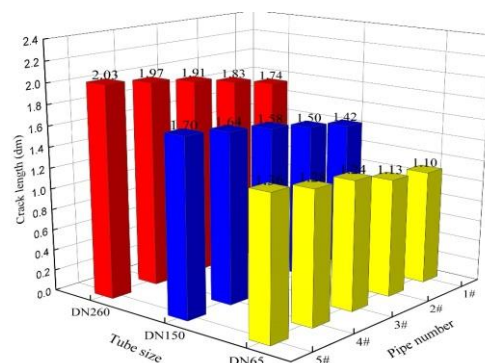
Figure 4. Effect of pipe size and wall thickness on rapid crack propagation

when the pipe diameter is reduced to DN63. This proves that the larger the outside diameter of the pipe and the thicker the wall, the greater the risk of RCP damage at low temperatures.

4. DISCUSSION

The effect of impact knife speed on crack extension is shown in Figure 5. For GS-001 pipe, the crack length was 11 mm at the impact knife speed of 9 m/s and 24, 210 and 239 mm at the impact knife speeds of 10, 15 and 20 m/s. For GS-003 pipe, the crack length was 17 mm at the impact knife speed of 9 m/s and 55, 252 and 256 mm at the impact knife speeds of 10, 15 and 20 m/s, respectively. When the impact knife speed is less than 9 m/s, the pipe cracking does not occur any damage, and only when the impact knife speed is greater than 9 m/s, the effective impact can occur, but the crack cracking length does not increase rapidly with the increase of impact speed, and there is no obvious change of crack cracking length when the impact knife speed is greater than 20 m/s.

A comparison of the notched impact strength and critical pressure values of the simply supported beam is shown in Figure 6. A specific feature of polymers is their ability to deform with respect to time under applied loads. So, for our samples the impact strength for the polyethylene pipeline was 1.021 MPa and 1.56, 1.819, 2.029, 0.225 MPa for pipe diameters of 31.9 mm, 18.2 mm, 17.4 mm, at an ambient temperature of 23°C. The impact toughness for polyethylene pipework was always greater than or equal to 1.8 MPa. The samples with lower values of notched impact strength of the simple beam also had lower value. The samples with the highest notched impact strength of the simple beam also had better RCP performance, which indicates that there is a relationship between the impact strength and RCP performance of the material. At the same time, the notched impact strength and values are not linear, for example, the impact strength of GS-001 is higher than that of GS-002, but the value of
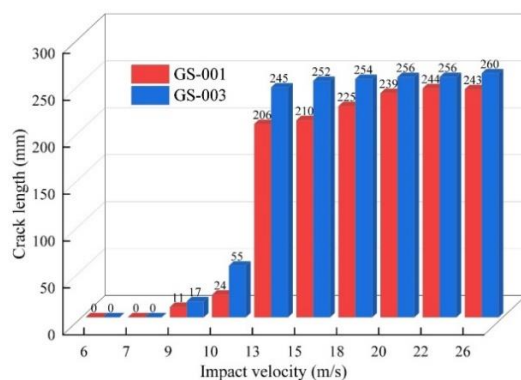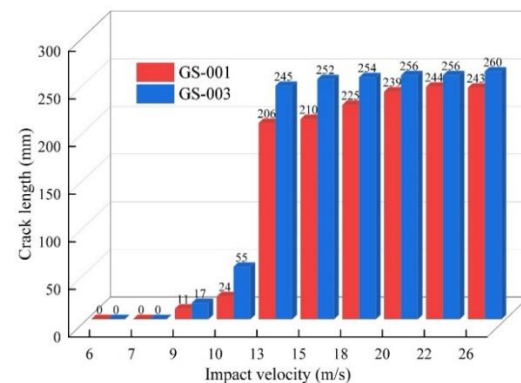
Figure 6. Effect of notched impact strength of simple support beam on crack propagation

GS-002 is higher than that of GS-001. This indicates that the notched impact strength and the critical pressure values of the special materials for pipes are not in complete correspondence.

5. CONCLUSION

The experience of operation of gas pipelines made of polyethylene pipes has shown high resistance of the material to natural gas and less resistance to lower resistance to gaseous propane-butane mixture. From exposure to the vapour phase of these gases the material swells, and at prolonged stay in the liquid phase, it loses some of its mass. This is particularly low-density polyethylene, which swells considerably when exposed to these gases.

Like paraffins, polyethylene is inert to the action of many other substances, such as water, acids, alkalis. The active substances that that have some effect on polyethylene polyethylene include aromatic hydrocarbons (benzene, toluene, xylene), alcohols (methyl, ethyl), oils (vegetable, mineral, silicone), animal fats, inorganic oils (metal-containing oils), synthetic detergents. detergents. The impact of active media is manifested to a greater extent on polyethylene structures under stress. К passive substances include water, inorganic acids, inorganic salts, multi-atomic alcohols (glycerin, polyethylene, polyethylene, etc.). alcohols (glycerine, glycol), paraffins, etc.

This paper analyzes the factors influencing the role of rapid crack expansion in PE pipe using a random forest algorithm with recursive feature elimination. the average crack length for the DN260 size is 189 mm and is within 20 m/s, the faster the impact knife speed, the greater the length of the crack. There are many factors affecting the rapid cracking of PE pipes, mainly influenced by the material's own factors and external factors.

(1) Different types of PE resin prepared pipes have different ability to resist rapid crack expansion, such as PE100 prepared pipes are better than PE80 pipes.

Figure 5. Effect of impact knife velocity on crack propagation

(2) The larger the diameter of PE pipe, the more likely it is to cause rapid crack expansion, while the effect of wall thickness on rapid cracking of pipe depends on the situation.

(3) Under the same conditions, the higher the critical pressure value that the pipe can withstand, the better the pipe's resistance to rapid crack expansion.

(4) The use of temperature directly affects the flexibility of PE pipe, and the use of PE pipe in low temperature conditions is more likely to cause rapid crack expansion of the pipe.

6. REFERENCES

1. Wu, Y., You, X. and Zha, S., "Investigation of mechanical behavior of buried dn110 polyethylene pipe with a scratch defect under land subsidence", *Engineering Failure Analysis*, Vol. 125, (2021), 105371, https://doi.org/10.3390/polym14050987

2. Schipachev, A., Fetisov, V., Nazyrov, A. and Khamrakulov, A., "Study of the pipeline in emergency operation and assessing the magnitude of the gas leak", *Energies*, Vol. 15, No. 14, (2022), 5294, https://doi.org/10.3390/en15145294

3. Guo, Z., Xu, R. and Xue, P., "Study on preparation of ultra-high-molecular-weight polyethylene pipe of good thermal-mechanical properties modified with organo-montmorillonite by screw extrusion", *Materials*, Vol. 13, No. 15, (2020), 3342, https://doi.org/10.3390/ma13153342

4. Kim, T., Deveci, S., Yang, I., Stakenborghs, B. and Choi, S., "Visual, non-destructive, and destructive investigations of polyethylene pipes with inhomogeneous carbon black distribution for assessing degradation of structural integrity", *Polymers*, Vol. 14, No. 5, (2022), 1067, https://doi.org/10.3390/polym14051067

5. Das, S. and Dhar, A.S., "Nonlinear time-dependent mechanical behavior of medium-density polyethylene pipe material", *Journal of Materials in Civil Engineering*, Vol. 33, No. 5, (2021), 04021068, https://doi.org/10.1061/(ASCE)MT.1943-5533.0003695

6. Istrate, I.-R., Juan, R., Martin-Gamboa, M., Domínguez, C., García-Muñoz, R.A. and Dufour, J., "Environmental life cycle assessment of the incorporation of recycled high-density polyethylene to polyethylene pipe grade resins", *Journal of Cleaner Production*, Vol. 319, (2021), 128580, https://doi.org/10.1016/j.jclepro.2021.128580

7. Wee, J.-W., Park, S.-Y. and Choi, B.-H., "Modeling and application of discontinuous slow crack growth behaviors of high-density polyethylene pipe with various geometries and loading conditions", *Engineering Fracture Mechanics*, Vol. 236, (2020), 107205.

8. Patadia, H., Lively, K., Lamborn, M., Maeger, P. and Sukhadia, A., "Rapid crack propagation (RCP) performance of unimodal medium density polyethylene (mdpe) pipe", *Plastics Engineering*, Vol. 69, No. 5, (2013), 12-17, https://doi.org/10.1016/j.engfracmech.2020.107205

9. Deblieck, R.A., van Beek, D., McCarthy, M., Mindermann, P., Remerie, K., Langer, B., Lach, R. and Grellmann, W., "A simple intrinsic measure for rapid crack propagation in bimodal polyethylene pipe grades validated by elastic–plastic fracture mechanics analysis of data from instrumented charpy impact test", *Polymer Engineering & Science*, Vol. 57, No. 1, (2017), 13-21, https://doi.org/10.1002/j.1941-9635.2013.tb01002.x

10. Cerpentier, R.R., Van Vliet, T., Pastukhov, L.V., Van Drongelen, M., Boerakker, M.J., Tervoort, T.A. and Govaert, L.E., "Fatigue-crack propagation of high-density polyethylene homopolymers: Influence of molecular weight distribution and temperature", *Macromolecules*, Vol. 54, No. 24, (2021), 11508-11521, https://doi.org/10.1021/acs.macromol.1c01945

11. Sajid, T., Tanveer, S., Sabir, Z. and Guirao, J., "Impact of activation energy and temperature-dependent heat source/sink on maxwell–sutterby fluid", *Mathematical Problems in Engineering*, Vol. 2020, (2020), 1-15, https://doi.org/10.1155/2020/5251804

12. Bo, Y., Yijiang, L., Maodong, L., Wei, Z., Wenbo, L. and Zhigang, W., "Research progress in cyclic crack round bar test for polyethylene pipes", *China Plastics*, Vol. 33, No. 10, (2019), 128.

13. Guirao, J.L., Sabir, Z. and Saeed, T., "Design and numerical solutions of a novel third-order nonlinear emden–fowler delay differential model", *Mathematical Problems in Engineering*, Vol. 2020, (2020), 1-9.

14. Asghari, F.B., Jaafari, J., Yousefi, M., Mohammadi, A.A. and Dehghanzadeh, R., "Evaluation of water corrosion, scaling extent and heterotrophic plate count bacteria in asbestos and polyethylene pipes in drinking water distribution system", *Human and Ecological Risk Assessment: an International Journal*, Vol. 24, No. 4, (2018), 1138-1149, https://doi.org/10.1080/10807039.2017.1407632

15. Litvinenko, V., Bowbrick, I., Naumov, I. and Zaitseva, Z., "Global guidelines and requirements for professional competencies of natural resource extraction engineers: Implications for esg principles and sustainable development goals", *Journal of Cleaner Production*, Vol. 338, (2022), 130530, https://doi.org/10.1016/j.jclepro.2022.130530

16. Kukharova, T.V., Ilyushin, Y.V. and Asadulagi, M.-A.M., "Investigation of the oa-300m electrolysis cell temperature field of metallurgical production", *Energies*, Vol. 15, No. 23, (2022), 9001, https://doi.org/10.3390/en15239001

17. Stroykov, G., Babyr, N., Ilin, I. and Marchenko, R., "System of comprehensive assessment of project risks in the energy industry", *International Journal of Engineering, Transactions A: Basics*, Vol. 34, No. 7, (2021), 1778-1784, https://doi.org/10.5829/ije.2021.34.07a.22

18. Bolobov, V., Martynenko, Y.V., Voronov, V., Latipov, I. and Popov, G., "Improvement of the liquefied natural gas vapor utilization system using a gas ejector", *Inventions*, Vol. 7, No. 1, (2022), 14, https://doi.org/10.3390/inventions7010014

19. Marinina, O., Tsvetkova, A., Vasilev, Y., Komendantova, N. and Parfenova, A., "Evaluating the downstream development strategy of oil companies: The case of rosneft", *Resources*, Vol. 11, No. 1, (2022), 4, https://doi.org/10.3390/resources11010004

20. Nikolaev, A.K. and Zaripova, N.A., "Substantiation of analytical dependences for hydraulic calculation of high-viscosity oil transportation", *Записки Горного института*, Vol. 252, No., (2021), 885-895, https://doi.org/10.31897/PMI.2021.6.1

21. Baktizin, R.N., Zaripov, R.M., Korobkov, G.E. and Masalimov, R.B., "Assessment of internal pressure effect, causing additional bending of the pipeline", *Записки Горного института*, Vol. 242, (2020), 160-168, https://doi.org/10.31897/pmi.2020.2.160

22. Vasiliev, G.G., Dzhaljabov, A.A. and Leonovich, I.A., "Analysis of the causes of engineering structures deformations at gas industry facilities in the permafrost zone", *Записки Горного института*, Vol. 249, (2021), 377-385, https://doi.org/10.31897/PMI.2021.3.6

23. Liu, Z. and Kleiner, Y., "State of the art review of inspection technologies for condition assessment of water pipes", *Measurement*, Vol. 46, No. 1, (2013), 1-15, https://doi.org/10.1016/j.measurement.2012.05.032

24. Naseri, M. and Barabady, J., "System-reliability analysis by use of gaussian fuzzy fault tree: Application in arctic oil and gas facilities", *Oil and Gas Facilities*, Vol. 4, No. 03, (2015), 085-096, https://doi.org/10.2118/170826-PA

25. Rajeev, P. and Kodikara, J., "Numerical analysis of an experimental pipe buried in swelling soil", *Computers and Geotechnics*, Vol. 38, No. 7, (2011), 897-904, https://doi.org/10.1016/j.compgeo.2011.06.005

26. Thaduri, A., Galar, D. and Kumar, U., "Railway assets: A potential domain for big data analytics", *Procedia Computer Science*, Vol. 53, (2015), 457-467, https://doi.org/10.1016/j.procs.2015.07.323

27. Undertaking, S.R.J. and Plan, M.-A.A., "European union: Brussels", *Belgium, November*, (2015), https://ec.europa.eu/transport/sites/default/files/2018-transport-in-the-eu-current-trends-and-issues.pdf

28. Yazdekhasti, S., Piratla, K.R., Atamturktur, S. and Khan, A.A., "Novel vibration-based technique for detecting water pipeline leakage", *Structure and Infrastructure Engineering*, Vol. 13, No. 6, (2017), 731-742, https://doi.org/10.1080/15732479.2016.1188318

29. Zio, E. and Zio, E., "Monte carlo simulation: The method, Springer, (2013). https://doi.org/10.1007/978-1-4471-4588-2

30. Kim, J.-H., Sharma, G., Boudriga, N., Iyengar, S.S. and Prabakar, N., "Autonomous pipeline monitoring and maintenance system: A rfid-based approach", *EURASIP Journal on Wireless Communications and Networking*, Vol. 2015, No. 1, (2015), 1-21, https://doi.org/10.1186/s13638-015-0495-y

31. Mohamed, N. and Jawhar, I., "A fault tolerant wired/wireless sensor network architecture for monitoring pipeline infrastructures", in 2008 Second International Conference on Sensor Technologies and Applications (sensorcomm 2008), IEEE. (2008), 179-184. https://doi.org/10.1109/SENSORCOMM.2008.116

32. Narayanan, L.K. and Sankaranarayanan, S., "Multi-agent based water distribution and underground pipe health monitoring system using iot", in 16th International Conference on Information Technology-New Generations (ITNG 2019), Springer. (2019), 395-400. https://doi.org/10.1007/978-3-030-14070-0_54

33. Gafarova, V., Kuzeev, I. and Schipachev, A.M., "Investigation of the magnetic nanoparticles interaction on inert carriers", *Key Engineering Materials*, Vol. 854, (2020), 80-86, https://doi.org/10.4028/www.scientific.net/KEM.854.80

34. Mohamed, N., Jawhar, I. and Shuaib, K., "Reliability challenges and enhancement approaches for pipeline sensor and actor networks", in ICWN, Citeseer. (2008), 46-51. http://www.middleware-tech.net/papers/ICWN2008.pdf

35. Shammazov, I.A., Batyrov, A.M., Sidorkin, D.I. and Van Nguyen, T., "Study of the effect of cutting frozen soils on the supports of above-ground trunk pipelines", *Applied Sciences*, Vol. 13, No. 5, (2023), 3139, https://doi.org/10.3390/app13053139

36. Jin, Y. and Eydgahi, A., "Monitoring of distributed pipeline systems by wireless sensor networks", in Proceedings of The. (2008), 213-222. https://www.ijme.us/cd_08/PDF/213%20%20IT304.pdf

37. Fetisov, V., Shalygin, A.V., Modestova, S.A., Tyan, V.K. and Shao, C., "Development of a numerical method for calculating a gas supply system during a period of change in thermal loads", *Energies*, Vol. 16, No. 1, (2022), 60, https://doi.org/10.3390/en16010060

38. Stoianov, I., Nachman, L., Madden, S. and Tokmouline, T., "Pipeneta wireless sensor network for pipeline monitoring", in Proceedings of the 6th international conference on Information processing in sensor networks. (2007), 264-273. https://doi.org/10.1145/1236360.1236396

39. Liu, J., Zhang, L., Mu, X. and Zhang, P., "Studies of electrochemical corrosion of low alloy steel under epoxy coating exposed to natural seawater using the wbe and eis techniques", *Progress in Organic Coatings*, Vol. 111, (2017), 315-321, doi: https://doi.org/10.1016/j.porgcoat.2017.06.012

40. Palaev, A., Shammazov, I. and Dzhemilev, E., "Research of the impact of ultrasonic and thermal effects on oil to reduce its viscosity", in Journal of Physics: Conference Series, IOP Publishing. Vol. 1679, No. 5, (2020), 052073. https://doi.org/10.1088/1742-6596/1679/5/052073

41. Mason, J.F., Stanley, M., Ponda, A. and Demicoli, D., "Case study: Engineered polyamide 12 (pa12) pipeline liner for management of sour gas corrosion at elevated temperatures", in NACE CORROSION, NACE. (2017), NACE-2017-9592. https://onepetro.org/NACECORR/proceedings-abstract/CORR17/All-CORR17/NACE-2017-9592/125639

42. Mason, J., "Thermoplastic liners for oilfield pipelines", *Oil and Gas Pipelines*, (2015), 447-456, https://doi.org/10.1002/9781119019213.ch31

43. Rueda, F., Otegui, J.L. and Frontini, P., "Numerical tool to model collapse of polymeric liners in pipelines", *Engineering Failure Analysis*, Vol. 20, (2012), 25-34, https://doi.org/10.1016/j.engfailanal.2011.10.003

44. Rueda, F., Marquez, A., Otegui, J. and Frontini, P.M., "Buckling collapse of hdpe liners: Experimental set-up and fem simulations", *Thin-Walled Structures*, Vol. 109, (2016), 103-112, https://doi.org/10.1016/j.tws.2016.09.011

45. Khalid, H.U., Ismail, M.C. and Nosbi, N., "Permeation damage of polymer liner in oil and gas pipelines: A review", *Polymers*, Vol. 12, No. 10, (2020), 2307, https://doi.org/10.3390/polym12102307

46. Fetisov, V., Nikolaev, A. and Lykov, Y.V., "Aggregative simulation method for implementing mathematical models for gas transmission systems", in IOP Conference Series: Materials Science and Engineering, IOP Publishing. Vol. 327, No. 2, (2018), 022033. https://doi.org/10.1088/1757-899X/327/2/022033

47. Gibson, A., Linden, J., Elder, D. and Leong, K., "Non-metallic pipe systems for use in oil and gas", *Plastics, Rubber and Composites*, Vol. 40, No. 10, (2011), 465-480, https://doi.org/10.1179/1743289811Y.0000000006

48. Ritums, J., Mattozzi, A., Gedde, U.W., Hedenqvist, M.S., Bergman, G. and Palmlöf, M., "Mechanical properties of high-density polyethylene and crosslinked high-density polyethylene in crude oil and its components", *Journal of Polymer Science Part B: Polymer Physics*, Vol. 44, No. 4, (2006), 641-648, doi: https://doi.org/10.1002/polb.20729

49. Duarte-Poveda, G.I., Valera-Rosales, M.M., Manrique-Rojas, M. and Mateus-Barragán, M., "Evaluation and implementation of high density polyethylene liner: Alternative of solution to corrosion-wear problems in flowlines", *CT&F-Ciencia, Tecnología y Futuro*, Vol. 9, No. 1, (2019), 65-72, https://doi.org/10.29047/01225383.153

50. Zakaria, N., Merican, Z. and Hamza, M., "Performance and critical issues of polymer liners in pipeline industry: A review", *Materials Today: Proceedings*, Vol. 16, (2019), 2389-2397, https://doi.org/10.1016/j.matpr.2019.06.143

51. Durbin, T.D., Karavalakis, G., Norbeck, J.M., Park, C.S., Castillo, J., Rheem, Y., Bumiller, K., Yang, J., Van, V. and Hunter, K., "Material compatibility evaluation for elastomers, plastics, and metals exposed to ethanol and butanol blends", *Fuel*, Vol. 163, (2016), 248-259, https://doi.org/10.1016/j.fuel.2015.09.060

52. Craster, B. and Jones, T.G., "Permeation of a range of species through polymer layers under varying conditions of temperature and pressure: In situ measurement methods", *Polymers*, Vol. 11, No. 6, (2019), 1056, https://doi.org/10.3390/polym11061056

53. Fetisov, V., Ilyushin, Y.V., Vasiliev, G.G., Leonovich, I.A., Müller, J., Riazi, M. and Mohammadi, A.H., "Development of the

automated temperature control system of the main gas pipeline", *Scientific Reports*, Vol. 13, No. 1, (2023), 3092, https://doi.org/10.1038/s41598-023-29570-4

54. Tamai, H., Jinkawa, S. and Sonoda, Y., "Damage evaluation and protection method of resin pipe for gas conduit subjected to impact load", *International Journal of Protective Structures*, Vol. 11, No. 4, (2020), 423-447, https://doi.org/10.1177/2041419620902791

55. Guoquan, Q., Hongxia, Y., Dongtao, Q., Bin, W. and Houbu, L., "Analysis of cracks in polyvinylidene fluoride lined reinforced thermoplastic pipe used in acidic gas fields", *Engineering*

Failure Analysis, Vol. 99, (2019), 26-33, https://doi.org/10.1016/j.engfailanal.2019.01.079

56. Chen, G., Yang, Y., Zhou, C., Zhou, Z. and Yan, D., "Thermal-oxidative aging performance and life prediction of polyethylene pipe under cyclic and constant internal pressure", *Journal of Applied Polymer Science*, Vol. 136, No. 28, (2019), 47766, https://doi.org/10.1002/app.47766

57. Adib, A., Dominguez, C., García, R., Garrido, M. and Rodríguez, J., "Influence of specimen geometry on the slow crack growth testing of hdpe for pipe applications", *Polymer Testing*, Vol. 48, (2015), 104-110, https://doi.org/10.1016/j.polymertesting.2015.09.012
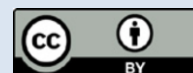
Persian Abstract

چکیده

مطالعه عوامل موثر بر عملکرد لوله پلی اتیلن در برابر انبساط سریع ترک از اهمیت زیادی برای استفاده ایمن از لوله پلی اتیلن برخوردار است. این مقاله نقش هر مرحله در الگوریتم را بر اساس مبنای نظری جنگل تصادفی تجزیه و تحلیل می‌کند و یک روش جنگل تصادفی بهبود یافته مبتنی بر حذف ویژگی بازگشتی با تغییر قوانین تقسیم گره برای رفع کاستی‌های دقت طبقه‌بندی تصادفی جنگل پیشنهاد می‌کند. این روش برای تجزیه و تحلیل اثر انبساط سریع ترک لوله پلی اتیلن از نظر اندازه لوله و ضخامت دیواره، سرعت ضربه چاقوی ضربه ای و مقاومت ضربه ای بریدگی تیرهای تکیه گاه ساده استفاده می شود. در شرایط یکسان، طول ترک توسعه یافته لوله‌های DN260 ،DN150 و DN65 به ترتیب ۱۹۷، ۱۶٤ و ۱۲۸ میلی‌متر است، در حالی که طول ترک‌های لوله‌های PE80 در سرعت‌های ضربه‌ای ۱۰، ۱۵ و ۲٤، ۲۱۰ و ۲۳۹ میلی‌متر است. m/s به ترتیب. هر چه مقاومت ضربه ای بریدگی تیر ساده بیشتر باشد، مقدار فشار بحرانی بالاتر و مقاومت RCP بهتر است. مطالعه گسترش ترک سریع لوله پلی اتیلن بر اساس الگوریتم یادگیری عمیق می تواند عوامل داخلی و خارجی اصلی موثر بر مقاومت RCP لوله پلی اتیلن را شناسایی کرده و مبنای محکمی برای پیش بینی عمر لوله پلی اتیلن فراهم کند.

International Journal of Engineering

Enhancing Comfort in Tropical Institutional Buildings: Integrating Thermal, Acoustic and Visual Performance with a Unified Index

S. Yarramsetty*, MVN. Siva Kumar, P. Anand Raj

Department of Civil Engineering, NIT Warangal, Telangana State, India

P A P E R   I N F O

A B S T R A C T

This study explores the relationship between a country's level of development and its educational standards, emphasizing the significance of well-equipped universities in ensuring high-quality education. While research on comfort in educational buildings has often focused on individual parameters, such as thermal, acoustic, and visual elements, this paper proposes a new metric that integrates these factors to assess environmental comfort. The research was conducted in six hostel rooms at the National Institute of Technology Warangal (NITW) campus in India, utilizing both objective measurements and subjective surveys. Three single measures were introduced: a thermo-hygrometric index, an audio comfort index, and a visual illumination index, each normalized within a 0-1 range denoting comfort and discomfort conditions. A final total comfort index for each room was established by assigning appropriate weights to the three factors. The findings were compared to the questionnaire responses, evaluating the effectiveness of the proposed methodology. The results indicate a comprehensive assessment of indoor environmental comfort, with acoustic factors showing the least impact on overall comfort conditions. The study recommends equal weighting for thermal, acoustic, and lighting parameters when computing the combined comfort index. The building achieved an overall comfort rating of 0.64 out of 1, indicating a comfortable environment. The study also shows that there is a strong correlation between the new combined comfort index and the results from the questionnaire. This research contributes a straightforward and integrated approach to gauge comfort levels in educational buildings and lays the groundwork for further assessments of institutional building performance.

1. INTRODUCTION

There are over one million five hundred sixty-nine thousand educational institutions in India, including several public and a significant number of privately held structures [1]. Government structures significantly contribute to greenhouse gas emissions (GHG). As a result, it is critical to assess the actual performance of university facilities. It has been discovered that the utilization phase of the created environment consumes a significant amount of energy [2, 3]. Nistratov et al. [4] innovated a method employing composite waste as environmentally-friendly building materials, cutting

landfill waste costs and reducing production expenses by substituting primary materials. Significant energy savings and CO_2 emission reductions can be realized during the use phase of buildings [5-7]. Occupants spend a large portion of their lives indoors, in built-up environments. Throughout their undergraduate or graduate studies, students in the age range of 18-26 spend the majority of their time (87%) inside buildings. Hence, interior spaces should include the elements that provide a stimulating atmosphere to advance students' learning and analytical thinking [8, 9].

The building sector in India consumes around 35% of the total energy, with an annual increase of 8%. Various techniques and methods are being developed to address this issue [10-12]. The structure's use phase, which includes all amenities for the users' maximum

*Corresponding Author: email: *sraoystp@student.nitw.ac.in*
(S. Yarramsetty)

comfort, accounts for approximately 73% of total building energy [13-16]. In order to maintain thermal comfort, educational buildings consume a sizable quantity of energy. The overall energy consumption in the Indian educational building stock reaches 4,832 GWh, according to the Energy use in COmmercial buildings (ECO-III) study [17]. Thermal comfort can have a significant impact on the learning process and on the motivation to engage in academic pursuits [18-22]. Haverinen-Shaughnessy et al. [19] discovered strong correlations between good math and reading, exam results and interior temperature, ventilation rate, and cleanliness of high contact surfaces. Lee et al. [21] reported similar findings in four university classes in Hong Kong, demonstrating high correlations between votes and total indoor environmental quality, particularly for auditory components. Toyinbo et al. [22] discovered a link between poorer mathematics exam scores in school buildings and non-recommended ventilation rates. Yang et al. [18] attempted to assess the influence of classroom characteristics on student happiness and performance. According to Wargocki and Wyon [20], poor indoor environmental quality affects learning performance by 30%. Doi [23] and Musa et al. [24] examined how passive cooling technologies can regulate urban development's impact on thermal comfort.

A recent review conducted by Zomorodian et al. [25] identified 48 studies on thermal comfort in educational buildings published in past decades. Among these studies, 25% focused on elementary and middle schools, 34% on secondary and high schools, and the remaining 41% on universities. Recent field investigations in primary and secondary schools have highlighted that children, due to their higher metabolism, experience thermal comfort differently than adults [26-30]. Notably, the neutral comfort temperature was found to be 23.1 °C in primary schools, 23.8 °C in secondary and high schools, and 25.1 °C in universities [25]. These findings emphasize the importance of considering different age groups' thermal comfort requirements in educational buildings. Furthermore, the acoustical characteristics of primary, secondary, and tertiary-level classrooms as well as their impact on pupil success were studied. Yang and Bradley [31] conducted speech tests on elementary school pupils and adults and discovered that the intelligibility of speech for young children is influenced by reverberation time (RT), which is lower than the signal-to-noise ratio. According to Klatte et al. [32] background noise has a greater negative impact on children's speech perception and listening comprehension than it does on adults. Hodgson [33] demonstrated that the British Columbia University's classrooms had severe reverberation, low speech volumes, particularly at the rear of the rooms, and extremely noisy ventilation systems. They also created a questionnaire to assess perception of the listening environment. likewise Zannin and Marcon [34] learned that a Brazilian public school had inadequate acoustics [35].

Finally yet importantly, it is understood that having comfortable visual environments in classrooms is essential for learning and benefits the educational process. Michael and Heracleous [36] looked into how well a typical educational institution in Cyprus utilized natural lighting and suggested improvements to enhance visual comfort in classes. For the purpose of meeting the needs of the students in Athens' south-facing classrooms, Meresi [37] developed a particular light shelf for shade and light redirection as well as semitransparent, adjustable exterior shutters. Through the use of simulations and questionnaires, Korsavi et al. [38] examined a typical high school in Kashan, Iran. The results of the questionnaire revealed a wider range of sunlight acceptability, and the simulation results revealed a more upbeat approach [39].

The previous studies primarily focus on examining the effects of individual factors on environmental comfort, with limited attempts to comprehensively assess the cumulative impact of various perspectives. In order to gauge students' perceptions of acoustic and lighting comfort, tailored questionnaires were developed. By analyzing the mean responses to questions closely aligned with measured data, six acoustic indices and four visual indicators were formulated. These recommended indices are amalgamated in this study into a unified index that encompasses three distinct attributes: thermal-hygrometric, auditory, and lighting comfort conditions. For each attribute, three specific single indices are initially proposed: the Predicted Mean Vote (PMV) Index for thermal-hygrometric settings, the Sound Index for acoustic comfort, and the Visual Index for lighting conditions. These indices are dimensionless and normalized within the 0 to 1 range, where values nearing 1 indicate favorable comfort conditions, while those nearing 0 signify unfavorable ones. Based on the correlation between questionnaire responses and collected data, each index was computed. Following prior research, equal importance was assigned to lighting, acoustics, and thermos-hygrometry comfort. Consequently, a composite comfort index is recommended and calculated for each classroom using these weighted factors.

The aim of this study by the authors is to investigate how the environment influences occupant comfort, considering aspects of thermal, acoustic, and lighting conditions. These fundamental factors play a vital role in shaping overall comfort conditions and can be managed through a combination of active measures such as utilizing plants and passive strategies like enhancing the building envelope [40].

2. METHODOLOGY

2. 1. Available Data & Case Study   The investigation comprised the examination of six hostel rooms situated on the premises of the National Institute of Technology Warangal (NITW) campus. The methodology's visual representation is captured by the flowchart in Figure 1. These particular rooms are located within a hostel complex boasting a total capacity of 1,800 rooms (1.8k hostel/Ultra mega hostel) and are specifically designated as A3-13, B3-50, A7-12, B7-20, and B7-48. The selection of these rooms was guided by factors such as the availability of students for active participation in the investigation and survey activities. A comprehensive consolidation of essential details concerning the hostel rooms, encompassing dimensions and occupancy particulars, is outlined in Table 1. Notably, this study maintained a dedicated focus on single sharing rooms to ensure coherence and uniformity within the analytical framework. Figure 2 depicts the arrangement of single and double sharing. Figures 3 and 4 depict a typical floor plan, ariel view, and front view of the 1.8K hostel. The hostel rooms were studied in terms of thermo-hygrometrical, lighting, and acoustical conditions.

The measurements were taken at a height of 0.75 m to represent the students' usual sitting space, as shown in Figure 5. Experimental measurements of natural ventilated illumination and acoustical conditions were measured with various instruments. Table 2 lists the instruments used to collect the data.

2. 2. Analysis of Questionnaire Data   The experimentally measured data are compared to the responses from the questionnaire based on the questions shown in Table 3. To accomplish this, each question is linked to each measured value in order to assess the subjective parameters that are most closely related to the experimental data. Figure 5 depicts the experimental data collection.

2. 3. The Individual Proposed Indexes Individual indexes are evaluated for each parameter under consideration, and by combining individual indexes, a final single index that describes acoustic,
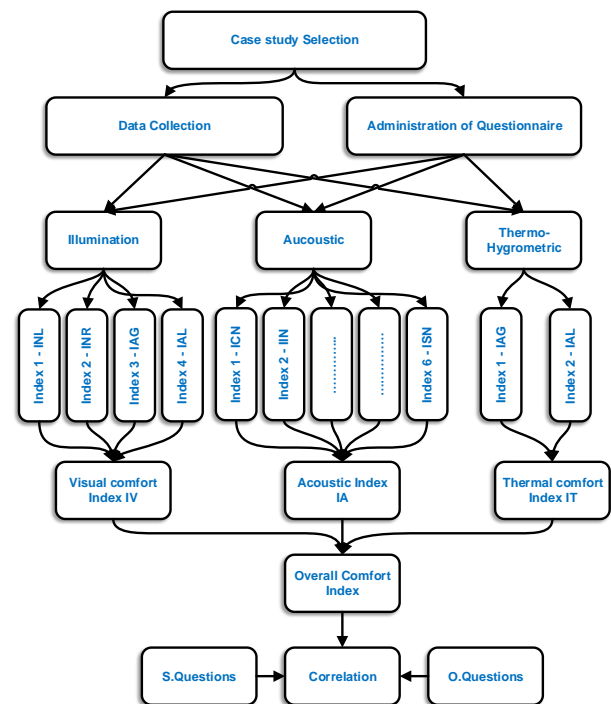
Figure 1. Flowchart showing Methodology

TABLE 1. Characteristics of Hostel rooms

Room type	Sharing	Length (m)	Width (m)	Height (m)	Floor area (m²)	Volume (m³)	Door surface (m²)	Window surface (m²)
A	1	3.55	3.00	2.80	10.65	29.82	1.99	2.16
B	1	3.64	3.00	2.80	10.92	30.58	1.99	2.16
C	1	3.53	3.00	2.80	10.59	29.65	1.99	2.16
D	1	4.09	3.00	2.80	12.27	34.36	1.99	2.16
E	1	3.18	3.00	2.80	09.54	26.71	1.99	2.16
F	1	3.77	3.00	2.80	11.31	31.67	1.99	2.16
G	2	3.28	4.20	2.80	13.78	38.57	1.99	2.16
H	2	3.78	4.20	2.80	15.88	44.45	1.99	2.16
I	2	3.55	4.20	2.80	14.91	41.75	1.99	2.16
J	2	3.11	4.20	2.80	13.06	36.57	1.99	2.16
K	2	3.50	4.20	2.80	14.70	41.16	1.99	2.16
L	2	3.77	4.20	2.80	15.83	44.33	1.99	2.16
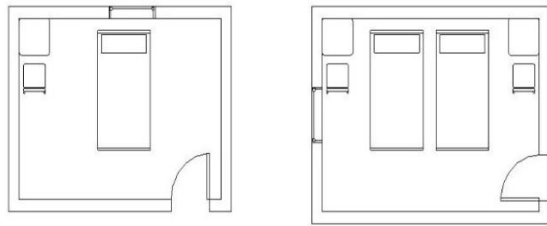
Figure 2. Typical Single and Double sharing arrangement
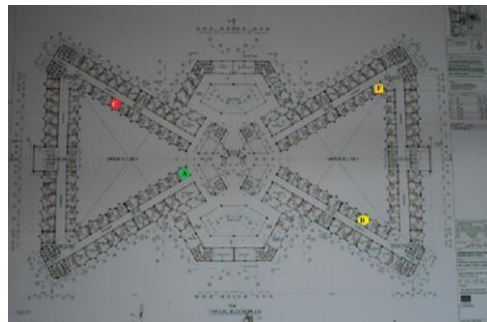
(a)

(b)

Figure 3. Top view of the building a) Plan view of 7th floor b) Birds eye view

Figure 4. Front view of the 1.8K hostel

Figure 5. Illustrates the aggregation of factual data

lighting, and thermal-hygrometric comfort conditions must be established. Individual indices are calculated by taking into account the various questionnaire survey indexes listed in the corresponding section. Each index is given weight based on the degree of correlation between the perceived and measured values. The average of the answers to the questions is used as the index value, which ranges from 0 to 10. The dimensionless single parameter index is calculated by normalizing the value (0 to 1) and dividing it by 10.

2. 3. 1. Acoustic Index I_A   The acoustic index I_A is calculated as follow:

$$I_A = \frac{\begin{matrix}0.1*(10-ICN)+0.1*IIN+0.4*(10-IDN)\\+0.2*(10-ION)+0.1*(10-IRN)+0.1*(10-ISN)\end{matrix}}{10} \quad .(1)$$

where ICN, IIN, IDN, ION, IRN and ISN are explained in Table 3. The weightage for each question is given in proportion to its correlation with the experimental data, with the question that is most correlated with the experimental data receiving the most weightage. ICN is given a 10% weight. IIN receives 10% of the weight, while IDN receives 40% of the weight. ION receives a 20% weightage, IRN receives a 10% weightage, and ISN receives a 10% weightage. It is important to note that an increase in mean votes for the indexes ICN, IDN, ION, IRN, and ISN is detrimental to acoustic comfort; therefore, a complement of 10 was considered in the average.

2. 3. 2. Visual Comfort Index I_V   The lighting index I_{vc} is calculated as follow:

$$I_{VC} = \frac{0.46*INL+0.01*INR+0.03*(10-IAG)+0.5*(10-IAL)}{10} \quad .(2)$$

TABLE 2. Comfort parameters range, accuracy and resolution

Parameter		Units	Range	Accuracy	Resolution	Instrument system
Air Temperature	Ti	ºC	-50ºC to +70ºC (-58ºF to + 158ºF)	± 1ºC	0.1ºC	HTC-1, Digital Hygrometer Temperature Humidity Meter
Air Relative Humidity	Rh	%RH	10% RH to 99% RH	±5% RH	1%	
Sound	Si	dB	35 dB to 130 dB	1 dB	1dB	Digital Sound Level Meter
Illumination	Li	Lux	0 Lux to 200000 Lux	+ 3%	0.01 Lux	HTC Lux meter LX-103

TABLE 3. Acoustic, Lighting and Thermal questionnaires: selected questions and correspondent indexes

	No.	Question	Index
Acoustic	1	Hostel mates making noise in the corridors	ICN- Corridor Noise Index
	2	Internal noise (fan, phone, etc)	IIN- Internal Noise Index
	3	Noises that disturbs once in a day	IDN- Daily Noise Index
	4	Noises that disturbs occasionally	ION- Occasional Noise Index
	5	Do these noises disturbs you while taking rest	IRN- Rest Noise Index
	6	Do these noises disturbs you while you studying	ISN- Study Noise Index
Lighting	1	Amount of light entering through the windows	INL- Natural Light Index
	2	Experience discomfort due light reflecting from outside	INR- Reflection Light Index
	3	Inside the room, dark patches and too bright locations created by window	IAG- Lighting Annoying Glares Index
	4	How frequently you use artificial lighting in room	IAL- Artificial Light Index
Thermal	1	The heat entering through windows from natural source (sun) in winter	INH- Natural Heat Index
	2	The heat shield by the windows and wall (summer)	IIH- Internal Heat Index

Table 3 defines the terms INL, INR, IAG, and IAL. INL receives 46% of the weightage, INR receives 1%, IAG receives 3%, and IAL receives 50% of the weightage. We used a negative value in the calculations by subtracting the votes from 10. Because an increase in mean votes for the indices IAG and IAL reduces visual comfort.

2. 3. 3. Thermal Comfort Index I_T   The predicted mean value can be used to assess thermal comfort (PMV). The PMV value will range between -3 and +3. I_{PMV}, with a value ranging from 0 to 1, is calculated from PMV using the following formula, taking into account the linear relationship depicted in Figure 6.

$$I_{PMV} = |(|PMV|+1) - (|PMV|*4/3)| \qquad (3)$$

When PMV is -3 or +3, IPMV has a value of 0 and has a maximum value of 1 when PMV is 0. The intermediate values will have a linear trend ranging from 0 to 1.

2. 3. 4. The New Overall Comfort Index I_{NCC} The weighted average values of individual comfort indices are added to calculate the new overall comfort index. The equal weights of three individual comfort indexes, which are normalised to the 0-1 range. The formula for calculating the new combined comfort index is given below:

$$I_{NCC} = 0.33*I_A + 0.33*I_V + 0.33*I_T \qquad .(4)$$

3. RESULTS

During the month of October 2018, data was collected for seven days. The information gathered is related to thermal, lighting, and acoustical conditions [41]. Table 4 displays the mean values of the observed data.

In the brief autumn month of October, the minimum value of mean indoor temperature reaches 30.1ºC (room B7-18), corresponding to an outdoor temperature of 31.70ºC [8]. Indoor temperatures reach a maximum of 30.56ºC. (room A7-12). As a result, there is not much of a temperature difference between the rooms; they are almost all the same temperature. Acoustic results show
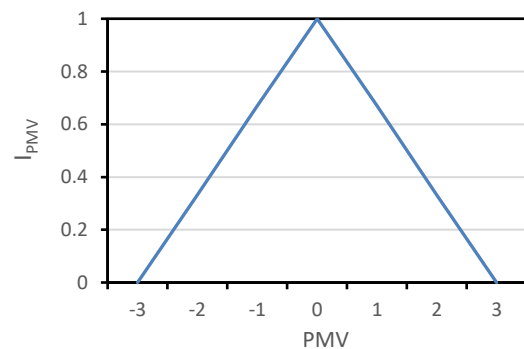
Figure 6. PMV Vs I_{PMV}

TABLE 4. Mean values of observed data of one week

Parameter	Temp Ti_d	Humidity (%)	Sound (dB)	Illuminance (lux)
Out door	31.7	50.05	65.7	494.6
A3-13	30.29	54.64	67.66	183.71
B3-50	30.16	54.67	65.6	284.18
A7-12	30.56	54.45	71.56	483.09
A7-46	30.35	54.95	71.91	294.81
B7-20	30.35	54.95	70.95	465.14
B7-48	30.1	55.56	68.29	178.84

Ti_d – Temp. INDOOR

that sound levels in all rooms exceed 60dB. The maximum sound level was 71.91 dB (room A7-46), which could be attributed to the fact that there were more people in the room most of the time.

3. 1. Acoustic Index IA   The acoustic survey results are tabulated in Table 5. Acoustic indices are derived using Equation (1) from the survey responses. Among the rooms, B7-48 exhibits the highest internal noise, while Room A3-13 attains the most favorable value (8.12 for occasional noise). A comparative assessment is presented in Table 5, confirming Room A3-13's superior performance. Upon reviewing the IA values in Table 5, it becomes evident that Room A3-13 excels with an acoustic comfort index of 0.68. Notably, almost all rooms yield an acoustic index above 0.6 (excluding B7-20 with 0.59). The consistent acoustic index values within the 0-1 scale across rooms indicate uniform behavior. Values surpassing 0.6 within the 0-1 range signify satisfactory performance, underscoring good acoustic comfort across all rooms.

3. 2. Visual Parameter Comfort Index– IVC
Table 6 lists the illumination comfort index values. Room A7-12 is found to have a high level of visual comfort (0.75), as well as a high illumination value of 483.18 lux and low annoying glare formation from natural light. All rooms with a visual comfort index greater than 0.5 are considered visually comfortable. Because of higher glare formation due to natural lighting, rooms A3-13 and B7-48 have a lower visual comfort index (0.56).

3. 3. Thermal Comfort Index IT   The thermal sensation is evaluated on a 10-point scale (0-10), which is then converted into the traditional Fanger scale (7–value). Because this survey is taking place during the brief autumn month of October, and all average measured temperatures are above 30 degrees Celsius, the scale is converted to the warm side (0 to 3) of the Fahrenheit scale. If the response is 10, PMV is set to 0 and IPMV is set to 1, which is more comfortable. If the response is 0, it indicates that the occupant is more dissatisfied, resulting in a -3 on the fanger scale and an I_{PMV} of 0. Many factors influence thermal comfort, including metabolism, clothing resistance, air velocity, mean radiant temperature, and relative humidity. Due to the lack of equipment, the only factors considered in this thermal comfort evaluation are temperature and relative humidity. Table 7 contains the PMV and IPMV. Room A has good thermal comfort (I_{PMV} = 0.81) while Room D has I_{PMV} = 0.74. The remaining space has an index of around 0.6.

3. 4. The New Overall Comfort Index INCC   By substituting the individual indices in Equation (4), the new combined overall comfort index is calculated. The total index value of the rooms is furnished in Table 8. The new combined comfort index is measured on a scale of 0 to 1, with 0 being the worst and 1 being the best. More than 0.65 is considered comfortable shwon by smile face. Neutral is 0.45 to 0.65 shown by emotionless face, and Uncomfortable is lessthan 0.45 shown by sad face. According to this classification, rooms A3-13, A7-12, and A7-46 are comfortable, while the remaining rooms have a comfort index of less than 0.6 and fall into the neutral category. The NCC for all

TABLE 5. Acoustic Index (I_A) based on questionnaire

	Room	A3-13	B3-50	A7-12	A7-46	B7-20	B7-48
Acoustic Index	10-ICN	6.37	5.73	6.71	5.87	5.68	6.18
	IIN	5.81	5.50	6.00	4.35	4.23	3.36
	10-IDN	6.75	6.41	6.67	6.26	6.23	7.23
	10-ION	8.12	6.5	7.52	7.78	6.27	6.77
	10-IRN	7.12	6.55	6.86	7.00	6.32	6.64
	10-ISN	5.69	5.18	5.38	6.17	5.27	6.45
	I_A	**0.68**	0.62	0.67	0.64	0.59	0.65

TABLE 6. Visual comfort index I_V based on questionnaire

	Room	A3-13	B3-50	A7-12	A7-46	B7-20	B7-48
Visual comfort index	INR	7.31	5.68	7.19	6.52	5.41	5.09
	10-IAG	5.25	4.95	5.71	5.65	5.36	6.32
	10-IAL	5.06	6.45	6.86	4.96	5.64	4.45
	IVC	0.56	0.66	**0.75**	0.61	0.62	0.56

TABLE 7. PMV & I_{PMV} values

Room	PMV	I_{PMV}
A	0.57	0.81
B	1.41	0.53
C	1.17	0.61
D	0.77	0.74
E	1.25	0.58
F	1.23	0.59

TABLE 8. New combined comfort index value of rooms

Index	A3-13	B3-50	A7-12	A7-46	B7-20	B7-48
I_A	0.68	0.62	0.67	0.64	0.59	0.65
I_V	0.56	0.66	0.75	0.61	0.62	0.56
I_T	0.81	0.53	0.61	0.74	0.58	0.59
I_{NCC}	**0.68**	0.60	**0.67**	**0.66**	0.59	0.59

observed rooms is plotted in Figure 7, and it is observed that rooms B3-50, B7-20, and B7-48 have low thermal index values because their windows face the Sun for a longer period of time than the remaining rooms.

Correlating the Indoor Comfort Combined Index (INCC) with mean votes from occupants on thermal, acoustic, and lighting aspects (calculated as the arithmetic average of the three votes). Mean votes for specific questions (with refering to Table 3, mean votes of Aucoustic:Q2, Lightning:Q1 and Thermal:Q1) are categorized as Mean values of simple questions (Mean S.Q), while mean votes for all questions are categorized as Mean values of Overall Questions (Mean O.Q). The approach evaluates the suitability of INCC for describing room comfort comprehensively. Outcomes are presented in Table 9, showing good correspondence between rooms and INCC for various comfort conditions using both Mean S.Q and Mean O.Q. Specific rooms (B7-20 and B7-40) are rated neutral with INCC 0.59, aligning with occupants' mean votes. Discrepancies arise, such as in room A7-46, where INCC doesn't fully match occupants' votes on acoustic and visual comfort. Reasonable correlation coefficients of 0.67 and 0.79, for Mean S.Q and Mean O.Q respectively, indicate a solid link between INCC and occupant votes.

4. DISCUSSION

This study has examined a novel composite comfort index that integrates thermal, acoustic, and lighting aspects within an educational building. A comprehensive analysis was conducted by cross-referencing the responses obtained from Table 3's questionnaire with empirical measurements. Each question was matched with corresponding measurements, facilitating an assessment of the questionnaire's key subjective elements in relation to real-world data. The subsequent section delves into the correlation between the combined comfort index (INCC) and the average occupant ratings for heat, noise, and lighting factors (Figure 8). This investigation aims to establish whether the newly proposed INCC indicators effectively characterize the collective comfort conditions within the room. The findings in Table 9 underscore that rooms A3-13, A7-12, and A7-46 exhibit notably improved comfort conditions in comparison to other spaces. Room A3-13 demonstrates a heightened thermal comfort index (IT = 0.81) but a relatively lower visual comfort index (IV = 0.56), contrasting with room B3-50's lower thermal comfort (IT = 0.53) and elevated visual comfort (IV = 0.66). The compromised state of the thermo-hygrometric dimension is likely to additionally, Table 10 presents the relative weights assigned to acoustic, thermal, and lighting parameters for overall indoor environmental comfort, as gleaned from prior field studies. This facilitates parameter-level comparisons to provide comprehensive insights. While study data from various geographical regions can't be directly correlated, it's noteworthy that acoustics had the least influence on the overall indoor environmental comfort conditions among the three parameters examined. Field studies did not yield conclusive trends in comfort parameter weighting. Buratti [50] suggests that acoustic, thermal, and illumination factors hold nearly equal importance, which aligns with the findings of this study.

Figure 7. Comparison of indices of rooms

TABLE 9. Comparison between INCC and mean votes

Room	Comfort			Mean Vote		INCC
	Acoustic	Visual	Thermal	S.Q	O.Q	
A3-13	🙂	😐	🙂	7.11	7.06	0.68
B3-50	😐	🙂	😐	6.10	6.52	0.60
A7-12	🙂	🙂	😐	8.56	7.65	0.67
A7-46	😐	😐	🙂	8.11	7.27	0.66
B7-20	😐	😐	😐	4.10	5.13	0.59
B7-48	🙂	😐	😐	6.17	5.49	0.59
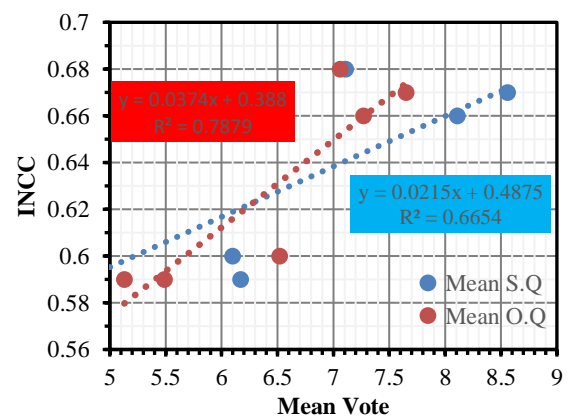
Figure 8. Correlation of INCC with Mean Vote

TABLE 10. Summarization of previous studies based on indoor environmental comfort

Comfort Parameter weightage			Sample size	Type of analysis	Reference
Acoustical	Thermal	Illumination			
0.11	0.10	0.46	1000 denizens (US)	Pearson Product-moment correlations	[42]
0.20	0.21	0.16	12 advisors (Taiwan)	AHP	[43]
0.5	0.28	0.25	852 secondary school students (Italy)	Pearson coefficient	[44]
4.74	6.09	3.70	293 denizens (Hong Kong)	Multivariate regression	[45]
0.22	0.32	0.17	500 denizens (Beijing & Shanghai)	Multivariate regression	[46]
0.18	0.30	0.16	68 denizens (UK)	Multivariate regression	[47]
0.16	0.17	0.15	Standard code - EN15251	Relative weightage vector	[48]
0.18	0.33	0.30	17 denizens (Italy)	Multivariate regression	[49]
0.36	0.34	0.30	928 denizens	Questionnaires	[50]

The INCC indicators exhibit a notable alignment with the three distinct comfort conditions, as observed through Mean S.Q and Mean O.Q measurements (refer Table 9). Classrooms B7-20 and B7-40 are assessed as neutral with an INCC value of 0.59, which resonates with occupants' average votes of 5.13 and 5.49 (Mean O.Q). The potential influence of poor thermo-hygrometric conditions on these rooms is plausible. For room A7-46, the INCC value does not closely mirror the occupants' mean vote (neutral for acoustic and visual comfort). It is conceivable that students attributed more significance to the thermal aspect. A noteworthy correlation was identified between the mean votes assigned to the rooms and the INCC, established for both S.Q and O.Q metrics. The obtained R^2 values from this analysis are substantial, registering 0.67 and 0.79, respectively. This consistency aligns with the efficacy of the composite thermal, acoustic, and visual comfort indicator formulation. Conducting a broader experimental campaign with the new questionnaire could provide valuable validation of the newly proposed index. This approach involves calculating the index using data distinct from those used to develop the methodology, thereby augmenting its robustness.

5. CONCLUSION

This study introduces a pioneering approach to comprehensively assess the comfort levels within institutional buildings, unveiling a newly devised combined comfort index. Through an intricate analysis of thermal, acoustic, and visual comfort factors in six university hostel rooms, this research formulates a comprehensive model for evaluating comfort that goes beyond conventional parameters. The distinctive aspect lies in its ability to holistically measure comfort through

a user-friendly questionnaire. The significance of each question aligns with its correlation to real-world data, leading to higher weighting for questions closely connected to actual experiences.

Building upon this framework, distinct equations are crafted for each comfort parameter (thermal, acoustic, and lighting). These parameters are subsequently normalized within a 0–1 range, where enhancements in comfort elevate dimensionless values from 0 to 1. Drawing from preceding research, equal importance is assigned to the three comfort-related indexes -IT (Thermal Index), IA (Acoustic Index), and IV (Illumination Index) -to establish the equation for the New Combined Comfort Index. By amalgamating individual indexes with uniform weights, a consolidated index emerges as the ultimate metric. The building's overall comfort achieves a rating of 0.64 out of 1, characterizing it as a comfortably conducive environment. Notably, a robust correlation emerges between room-specific mean votes and the INCC, substantiated through both S.Q and O.Q metrics. The ensuing R^2 values, 0.67 and 0.79 respectively, underscore the statistical robustness of this association.

This study not only introduces a fresh paradigm for evaluating comprehensive comfort but also demonstrates its practicality by devising the New Combined Comfort Index. Such insights open avenues for advanced strategies in designing and enhancing comfort conditions in built spaces.

6. REFERENCES

1. MHRD, D. "Educational Institutions Statistics India 2016." Retrieved June 10, 2019, from http://dise.in/ and http://mhrd.gov.in/statist

2. Nässén, J., Holmberg, J., Wadeskog, A., and Nyman, M. "Direct

and indirect energy use and carbon emissions in the production phase of buildings: An input-output analysis." *Energy*, Vol. 32, No. 9, (2007), 1593-1602. https://doi.org/10.1016/j.energy.2007.01.002

3. Yohanis, Y. G., and Norton, B. "Life-cycle operational and embodied energy for a generic single-storey office building in the UK." *Energy*, Vol. 27, No. 1, (2002), 77-92. https://doi.org/10.1016/S0360-5442(01)00061-5

4. Nistratov, A. V., Klimenko, N. N., Pustynnikov, I. V., and Vu, L. K. "Thermal Regeneration and Reuse of Carbon and Glass Fibers from Waste Composites." *Emerging Science Journal*, Vol. 6, No. 5, (2022), 967-984. https://doi.org/10.28991/ESJ-2022-06-05-04

5. Airaksinen, M., and Matilainen, P. "A Carbon footprint of an office building." *Energies*, Vol. 4, No. 8, (2011), 1197-1210. https://doi.org/10.3390/en4081197

6. Wu, H. J., Yuan, Z. W., Zhang, L., and Bi, J. "Life cycle energy consumption and CO_2 emission of an office building in China." *The International Journal of Life Cycle Assessment*, Vol. 17, No. 2, (2012), 105-118. https://doi.org/10.1007/s11367-011-0342-2

7. Yarramsetty, S., Rohullah, M. S., and Anand, M. V. N. S. "An investigation on energy consumption in residential building with different orientation : a BIM approach." *Asian Journal of Civil Engineering*, No. 0123456789, (2019). https://doi.org/10.1007/s42107-019-00189-z

8. Thapa, S., Bansal, A. K., and Panda, G. K. "Thermal comfort in naturally ventilated office buildings in cold and cloudy climate of Darjeeling, India - An adaptive approach." *Energy and Buildings*, Vol. 160, (2018), 44-60. https://doi.org/10.1016/j.enbuild.2017.12.026

9. Dear, R. De, Kim, J., Candido, C., Deuble, M., Dear, R. De, Kim, J., Candido, C., and Deuble, M. "classrooms Adaptive thermal comfort in Australian school classrooms," No. May, (2015), 37-41. https://doi.org/10.1080/09613218.2015.991627

10. BEE. "Energy benchmarks for Commercial Buildings Bureau of Energy Efficiency 4 th Floor, Sewa Bhawan, R.K. Puram, New Delhi-110066 Website : www.beenet.in." Retrieved January 21, 2023, from http://eecbindia.com/

11. Bangia, T., and Raskar, R. "Cohesive Methodology in Construction of Enclosure for 3.6m Devasthal Optical Telescope." *HighTech and Innovation Journal*, Vol. 3, No. 2, (2022), 162-174. https://doi.org/10.28991/HIJ-2022-03-02-05

12. Barreca, F., Arcuri, N., Cardinali, G. D., Fazio, S. Di, Rollo, A., and Tirella, V. "A Highly Sustainable Timber-Cork Modular System for Lightweight Temporary Housing." *Civil Engineering Journal (Iran)*, Vol. 8, No. 10, (2022), 2336-2352. https://doi.org/10.28991/CEJ-2022-08-10-020

13. BEE. *Energy Conservation Building Code 2017*.

14. Rawal, R., Vaidya, P., Ghatti, V., Ward, A., Group, T. W., Seth, S., Jain, A., and Parthasarathy, T. "Energy Code Enforcement for Beginners : A Tiered Approach to Energy Code in India," No. Cbre 2011, (2012), 313-324.

15. Rincon, L., Castell, A., Perez, G., Sole, C., Boer, D., and Cabeza, L. F. "Evaluation of the environmental impact of experimental buildings with different constructive systems using Material Flow Analysis and Life Cycle Assessment." *Applied Energy*, Vol. 109, (2013), 544-552. https://doi.org/10.1016/j.apenergy.2013.02.038

16. Taherkhani, R., Alviri, M., Panahi, P., and Hashempour, N. "Low Embodied Carbon and Energy Materials in Building Systems: A Case Study of Reinforcing Clay Houses in Desert Regions." *International Journal of Engineering, Transactions B: Applications*, Vol. 36, No. 8, (2023), 1409-1428. https://doi.org/10.5829/ije.2023.36.08b.02

17. Kumar, S. *USAID ECO - III Project Energy Use in commercial buildings - Key findings from the national benchmarking study*. Retrieved from USAID - INDIA

18. Yang, Z., Becerik-gerber, B., and Mino, L. "A study on student perceptions of higher education classrooms : Impact of classroom attributes on student satisfaction and performance." *Building and Environment*, Vol. 70, (2013), 171-188. https://doi.org/10.1016/j.buildenv.2013.08.030

19. Ulla, Haverinen-shaughnessy; Shaughnessy, Richard J; Cole, Eugene C; Toyinbo, O., and Moschandreas, D. J. "An assessment of indoor environmental quality in schools and its association with health and performance." *Building and Environment*, Vol. 93, (2015), 35-40. https://doi.org/10.1016/j.buildenv.2015.03.006

20. Wargocki, P., and Wyon, D. P. "Providing better thermal and air quality conditions in school classrooms would be cost-effective." *Building and Environment*, Vol. 59, , (2013), 581-589. https://doi.org/10.1016/j.buildenv.2012.10.007

21. Lee, M. C., Mui, K. W., Wong, L. T., Chan, W. Y., Lee, E. W. M., and Cheung, C. T. "Student learning performance and indoor environmental quality (IEQ) in air-conditioned university teaching rooms." *Building and Environment*, Vol. 49, No. 1, (2012), 238-244. https://doi.org/10.1016/j.buildenv.2011.10.001

22. Toyinbo, O., Shaughnessy, R., Turunen, M., Putus, T., Metsamuuronen, J., Kurnitski, J., and Haverinen-Shaughnessy, U. "Building characteristics , indoor environmental quality , and mathematics achievement in Finnish elementary schools." *Building and Environment*, Vol. 104, (2016), 114-121. https://doi.org/10.1016/j.buildenv.2016.04.030

23. Doi, R. "Are New Residential Areas Cooler than Older Ones?" *Emerging Science Journal*, Vol. 6, No. 6, (2022), 1346-1357. https://doi.org/10.28991/ESJ-2022-06-06-08

24. Musa, H. H., Hussein, A. M., Hanoon, A. N., Hason, M. M., and Abdulhameed, A. A. "Phases of Urban Development Impact on the Assessment of Thermal Comfort: A Comparative Environmental Study." *Civil Engineering Journal (Iran)*, Vol. 8, No. 5, (2022), 951-966. https://doi.org/10.28991/CEJ-2022-08-05-08

25. Zomorodian, Z. S., Tahsildoost, M., and Hafezi, M. "Thermal comfort in educational buildings: A review article." *Renewable and Sustainable Energy Reviews*, Vol. 59, , (2016), 895-906. https://doi.org/https://doi.org/10.1016/j.rser.2016.01.033

26. Nam, I., Yang, J., Lee, D., Park, E., and Sohn, J.-R. "A study on the thermal comfort and clothing insulation characteristics of preschool children in Korea." *Building and Environment*, Vol. 92, (2015), 724-733. https://doi.org/https://doi.org/10.1016/j.buildenv.2015.05.041

27. Teli, D., Jentsch, M. F., and James, P. A. B. "The role of a building's thermal properties on pupils' thermal comfort in junior school classrooms as determined in field studies." *Building and Environment*, Vol. 82, (2014), 640-654. https://doi.org/https://doi.org/10.1016/j.buildenv.2014.10.005

28. Almeida, R. M. S. F., Ramos, N. M. M., and de Freitas, V. P. "Thermal comfort models and pupils' perception in free-running school buildings of a mild climate country." *Energy and Buildings*, Vol. 111, (2016), 64-75. https://doi.org/https://doi.org/10.1016/j.enbuild.2015.09.066

29. Trebilcock, M., Soto-Muñoz, J., Yañez, M., and Figueroa-San Martin, R. "The right to comfort: A field study on adaptive thermal comfort in free-running primary schools in Chile." *Building and Environment*, Vol. 114, (2017), 455-469. https://doi.org/https://doi.org/10.1016/j.buildenv.2016.12.036

30. Wang, D., Jiang, J., Liu, Y., Wang, Y., Xu, Y., and Liu, J. "Student responses to classroom thermal environments in rural primary and secondary schools in winter." *Building and Environment*, Vol. 115, (2017), 104-117.

https://doi.org/https://doi.org/10.1016/j.buildenv.2017.01.006

31. Yang, W., and Bradley, J. S. "Effects of room acoustics on the intelligibility of speech in classrooms for young children." *The Journal of the Acoustical Society of America*, Vol. 125, No. 2, (2009), 922-933. https://doi.org/10.1121/1.3058900

32. Klatte, M., Lachmann, T., and Meis, M. "Effects of noise and reverberation on speech perception and listening comprehension of children and adults in a classroom-like setting." *Noise and Health*, Vol. 12, No. 49, (2010), 270-282. https://doi.org/10.4103/1463-1741.70506

33. Hodgson, M. "Rating, ranking, and understanding acoustical quality in university classrooms." *The Journal of the Acoustical Society of America*, Vol. 112, No. 2, (2002), 568-575. https://doi.org/10.1121/1.1490363

34. Zannin, P. H. T., and Marcon, C. R. "Objective and subjective evaluation of the acoustic comfort in classrooms." *Applied Ergonomics*, Vol. 38, No. 5, (2007), 675-680. https://doi.org/10.1016/j.apergo.2006.10.001

35. Khalvati, F., and Omidvar, A. "Prediction of Noise Transmission Loss and Acoustic Comfort Assessment of a Ventilated Window using Statistical Energy Analysis." *International Journal of Engineering, Transactions C: Aspects*, Vol. 32, No. 3, (2019), 451-459. https://doi.org/10.5829/ije.2019.32.03c.14

36. Michael, A., and Heracleous, C. "Assessment of natural lighting performance and visual comfort of educational architecture in Southern Europe: The case of typical educational school premises in Cyprus." *Energy and Buildings*, Vol. 140, (2017), 443-457. https://doi.org/10.1016/j.enbuild.2016.12.087

37. Meresi, A. "Evaluating daylight performance of light shelves combined with external blinds in south-facing classrooms in Athens, Greece." *Energy and Buildings*, Vol. 116, (2016), 190-205. https://doi.org/10.1016/j.enbuild.2016.01.009

38. Korsavi, S. S., Zomorodian, Z. S., and Tahsildoost, M. "Visual comfort assessment of daylit and sunlit areas: A longitudinal field survey in classrooms in Kashan, Iran." *Energy and Buildings*, Vol. 128, (2016), 305-318. https://doi.org/10.1016/j.enbuild.2016.06.091

39. Rahman, N. A. A., Kamaruzzaman, S. N., and Akashah, F. W. "A Review of Optimization Techniques Application for Building Performance Analysis." *Civil Engineering Journal (Iran)*, Vol. 8, No. 4, (2022), 823-842. https://doi.org/10.28991/CEJ-2022-08-04-014

40. Kharazi, B. A., Alvanchi, A., and Taghaddos, H. "A Novel Building Information Modeling-based Method for Improving Cost and Energy Performance of the Building Envelope." *International Journal of Engineering, Transactions B: Applications*, Vol. 33, No. 11, (2020), 2162-2173. https://doi.org/10.5829/ije.2020.33.11b.06

41. Sutarja, I. N., Ardana, M. D. W., and Putra, I. D. G. A. D. "The post-disaster house: Simple instant house using lightweight steel structure, bracing, and local wood wall." *International Journal of Engineering, Transactions B: Applications*, Vol. 34, No. 2, (2021), 348-354. https://doi.org/10.5829/IJE.2021.34.02B.06

42. Marans, R. W., and Yan, X. "Lighting quality and environmental satisfaction in open and enclosed offices." *The Journal of Architectural and Planning Research*, (1989), 118-131. https://doi.org/www.jstor.org/stable/43028916

43. Chiang, C. M., and Lai, C. M. "A study on the comprehensive indicator of indoor environment assessment for occupants' health in Taiwan." *Building and Environment*, Vol. 37, No. 4, (2002), 387-392. https://doi.org/10.1016/S0360-1323(01)00034-8

44. Astolfi, A., and Pellerey, F. "Subjective and objective assessment of acoustical and overall environmental quality in secondary school classrooms." *The Journal of the Acoustical Society of America*, Vol. 123, No. 1, (2008), 163-173. https://doi.org/10.1121/1.2816563

45. Wong, L. T., Mui, K. W., and Hui, P. S. "A multivariate-logistic model for acceptance of indoor environmental quality (IEQ) in offices." *Building and Environment*, Vol. 43, No. 1, (2008), 1-6. https://doi.org/10.1016/j.buildenv.2007.01.001

46. Cao, B., Ouyang, Q., Zhu, Y., Huang, L., Hu, H., and Deng, G. "Development of a multivariate regression model for overall satisfaction in public buildings based on field studies in Beijing and Shanghai." *Building and Environment*, Vol. 47, No. 1, (2012), 394-399. https://doi.org/10.1016/j.buildenv.2011.06.022

47. Ncube, M., and Riffat, S. "Developing an indoor environment quality tool for assessment of mechanically ventilated office buildings in the UK - A preliminary study." *Building and Environment*, Vol. 53, (2012), 26-33. https://doi.org/10.1016/j.buildenv.2012.01.003

48. Marino, C., Nucara, A., and Pietrafesa, M. "Proposal of comfort classification indexes suitable for both single environments and whole buildings." *Building and Environment*, Vol. 57, No. December 2002, (2012), 58-67. https://doi.org/10.1016/j.buildenv.2012.04.012

49. Fassio, F., Fanchiotti, A., and de Lieto Vollaro, R. "Linear, non-linear and alternative algorithms in the correlation of IEQ factors with global comfort: A case study." *Sustainability (Switzerland)*, Vol. 6, No. 11, (2014), 8113-8127. https://doi.org/10.3390/su6118113

50. Buratti, C., Belloni, E., Merli, F., and Ricciardi, P. "A new index combining thermal, acoustic, and visual comfort of moderate environments in temperate climates." *Building and Environment*, Vol. 139, No. April, (2018), 27-37. https://doi.org/10.1016/j.buildenv.2018.04.038

Persian Abstract

چکیده

این مطالعه رابطه بین سطح توسعه یک کشور و استانداردهای آموزشی آن را بررسی می‌کند و بر اهمیت دانشگاه‌های مجهز در تضمین آموزش با کیفیت بالا تأکید می‌کند. در حالی که تحقیقات در مورد راحتی در ساختمان‌های آموزشی اغلب بر پارامترهای فردی مانند عناصر حرارتی، صوتی و بصری متمرکز شده است، این مقاله معیار جدیدی را پیشنهاد می‌کند که این عوامل را برای ارزیابی آسایش محیطی ادغام می‌کند. این تحقیق در شش اتاق خوابگاه در پردیس موسسه ملی فناوری (NITW) Warangal در هند، با استفاده از اندازه‌گیری‌های عینی و نظرسنجی‌های ذهنی انجام شد. سه معیار منفرد معرفی شد: یک شاخص گرما- رطوبت سنجی، یک شاخص راحتی صوتی، و یک شاخص روشنایی بصری، که هر کدام در محدوده ۱-۰ نرمال شده اند که نشان دهنده شرایط راحتی و ناراحتی است. یک شاخص نهایی آسایش کلی برای هر اتاق با تخصیص وزن های مناسب به سه عامل ایجاد گردید. یافته ها با پاسخ های پرسشنامه مقایسه شد و اثربخشی روش پیشنهادی ارزیابی شد. نتایج نشان‌دهنده یک ارزیابی جامع از راحتی محیط داخلی است، با عوامل صوتی که کمترین تأثیر را بر شرایط کلی آسایش نشان می‌دهند. این مطالعه وزن برابر برای پارامترهای حرارتی، صوتی و روشنایی را هنگام محاسبه شاخص راحتی ترکیبی توصیه می‌کند. این ساختمان امتیاز کلی آسایش ۰.۶٤ از ۱ را به دست آورد که نشان دهنده یک محیط راحت است. این مطالعه همچنین نشان می دهد که همبستگی قوی بین شاخص آسایش ترکیبی جدید و نتایج حاصل از پرسشنامه وجود دارد. این تحقیق یک رویکرد ساده و یکپارچه برای سنجش سطوح آسایش در ساختمان‌های آموزشی ارائه می‌کند و زمینه را برای ارزیابی‌های بیشتر عملکرد ساختمان‌های سازمانی فراهم می‌کند.

International Journal of Engineering

Journal Homepage: www.ije.ir

Design and Performance Analysis of 6H-SiC Metal-Semiconductor Field-Effect Transistor with Undoped and Recessed Area under Gate in 10nm Technology

A. Krishnamurthy[a], D. Venkatarami Reddy[b], E. Radhamma[c], B. Jyothirmayee[d], D. Sreenivasa Rao[e], V. Agarwal[e], B. Balaji*[e]

[a] Department of Electronics and Communication Engineering, Princeton Institution of Engineering and Technology for Women, Hyderabad, India
[b] Department of Electronics and Communication Engineering, Kodada Institute of Technology and Science for Women, Kodad, TS, India
[c] Department of Electronics and Communication Engineering, Teegala Krishna Reddy Engineering College, Meerpet, Hyderabad, TS, India
[d] Department of Electronics and Communication Engineering, Sana Engineering College, Kodad, TS, India
[e] Department of Electronics and Communication Engineering, Koneru Lakshmaiah Education Foundation, Green Fields, Vaddeswaram, Andhra Pradesh, India

A B S T R A C T

In this paper, the impact of the undoped and recessed gate structure on the performance of the silicon carbide metal semiconductor field effect transistor is presented. The importance of the silicon carbide metal semiconductor field effect transistor analyzed using technology computer aided design simulations in 10 nanometer technology. The proposed undoped gate structure has minimized ionized impurity scattering, leading to increased electron mobility and improved carrier concentration. Performance metrics such as drain current, transconductance, subthreshold slope, and cutoff frequency were evaluated and compared with conventional silicon carbide metal semiconductor field effect transistor structures. The proposed device exhibits superior current driving capabilities, enhanced transconductance, and reduced leakage currents, leading to improved power efficiency. Moreover, the recessed gate structure contributes to a significant reduction in short-channel effects, making the device more suitable for high frequency applications. The simulation parameters were calculated and compared with conventional structure with the length of the source and drain in 10 nanometer node. Therefore the drain current of this proposed device has been improved by 68%.

doi: 10.5829/ije.2023.36.12c.16

NOMENCLATURE

Sic	Silicon Carbide	Ion	On state current
HfO_2	Hafnium oxide	Ioff	Off state current
SiO_2	Silicon dioxide	I_d	Drain Current
Gm	Transconductance	Vgs	Gate to source voltage
G_d	Drain conductance	TCAD	Technology Computer Aided Desisn

1. INTRODUCTION

The fundamental principle of Metal-Semiconductor Field-Eeffect Transistor (MESFET) is based on the modulation of the current flow in a semiconductor channel by an externally applied electric field. This control is achieved through the formation of a ShottkyReporting research finding barrier between the metal gate electrode and the semiconductor channel, enabling the device to act as a voltage-controlled amplifier [1]. In the present semiconductor technology, Silicon Carbide (SiC) has emerged as a revolutionary material due to its unique properties that offer significant advantages over conventional silicon-based devices. Among the various SiC devices, the Silicon Carbide Metal-Semiconductor Field-Effect Transistor (6H-SiC MESFET) stands out as a promising material for High-power and High-frequency applications. 6H-SiC has a wide band gap, which allows the device to operate at elevated temperatures while maintaining stable

*Corresponding Author Email: vahividi@gmail.com (B. Balaji)

performance [2]. The high thermal conductivity of SiC further ensures efficient heat dissipation, reducing the liability of thermal breakdown at high power level and high band gap level.

In recent years symbolic advancements in silicon carbide (6H-SiC) fabrication processes have allowed for the realization of smaller feature sizes and more complex device structures [3]. As a result, 6H-SiC MESFETs have seen continuous improvement in their performance characteristics, making them even more attractive for cutting-edge electronic systems. Moreover, the absence of reverse recovery losses in SiC devices in silicon-based devices, leads to lower switching losses and improved energy efficiency. This makes 6H-SiC MESFETs highly desirable for power amplifier applications, where minimizing losses is critical to achieving high power efficiency [4, 5]. The 6H-SiC MESFET represents a semiconductor device with exceptional material properties and its unique advantages, such as high electron mobility, wide band gap, and excellent thermal conductivity, make it an attractive one for modern electronic systems demanding superior performance and energy efficiency.

Metal semiconductor field effect transistor (MESFET) has played a crucial role in various applications, ranging from low-noise amplifiers to high-frequency communication systems [6]. To enhance the performance of MESFETs, designers have been exploring innovative design approaches [7]. One such approach involves the integration of an undoped and recessed area under the gate region, which has shown promising potential for improving device characteristics. By eliminating dopants from the gate region, ionized impurity scattering is reduced, resulting in higher electron mobility and improved carrier concentration. Furthermore, the recessed gate architecture provides precise control over the gate-to-channel distance, mitigating short-channel effects and enhancing gate control over throughout the channel [8].

The MESFET operates based on the modulation of the conductivity of a semiconductor channel between the source and drain regions by the voltage applied to the gate electrode [9]. The metal gate forms a Schottky barrier, controlling the flow of charge carriers, and electrons in the case of n-channel MESFETs through the channel. The undoped feature involves intentionally leaving the gate region free of dopants, avoiding the introduction of ionized impurities that can cause scattering and reduce carrier mobility [10]. Additionally, the incorporation of a recessed gate area provides the opportunity to achieve better control over the gate-to-channel distance. This control is essential for minimizing short-channel effects, which become more pronounced as transistor dimensions are scaled down. By effectively reducing short-channel effects, the proposed design can improve the device's subthreshold characteristics and mitigate issues related to device design miniaturization.

One of the major challenges in designing SiC MESFETs is reducing the detrimental effects of dopants in the gate region. Dopants can lead to ionized impurity scattering, degrading the device's electron mobility and overall performance. To overcome this limitation, we proposed an undoped gate structure, where the gate region remains free of any doping materials, thus minimizing scattering effects and enhancing electron mobility.

The second section presented the proposed device and utilized parameters. The result and discussions of drain current characteristics are presented in the third section. The conclusion is presented in the final section.

2. STRUCTURE OF PROPOSED DEVICE

The design of a 6H-SiC metal-semiconductor field-effect transistor (MESFET) with an undoped and recessed gate structure using 10nm technology to explore the potential benefits of advanced semiconductor manufacturing processes combined with innovative gate engineering. The proposed undoped gate structure has minimized ionized impurity scattering, leading to increased electron mobility and improved carrier. The device consists of a silicon carbide substrate that acts as the foundation for the entire device, providing a robust and thermally conductive material to support the active region. Figure 1 illustrates the proposed 6H-SiC device.

Source and drain regions are heavily doped to facilitate efficient carrier injection and extraction, ensuring low contact resistance [11, 12]. The channel region lies between the source and drain regions and is responsible for carrying the majority of carriers. The gate region comprises a metal contact on the 6H-SiC surface. In this design, the gate is intentionally left undoped, free of any ionized impurities, to enhance carrier mobility [13]. A precisely engineered recessed area is created under the gate region to optimize the gate control and reduce short-channel effects. The undoped gate design to minimize ionized impurity scattering, which can significantly impact the electron mobility in traditional doped-gate MESFETs. By avoiding dopants in the gate region, the device benefits from enhanced electron
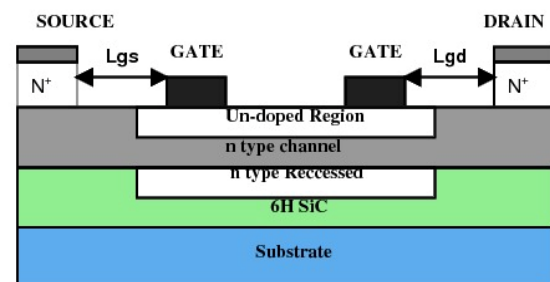
Figure 1. Proposed 6H-SiC device

mobility and improved current conduction. The recessed area under the gate allows for better control of the gate-to-channel distance. This design feature is critical for mitigating short-channel effects, such as drain-induced barrier lowering (DIBL) and subthreshold swing degradation. Precise control over the gate-to-channel distance enables improved gate control and better device performance is shown in Figure 1 compared to the conventional structure [14].

The device is designed using cutting-edge 10nm technology, which enables smaller feature sizes and advanced process techniques [15, 16]. This technology node provides enhanced gate control, reduced parasitic capacitances, and improved gate dielectric properties, enabling superior high-frequency capabilities and power efficiency.

The proposed device compared with conventional MESFET structure is shown in Figure 2.

The proposed 6H-SiC MESFET with an undoped and recessed area in 10nm node utilized the different parameters for the simulation as shown in Tables 1 and 2. Tables 3 and 4 represent the values of Ion and Ioff current, for different values of length of source and drain.
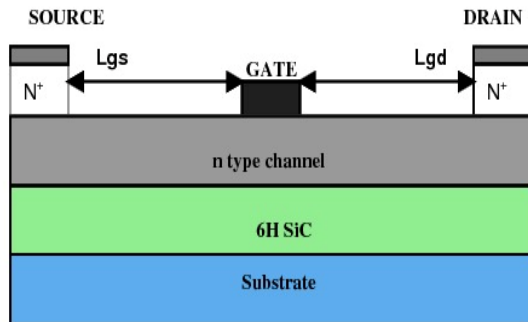
Figure 2. Conventional MESFET

TABLE 1. Used parameter for the proposed MESFET

Parameter	Proposed device
Length of device (W_L)	60 nm
Gate Length (L_G)	10 nm
Source Length (L_S)	30 nm
Drain Length (L_D)	30 nm
Channel Length (L_C)	10 nm
Doping of Source (D_S)	$1x10^{18}$ cm^{-3}
Doping of Drain (D_D)	$1x10^{19}$ cm^{-3}
Doping of Channel (D_C)	$1x10^{20}$ cm^{-3}
Work Function (W_F)	4.8eV
Thickness of SiC	2nm
Oxide thickness	3nm

TABLE 2. Ion and Ioff currents of proposed device

Architecture	I_{OFF} (A/μm)	I_{ON} (A/μm)	I_{ON} /I_{OFF}
C-MESFET	1.11E-09	4.02E-04	2.12E+04
Ls	2.02E-10	3.10E-04	3.01E+04
Ld	2.11E-10	3.12E-04	1.121E+05
Proposed device	3.17E-10	3.10E-04	4.11E+06

TABLE 3. Ion and Ioff currents of proposed device at Ls and Ld

Architecture	I_{OFF} (A/μm)	I_{ON} (A/μm)	I_{ON}/I_{OFF}
Ls	5.19E-11	4.02E-04	5.01E+06
Ld	3.11E-10	4.11E-04	3.19E+05
Proposed device	2.10E-09	5E-03	2.191E+04

TABLE 4. Ion and Ioff currents of proposed device at doping

Architecture	I_{OFF} (A/μm)	I_{ON} (A/μm)	I_{ON}/I_{OFF}
$1x10^{16}$ cm^{-3} - Source	1.10E-10	3.12E-04	1.12E+05
$1x10^{17}$ cm^{-3} - Drain	1.21E-10	3.18E-04	2.78E+05
$1x10^{18}$ cm^{-3} -Channel	3.19E-10	2.98E-04	3.80E+06

The recessed gate architecture allows for precise control over the gate-to-channel distance, effectively reducing short-channel effects [17]. This improved gate control enhances the device's overall performance and stability. The combination of the undoped gate and recessed structure contributes to higher power efficiency in the 6H-SiC MESFET [18]. The reduction in short-channel effects and improved electron mobility result in lower power dissipation, making it suitable for power-sensitive applications [19].

The incorporation of an undoped and recessed region beneath the gate introduces a novel structural modification to the traditional MESFET design. This alteration has the potential to significantly impact device performance with key limitations of conventional MESFET. The undoped and recessed gate design can substantially lower gate-source and gate-drain capacitances. This reduction in capacitance enhances the device's high-frequency operation, making it well-suited for high frequency applications with low power consumption, and high-speed signal processing. This includes fields such as wireless communication, radar systems, and high-frequency electronics. The proposed device concept paves the way for further research and development and can explore various design variations and optimize parameters to extract even more performance benefits from the undoped and recessed gate structure.

3. RESULTS AND DISCUSSIONS

3. 1. Drain Current Characteristics   The drain current vs. drain voltage characteristic of 6H-SiC represents the relationship between the drain current (Id) flowing through the device and the drain voltage (Vds) applied across the drain and source terminals [20]. Compared to conventional SiC MESFETs, the 6H-SiC MESFET with the undoped and recessed gate design is exhibited higher drain currents for a given drain voltage. The absence of dopants in the gate region reduces ionized impurity scattering, leading to enhanced electron mobility and improved carrier concentration. As a result, the device can achieve higher drain currents at different oxide thickness as shown in Figure 3. The Id-Vds curve shows a more saturation behavior for the proposed MESFET design. With the undoped and recessed gate structure, the short-channel effects are reduced, leading to improved gate control and saturation behavior. This allows the device to operate more efficiently in the saturation region, providing better linearity and stability. The undoped gate structure reducing subthreshold leakage currents. In subthreshold operation, the absence of dopants in the gate region minimizes off-state leakage, leading to improved power efficiency. The Id-Vds curve will handle higher output currents while maintaining low on-resistance [11, 21].

The recommended and typical transistors function in depletion mode, where the highest drain current occurs when the gate voltage is zero. As a result, their peak currents were compared at this point. In a new design, the gate-channel bias causes depletion at the upper region of the channel. This bias prompts carriers to move at the channel's lower region, facilitating the flow of drain current. Consequently, the lower end channel area will significantly influences drain current flow. In the new design, introducing a channel into the p-buffer layer increases the thickness of the lower silicon channel area. This augmentation boosts electron concentration and mobility in this region, thereby enhancing drain current region.
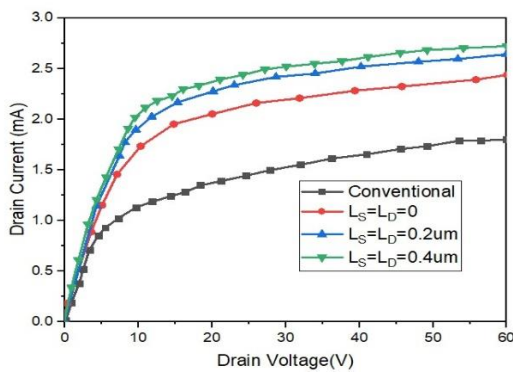
3. 2. Gate to Source Capacitance   The gate to source capacitance (Cgs) is a critical parameter that characterizes the capacitive coupling between the gate and source terminals of proposed 6H-SiC MESFET [22, 23]. It plays a significant role in determining the high-frequency performance of the device, as it directly impacts the device's switching speed and overall signal handling capabilities. By eliminating dopants in the gate region, the depletion region width is minimized, leading to lower capacitance between the gate and the channel. This reduction in gate capacitance results in improved high-frequency performance. The Cgs vs frequency curve show a more frequency response for the 6H-SiC MESFET with the undoped and recessed gate structure. The recessed gate design enables precise control over the gate-to-channel distance, mitigating short-channel effects and minimizing parasitic capacitances. As a result, the device can maintain a lower Cgs value over a broader frequency range shown in Figure 4.

The suggested configuration of the transistors alters their electrical characteristics, affecting parameters like gate-source and gate-drain capacitors. Modifications in the electric charge distribution beneath the gate on the source side cause variations in the gate-source capacitor, while changes on the drain side induce adjustments in the gate-drain capacitor. Consequently, by implementing structural alterations in these transistors, it becomes possible to decrease the charge accumulation in these regions, subsequently reducing the capacities of both gate-source and gate-drain capacitors. Introducing nondoped regions beneath the gate of the proposed transistor contributes to decreased gate capacitance, consequently enhancing the speed of the transistor and improvement in the performance.

3. 3. Gate to Drain Capacitance   The proposed undoped and recessed gate structure is resultant in reduced gate to drain capacitance compared to conventional MESFETs. The absence of dopants in the gate region leads to a narrower depletion region, reducing the capacitance between the gate and the drain. The Cgd

Figure 3. Drain current vs drain voltage Characteristics at different Ls and Ld
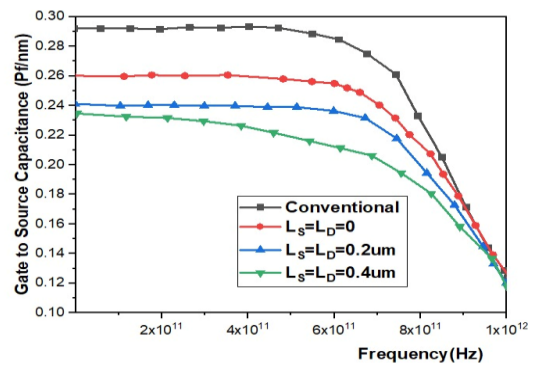
Figure 4. Gate to source capacitance vs frequency at different Ls and Ld

vs frequency shows frequency response for the 6H-SiC MESFET with the undoped and recessed gate structure. The precise control over the gate-to-channel distance achieved by the recessed gate design results in minimized parasitic capacitances, including Cgd. This characteristic allows the device to maintain a lower Cgd value across a wider frequency range. The reduction in Gate-Drain Capacitance is particularly significant in suppressing the miller effect. The miller effect is an undesirable phenomenon in amplifiers, where the Cgd couples with the output capacitance, resulting in signal feedback and potential instability. With the lower Cgd in the proposed MESFET design, the impact of the Miller effect is mitigated, contributing to better amplifier performance as shown in Figure 5.

3. 4. Lateral Electric Field   The lateral electric field (E-field) distribution along the channel length of proposed MESFET is essential to analyze the E-field behavior, particularly for short-channel devices, as it directly affects carrier mobility, hot-carrier effects, and breakdown voltage [24, 25]. The undoped gate structure shows a reduction in the lateral electric field compared to conventional MESFETs at different lengths of source and drain. The absence of dopants in the gate region minimizes the potential gradients, leading to a more uniform distribution of the lateral electric field along the channel length. This reduction in E-field is beneficial for maintaining high electron mobility and reducing the impact of hot-carrier effects [26, 27]. The recessed gate design further enhances the reduction of short-channel effects by allowing better control over the gate-to-channel distance. Short-channel effects, such as drain-induced barrier lowering (DIBL) and subthreshold slope degradation, are minimized, leading to improved device performance for short-channel lengths [28]. The reduced lateral electric field in combination with precise gate control results in better subthreshold characteristics and improved transistor behavior. The lateral electric field significantly influences the breakdown voltage of the

Figure 5. Gate to drain capacitance vs frequency at different Ls and Ld

MESFET. By reducing the lateral electric field, the proposed design can enhance the device's ability to handle high voltages without encountering premature breakdown as shown in Figure 6 [29].

The proposed structural design has the potential to cause alterations in electrical parameters, particularly in the lateral distribution of the electric field. This is attributed to the fact that the highest electric field strength is typically found at the corner of the gate in close proximity to the drain region. Modifications made to the physical structure in this specific area can result in shifts in the way the electric field is distributed. Conversely, the electric field's strength is directly linked to the impurity carrier concentrations which are the present within the channel region. Furthermore, the breakdown voltage of the device exhibits an inverse relationship with the electric field strength. Consequently, decreasing the impurity concentration beneath the gate, particularly at the drain side, serves to reduce the maximum electric field magnitude. This reduction, in turn, contributes to an increase in the device's breakdown voltage.

3. 5. Output Resistance   The output resistance (Ro) is to characterize the small-signal behavior of the proposed MESFET. It represents the change in drain-source voltage (Vds) for a given change in drain current (Id) when the device is operated in its small-signal region [30, 31]. The output resistance plays a very important role in determining the gain and linearity of the device, particularly in amplifier applications. The undoped gate structure and the recessed gate design contribute to an improvement in output resistance compared to conventional MESFETs. The absence of dopants in the gate region leads to reduced scattering effects and higher electron mobility, resulting in better output resistance [32]. The enhanced output resistance contributes to improved linearity in the 6H-SiC MESFET with undoped and recessed gate structure. In amplifier applications, higher output resistance leads to a more linear relationship between the input signal and the output signal, reducing signal distortion and improving the fidelity of the amplified signal. The output resistance has a direct impact on the device's voltage gain. A higher output resistance implies a higher voltage gain for the MESFET as shown in Figure 7.

The output resistance and output conductance share an inverse relationship. Consequently, the output resistance showcases how the drain current's changes relate to alterations in the drain to source voltage reange and gate to source voltages. The performance of the suggested transistor relies on the influence of the drain voltage on drain current. Consequently, lower output conductance values are more desirable, while higher output resistance values are advantageous. In terms of variations in drain voltage, the output resistance is assessed across different Ls (source length) and Ld (drain length) values, with a constant channel thickness of T u
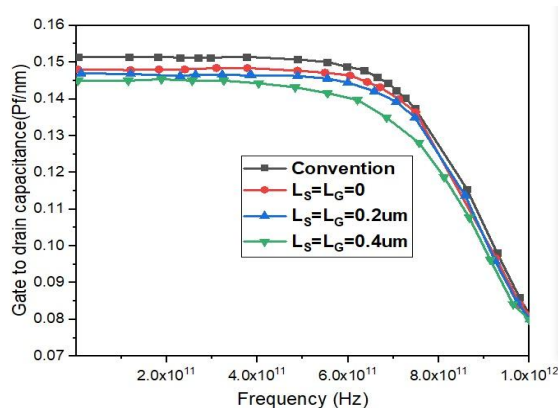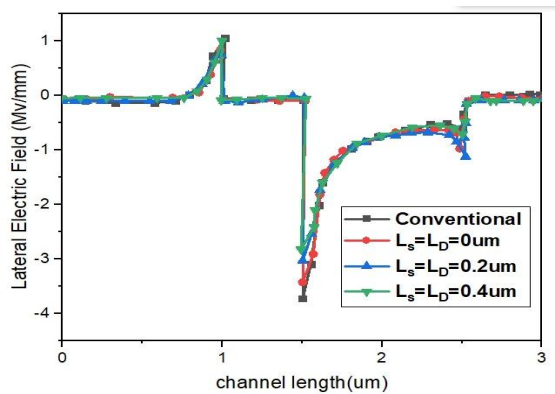
Figure 6. Lateral electric field and channel length at different values of Ls and Ld
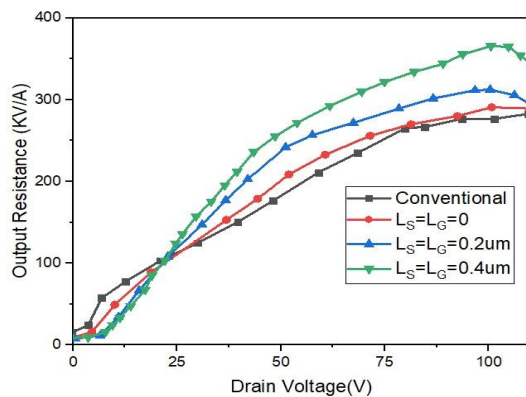
Figure 7. Output resistance vs Drain voltage at various values of Ls and Ld

= 10 nm. Notably, the proposed transistor configuration yields larger output resistance compared to the conventional structure across various combinations of Ls and Ld.

4.CONCLUSION

In this work, we have presented the drain current characteristics of 6H-SiC MESFET with UR region under the gate. The length of channel region is 10nm is considered to reduce peak electric field and improves the breakdown voltage compared to conventional device with various values of Ls and Ld. This structure is invented using silvaco tool and the simulation results of Ion and Ioff substantially increases and decreases. Due to undoped and recessed region with 10nm technology, the drain current of proposed device increases by 68%. The gate to drain capacitance and gate to source capacitance is reduced due to this new structure. The advanced structure is more efficient and suitable for high frequency and high-speed operation.

5.REFERENCES

1. Gowthami, Y., Balaji, B. and Srinivasa Rao, K., "Performance analysis and optimization of asymmetric front and back pi gates with dual material in gallium nitride high electron mobility transistor for nano electronics application", *International Journal of Engineering, Transactions A: Basics*, Vol. 36, No. 7, (2023), 1269-1277, doi: 10.5829/ije.2023.36.07a.08.

2. Radhamma, E., Vemana Chary, D., Krishnamurthy, A., Venkatarami Reddy, D., Sreenivasa Rao, D., Gowthami, Y. and Balaji, B., "Performance analysis of high-k dielectric heterojunction high electron mobility transistor for rf applications", *International Journal of Engineering, Transactions C: Aspects*, Vol. 36, No. 9, (2023), 1652-1658, doi: 10.5829/ije.2023.36.09c.09.

3. Bhat, A.M., Shafi, N., Sahu, C. and Periasamy, C., "Algan/gan hemt ph sensor simulation model and its maximum transconductance considerations for improved sensitivity", *IEEE Sensors Journal*, Vol. 21, No. 18, (2021), 19753-19761, https://doi.org/10.1109/JSEN.2021.3100475

4. Jiang, S., Cai, Y., Feng, P., Shen, S., Zhao, X., Fletcher, P., Esendag, V., Lee, K.-B. and Wang, T., "Exploring an approach toward the intrinsic limits of gan electronics", *ACS Applied Materials & Interfaces*, Vol. 12, No. 11, (2020), 12949-12954, https://doi.org/10.1021/acsami.9b19697

5. Gowthami, Y., Balaji, B. and Rao, K.S., "Design and performance evaluation of 6nm hemt with silicon sapphire substrate", *Silicon*, Vol. 14, No. 17, (2022), 11797-11804, https://doi.org/10.1007/s12633-022-01900-7

6. Kumar, P.K., Balaji, B. and Rao, K.S., "Performance analysis of sub 10 nm regime source halo symmetric and asymmetric nanowire mosfet with underlap engineering", *Silicon*, Vol. 14, No. 16, (2022), 10423-10436, https://doi.org/10.1007/s12633-022-01747-y

7. Howldar, S., Balaji, B. and Srinivasa Rao, K., "Design and qualitative analysis of hetero dielectric tunnel field effect transistor device", *International Journal of Engineering, Transactions C: Aspects*, Vol. 36, No. 6, (2023), 1129-1135, doi: 10.5829/ije.2023.36.06c.11.

8. Mokhtari, A. and Kabiri, P., "A new multi-valued logic buffer and inverter using mosfet based differential amplifier", *International Journal of Engineering, Transactions A: Basics*, Vol. 35, No. 1, (2022), 150-160, doi: 10.5829/ije.2022.35.01A.14.

9. Dixit, A. and Gupta, N., "A compact model of gate capacitance in ballistic gate-all-around carbon nanotube field effect transistors", *International Journal of Engineering, Transactions A: Basics*, Vol. 34, No. 7, (2021), 1718-1724, doi: 10.5829/IJE.2021.34.07A.16.

10. Goel, A., Rewari, S., Verma, S., Deswal, S. and Gupta, R., "Dielectric modulated junctionless biotube fet (dm-jl-bt-fet) bio-sensor", *IEEE Sensors Journal*, Vol. 21, No. 15, (2021), 16731-16743, https://doi.org/10.1109/JSEN.2021.3077540

11. Janakiraman, V., Baskaran, S. and Kumutha, D., "Silicon nitride back barrier in algan/gan hemt to enhance breakdown voltage for satellite applications", *Silicon*, Vol. 13, No. 10, (2021), 3531-3536, https://doi.org/10.1007/s12633-020-00817-3

12. Chugh, N., Kumar, M., Bhattacharya, M. and Gupta, R., "Extraction of admittance parameters of symmetrically doped algan/gan/algan dh-hemt for microwave frequency applications", *Microsystem Technologies*, Vol. 27, (2021), 4065-4072, https://doi.org/10.1007/s00542-020-04805-w

13. Nishitani, T., Yamaguchi, R., Asubar, J., Tokuda, H. and Kuzuhara, M., "Improved on-state breakdown characteristics in algan/gan mos-hemts with a gate field plate", in 2019 Compound Semiconductor Week (CSW), IEEE. (2019), 1-2. https://doi.org/10.1109/ICIPRM.2019.8819284

14. Mehrabani, A.H., Fattah, A. and Rahimi, E., "Design and simulation of a novel hetero-junction bipolar transistor with gate-controlled current gain", *International Journal of Engineering, Transactions C: Aspects*, Vol. 36, No. 03, (2023), 433, doi: 10.5829/ije.2023.36.03c.01.

15. Rafiee, A., Nickabadi, S., Nobarian, M., Tagimalek, H. and Khatami, H., "Experimental investigation joining al 5083 and high-density polyethylen by protrusion friction stir spot welding containing nanoparticles using taguchi method", *International Journal of Engineering, Transactions C: Aspects,*, Vol. 35, No. 6, (2022), 1144-1153, doi: 10.5829/ije.2022.35.06c.06.

16. Wei, J., Zhang, M., Li, B., Tang, X. and Chen, K.J., "An analytical investigation on the charge distribution and gate control in the normally-off gan double-channel mos-hemt", *IEEE Transactions on Electron Devices*, Vol. 65, No. 7, (2018), 2757-2764, https://doi.org/10.1109/TED.2018.2831246

17. Kumar, S. and Sahoo, G., "A random forest classifier based on genetic algorithm for cardiovascular diseases diagnosis (research note)", *International Journal of Engineering, Transactions B: Applications,*, Vol. 30, No. 11, (2017), 1723-1729, doi: 10.5829/ije.2017.30.11b.13.

18. Balaji, B., Srinivasa Rao, K., Girija Sravani, K., Bindu Madhav, N., Chandrahas, K. and Jaswanth, B., "Improved drain current characteristics of HFO₂/SiO₂ dual material dual gate extension on drain side-tfet", *Silicon*, Vol. 14, No. 18, (2022), 12567-12572, https://doi.org/10.1007/s12633-022-01955-6

19. Kumar, P.K., Balaji, B. and Rao, K.S., "Halo-doped hetero dielectric nanowire mosfet scaled to the sub-10 nm node", *Transactions on Electrical and Electronic Materials*, Vol., No., (2023), 1-11, https://doi.org/10.1007/s42341-023-00448-6

20. Emami, N. and Kuchaki Rafsanjani, M., "Extreme learning machine based pattern classifiers for symbolic interval data", *International Journal of Engineering, Transactions B: Applications,*, Vol. 34, No. 11, (2021), 2545-2556, doi: 10.5829/IJE.2021.34.11B.17

21. Balaji, B., Rao, K.S., Aditya, M. and Sravani, K.G., "Device design, simulation and qualitative analysis of gaasp/6h-sic/gan metal semiconductor field effect transistor", *Silicon*, Vol. 14, No. 14, (2022), 8449-8454, https://doi.org/10.1007/s12633-022-01665-z

22. Gassoumi, M., Helali, A., Gassoumi, M., Gaquiere, C. and Maaref, H., "High frequency analysis and small-signal modeling of algan/gan hemts with SiO₂/sin passivation", *Silicon*, Vol. 11, (2019), 557-562, https://doi.org/10.1007/s12633-018-9767-6

23. Huang, S., Wang, X., Liu, X., Wang, Y., Fan, J., Yang, S., Yin, H., Wei, K., Wang, W. and Gao, H., "Monolithic integration of e/d-mode gan mis-hemts on ultrathin-barrier algan/gan heterostructure on si substrates", *Applied Physics Express*, Vol. 12, No. 2, (2019), 024001, https://doi.org/10.7567/1882-0786/aafa0e

24. Kargarrazi, S., Yalamarthy, A.S., Satterthwaite, P.F., Blankenberg, S.W., Chapin, C. and Senesky, D.G., "Stable operation of algan/gan hemts for 25 h at 400° c in air", *IEEE Journal of the Electron Devices Society*, Vol. 7, (2019), 931-935, https://doi.org/10.1109/JEDS.2019.2937008

25. Huang, S., Wang, X., Liu, X., Zhao, R., Shi, W., Zhang, Y., Fan, J., Yin, H., Wei, K. and Zheng, Y., "Capture and emission mechanisms of defect states at interface between nitride semiconductor and gate oxides in gan-based metal-oxide-semiconductor power transistors", *Journal of Applied Physics*, Vol. 126, No. 16, (2019), https://doi.org/10.1063/1.5125825

26. Hamza, K.H. and Nirmal, D., "A review of gan hemt broadband power amplifiers", *AEU-International Journal of Electronics and Communications*, Vol. 116, (2020), 153040, https://doi.org/10.1016/j.aeue.2019.153040

27. Wu, Y., Zhang, J., Zhao, S., Zhang, W., Zhang, Y., Duan, X., Chen, J. and Hao, Y., "More than 3000 v reverse blocking schottky-drain algan-channel hemts with> 230 mw/cm 2 power figure-of-merit", *IEEE Electron Device Letters*, Vol. 40, No. 11, (2019), 1724-1727, https://doi.org/10.1109/LED.2019.2941530

28. Fouladinia, F. and Gholami, M., "Decimal to excess-3 and excess-3 to decimal code converters in qca nanotechnology", *International Journal of Engineering, Transactions C: Aspects,*, Vol. 36, No. 9, (2023), 1618-1625, doi: 10.5829/ije.2023.36.09c.05.

29. Sravani, S.S., Balaji, B., Rao, K.S., Babu, A.N., Aditya, M. and Sravani, K.G., "A qualitative review on tunnel field effect transistor-operation, advances, and applications", *Silicon*, Vol. 14, No. 15, (2022), 9263-9273, https://doi.org/10.1007/s12633-022-01660-4

30. Gowthami, Y., Balaji, B. and Rao, K.S., "Design and analysis of a symmetrical low-κ source-side spacer multi-gate nanowire device", *Journal of Electronic Materials*, Vol. 52, No. 4, (2023), 2561-2568, https://doi.org/10.1007/s11664-023-10217-z

31. Ranjan, R., Kashyap, N. and Raman, A., "Novel vertical gaa-algan/gan dopingless mis-hemt: Proposal and investigation", *Transactions on Electrical and Electronic Materials*, Vol. 22, (2021), 473-480, https://doi.org/10.1007/s42341-020-00252-6

32. Raman, A., Chattopadhyay, S.P., Ranjan, R., Kumar, N., Kakkar, D. and Sharma, R., "Design and investigation of dual dielectric recessed-gate algan/gan hemt as gas sensor application", *Transactions on Electrical and Electronic Materials*, Vol. 23, No. 6, (2022), 618-623, https://doi.org/10.1007/s42341-022-00391-y
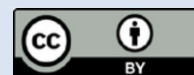
Persian Abstract

چکیده

در این مقاله تاثیر ساختار دروازه بدون دود و فرورفته بر عملکرد ترانزیستور اثر میدان نیمه هادی فلزی کاربید سیلیکون ارائه شده است. اهمیت ترانزیستور اثر میدان نیمه هادی فلزی کاربید سیلیکون با استفاده از شبیه‌سازی‌های طراحی به کمک کامپیوتر در فناوری ۱۰ نانومتری تحلیل شد. ساختار دروازه بدون لایه پیشنهادی پراکندگی ناخالصی یونیزه شده را به حداقل رسانده است که منجر به افزایش تحرک الکترون و بهبود غلظت حامل می شود. معیارهای عملکرد مانند جریان تخلیه، رسانایی، شیب زیرآستانه، و فرکانس برش با ساختارهای ترانزیستوری اثر میدان نیمه هادی فلزی کاربید سیلیکون معمولی ارزیابی و مقایسه شدند. دستگاه پیشنهادی قابلیت‌های هدایت جریان برتر، رسانایی افزایش یافته و جریان‌های نشتی را کاهش می‌دهد که منجر به بهبود راندمان انرژی می‌شود. علاوه بر این، ساختار دروازه فرورفته به کاهش قابل توجه اثرات کانال کوتاه کمک می کند و دستگاه را برای کاربردهای فرکانس بالا مناسب تر می کند. پارامترهای شبیه سازی با ساختار معمولی با طول منبع و زهکش در گره ۱۰ نانومتری محاسبه و مقایسه شد. بنابراین جریان تخلیه این دستگاه پیشنهادی ۶۸ درصد بهبود یافته است.

International Journal of Engineering

Experimental Study to Evaluate Antisymmetric Reinforced Concrete Deep Beams with Openings under Concentrated Loading Using Strut and Tie Model

A. S. J. Al-Zuheriy*

Civil Engineering Department, University of Technology – Iraq, Baghdad, Iraq

A B S T R A C T

The Strut-and-Tie modeling (STM) technique represents an applicable and valuable method for structural engineers to design disturbed regions (D-regions) of reinforced concrete structures where the assumption of plane sections remaining plane after loading is inapplicable. The most important aspect to guarantee the suitable structural and economic performance of the design is finding a suitable truss-analogy model, leading to the use of a more efficient model in structural buildings. The evaluation of the antisymmetric Strut-and-Tie models (STM) with openings under different concentrated external loads has not been comprehensively investigated in the literature. So, to address this gap, the goal of this paper is to achieve the most efficient reinforcement layout design in antisymmetric reinforced concrete deep beams with openings under concentrated loading using the strut and tie model. The experimental work was conducted and included (3) antisymmetric reinforced concrete deep beams with openings that were tested under different concentrated loadings (25, 35, and 16 kips for Specimens 1, 2, and 3, respectively) using the strut and tie model. The ANSYS FEM software is used for the initial strut and tie analysis, and the RISA-3D structural analysis program is used to find the internal forces for all members under concentrated external loads in each specimen. The findings of this paper show that Specimen 1 had the highest efficiency of 1.67, while Specimen 3 had the lowest efficiency of 1.31. It can be concluded that the efficient reinforcement layout of the strut and tie model leads to the highest efficiency of the model, regardless of the value of the externally applied load.

doi: 10.5829/ije.2023.36.12c.17

Graphical Abstract

Group	Reinforcement (lb)	Ultimate Load (kips)	Design Load (kips)	Deflection at Ultimate (in)	Efficiency (kips/lb)
1	13.17	22	25	0.14	1.67
2	19.767	29.297	35	0.22	1.48
3	13.51	17.75	16	0.34	1.31

Load/weight ratio efficiencies for each specimen
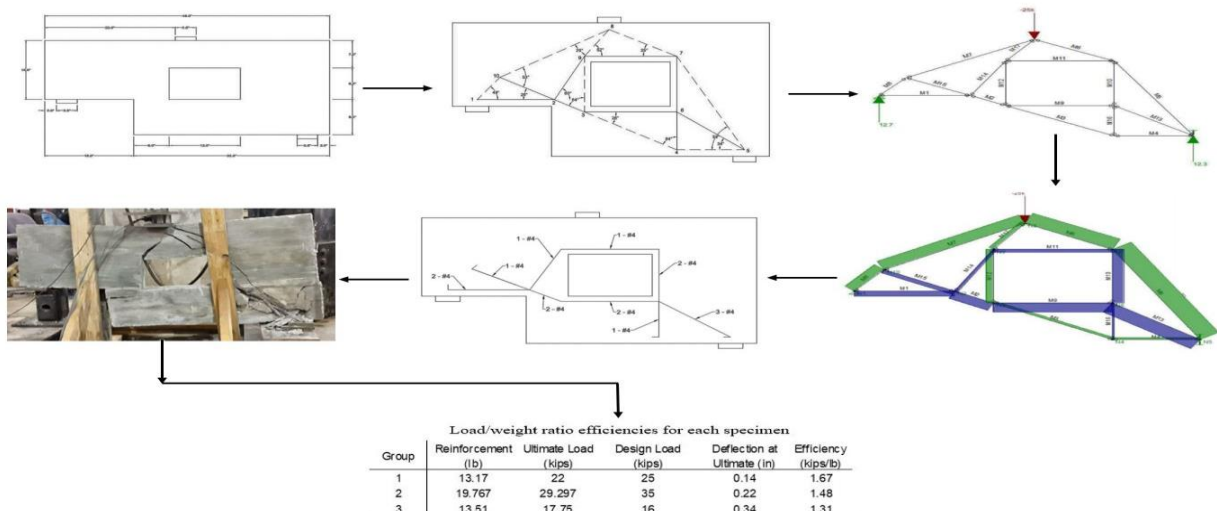
*Corresponding Author Email: ahmed.sh.jeber@uotechnology.edu.iq (A. S. J. Al-Zuheriy)

1. INTRODUCTION

Overall, in the world, reinforced concrete structures have been utilized in a wide range of ways. The safe and economical design of reinforced concrete structures is always an important challenge for civil engineers, especially since their point of view is oriented toward developing a sustainable world. In general, reinforced concrete structures are divided into two main groups based on their behavior under loading: the Bernoulli group (B-group), which has linear strain distributions, for example, all the standard and commonly structural concrete members, and the Disturbed group (D-group), which has nonlinear strain distributions, for instance, the nonstandard or unconventional structural concrete members (Strut-and-Tie models) (STM). The main reasons for the nonlinear strain distribution are the low slenderness and geometrical discontinuities. To select accurate, effective, and reasonable methods for design, the nonlinearity and discontinuity of the D-group members represent big challenges for civil engineers. For over two decades and among many methods, the strut-and-tie modeling (STM) method has been utilized in a wide range to design the D-group of reinforced concrete members [1]. Building code requirements for standard and commonly used structural concrete members have been part of the design codes for quite some time. However, the design codes previously had little guidance on designing nonstandard or unconventional members. To account for these nonstandard members, design codes have included guidelines for the design of such members by incorporating a strut and tie model design approach. Over the years, tests and research have been performed on the strut and tie model designs to be recommended and implemented into the various design codes [1-6].

At the end of the nineteenth century and the beginning of the twentieth century, Ritter [7] and Mörsch [8] proposed the STM method, which is a truss-like method leading to simplifying the complex force transfer mechanism. Schlaich et al. [9] presented a comprehensive work on the strut-and-tie modeling techniques, leading to an extensive investigation of using this method. Further research to generalize this method as a consistent design method was done by Schlaich and Schäfer [10]. After that, a lot of researchers studied and reported many different types of techniques and algorithms related to the strut-and-tie modeling (STM) technique. An evolutionary structural optimization method was demonstrated by Xie and Steven [11]. This method worked on creating strut-and-tie models by optimization of the topology. As well as based on Xie and Steven [11], Yang et al. [12] developed a bidirectional evolutionary optimization method. Then, Liang et al. [13, 14] proposed a performance-based optimization method for strut-and-tie modeling. In the first decade of the twenty-first century, many researchers [15-20]

introduced the important developments of the strut-and-tie modeling technique and experienced different types of algorithms to develop this method.

In the second decade of the twenty-first century, the strut-and-tie modeling (STM) technique was developed, and new procedures were performed for strut-and-tie modeling through the established full homogenization optimization method [21], the smooth evolutionary structural optimization method [22], and the hybrid technique combining different methods [23-25]. El-Metwally and Chen [26] proposed a method that requires an equilibrium of the axial force while neglecting the compatibility of strain. In the STM method, the cracking of concrete and compatibility conditions were implemented to predict the ultimate behavior of concrete structures [27]. Many researchers conducted experimental work on various STM designs to validate their effectiveness and safety [28]. The effect of loading during an earthquake has been investigated in the literature [29, 30]. In respect of each load combination, a basis is created based on their previously proposed generation methods, the optimization-based Strut-and-Tie models (OPT-STMs), which resulted in economical and safe designs compared to traditional models [31-33]. A seismic vulnerability index methodology was improved to be used uniformly in reinforced concrete structures overall the world according to the earthquake design principles [34, 35]. The reinforced high-strength concrete beams' structural behavior was numerically investigated by Jabbar et al. [36]. The article introduced an experimental study to estimate an equation for accounting for deflection in reinforced concrete beams by utilizing the shear steel plates as a stirrup [37]. By employing a suitable strut-and-tie model, the results of experimental work on deep beam concrete samples consisting of recycled aggregates were introduced by Chaudhari and Suryawanshi [38].

Over the years, tests and research have been performed on the different strut-and-tie model designs. As a result of the literature review, this study is considered unique from previous research because no other study has attempted to investigate and evaluate the antisymmetric reinforced concrete deep beams with openings under concentrated loading using the strut and tie model. The goal of the paper is to achieve the most efficient reinforcement layout design (this was evaluated by the load capacity to the total steel weight ratio) among the three strut-and-tie models (STM) that are used in the antisymmetric reinforced concrete deep beams. To achieve this goal, the experimental work was conducted and included (3) antisymmetrically reinforced concrete deep beams with openings that were tested under different concentrated loading using the strut and tie model. The 3 unconventional concrete members (antisymmetric reinforced concrete deep beams with openings) were poured and tested under different

concentrated external loads equal to 25, 35, and 16 kips for Specimens 1, 2, and 3, respectively.

2. EXPERIMENTAL WORK

The experimental work included (3) antisymmetric reinforced concrete deep beams with openings that were tested under different concentrated loads using the Strut and Tie Model with 4,500 psi as the nominal compressive strength. All the samples had a width of 48 inches and a height of 24 inches. The beam's effective depth is 3.5 inches. The 3 unconventional concrete members (antisymmetric reinforced concrete deep beams with openings) were poured and tested under different concentrated external loads equal to 25, 35, and 16 kips for Specimens 1, 2, and 3, respectively. The following describes the experimental work performed for this paper.

2. 1. Initial Guidelines   The geometry of the unconventional concrete member is shown in Figure 1. The work involved designing the steel reinforcement without load or phi factors. It was originally assumed that the concrete strength was 4,500 psi for the design and analysis of the strut and tie model. Figures 2 and 3 are images of the stress profile created using the ANSYS FEM software. Figure 2 is a contour of the stresses in the concrete member with a certain load. Figure 3 shows arrows oriented in the direction of the stresses distributed along the member. These FEM results were used for the initial strut and tie analysis.

2. 2. STM Analysis   After the ANSYS analysis was performed, several strut and tie models were designed and analyzed by considering tension and compression zones. The bottom left corner of the central opening was the critical tension part; therefore, constraints in this zone were addressed by adding tie bars. Figure 4 is the final strut and tie model design that was used for the final reinforcement layout. The design in Figure 4 shows the location of all struts and ties with the corresponding

Figure 2. The contour of the stresses in the concrete member using ANSYS
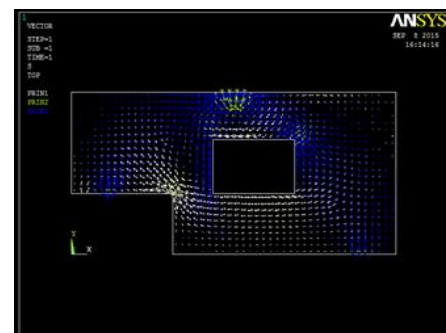
Figure 3. Arrows demonstrating the stress orientation of the concrete obtained with ANSYS
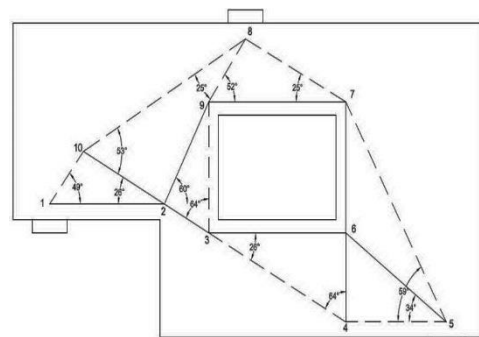
Figure 4. Strut and tie design

angles for each. All strut and tie angles are within the allowable limits of 25° and 65°. A cover of 1.2 inches was given along the supports and 1 inch of cover was given around the central opening of the concrete member. The lengths of the strut and ties can be seen in Table 1.

After the strut and tie model was designed using ANSYS, the model was analyzed using the RISA-3D structural analysis program to find the internal forces for all members under a concentrated external load equal to 25 kips. Figure 5 shows the members and nodes. Figure 6 shows the reaction forces at each support. Figure 7 shows the compression (struts) members, which are depicted in green, and the tension members (ties), depicted in blue.

Figure 1. The geometry of the unconventional reinforced concrete member

TABLE 1. Member length of struts and ties between nodes

Member	Node	Length (in)
M1	1-2	11.72
M2	2-3	5.04
M3	3-4	15.56
M4	4-5	10.25
M5	5-7	19.68
M6	7-8	11.32
M7	8-10	18.64
M8	1-10	5.30
M9	3-6	14.00
M10	6-7	10.00
M11	7-9	14.00
M12	3-9	10.00
M13	5-6	12.30
M14	2-9	9.02
M15	2-10	9.19
M16	4-6	6.80
M17	8-9	6.09

*Light gray member denotes tension tie
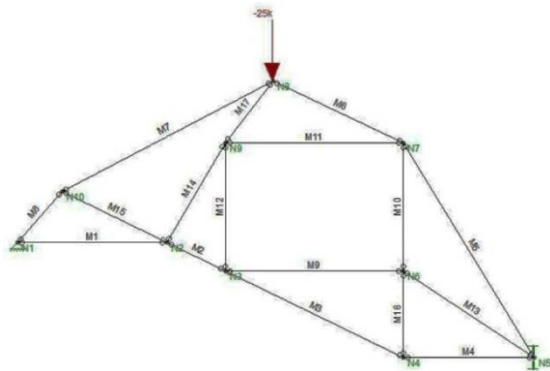
Figure 5. Strut and tie design imputed into RISA with a design load of 25 kips for force analysis
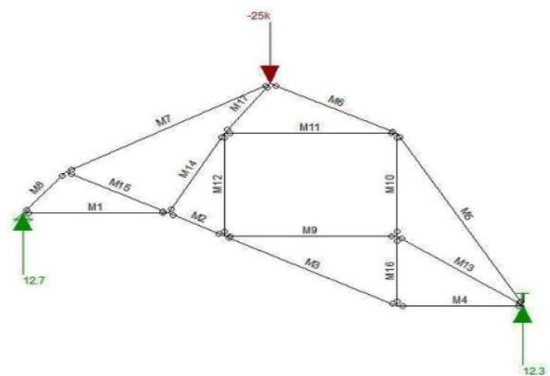
Figure 6. Support reactions were obtained from RISA using a 25-kip load for the strut and tie model
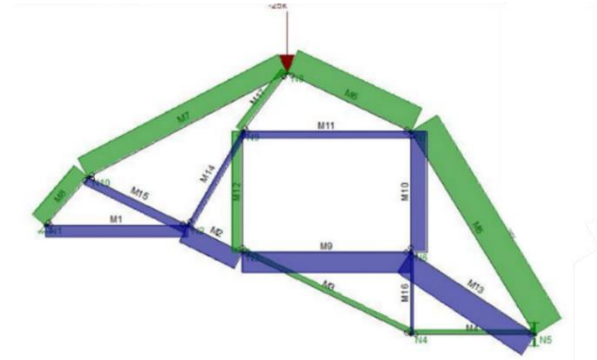
Figure 7. Member forces for the strut and tie design with 25 kips. Compression members are depicted in green, while tension members are in blue

2. 3. STM Rebar Design   Once the strut and tie model was created, it was focused on maximizing the efficiency of the steel rebar layout for the specimen. Axial forces for the members of the strut and tie model were found from a 25 kip loading through the RISA model. These values were used as a baseline to interpolate axial forces from 10 to 30 kip as stated in Table 2. Using these calculations, the amount of required steel was calculated using Equation (1).

$$A_{s,req.} = \frac{T}{fy} \tag{1}$$

The required area of steel was used to find the number of required steel rebars. The calculation was considered for No. 2, 3, and 4 bars. The volume of steel for each bar was calculated using the lengths between nodes and the cross-sectional area of the different rebar sizes. The most efficient loading for each bar was calculated as a tensile force/volume value, as stated in Table 3. The highest value was found to be an efficiency of 0.94 kips/volume for the 25-kip loading. To ensure the width of the struts and ties throughout the model would not exceed the dimensions of the specimen, a strut and tie width analysis was performed. To determine the width of the struts/ties, the strength of each node, f_{cn}, and the strength of each strut, f_{cs}, were found. The following equations were used to determine the strength of the nodes and struts:

$$f_{cn} = 0.85 * \beta_n * f'c \tag{2}$$

$$f_{cs} = 0.85 * \beta_s * f'c \tag{3}$$

The β_n and β_s factors are based on the axial forces applied at each node. The fewer tensile forces acting on a node, the stronger that node will be. There are no defined values for the β_n or β_s factors for a T-T-T (Tension-Tension-Tension) node, therefore, it was assumed to be a C-T-T (Compression-Tension-Tension) node. Table 4 presents the strength of each strut and node. Once the strengths of the nodes and struts were determined for each node the two values were compared. The lower value of f_{cn} and f_{cs} for each node was used as

TABLE 2. Axial forces in struts and ties under design loads

Load (kips)	10	11	12	13	14	15	16	17	18	19	20	21	22	23	24	25	26	27	28	29	30
Members											Axial Force (kips)										
M1	-4.36	-4.79	-5.23	-5.66	-6.1	-6.53	-6.97	-7.41	-7.84	-8.28	-8.71	-9.15	-9.58	-10.02	-10.45	-10.8	-11.33	-11.76	-12.2	-12.63	-13.07
M2	-6.88	-7.56	-8.25	-8.94	-9.63	-10.31	-11	-11.69	-12.38	-13.06	-13.75	-14.44	-15.13	-15.81	-16.5	-17.19	-17.88	-18.57	-19.25	-19.94	-20.63
M3	1.84	2.02	2.2	2.39	2.57	2.75	2.94	3.12	3.3	3.49	3.67	3.86	4.04	4.22	4.41	4.59	4.77	4.96	5.14	5.32	5.51
M4	1.66	1.82	1.99	2.15	2.32	2.48	2.65	2.82	2.98	3.15	3.31	3.48	3.64	3.81	3.97	4.14	4.31	4.47	4.64	4.8	4.97
M5	11.88	13.06	14.25	15.44	16.63	17.81	19	20.19	21.38	22.56	23.75	24.94	26.13	27.31	28.5	29.69	30.88	32.07	33.25	34.44	35.63
M6	9.75	10.73	11.7	12.68	13.65	14.63	15.6	16.58	17.55	18.53	19.5	20.48	21.45	2.43	23.4	24.38	25.36	26.33	27.31	28.28	26
M7	8.05	8.85	9.66	10.46	11.27	12.07	12.88	13.68	14.49	15.29	16.1	16.9	17.71	18.51	19.32	20.12	20.92	21.73	22.53	23.34	24.14
M8	6.68	7.35	8.02	8.68	9.35	10.02	10.69	11.36	12.02	12.69	13.36	14.03	14.7	15.36	16.03	16.7	17.37	18.04	18.7	19.37	20.04
M9	-7.84	-8.62	-9.4	-10.19	-10.97	-11.75	-12.54	-13.32	-14.1	-14.89	-15.67	-16.46	-17.24	-18.02	-18.18	-19.59	-20.37	-21.16	-21.94	-22.72	-23.51
M10	-6	-6.6	-7.2	-7.81	-8.41	-9.01	-9.61	-10.21	-10.81	-11.41	-12.01	-12.61	-13.21	-13.81	-14.41	-15.01	-15.61	-16.21	-16.81	-17.41	-18.01
M11	-2.64	-2.91	-3.17	-3.44	-3.7	-3.97	-4.23	-4.49	-4.76	-5.02	-5.29	-5.55	-5.82	-6.08	-6.35	-6.61	-6.87	-7.14	-7.4	-7.67	-7.93
M12	3.8	4.18	4.56	4.95	5.33	5.71	6.09	6.47	6.85	7.23	7.61	7.99	8.37	8.75	9.13	9.51	9.89	10.27	10.65	11.03	11.41
M13	-9.41	-10.35	-11.29	-12.23	-13.17	-14.11	-15.05	-15.99	-16.93	-17.88	-18.82	-19.76	-20.7	-21.64	-22.58	-23.52	-24.46	-25.4	-26.34	-27.28	-28.22
M14	-1.9	-2.09	-2.28	-2.48	-2.67	-2.86	-3.05	-3.24	-3.43	-3.62	-3.81	-4	-4.19	-4.38	-4.57	-4.76	-4.95	-5.14	-5.33	-5.52	-5.71
M15	-3.1	-3.41	-3.72	-4.03	-4.34	-4.65	-4.96	-5.27	-5.58	-5.89	-6.2	-6.51	-6.82	-7.13	-7.44	-7.75	-8.06	-8.37	-8.68	-8.99	-9.3
M16	-0.8	-0.88	-0.96	-1.05	-1.13	-1.21	-1.29	-1.37	-1.45	-1.53	-1.61	-1.69	-1.77	-1.85	-1.93	-2.01	-2.09	-2.17	-2.25	-2.33	-2.41
M17	2.74	3.01	3.29	3.56	3.84	4.11	4.38	4.66	4.93	5.21	5.48	5.75	6.03	6.3	6.58	6.85	7.12	7.4	7.67	7.95	8.22

*Light gray member denotes tension tie

TABLE 3. Load/Volume efficiency calculations for tension ties under design loads

Load (kips)	10	11	12	13	14	15	16	17	18	19	20	21	22	23	24	25	26	27	28	29	30
Member											Volume #2 bars (in³)										
M1	1.149	1.723	1.723	1.723	1.723	1.723	2.297	2.297	2.297	2.297	2.297	2.872	2.872	2.872	2.872	2.872	3.446	3.446	3.446	3.446	3.446
M2	0.987	0.987	0.987	1.234	1.234	1.234	1.234	1.480	1.480	1.480	1.727	1.727	1.727	1.974	1.974	1.974	2.220	2.220	2.220	2.467	2.467
M9	2.744	2.744	3.430	3.430	3.430	4.116	4.116	4.802	4.802	4.802	5.488	5.488	5.488	6.174	6.174	6.174	6.860	6.860	6.860	7.546	7.546

Member	10	11	12	13	14	15	16	17	18	19	20	21	22	23	24	25	26	27	28	29	30
M 10	1.470	1.470	1.960	1.960	1.960	2.450	2.450	2.450	2.450	2.940	2.940	2.940	2.940	3.430	3.430	3.430	3.920	3.920	3.920	3.920	4.410
M11	1.372	1.372	1.372	1.372	1.372	1.372	1.372	2.058	2.058	2.058	2.058	2.058	2.058	2.058	2.058	2.058	2.744	2.744	2.744	2.744	2.744
M 13	3.014	3.014	3.616	3.616	3.616	4.219	4.219	4.822	4.822	5.425	5.425	5.425	6.027	6.027	6.630	6.630	7.233	7.233	7.233	7.835	7.835
M 14	0.442	0.442	0.884	0.884	0.884	0.884	0.884	0.884	0.884	0.884	0.884	0.884	0.884	0.884	1.326	1.326	1.326	1.326	1.326	1.326	1.326
M 15	0.901	0.901	0.901	0.901	0.901	1.351	0.351	1.351	1.351	0.351	1.351	0.351	1.801	0.801	1.801	1.801	1.801	1.801	1.801	2.251	2.251
M 16	0.333	0.333	0.333	0.333	0.333	0.333	0.333	0.333	0.333	0.333	0.333	0.333	0.333	0.333	0.333	0.333	0.333	0.333	0.666	0.666	0.666
Total Volume	12.411	12.985	15.206	15.452	15.452	17.681	18.256	20.477	20.477	21.570	22.503	23.077	24.130	25.553	26.597	26.597	29.883	29.883	30.216	32.202	32.692
Load/Volume	0.806	0.847	0.789	0.841	0.906	0.848	0.876	0.830	0.879	0.881	0.889	0.910	0.912	0.900	0.902	0.940	0.870	0.904	0.927	0.901	0.918
Load (kips)	10	11	12	13	14	15	16	17	18	19	20	21	22	23	24	25	26	27	28	29	30

Member	Volume #3 bars (in³)																				
M1	1.289	1.289	2.579	2.579	2.579	2.579	2.579	2.579	2.579	2.579	2.579	2.579	2.579	3.868	3.868	3.868	3.868	3.868	3.868	3.868	3.868
M2	1.108	1.108	1.108	1.108	1.108	1.662	1.662	1.662	0.662	1.662	1.662	1.662	2.215	2.215	2.215	2.215	2.215	2.215	2.215	2.769	2.769
M9	3.080	3.080	3.080	4.620	4.620	4.620	4.620	4.620	4.620	6.160	6.160	6.160	6.160	6.160	6.160	6.160	7.700	7.700	7.700	7.700	7.700
M 10	2.200	2.200	2.200	2.200	2.200	2.200	2.200	3.300	3.300	3.300	3.300	3.300	3.300	3.300	4.400	4.400	4.400	4.400	4.400	4.400	4.400
M11	1.540	1.540	1.540	1.540	1.540	1.540	1.540	1.540	1.540	3.080	3.080	3.080	3.080	3.080	3.080	3.080	3.080	3.080	3.080	3.080	3.080
M 13	2.706	4.059	4.059	4.059	4.059	4.059	5.412	5.412	5.412	5.412	5.412	5.412	6.765	6.765	6.765	6.765	6.765	8.118	8.118	8.118	8.118
M 14	0.992	0.992	0.992	0.992	0.992	0.992	0.992	0.992	0.992	0.992	0.992	0.992	0.992	0.992	0.992	0.992	1.984	1.984	1.984	1.984	1.984
M 15	1.011	1.011	1.011	1.011	1.011	1.011	2.022	2.022	2.022	2.022	2.022	2.022	2.022	2.022	2.022	2.022	2.022	2.022	2.022	2.022	2.022
M 16	0.748	0.748	0.748	0.748	0.748	0.748	0.748	0.748	0.748	0.748	0.748	0.748	0.748	0.748	0.748	0.748	0.748	0.748	0.748	0.748	0.748
Total Volume	14.674	16.027	17.316	18.856	18.856	19.410	21.774	22.874	22.874	25.954	25.954	25.954	27.861	29.150	29.150	30.250	32.782	34.135	34.135	34.689	34.689
Load/Volume	0.681	0.686	0.693	0.689	0.742	0.773	0.735	0.743	0.787	0.732	0.771	0.809	0.790	0.789	0.823	0.826	0.793	0.791	0.820	0.836	0.865
Load (kips)	10	11	12	13	14	15	16	17	18	19	20	21	22	23	24	25	26	27	28	29	30

Member	Volume #4 bars (in³)																				

M1	2.344	2.344	2.344	2.344	2.344	2.344	2.344	2.344	2.344	2.344	2.344	4.688	4.688	4.688	4.688	4.688	4.688	4.688	4.688	4.688	4.688
M2	1.007	1.007	1.007	0.007	2.014	2.014	2.014	2.014	2.014	2.014	2.014	2.014	2.014	2.014	2.014	2.014	2.014	3.021	3.021	3.021	3.021
M9	2.800	2.800	5.600	5.600	5.600	5.600	5.600	5.600	5.600	5.600	5.600	5.600	5.600	8.400	8.400	8.400	8.400	8.400	8.400	8.400	8.400
M 10	2.000	2.000	2.000	2.000	2.000	4.000	4.000	4.000	4.000	4.000	4.000	4.000	4.000	4.000	4.000	4.000	4.000	4.000	4.000	4.000	6.000
M11	2.800	2.800	2.800	2.800	2.800	2.800	2.800	2.800	2.800	2.800	2.800	2.800	2.800	2.800	2.800	2.800	2.800	2.800	2.800	2.800	2.800
M 13	4.920	4.920	4.920	4.920	4.920	4.920	4.920	4.920	4.920	4.920	7.380	7.380	7.380	7.380	7.380	7.380	7.380	7.380	7.380	9.840	9.840
M 14	1.804	1.804	1.804	1.804	1.804	1.804	1.804	1.804	1.804	1.804	1.804	1.804	1.804	1.804	1.804	1.804	1.804	1.804	1.804	1.804	1.804
M 15	1.838	1.838	1.838	1.838	1.838	1.838	1.838	1.838	1.838	1.838	1.838	1.838	1.838	1.838	1.838	1.838	1.838	1.838	1.838	1.838	3.676
M 16	1.360	1.360	1.360	1.360	1.360	1.360	1.360	1.360	1.360	1.360	1.360	1.360	1.360	1.360	1.360	1.360	1.360	1.360	1.360	1.360	1.360
Total Volume	20.873	20.873	23.673	23.673	24.680	26.680	26.680	26.680	26.680	26.680	29.140	31.484	31.484	34.284	34.284	34.284	34.284	35.291	35.291	37.751	41.589
Load/Volume	0.479	0.527	0.507	0.549	0.567	0.562	0.600	0.637	0.675	0.712	0.686	0.667	0.699	0.671	0.700	0.729	0.758	0.765	0.793	0.768	0.721
Most Efficient	0.806	0.847	0.789	0.841	0.906	0.848	0.876	0.830	0.879	0.881	0.889	0.910	0.912	0.900	0.902	0.940	0.870	0.904	0.927	0.901	0.918

TABLE 4. Strength of nodes and struts under design loads

	Node 1 (CCT)	Node 2 (TTT)	Node 3 (CTT)	Node 4 (CCT)	Node 5 (CCT)	Node 6 (TTT)	Node 7 (CTT)	Node 8 (CCC)	Node 9 (CTT)
Strength of Node (psi)	3060	2486	2486	3060	3060	2486	2486	3825	2486
Strength of Strut (psi)	2869	2869	2869	2869	2869	2869	2869	2869	2869
Usable Strength (psi)	2869	2486	2486	2869	2869	2486	2486	2869	2486

the usable strength, f_{ce}, in the calculation of the width of the struts/ties using the following equation:

$$w_t = \frac{P}{f_{ce} * 3.5 \ in} \tag{4}$$

The width of all struts and ties for the specimen can be found in Table 5. For the 25-kip design loading the width of all struts and ties was found to be within the dimensions of the specimen, therefore, the full strength of the strut and tie layout could be utilized.

The selection of steel rebar for the model was based primarily on the number of possible bars that fit within the 3.5-inch thickness of the specimen. The maximum amount of any size bar that would fit was 3 bars, based on spacing and ease of placing the bars when constructing

the specimen. Therefore, mostly No. 4 bars were used in high-stress areas such as members 9 and 13, which used 2 No. 4 and 3 No. 4 bars, respectively. A cross-section of the steel rebar layout used can be found in Figure 8. The efficiency of this rebar layout was 0.729 kips/volume, which is about 37% less than the most efficient layout calculated. This efficiency was found to be satisfactory due to the feasibility and ease of constructability parameters.

The steel layout was constructed using 5 continuous pieces of rebar. This procedure was done to ensure an effective amount of development length was present at each node. The continuation of rebar through most of the nodes also increased the stability and strength at the nodes.

TABLE 5. Width of struts and ties under design loads

Load (kips)	10	11	12	13	14	15	16	17	18	19	20	21	22	23	24	25	26	27	28	29	30
Member										Width Of Strut/Tie (in)											
M1	0.434	0.477	0.521	0.564	0.607	0.651	0.694	0.738	0.781	0.824	0.868	0.911	0.954	0.998	1.041	1.085	1.128	1.171	1.215	1.258	1.302
M2	0.685	0.753	0.822	0.890	0.959	1.027	1.096	1.164	1.233	1.301	1.370	1.438	1.507	1.575	1.644	1.712	1.781	1.849	1.917	1.986	2.054
M3	0.183	0.201	0.219	0.238	0.256	0.274	0.293	0.311	0.329	0.347	0.366	0.384	0.402	0.421	0.439	0.457	0.475	0.494	0.512	0.530	0.549
M4	0.165	0.181	0.198	0.214	0.231	0.247	0.264	0.280	0.297	0.313	0.330	0.346	0.363	0.379	0.396	0.412	0.429	0.445	0.462	0.478	0.495
M5	1.183	1.301	1.419	1.538	1.656	1.774	1.892	2.011	2.129	2.247	2.366	2.484	2.602	2.720	2.839	2.957	3.075	3.194	3.312	3.430	3.548
M6	0.971	1.068	1.166	1.263	1.360	1.457	1.554	1.651	1.748	1.845	1.943	2.040	2.137	2.234	2.331	2.428	2.525	2.622	2.720	2.817	2.914
M7	0.802	0.882	0.962	1.042	1.122	1.202	1.282	1.363	1.443	1.523	1.603	1.683	1.763	1.844	1.924	2.004	2.084	2.164	2.244	2.324	2.405
M8	0.665	0.732	0.798	0.865	0.931	0.998	1.064	1.131	1.198	1.264	1.331	1.397	1.464	1.530	1.597	1.663	1.730	1.796	1.863	1.929	1.996
M9	0.780	0.858	0.937	1.015	1.093	1.171	1.249	1.327	1.405	1.483	1.561	1.639	1.717	1.795	1.873	1.951	2.029	2.107	2.185	2.263	2.341
M10	0.598	0.658	0.718	0.777	0.837	0.897	0.957	1.017	1.076	1.136	1.196	1.256	1.316	1.375	1.435	1.495	1.555	1.615	1.674	1.734	1.794
M11	0.263	0.290	0.316	0.342	0.369	0.395	0.421	0.448	0.474	0.500	0.527	0.553	0.579	0.606	0.632	0.658	0.685	0.711	0.737	0.764	0.790
M12	0.379	0.417	0.455	0.493	0.530	0.568	0.606	0.644	0.682	0.720	0.758	0.796	0.833	0.871	0.909	0.947	0.985	1.023	1.061	1.099	1.137
M13	0.937	1.031	1.124	1.218	1.312	1.405	1.499	1.593	1.687	1.780	1.874	1.968	2.061	2.155	2.249	2.342	2.436	2.530	2.624	2.717	2.811
M14	0.190	0.209	0.228	0.247	0.265	0.284	0.303	0.322	0.341	0.360	0.379	0.398	0.417	0.436	0.455	0.474	0.493	0.512	0.531	0.550	0.569
M15	0.309	0.340	0.370	0.401	0.432	0.463	0.494	0.525	0.556	0.587	0.617	0.648	0.679	0.710	0.741	0.772	0.803	0.834	0.864	0.895	0.926
M16	0.080	0.088	0.096	0.104	0.112	0.120	0.128	0.136	0.144	0.152	0.160	0.168	0.176	0.184	0.192	0.200	0.208	0.216	0.224	0.232	0.240
M17	0.273	0.300	0.327	0.355	0.382	0.409	0.437	0.464	0.491	0.518	0.546	0.573	0.600	0.628	0.655	0.682	0.710	0.737	0.764	0.791	0.819

*Light gray member denotes tension tie

3. RESULTS AND DISCUSSION

The experimental results were analyzed in terms of crack patterns, load deflection analysis, and load-to-steel weight ratio to find the efficiency of the antisymmetric reinforced concrete deep beams with openings under concentrated loading using the Strut and Tie Model. The following are the results obtained from the testing performed on the specimens.
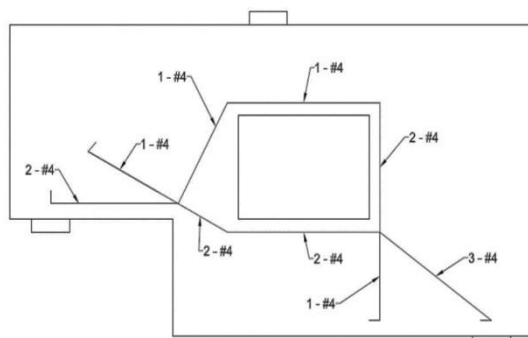
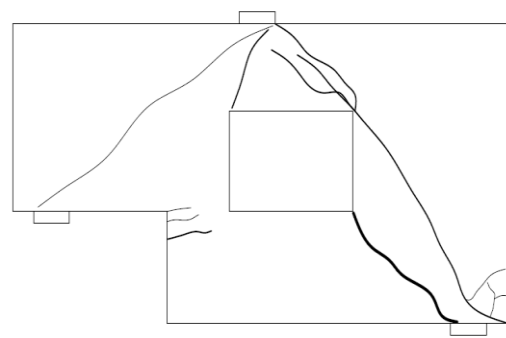**Figure 8.** Steel rebar layout for the concrete specimen

Figure 9. The crack pattern of Specimen 1 at failure

3.1. Crack Patterns   In each structural element test, the crack patterns give an idea about the mode of failure. The failure mode and crack patterns are illustrated in Figures 9 to 12. The crack patterns induced on Specimen 1 were studied as shown in Figure 9. The first specimen showed a shear failure mode. At the early load stage, a visible crack was formed first at the bottom right support toward the applied point load. Cracking then began to form at the top left corner of the central opening. Once the cracking fully developed, shear failure rapidly occurred at the peak load as shown in Figure 10. Specimen 2 showed a local shear failure at two separate locations, at the top and bottom of the central opening. During the service load, a crack started from the point load and propagated to the top right corner of the central opening, resulting in local shear failure. A new crack then began to develop at the bottom of the specimen and progressed towards the central opening, creating the second area of local shear failure, as shown in Figure 11. The crack patterns for Specimen 3 were investigated and showed a flexural mode of failure with local shear failure. At the service load stage, a crack was formed at the bottom end of the specimen and propagated vertically toward the central opening. Many visible hairline cracks developed at the top left corner of the opening and went rapidly to the point load where crushing had already occurred in concrete beneath the bearing plate, as shown in Figure 12.

3. 2. Load Deflection Analysis   The load-deflection curve for all specimens was investigated. All specimens failed at peak loads lower than design loads, except Specimen 3. Load-deflection curves for each specimen showed an approximately linear response until the peak load. For Specimen 1, the ultimate load was 22 kips with 0.14-inch deflection, while its design capacity was 25 kips. The specimen exhibited a rapid drop at the peak load, which is an indication of shear failure. Specimen 2 achieved the highest peak load of 29.297 kips with 0.22 inches of deflection; however, the design load for this specimen was 35 kips. The specimen also shows a rapid loading drop after the peak load, resulting in a shear

Figure 10. The failure mode in Specimen 1

Figure 11. The failure mode in Specimen 2

Figure 12. The failure mode in Specimen 3

failure. The final Specimen 3 reached an ultimate load of 17.75 kips with 0.34 inches of deflection, which was

slightly greater than the design load of 17 kips. The progressive downward trend of the deflection after the peak load indicates the behavior of a flexural failure followed by local shear failure at the rapid drop in loading.

3. 3. Load to Steel Weight Ratio   Efficiency in terms of load/weight of steel was the defining parameter in determining which specimen was the most effective. To establish the best reinforcement layout the weight of each specimen was calculated and divided by the ultimate load reached during testing. The weights for each type of reinforcement, flexural and shear, and the total reinforcement for each specimen, including the weight of the bar hooks, as summarized in Table 6.

Specimen 1 used the least amount of total reinforcement steel at 13.17 lb. This low weight was due to the exclusion of shear reinforcement in the steel design layout. Specimen 2 included shear reinforcement in the amount of 2.578 lb, but the flexural reinforcement of 17.189 lb amassed a total reinforcement weight of 19.767 lb. Specimen 3 used both flexural and shear reinforcement of 8.8 lb and 4.71 lb, respectively, measuring 13.51 lb of total reinforcement.

The specimen with the highest efficiency was Specimen 1 with a value of 1.67 kips/lb of steel. This specimen was 12.8% and 27.4% more efficient than Specimens 2 and 3, respectively. The efficiency for each specimen stated in Table 7.

TABLE 6. Weights of each type of reinforcement used in the strut and tie model for each specimen

Specimens	Flexural Reinforcement	Shear Reinforcement	Total Reinforcement
	Weight (1b)	Weight (1b)	Weight (1b)
1	13.170	0.000	13.170
2	17.189	2.578	19.767
3	8.800	4.710	13.510

TABLE 7. Load/weight ratio efficiencies for each specimen

Specimens	Reinforcement	Ultimate Load	Design Load	Deflection at	Efficiency
	(lb)	(kips)	(kips)	Ultimate (in)	(kips/lb)
1	13.170	22.000	25.000	0.140	1.670
2	19.767	29.297	35.000	0.220	1.480
3	13.510	17.750	16.000	0.340	1.310

4. CONCLUSIONS

1. It can be concluded that the efficient reinforcement layout of the strut and tie model leads to the highest efficiency of the model, regardless of the value of the externally applied load.
2. A comparison between the three specimens showed Specimen 1 had the highest efficiency of 1.67, while Specimen 3 had the lowest efficiency of 1.31. Specimen 1 reached 88% of its designed load, while Specimen 2 reached 83.7% of its design load.
3. By looking at the mode failure of Specimen 1, which failed due to shear, if the specimen included shear reinforcement, the design load may have been attained.
4. Due to the exclusion of shear reinforcement in Specimen 1, the ductility of the specimen was much lower compared to the other specimens.
5. All specimens were within the serviceability limit for deflection of 0.48 inches. The deflection of Specimen 1 was 57% less than Specimen 2 and 143% less than Specimen 3. The lack of ductility in this specimen leads to brittle failure.
6. From the analysis of these results, it is clear that the strut and tie model of Specimen 1 would have provided reasonable ductility for the applied load if shear reinforcement had been added to the deeper section of the specimen.
7. Based on the results of the research, reinforcement of antisymmetric reinforced concrete deep beams can be designed. Fundamental tests of at least 20 samples must be done before the production of the respective ones.

5. REFERENCES

1. Shear, A.-A.C.o. and Torsion, "Recent approaches to shear design of structural concrete", *Journal of Structural Engineering*, Vol. 124, No. 12, (1998), 1375-1417, https://doi.org/10.1061/(ASCE)0733-9445(1998)124:12(1375)

2. "American association of state highway officials and transportation (aashto), "lrfd bridge design specifications. 7th edition ed."", in AASHTO, Washington, DC, (2014 of Conference).

3. Committee, A., "Building code requirements for structural concrete (aci 318-08) and commentary, American Concrete Institute. (2008).

4. Association, C.S., "Design of concrete structures (csa a23. 3-04)", *CSA, Rexdale, Ontario*, (2004).

5. Institution, B.S., "Eurocode 2: Design of concrete structures: Part 1-1: General rules and rules for buildings, British Standards Institution, (2004).

6. Taerwe, L. and Matthys, S., *Fib model code for concrete structures 2010*. 2013, Ernst & Sohn, Wiley.

7. Ritter, W., "The hennebique design method (die bauweise hennebique)", *Schweizerische Bauzeitung (Zurich)*, Vol. 33, No. 7, (1899), 59-61.

8. Mörsch, E., "Concrete-steel construction:(der eisenbetonbau), Engineering news publishing Company, (1909).

9. Schlaich, J., Schäfer, K. and Jennewein, M., "Toward a consistent design of structural concrete", *PCI journal*, Vol. 32, No. 3, (1987), 74-150.

10. Schlaich, J. and Schafer, K., "Design and detailing of structural concrete using strut-and-tie models", *Structural Engineer*, Vol. 69, No. 6, (1991), 113-125.

11. Xie, Y.M. and Steven, G.P., "A simple evolutionary procedure for structural optimization", *Computers & Structures*, Vol. 49, No. 5, (1993), 885-896, https://doi.org/10.1016/0045-7949(93)90035-C.

12. Yang, X.Y., Xie, Y.M., Steven, G.P. and Querin, O., "Bidirectional evolutionary method for stiffness optimization", *AIAA Journal*, Vol. 37, No. 11, (1999), 1483-1488, https://doi.org/10.2514/2.626

13. Liang, Q.Q., Xie, Y.M. and Steven, G.P., "Topology optimization of strut-and-tie models in reinforced concrete structures using an evolutionary procedure", *Structural Journal*, Vol. 97, No. 2, (2000), 322-330.

14. Liang, Q.Q., Xie, Y.M. and Steven, G.P., "Generating optimal strut-and-tie models in prestressed concrete beams by performance-based optimization", *ACI Structural Journal*, Vol. 98, No. 2, (2001), 226-232.

15. Cai, C.S., "Three-dimensional strut-and-tie analysis for footing rehabilitation", *Practice Periodical on Structural Design and Construction*, Vol. 7, No. 1, (2002), 14-25, https://doi.org/10.1061/(ASCE)1084-0680(2002)7:1(14)

16. Leu, L.-J., Huang, C.-W., Chen, C.-S. and Liao, Y.-P., "Strut-and-tie design methodology for three-dimensional reinforced concrete structures", *Journal of Structural Engineering*, Vol. 132, No. 6, (2006), 929-938, https://doi.org/10.1061/(ASCE)0733-9445(2006)132:6(929)

17. Nagarajan, P. and Pillai, T.M., "Development of strut and tie models for simply supported deep beams using topology optimization", *Sonklanakarin Journal of Science and Technology*, Vol. 30, No. 5, (2008), 641.

18. Bruggi, M., "Generating strut-and-tie patterns for reinforced concrete structures using topology optimization", *Computers & Structures*, Vol. 87, No. 23-24, (2009), 1483-1495, https://doi.org/10.1016/j.compstruc.2009.06.003

19. Guest, J.K., "Imposing maximum length scale in topology optimization", *Structural and Multidisciplinary Optimization*, Vol. 37, (2009), 463-473, https://doi.org/10.1007/s00158-008-0250-7

20. Guest, J.K. and Moen, C.D., "Reinforced concrete design with topology optimization", in Structures Congress 2010: 19th Analysis and Computation Specialty Conference. (2010), 445-454. https://doi.org/10.1061/41131(370)39

21. Herranz, J.P., Santa María, H., Gutierrez, S. and Riddell, R., "Optimal strut-and-tie models using full homogenization optimization method", *ACI Structural Journal*, Vol. 109, No. 5, (2012), 605.

22. Almeida, V.S., Simonetti, H.L. and Neto, L.O., "Comparative analysis of strut-and-tie models using smooth evolutionary structural optimization", *Engineering Structures*, Vol. 56, (2013), 1665-1675, https://doi.org/10.1016/j.engstruct.2013.07.007

23. Palmisano, F. and Elia, A., "Shape optimization of strut-and-tie models in masonry buildings subjected to landslide-induced settlements", *Engineering Structures*, Vol. 84, (2015), 223-232, https://doi.org/10.1016/j.engstruct.2014.11.030

24. Palmisano, F., Alicino, G. and Vitone, A., "Nonlinear analysis of rc discontinuity regions by using the bi-directional evolutionary structural optimization method", in Proc. of the OPT-I, An

International Conference on Engineering and Applied Sciences Optimization. (2014), 749-758.

25. Bruggi, M., "A numerical method to generate optimal load paths in plain and reinforced concrete structures", *Computers & Structures*, Vol. 170, (2016), 26-36, https://doi.org/10.1016/j.compstruc.2016.03.012

26. El-Metwally, S. and Chen, W.-F., "Structural concrete: Strut-and-tie models for unified design, CRC Press, (2017).

27. Chen, H., Yi, W.-J. and Hwang, H.-J., "Cracking strut-and-tie model for shear strength evaluation of reinforced concrete deep beams", *Engineering Structures*, Vol. 163, (2018), 396-408, https://doi.org/10.1016/j.engstruct.2018.02.077

28. Geevar, I. and Menon, D., "Strength of reinforced concrete pier caps-experimental validation of strut-and-tie method", *ACI Structural Journal*, Vol. 116, No. 1, (2019).

29. Al-Ameri, A., Jawad, F. and Fattah, M., "Vertical and lateral displacement response of foundation to earthquake loading", *International Journal of Engineering, Transactions A: Basics*, Vol. 33, No. 10, (2020), 1864-1871, doi: 10.5829/IJE.2020.33.10A.05.

30. Hussein, A., Al-Neami, M. and Rahil, F., "Effect of hydrodynamic pressure on saturated sand supporting liquid storage tank during the earthquake", *International Journal of Engineering, Transactions B: Applications*, Vol. 34, No. 5, (2021), 1176-1183, doi: 10.5829/IJE.2021.34.05B.11.

31. Xia, Y., Langelaar, M. and Hendriks, M.A., "Automated optimization-based generation and quantitative evaluation of strut-and-tie models", *Computers & Structures*, Vol. 238, (2020), 106297, https://doi.org/10.1016/j.compstruc.2020.106297

32. Xia, Y., Langelaar, M. and Hendriks, M.A., "Optimization-based three-dimensional strut-and-tie model generation for reinforced concrete", *Computer-Aided Civil and Infrastructure Engineering*, Vol. 36, No. 5, (2021), 526-543, https://doi.org/10.1111/mice.12614

33. Xia, Y., Langelaar, M. and Hendriks, M.A., "Optimization-based strut-and-tie model generation for reinforced concrete structures under multiple load conditions", *Engineering Structures*, Vol. 266, (2022), 114501, https://doi.org/10.1016/j.engstruct.2022.114501

34. Kassem, M.M., Nazri, F.M., Farsangi, E.N. and Ozturk, B., "Improved vulnerability index methodology to quantify seismic risk and loss assessment in reinforced concrete buildings", *Journal of Earthquake Engineering*, Vol. 26, No. 12, (2022), 6172-6207, https://doi.org/10.1080/13632469.2021.1911888

35. Kassem, M.M., Nazri, F.M., Farsangi, E.N. and Ozturk, B., "Development of a uniform seismic vulnerability index framework for reinforced concrete building typology", *Journal of Building Engineering*, Vol. 47, (2022), 103838, https://doi.org/10.1016/j.jobe.2021.103838

36. Jabbar, A.M., Mohammed, D.H. and Hasan, Q.A., "A numerical study to investigate shear behavior of high-strength concrete beams externally retrofitted with carbon fiber reinforced polymer sheets", *International Journal of Engineering, Transactions B: Applications,*, Vol. 36, No. 11, (2023), 2112-2123, doi: 10.5829/IJE.2023.36.11B.15.

37. Mohammed, A., Al-Zuheriy, A. and Abdulkareem, B., "An experimental study to predict a new formula for calculating the deflection in wide concrete beams reinforced with shear steel plates", *International Journal of Engineering, Transactions B: Applications*, Vol. 36, No. 2, (2023), 360-371, doi: 10.5829/IJE.2023.36.02B.15.

38. Chaudhari, A.D. and Suryawanshi, S., "Development and calibration of an efficiency factor model for recycled aggregate concrete struts", *International Journal of Engineering, Transactions B: Applications*, Vol. 36, No. 8, (2023), 1449-1458, doi: 10.5829/IJE.2023.36.08B.05.

Persian Abstract

چکیده

تکنیک مدل‌سازی (STM) یک روش کاربردی و ارزشمند برای مهندسان سازه برای طراحی مناطق آشفته-D مناطق سازه‌های بتن مسلح است که در آن فرض باقی‌مانده مقاطع صفحه پس از بارگذاری غیرقابل اجرا است. مهمترین جنبه برای تضمین عملکرد مناسب سازه ای و اقتصادی طرح، یافتن یک مدل قیاسی خرپایی مناسب است که منجر به استفاده از مدل کارآمدتر در ساختمان های سازه می شود. ارزیابی مدل‌های ضد متقارن(STM) با دهانه‌های تحت بارهای خارجی متمرکز مختلف به طور جامع در ادبیات بررسی نشده است. بنابراین، برای پرداختن به این شکاف، هدف این مقاله دستیابی به کارآمدترین طرح آرماتور در تیرهای عمیق بتن مسلح ضد متقارن با بازشوهای تحت بارگذاری متمرکز با استفاده از مدل پایه و کراوات است. کار آزمایشی انجام شد و شامل (۳) تیرهای عمیق بتن مسلح ضد متقارن با دهانه‌هایی بود که تحت بارهای متمرکز مختلف (به ترتیب ۲۵، ۳۵، و ۱۶ کیپس برای نمونه‌های ۱، ۲ و ۳) با استفاده از مدل پایه و کراوات آزمایش شدند. نرم افزار ANSYS FEM برای آنالیز پایه و کراوات اولیه و برنامه تحلیل سازه RISA-3D برای یافتن نیروهای داخلی برای همه اعضا تحت بارهای خارجی متمرکز در هر نمونه استفاده می شود. یافته‌های این مقاله نشان می‌دهد که نمونه ۱ با ۱/۶۷ بیشترین بازده و نمونه ۳ با ۱/۳۱ کمترین راندمان را داشته است. می‌توان نتیجه گرفت که چیدمان تقویت‌کننده کارآمد مدل پایه و کراوات بدون در نظر گرفتن مقدار بار اعمال‌شده خارجی، منجر به بالاترین بازده مدل می‌شود.

AIMS AND SCOPE

The objective of the International Journal of Engineering is to provide a forum for communication of information among the world's scientific and technological community and Iranian scientists and engineers. This journal intends to be of interest and utility to researchers and practitioners in the academic, industrial and governmental sectors. All original research contributions of significant value focused on basics, applications and aspects areas of engineering discipline are welcome.

This journal is published in three quarterly transactions: Transactions A (Basics) deal with the engineering fundamentals, Transactions B (Applications) are concerned with the application of the engineering knowledge in the daily life of the human being and Transactions C (Aspects) - starting from January 2012 - emphasize on the main engineering aspects whose elaboration can yield knowledge and expertise that can equally serve all branches of engineering discipline.

This journal will publish authoritative papers on theoretical and experimental researches and advanced applications embodying the results of extensive field, plant, laboratory or theoretical investigation or new interpretations of existing problems. It may also feature - when appropriate - research notes, technical notes, state-of-the-art survey type papers, short communications, letters to the editor, meeting schedules and conference announcements. The language of publication is English. Each paper should contain an abstract both in English and in Persian. However, for the authors who are not familiar with Persian, the publisher will prepare the latter. The abstracts should not exceed 250 words.

All manuscripts will be peer-reviewed by qualified reviewers. The material should be presented clearly and concisely:

- *Full papers* must be based on completed original works of significant novelty. The papers are not strictly limited in length. However, lengthy contributions may be delayed due to limited space. It is advised to keep papers limited to 7500 words.
- *Research* notes are considered as short items that include theoretical or experimental results of immediate current interest.
- *Technical notes* are also considered as short items of enough technical acceptability with more rapid publication appeal. The length of a research or technical note is recommended not to exceed 2500 words or 4 journal pages (including figures and tables).

Review papers are only considered from highly qualified well-known authors generally assigned by the editorial board or editor in chief. Short communications and letters to the editor should contain a text of about 1000 words and whatever figures and tables that may be required to support the text. They include discussion of full papers and short items and should contribute to the original article by providing confirmation or additional interpretation. Discussion of papers will be referred to author(s) for reply and will concurrently be published with reply of author(s).

INSTRUCTIONS FOR AUTHORS

Submission of a manuscript represents that it has neither been published nor submitted for publication elsewhere and is result of research carried out by author(s). Presentation in a conference and appearance in a symposium proceeding is not considered prior publication.

Authors are required to include a list describing all the symbols and abbreviations in the paper. Use of the international system of measurement units is mandatory.

- On-line submission of manuscripts results in faster publication process and is recommended. Instructions are given in the IJE web sites: www.ije.ir-www.ijeir.info
- Hardcopy submissions must include MS Word and jpg files.
- Manuscripts should be typewritten on one side of A4 paper, double-spaced, with adequate margins.
- References should be numbered in brackets and appear in sequence through the text. List of references should be given at the end of the paper.
- Figure captions are to be indicated under the illustrations. They should sufficiently explain the figures.
- Illustrations should appear in their appropriate places in the text.
- Tables and diagrams should be submitted in a form suitable for reproduction.
- Photographs should be of high quality saved as jpg files.
- Tables, Illustrations, Figures and Diagrams will be normally printed in single column width (8cm). Exceptionally large ones may be printed across two columns (17cm).

PAGE CHARGES AND REPRINTS

The papers are strictly limited in length, maximum 8 journal pages (including figures and tables). For the additional to 8 journal pages, there will be page charges. It is advised to keep papers limited to 3500 words.

Page Charges for Papers More Than 8 Pages (Including Abstract)	
For International Author ***	**$55 / per page**
For Local Author	**100,000 Toman / per page**

AUTHOR CHECKLIST

- Author(s), bio-data including affiliation(s) and mail and e-mail addresses).
- Manuscript including abstracts, key words, illustrations, tables, figures with figure captions and list of references.
- MS Word files of the paper.